CONF-9104201--

ANL/APS/TM-9

Applications of Synchrotron Radiation to Chemical Engineering Science: Workshop Report

Proceedings of a workshop held at
Argonne National Laboratory
April 22-23, 1991

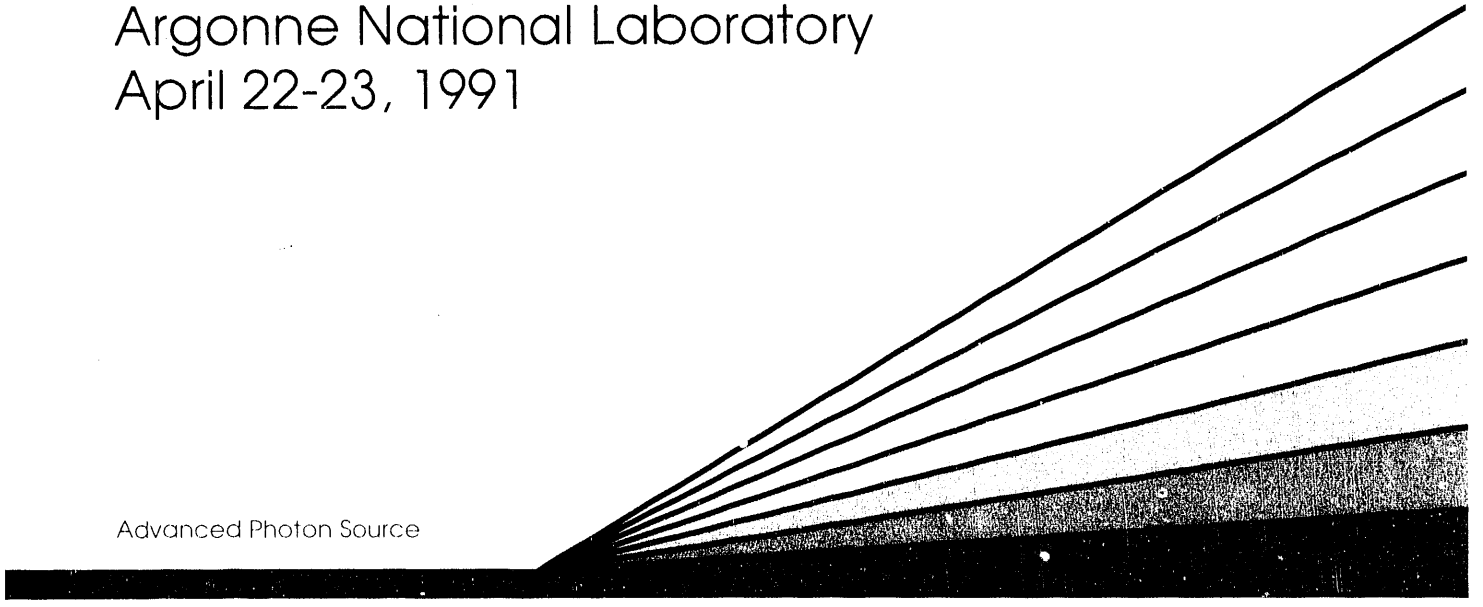

Advanced Photon Source

Argonne National Laboratory
operated by The University of Chicago for the U.S. Department of Energy under Contract W-31-109-Eng-38

Argonne National Laboratory, with facilities in the states of Illinois and Idaho, is owned by the United States government, and operated by The University of Chicago under the provisions of a contract with the Department of Energy.

Reproduced from the best available copy.

Available to DOE and DOE contractors from the
Office of Scientific and Technical Information
P.O. Box 62
Oak Ridge, TN 37831
Prices available from (615) 576-8401, FTS 626-8401

Available to the public from the
National Technical Information Service
U.S. Department of Commerce
5285 Port Royal Road
Springfield, VA 22161

Distribution Category:
Chemistry (UC-401)

ARGONNE NATIONAL LABORATORY
9700 South Cass Avenue
Argonne, Illinois 60439

ANL/APS/TM--9

DE92 007415

ANL/APS/TM-9

APPLICATIONS OF SYNCHROTRON RADIATION TO CHEMICAL ENGINEERING SCIENCE: WORKSHOP REPORT

Proceedings of a workshop held at
Argonne National Laboratory
April 22-23, 1991

Workshop Organizers:

Deon Ettinger, Division of Educational Programs
Victor A. Maroni, Materials Science Division/Chemical Technology Division
W. Elane Streets, Chemical Technology Division/Analytical Chemistry Division
Shiu-Wing Tam, Chemical Technology Division

July 1991

work sponsored by

U.S. DEPARTMENT OF ENERGY
Office of Energy Research

CONTENTS

CONTENTS (cont'd)

FOREWORD

The current generation of synchrotron research facilities has brought about a renaissance in diagnostic science. The Advanced Photon Source, the Advanced Light Source, and comparable synchrotron sources under construction in Europe and Japan will further enhance the powerful investigative capabilities afforded by intense photon beams. These capabilities could hardly be described more aptly than by the following poetic and prophetic lore Gene Ice shared with the workshop attendees:

How the Photons Became a Great Microprobe

When Gitchi Manitu, the great spirit, created the diagnostic microprobes, he created three great tribes. These were the ions, the electrons, and the photons. To each tribe he gave gifts to help them probe for elements so they might be useful and thrive. Now all the probes had different gifts, but for finding the few elements in a herd of others, none was as good as the photons. Yet though each photon was unexcelled in skill and cunning, they were few in number and could not come together for a great hunt. And so it was that the electron tribe prospered, for they bred like flies on the bloated Buffalo and were eager to join together for the great hunt. Then Gitchi Manitu looked down and saw that although the photons were each as 10,000 electrons, they did not prosper in their hunt and he said to himself, this is not good. So he built a special home for the photons where they could multiply like the stars in the sky and where the photons were born already joined together in the great hunt. And he called this place undulator and the photons went out and hunted the few elements and found them where the other tribes had not. And Gitchi Manitu smiled and said it was good, and he said to the photons, what shall we hunt today (Gene E. Ice, April 23, 1991)

ACKNOWLEDGMENTS

The *Workshop on Applications of Synchrotron Radiation to Chemical Engineering Science* was jointly sponsored by the Advanced Photon Source, the Chemical Technology Division, and the Division of Educational Programs at Argonne National Laboratory. The workshop organizers and attendees are grateful to these sponsors for making the workshop possible and to all of the invited speakers for sharing their insights and, in many cases, their research results.

The workshop organizers also wish to thank Martin J. Steindler, Milton Blander, David W. Green, and Dennis W. Dees for serving as session chairmen; Susan H. Barr and Susan Picologlou for their tireless efforts in helping with workshop arrangements and the preparation of this report. The assistance of Joan S. Brunsvold and Stephanie Malm in the preparation of workshop documents, registration materials, lodging arrangements, and many other matters is also gratefully acknowledged.

APPLICATIONS OF SYNCHROTRON RADIATION TO CHEMICAL ENGINEERING SCIENCE: WORKSHOP REPORT

ABSTRACT

This report contains extended abstracts that summarize presentations made at the *Workshop on Applications of Synchrotron Radiation to Chemical Engineering Science* held at Argonne National Laboratory (ANL), Argonne, IL, on April 22-23, 1991. The talks emphasized the application of techniques involving absorption, fluorescence, diffraction, and reflection of synchrotron x-rays, with a focus on problems in applied chemistry and chemcial engineering, as well as on the use of x-rays in topographic, tomographic, and lithographic procedures. The attendees at the workshop included experts in the field of synchrotron science; scientists and engineers from ANL, other national laboratories, industry, and universities; and graduate and undergraduate students who were enrolled in ANL educational programs at the time of the workshop.

The plenary address by Dr. Keith McHenry of Amoco Corporation provided a stimulating summary of challenges to chemical engineers in the energy and environment fields. Subsequent talks in the Plenary and Overview Session described the status of and special capabilities to be offered by the Advanced Photon Source (APS), as well as strategies and opportunities for utilization of synchrotron radiation to solve science and engineering problems. Invited talks given in subsequent sessions covered the use of intense infared, ultraviolet, and x-ray photon beams (as provided by synchrotrons) in traditional and nontraditional areas of chemical engineering research related to electrochemical and corrosion science, catalyst development and characterization, lithography and imaging techniques, and microanalysis. During the course of the workshop, the attendees had an opportunity to visit the APS site and to observe the results of the site preparation effort. Some of the workshop participants also stayed an extra day to attend a special round table discussion on strategies for gaining access to the APS. This discussion opened with an overview of APS user access policy given by Gopal Shenoy (APS).

PART I: PLENARY AND OVERVIEW PRESENTATIONS

ENERGY AND ENVIRONMENTAL CHALLENGES TO CHEMICAL ENGINEERS

Keith W. McHenry
Technology Department
Amoco Corporation
200 E. Randolph Dr., Chicago, IL 60601

1. Abstract

The National Research Council's report, *Frontiers in Chemical Engineering*, was written four years ago. Three high-priority research areas concerned with energy and the environment were identified in the report: *in situ* processing, liquid fuels for the future, and responsible management of hazardous wastes.

As outlined in the recently released *National Energy Strategy*, *in situ* processing is viewed by the Department of Energy (DOE) primarily through its use in enhanced oil recovery, and some research is still funded. Industry, driven by the economics of low oil prices, is doing little research on *in situ* processing but much more on reservoir characterization, a prerequisite to processing.

Research on liquid fuels for the future is driven more by environmental concerns now than by energy security concerns. An example is the Auto/Oil Air Quality Improvement Research Program. Its objective is the most cost-effective method for improving air quality through combinations of fuels and vehicles. Detailed measurements of emissions from various reformulated gasolines and methanol were made on representative vehicles. Early analyses of results show that complex interactions among fuel properties and vehicles control emissions and that the effects of all the fuels have minimal impact on ozone. The challenge to chemical engineers is to find those alternative fuels that, when combined with the right vehicles, will clean up the air.

Three strategies that have been used to manage sulfur emissions from a catalytic cracker exemplify responsible management of hazardous wastes. The first was to scrub out sulfur oxides from the stack. The second was to change the catalyst to enable recovery of sulfur by using a system already in place. The third was to remove sulfur from the feed and thus solve both the stack problem and problems resulting from the presence of sulfur in the products. The generic challenge is to find ways to clean up processes at the source rather than at the end of the waste pipe or stack.

It appears to be wise policy for the future to try to solve the alternative fuel problem as quickly and simply as possible. Otherwise, the nation will find itself with a costly and complex fuel and vehicle system that may have to be changed again in a generation. For the interim, we should look closely at reformulated gasoline followed by compressed natural gas, if necessary.

In the long run, vehicle systems based on electricity seem most promising for the middle of the next century. To deliver this technology we need to capitalize on three new high-priority research areas: batteries, fuel cells, and nuclear power. For

chemical engineers, future challenges of a different sort will be added to the technical challenges, among them are explaining to a skeptical public the wisdom of proceeding to design the interim system of alternative fuel(s) and to move expeditiously to a final solution.

2. Introduction

"Applications of Synchrotron Radiation to Chemical Engineering Science" is an exciting topic, one that would have been unheard of just a few years ago, and I commend your organizers for an outstanding workshop. The title of your workshop is not the topic of these remarks because it seemed useful to talk about two areas, energy and the environment, that are challenging chemical engineers to probe the depth of their science and the breadth of their eclectic education. I will leave it to you to relate what I have to say to synchrotron radiation.

The *Frontiers in Chemical Engineering Research* report of a few years ago will give us a vehicle to travel around the challenges. It will give us a look back. We will then compare what we find there to what we see out the window in April of 1991, aided by the administration's assessment of reality in the *National Energy Strategy*. And, finally, I will share my look into the ever-cloudy crystal ball to view the energy and environmental demands of the future.

3. The View from 1987

In the spring of 1988, the National Research Council published a book-sized report: *Frontiers in Chemical Engineering - Research Needs and Opportunities*. A steering committee of members of the National Academy of Engineering managed the process of producing the report with invaluable help from a host of volunteers, including Les Burris of Argonne. Despite the 1988 publication date, the report was essentially written in early 1987, and thus represents a four-year-old view. Let me hit some of the highlights of that view.

Eight high-priority research areas were identified in the report: biotechnology, electronic materials, microstructured materials, *in situ* processing of resources, liquid fuels for the future, responsible management of hazardous substances, advanced computational methods, and surface and interfacial engineering.

The two highly linked topics I'll talk about today, energy and the environment, are reflected in the technology list through *in situ* processing of resources, liquid fuels for the future, and responsible management of hazardous substances. It is interesting to note which potential funders were connected to these three areas in 1987.

In situ processing of resources was thought to be the primary purview of only the Department of Energy and the Bureau of Mines, with supporting interest by the National Science Foundation. It was expected that there would be little funding by industry.

In the energy field, that view has been proved about correct. The support by DOE of advanced oil recovery methods research, one kind of *in situ* processing research, has continued, and the topic is given prominent consideration in the *National Energy Strategy*. The National Science Foundation (NSF) continues to fund some basic research in surfactants, but, as pointed out in the *Frontiers* report, this is not the key problem in *in situ* recovery—reservoir characterization is. Industry is progressing very well on reservoir characterization through the use of new computing techniques and hardware. This work is not currently directed toward new methods of *in situ* processing, but rather toward more mundane uses like infill drilling and improvement of existing miscible floods. The DOE hopes to involve oil companies in consortia to do more research on advanced oil recovery, but it seems to me unlikely that this will happen. The reservoir models are highly proprietary and specific and not easy to share.

Continued and projected low oil prices, excluding the recent blip up from the Persian Gulf War, will support only those advanced oil recovery projects already in place, like carbon dioxide miscible flooding or steam flooding, and capital available for expansion is very scarce. Some of these projects remain in place only because of tax credits enacted in last year's budget reconciliation legislation.

More complex *in situ* processing, as illustrated by underground coal gasification, heavy oil cracking via combustion with injected air, or *in situ* shale oil recovery, is not currently of much interest. Because it is in these areas where chemical engineers would shine, we will leave advanced oil recovery to the geologists, geophysicists, and petroleum engineers and mention it no further.

Another 1987 high-priority research area of interest to chemical engineers in energy and environmental fields is liquid fuels for the future. Potential funders of that technology were thought to be DOE and industry, with secondary interest from NSF. That is basically a correct view, but there have been important qualitative changes in the objectives of the research.

The final high-priority environment- or energy-related area for research identified in the report was responsible management of hazardous wastes. Only two primary potential funders of research in this area were identified—the Environmental Protection Agency and industry—<u>not</u> DOE or DOD! As usual, NSF was identified as a supporting agency.

All in all, the authors of the *Frontiers* report did a credible job in picking high-priority research areas—not surprising after only four years of additional data on what technologies might be needed. However, they missed on some areas that were covered in the report but not given high priority - primarily because these have been a fast-moving four years. They also missed DOE's current 100 billion dollar interest in hazardous wastes, but that is excusable, given past precedents.

4. Looking Out the Window

As we look out the window at today's technological world of chemical engineers associated with energy or the environment, how do liquid fuels for the future and

responsible management of hazardous wastes stack up in importance? Do they jump up and down to get our attention? You bet they do!

The 1987 view of liquid fuels for the future leaned heavily towards the so-called synthetic fuels—liquids from tar sands, oil shale, and coal.

Tar sand deposits indigenous to the United States have never represented much potential fuel volume relative to liquid fuel sales. The topic of recovery of liquids from tar sands didn't get much attention in the *Frontiers* report and is getting even less research attention today. We need to remember, however, that world-wide resources of tar sands are huge and could well represent an economic cap on the price the world will pay for hydrocarbon fuels in the distant future.

Shale oil got more attention in 1987, but it, too, has been on a downward trend since then. Union Oil's announcement last month of its plan to close its Colorado shale oil plant and Occidental's withdrawal last fall from a joint oil shale project with DOE were driven by a number of factors. Short-term economics were clearly dominant in both cases. My personal opinion is that shale oil from the western slope of the Rockies will never be an important fuel source because of the resulting concentration of potential environmental problems in a relatively small area. Even if we elect to build giant tariff walls around North America, there are hydrocarbons in Canada and Mexico that can be produced with much less environmental impact. The only way the Rockies will serve as a fuel source is if we build tariff walls around the United States.

Coal continues to have appeal as a liquid fuel source because it is ubiquitous. Mines are already scattered in many places, so the environmental impact is perceived to be less. It is also appealing because of its chemical variety. One can do chemistry on several coals to improve a given conversion process, or fit a process to a specific coal. The *National Energy Strategy* specifically points to DOE's coal conversion research to produce alternative fuels. Amoco is a partner in that research, and we, too, believe that the economics can be improved to the NRC target of $30/barrel in the next few years. However, looming ever larger is the perception that converting high-carbon coal to low-carbon liquid fuels will have adverse effects on the global climate through excess carbon dioxide emissions. Measures to control CO_2 could be bad news for coal in all its forms.

A fourth source of liquid fuels mentioned in the *Frontiers* report was natural gas—methane. This area has also continued to generate research dollars. A recent entry is the Gas Utilization Research Forum, or GURF, a consortium of energy companies put together to do precompetitive research aimed at making methane into a transportation fuel.

Methane can become a liquid fuel in two ways. The 1987 report focused on the first way—chemical conversion of methane to liquid hydrocarbons. It mentioned a plant in New Zealand that uses the Mobil methanol-to-gasoline process. Just last year, Shell announced a semi-commercial plant in Indonesia and a possible future plant in North Africa, both using the Fischer-Tropsch process to convert methane to diesel fuel. What is significant about these two examples is their location. In

neither place was there the infrastructure to effectively burn the gas as a power-generating or heating fuel. This is remote natural gas, which must either be cryogenically liquefied or converted chemically to be shipped via tanker to other markets. While this may be a sensible money maker for the oil companies, it would not help this country's dependence on foreign energy sources.

However, a qualitatively different approach to liquid fuels of the future is being driven by the 1990 Clean Air Act. This is the search for fuels with environmental benefits rather than exclusively for fuels to replace foreign petroleum. Alternative fuels, to use the DOE terminology, that do both will get extra-high marks.

This approach leads directly to the second way of using methane, substituting it for liquid fuels simply by compressing it to high enough density to power a vehicle a reasonable number of miles. There is considerable automotive research needed to move beyond simple conversion of existing vehicles—which leads to high exhaust emissions and poor performance—to vehicles that are *optimized* for methane. There is also some intriguing chemical engineering research needed to explore ways of using adsorbents to reduce the fuel-tank pressure. Natural gas has a big advantage over other alternative fuels, especially if local compression costs can be decreased, because it is distributed almost everywhere.

However, the wide-spread use of natural gas as a vehicular fuel in our country will depend very much on the availability of Canadian and Mexican gas. While there is a current U.S. gas surplus, it could be used up quite quickly by converting a significant number of gasoline-powered vehicles to methane-powered vehicles. For example, conversion of 10 percent of the total gasoline fleet would require about a trillion cubic feet of gas annually, which is close to the supply-side increase projected by the *National Energy Strategy* for this decade. Even with Canadian or Mexican gas, we might have difficulty keeping up with the need for electric power plant fuel if we elect to rapidly phase out coal—let alone provide for a major increase in transportation fuel.

One way to phase in the use of natural gas as a vehicular fuel is to use it in private fleets that return to the same refueling point each day. This would implement provisions of the clean air act requiring tougher emissions standards for such fleets. The DOE would like those fleets to use alternative fuels to meet the standards and be able to go to public refueling points rather than to home base every night. I believe that the economics will support enough fleet sales to entice the automobile companies to make optimized natural-gas-only vehicles. If these demonstrate the fuel economy and emissions reductions theoretically possible, then consumers will be interested in buying them, and oil companies will provide service stations with natural gas capabilities. Tax policies on natural gas used as a motor fuel versus taxes on gasoline will clearly be an important nontechnical factor.

Natural gas is certainly not the only alternative fuel of interest for the nineties and beyond. The *National Energy Strategy* is particularly enamored with fuels from renewable sources, ethanol, and in the long range, methanol. The *Frontiers* report gave ethanol based on corn short shrift because of poor overall energy efficiency.

However, the *National Energy Strategy* cites new technology that may offer better economics with non-food-crop sources of biomass.

The *Strategy* document mentions propane and electricity as alternative fuels, but neither of those is likely to make much of a dent in the next 25 years—the former because of limited supply and the latter because of lack of economical technology.

By far, the most research on alternative fuels is currently being carried out on reformulated gasoline. Reformulated gasoline connotes gasoline whose gross composition or physical properties have been changed to decrease its contribution to emissions from the vehicle using it. I believe the first use of the term was by a domestic auto maker who was concerned about how to meet stricter emissions limits coming with the 1990 Clean Air Act. There was also concern about the sometimes-exaggerated claims for the benefits of methanol in early 1990.

As a consequence, in mid-1990 a program under the National Cooperative Research Act was organized by the three domestic auto builders and 14 major oil companies. The objective was to find the most cost-effective way to improve air-quality among the choices of reformulated gasoline in conventional vehicles, methanol in flexible fuel vehicles, and ethanol as a blending agent in average current gasoline-powered vehicles. It was, by far, the most comprehensive program of its kind ever attempted. The eventual experimental design called for some 3,500 tests of fuel/vehicle combinations. The variables in gasoline composition included high and low levels of aromatics, olefins, methyl tertiarybutyl ether, and the end boiling point of the gasoline. A separate set of experiments varied the ethanol content and vapor pressure of average gasoline, and a final set varied the sulfur content of average gasoline. The methanol tests included blends of 85 percent, 10 percent, and zero percent methanol in average gasoline. Thirty-four gasoline-powered vehicles of various ages and odometer readings greater than 10,000 miles, as well as 20 flexible-fuel-powered vehicles, were involved in the tests.

The dependent variables were mass emissions of hydrocarbons, nitrogen oxides, and carbon monoxide in the exhaust. In many tests, about 150 additional chemical species were measured. In addition, evaporative emissions over a diurnal cycle and running losses of fuel under hot operating conditions were also measured.

The detailed measurements were necessary to fulfill the objective of finding the most cost-effective way to improve air quality, not just the best way to reduce gross emissions from the vehicle. In most cases, the formation of ozone, the program's main target, depended on the reactivity in sunlight of the chemical species in the exhaust or evaporative emissions.

As a nontechnical aside, the politics and timing of the Clean Air Act completely outran the experimental program. When we announced it at the White House, Governor Sununu asked why we hadn't started sooner. The answer was (1) that we had already reduced the major smog-forming pollutant, nonmethane hydrocarbons, by more than 90 percent through catalytic mufflers and lead-free gasolines; (2) that we believed that more reductions were coming through lower gasoline vapor pressure; and (3) that reducing emissions from new vehicles would

have little effect on air quality because of other sources of hydrocarbons including high-emitting older cars. This latter prediction appears to be coming true. Nonetheless, the automobile and fuel sections of the Clean Air Act were written without the benefit of more than fragmentary data from other sources and were clearly flavored with farm-belt politics concerning ethanol.

The findings of the auto/oil program to date have shown that there are more independent composition variables than originally expected, so that it is difficult to interpret the mass of data without further study. The data are being made available to the public and federal and state clean air officials through a series of Technical Bulletins.

One rather clear-cut effect, discussed in Bulletin No. 2 (dated February 1991), was the decrease in all three mass exhaust emissions with decreased sulfur in the gasoline. This is thought to be caused by poisoning of the exhaust catalysts by sulfur. Tests run when the catalysts were first introduced covered the range of sulfur typically found in commercial gasoline—a few thousand down to a few hundred parts per million. The current tests covered two gasolines with sulfur levels of 500 ppm and 50 ppm. Apparently, the catalysts are still sulfur-poisoned at the lower end of the earlier test range and only begin to reversibly recover somewhere below 500 ppm. Needless to say, further testing is planned.

Bulletin No. 4, soon to be released, says that the best result with reformulated gasoline, when compared to the worst, shows ozone decreasing very little in air models of Los Angeles, Dallas, and New York. The Clean Air Act mandates the use of oxygen-containing compounds in gasoline and a reduction in aromatic content. The aromatics reduction can be avoided if certain emission criteria are met. It is much too early to say what the final composition should or will be.

The first phase of the program cost $15 million, and a second phase costing $25 million is just getting under way. It will contain more experiments to answer questions raised in Phase I, as well as 1993 prototype gasoline-powered vehicles and some prototype dedicated-methanol-powered vehicles.

At this point you may be wondering what all the reformulated gasoline technology has to do with chemical engineers. First, chemical engineers are spread throughout the auto/oil research program. For example, John Seinfeld of Caltech, a renowned chemical engineer, is our consultant on air modeling. But much more importantly, hoards of chemical engineers are hard at work on how to <u>make</u> reformulated gasoline, no matter what its composition may be.

Nearly all aspects of chemical engineering are involved—catalysis, as well as process research, design, engineering, and operation, to name a few. One of the most pressing research topics is how to economically optimize a refinery when products must meet narrow chemically based specifications. That may not sound so difficult to those of you familiar with chemical plants. However, a refinery operates with a feed stock—crude oil—whose composition changes as often as hourly and which must produce products that generate a very low margin per gallon. If your production is very much off optimum, that margin disappears.

Overlaid on these activities is the requirement that emissions from the refinery need to continually decrease—which leads us to our second energy- and environment-related high-priority research topic from the *Frontiers* report.

Responsible management of hazardous substances was defined broadly in the report, and research targets in air, water, land, and groundwater were described. High on the list was the design of processes that were nonpolluting by design.

Let me illustrate how some chemical engineers have met the challenge of protecting the environment through responsible management of hazardous wastes while getting ready for liquid fuels of the future.

My example process is catalytic cracking. The objective of a cat cracker is to lower the molecular weight of a crude fraction, which ranges from above diesel fuel on up to heavy power-plant fuel. The lower-molecular-weight products are blended with other refinery streams to make diesel fuel and gasoline.

The objective is achieved by contacting the feedstock with a catalyst at 700°C and separating catalyst and products after a few seconds. Some of the products contain sulfur, which comes from aromatic sulfur compounds in the feedstock. A small amount is in the gasoline, about 40 percent is in the diesel fuel, and nearly all the rest leaves the reaction zone as hydrogen sulfide. This compound is removed from the gaseous fraction of the product stream by absorption in an amine solution and conversion to elemental sulfur. It is recycled as sulfuric acid and primarily ends up as gypsum fill for phosphate mines in Florida: problem solved.

After separation from the products, the catalyst, which has an average particle size of about 50 microns, is contacted with air to burn off the carbonaceous deposit left by the cracking reaction. Unfortunately, about 10 percent of the sulfur in the feedstock is in that deposit and reaches the atmosphere as sulfur oxides in the cat cracker stack: new problem.

The straight-forward answer is to install a scrubber on the stack and absorb the sulfur oxides in a sodium or calcium solution or onto a dry adsorbent. But what to do with the resulting sludge or solid? Regenerating the absorbent is expensive and disposing of the sludge can create yet another problem.

Along comes a chemical engineer with a less-obvious answer—change the catalyst so that it adsorbs the sulfur oxides from the gas phase in the combustor and carries it back to the reactor where it is reduced to hydrogen sulfide, exits into the product recovery system, and is ultimately converted to elemental sulfur. The proper catalyst has been found and demonstrated: problem solved.

This might be where we would have stopped a few years ago, but the sulfur in the products has now become worrisome. Besides the effect of sulfur in gasoline I mentioned earlier, recent data have shown that sulfur in diesel fuel plays a major role in particulates formation in diesel engine exhaust. Regulation of sulfur in diesel fuel to low levels begins next year. Why not go back to the source, the feedstock, and remove the sulfur there?

The technology is available to do this, and removing the sulfur from the feedstock has at least marginal economic benefits because of improved yields in the cat cracker. Desulfurizing cat-cracker feed now looks quite attractive. It results in low sulfur gasoline, which helps prevent ozone formation; low sulfur diesel fuel, which reduces particulates in diesel exhaust; and reduced levels of sulfur oxides in the cat cracker stack: three problems solved.

To succeed in this endeavor, the engineers went back to the source of the pollutant rather than trying to clean up the effluents. It has taken a long time for older chemical engineers like me to get away from the process flow sheets of our college days that always had two streams pointing off the edge of the drawing—labeled WASTE and VENT. The American Institute of Chemical Engineers is now putting together a cooperative center to deal with process pollution at the source, and, as it succeeds, it will hasten the process of reeducation.

I've used this example to make the point that an engineer working in either field, the energy or the environment, is almost automatically working in the other field as well. For the energy engineer, if his or her whole job is not driven by the search for new energy sources to meet environmental concerns, it is driven by the necessity to make current sources more environmentally benign. And while there may be a few environmental engineering jobs without a connection to energy, it is not very far from concerns about how to treat a waste water stream from a plant to the question, "Why are they sending me this junk in the first place?"

So perhaps we can agree that liquid fuels for the future and responsible management of hazardous wastes were good choices for high-priority research areas by the authors of the *Frontiers* report. There have been twists and turns and the two fields have merged in some instances, but there are plenty of challenges for chemical engineers in both.

5. The Cloudy Crystal Ball

I'd like to turn in the last few minutes to the crystal ball and share some ideas about future research needs and opportunities for chemical engineers in the fields of energy and the environment.

I've already mentioned one idea—that energy production and use are inexorably tied to protection and improvement of the environment. That is as it should be, because all of us interested in energy live in that environment. Even if we can put up with the environment the way it is, we can be sure that our children and grandchildren will not. The vector of interest in the environment is definitely upward. The number of new products considered to be "green" has increased, according to an advertising agency survey, from less than one percent in 1985 to 5 percent in 1990. A recent poll indicated that fully one-third of a representative sample of the public would pay 10 percent more for a product in a package that could be recycled than for one in a package that could not. As we saw with reformulated gasoline, environmental concerns are frequently driving legislation faster than science and engineering can support the assumptions.

Just to illustrate the point again, Amoco recently completed a 20-year forecast of our key technology needs. Under all scenarios that we thought had a chance of representing the future, environmental technology was one of those key technologies. As a result, we are acting to strengthen the environmental technology areas where we appear to be weak.

To narrow the focus considerably—what is our nation to do about our transportation fuels in the next decade and the early part of the next century? The DOE, in the *National Energy Strategy*, appears to be opting for a free market approach with many alternatives. I certainly agree, and I think it behooves us to let the ultimate cost to the consumer of transportation be the guide, including as many of the externalities as possible, as the DOE suggests. Where we perhaps part company is in the thought that one of those externalities is the cost of a multiple-fuel interim program that would be in place until we can agree on a long range strategy for the middle of the next century.

Although even I am not old enough to remember it, I have heard stories about the early days of the telephone when multiple phone companies operated on separate transmission systems. In order to communicate with your friends, you had to have several phones—each hooked up to a different set of wires. The analogy is not perfect, but if each service station has to be hooked up to a gasoline distribution system, a methanol or ethanol system, and the gas company to fill all the vehicles that come over its driveway—or we have to build separate stations for each alternative fuel—the cost will be high.

We should move rapidly, therefore, to make a choice. Should we stay with reformulated gasoline or move to one—and preferably only one—of the other alternatives? My choice would be reformulated gasoline, moving toward compressed natural gas if reformulated gasoline does not provide a reasonable cleanup of the air in our cities. Chemical engineers can play a big part in this decision, not only by carrying out the research and development, but also by explaining the scientific and engineering realities in terms that the public can understand.

And what, then, about the long-term future? It is my personal belief that we have only two choices, both electricity based. One is the electric motor-battery combination; the other is the hydrogen fuel cell. Neither vehicle will emit primary air pollutants, but both will require pollution-free electric power generation. The battery-powered vehicle will require electricity for recharging, and the fuel-cell-powered vehicle will require generation of hydrogen by electrolysis.

I don't believe we have the data to make the choice between vehicles. We do, however, have two high-priority research areas to add to the *Frontiers* list: battery technology (including recharging) and fuel cell technology (including hydrogen supply). I know that there are programs in both here at Argonne, and my advice is only that we chemical engineers should eschew advocacy as much as possible and go about getting data and defining the key technological unknowns.

And finally, a pollution-free electric power plant leads to yet another high-priority research area for chemical engineers: fission and fusion technology—or perhaps two areas, one for each. Besides technical challenges for chemical and nuclear engineers, the challenge of explaining the pros and cons of each form of nuclear power and the pros and cons of both versus conventional power plants will be unrelenting. And, of course, I know that Argonne is working furiously on nuclear power. I'm not trying to be a good guest—I just happen to believe that you are on the right track!

6. Conclusion

To conclude, let me remind you that when we considered energy and the environment, the *Frontiers in Chemical Engineering* report of four years ago was right on with the names of high priority research areas but that today's content of those areas is different. Liquid fuels for the future is much more driven by environmental concerns now than by energy security concerns as it was then. This view is confirmed by the recent *National Energy Strategy*. The challenge to chemical engineers is to find those alternative fuels that, when combined with the right vehicles, will clean up the air.

Our discussion of responsible management of hazardous wastes presented the challenge to find ways to clean up processes at the source rather than at the end of the waste pipe or vent stack. We also concluded that engineers working in the energy field found their activities nearly completely entwined in the activities of engineers working in the environmental field.

When we looked into the future, we found that, for chemical engineers, challenges of a different sort were added to the technical challenges. These new challenges include explaining to a skeptical public the wisdom of proceeding to design the interim system of alternative fuel and, then, moving expeditiously to a final solution. The latter leads to three new high priority research areas: batteries, fuel cells, and nuclear power.

Insertion Device Radiation Sources

P. James Viccaro
Advanced Photon Source
Argonne National Laboratory
9700 S. Cass Avenue
Argonne, Illinois 60439

INTRODUCTION

Third generation synchrotron facilities, such as the 7-GeV Advanced Photon Source (APS) synchrotron facility at Argonne National Laboratory, will be powerful sources of hard x-rays with energies above 1 keV. For example, in addition to the availability of bending magnet radiation, the APS storage ring will have 34 straight sections for insertion device (ID) x-ray sources. The unique spectral properties and flexibility of these devices open new possibilities for research in essentially every area of science and technology. Existing and new techniques utilizing the full potential of these sources, such as the enhanced coherence, unique polarization properties, and high spectral brilliance, will permit experiments not possible with existing sources.

In the following presentation, the spectral properties of synchrotron ID sources are briefly reviewed. A summary of the specific properties of sources planned for the APS storage ring is then presented and relevant results for APS prototype ID sources are shown. Special x-ray sources for producing elliptically polarized x-rays at the APS facility are described and time structure properties of typical APS sources are discussed.

GENERAL PROPERTIES OF ID SOURCES

Both undulator and wiggler IDs at the APS will be composed of magnet arrays in a planar geometry. These magnet arrays set up a spatially oscillating magnetic field along the length of the device [1]. These arrays can either be made up of permanent magnets, with or without high-permeability magnetic poles, or electromagnets. Whatever the structure, the spectral properties of the devices are related to the generated peak magnetic field, B_0. In particular, the field results in an oscillating trajectory of the particle beam through the device. The amplitude and maximum slope angle depend linearly on both the field, B_0, and the period of the device through the deflection parameter, K, defined by:

$$K = 0.933\lambda_0 B_0,$$

where λ_0 is the ID magnetic period in cm, and B_0 is in tesla. For a K less than approximately 10, the maximum slope angle is given by,

$$\theta = K/\gamma,$$

where $\gamma = 1957\ E_r$ is the relativistic factor, and E_r is the ring energy in GeV. This is to be compared with the natural opening angle of synchrotron radiation,

$$\psi \sim 1/\gamma,$$

which is approximately 73 μrad for the 7-GeV APS storage ring.

The spectral properties of a given device will depend on the relative values of the maximum slope angle, θ, and the opening angle, ψ. In the undulator regime, where $K \sim 1$, the radiation from each part of the trajectory is within the radiation opening angle, and interference effects can occur. This interference causes spatial and frequency bunching that gives rise to the typical undulator spectrum consisting of narrow bands of radiation called harmonics. The energy at which these harmonics occur depends on the ring energy and the peak magnetic field in the device. For a single radiating particle, the radiative source size and divergence depend on the wavelength of the x-ray and the length of the undulator. Typically, the radiative divergence at the harmonic energy is a fraction of the natural radiation opening angle, ψ, and the photon flux at this energy is enhanced.

In the wiggler, where $K \geq 5$, the output from the device is a sum of intensities from each magnetic pole and the spectral output is similar to a bending magnet, but contained within a horizontal angular range of $\pm K/\gamma$. The spectral output on-axis is approximately N times the output from an equivalent bending magnet source, where N is the number of magnetic poles.

The spatial and angular distribution of the particle beam will affect the undulator spectrum most severely. Because the particles in the beam are independent, the effective source angular distribution and size are a convolution of the radiative and particle beam distribution parameters. The particle beam distributions are approximately Gaussian, as is the case for the central radiation cone at the principal harmonics. For the low-emittance APS storage ring, the particle beam vertical divergence is on the order of the Gaussian width (9 mrad) of the first harmonic central cone. In the horizontal direction, it is a factor of approximately two larger. As a first approximation, information concerning the number of photons in a given bandwidth contained within a given angular aperture can be estimated for the principal harmonics using the convoluted effective source spatial and angular properties.

The on-axis brilliance BL0 (sometimes referred to as brightness) is defined as:

$$\text{BL0} = \text{number of photons}/(0.1\%\text{BW mm2mrad2})$$

and is equivalent to the total flux at a given photon energy in a fixed bandwidth (BW) divided by the effective radiative source size and effective source divergence in the vertical and horizontal directions.

The on-axis brilliance at the principal harmonics of an undulator contains information concerning the approximate angular distribution of the source. In fact, the peak angular flux density of the central radiation cone is given approximately by the product of BL0 and the effective source area. As mentioned, the angular width is the convoluted width of the particle beam divergence and radiative width.

APS RADIATION SOURCES

Several IDs have been identified as standard x-ray sources for the APS. These include two planar undulator and two planar wiggler sources. Undulator A, which has the Nd-Fe-B and vanadium permendur hybrid geometry, is capable of spanning the photon energy interval from approximately 5 to 30 keV using first-harmonic radiation. Undulator B, which also has the hybrid structure, is tunable from approximately 13 to 20 keV. Wigglers A (with the hybrid structure) and B (which has magnetic structure based on electromagnets) have critical energies of 32.6 and 9.8 keV, respectively. These critical energies are above and below that for the bending magnet radiation of 19 keV.

The flux through a pin-hole with an angular opening equal to the angular width of the central radiation cone for the first harmonic of Undulator A is approximately 10^{13} photons/sec in 0.1% bandwidth at the energy of 8 keV. This value is typical for most undulator sources at the APS. The total flux within the central radiation cone is approximately 10^{14} photons/sec per 0.01% bandwidth at 8 keV.

APS UNDULATOR PROTOTYPE RESULTS

As part of the R&D effort, the APS has developed two prototype Undulator sources in order to evaluate construction techniques, critical construction tolerances, and performance. The first of these is a prototype of Undulator A with a period of 3.3 cm and a length of approximately 2 m. It was the first short period undulator to be used as a synchrotron x-ray source. The device was installed on the CESR/Cornell storage ring for a one month dedicated run [2]. The storage ring was modified to have approximately the same vertical emittance as the APS. The performance of the device was excellent and satisfied all the requirements for an undulator of this type installed on the APS. As part of the performance evaluation of the device, the effect of introducing a taper in the undulator gap was tested. In this mode, the first harmonic bandwidth increased by a factor of two. At the same time, the spatial distribution remained essentially unchanged. This result can be explained by the fact that the band width is determined essentially by the difference in entrance and exit peak fields caused by the taper in the gap. The spatial distribution at the harmonic, on the other hand, is determined by the energy of the emitted photon.

A second prototype is the undualtor for the U-5 straight section at the VUV storage ring at the National Synchrotron Light Source (NSLS). The device will be used by a multi-institutional materials research group in a diverse program. The undulator, which was delivered to the NSLS in March 1990, was tested and its performance evaluated in early summer of 1990. The device has a period of 7.5 cm and a length of 2.3 m. It has the lowest random field error of any built to date. Some of the essential design parameters can be obtained from [3].

SPECIAL PURPOSE IDs

Part of the R&D effort in this area will be placed on the development of techniques that utilize x-rays with a variable degree of elliptical polarization of ID sources in the region of 1 to 100 keV. In the low-energy part of this spectral region, techniques used for the investigation of elastic magnetic scattering and polarization processes will be prominent. In the high-energy portion of the spectrum, magnetic Compton scattering will be important.

At present, there is a significant amount of activity concerning the development of ID sources capable of producing circularly or elliptically polarized x-rays. These include:

- Asymmetric Wiggler [4]
- Elliptical Motion Multipole Wiggler[5]
- Helical Motion Crossed Undulator[6]
- Planar Helical Field Undulator [7,8]
- Crossed Planar Undulator[9]

Of the possible ID configurations, two have been chosen as candidate sources of variable polarized x-rays on the APS. The first is the crossed planar undulator first proposed by K. J. Kim [9] that is an efficient source on the APS for producing circularly polarized x-rays from 1 to 5 keV. Third harmonic radiation would extend the range up to 8 or 10 keV. The major advantage of this source is its time modulation capability because the degree of polarization depends on an electromagnetic phase shifter. The conceptual design consists of two hybrid sections with Nd-Fe-B magnets and vanadium permendur poles. The sections are in tandem with an electromagnetic phase shifter between them. The total length of the device is approximately 2.5-m.

The second device is a version of the elliptical motion multipole wiggler that has been recently been tested at the Photon Factory-KEK[5]. The device proposed for the APS has a period of approximately 20 cm and is 1 m in length. The critical energy will be approximately 30 keV and the device will span the range from above 8 keV to approximately 100 keV.

Other programs include permanent magnet IDs with enhanced magnetic designs capable of producing a high magnetic field. As undulators, these devices will exhibit larger photon energy tunability than current devices. As wigglers, these devices will be capable of achieving high critical fields above 50 keV.

These special devices are an important part of the R&D activity in ID source development at the APS. It is expected that APS users and scientific needs will spur activity in other areas of source development after the storage ring becomes operational.

REFERENCES

[1] Characteristics of the 7-GeV Advanced Photon Source: A Guide for Users, G. K. Shenoy, P. J. Viccaro, and D. M. Mills, ANL Report Number ANL 88-9

[2] Bilderback et al., Rev. Sci. Inst. 60, 1419 (1989)

[3] P. J. Viccaro, G. K. Shenoy, S. Kim, and S. D. Bader Rev. Sci. Inst. 60, 1813 (1989)

[4] J. Goulon, P. Elleaume, and D. Raoux, Nucl. Inst. and Meth. A254, 192 (1987)

[5] S. Yamamoto, H. Kawata, H. Kitamura, M. Ando, N. Saki, and N. Shiotani, Phys. Rev. Lett. 62, 2672 (1989)

[6] H. Onuki, N. Saito, and T. Saito, Appl. Phys. Lett. 52, 173 (1988)

[7] P. Elleaume et al. Submitted to Nucl. Inst. Meth.

[8] B. Diviacco and R. P. Walker, Submitted to Nuclear Inst. Meth.

[9] K.-J. Kim, Nucl. Inst. Meth. A246, 425 (1984)

OUTLINE OF PRESENTATION

Synchrotron Radiation Sources

1. General Properties of Synchrotron Sources

2. Wiggler and Undulator Insertion Device (ID) Synchrotron Sources
   - Frequency Distribution Within Power Envelope
   - Spatial Distribution
   - Brightness, Brilliance, and Flux
   - Polarization Properties
   - Time Structure

   (Mostly APS and APS Prototypes)

ADVANCED PHOTON SOURCE

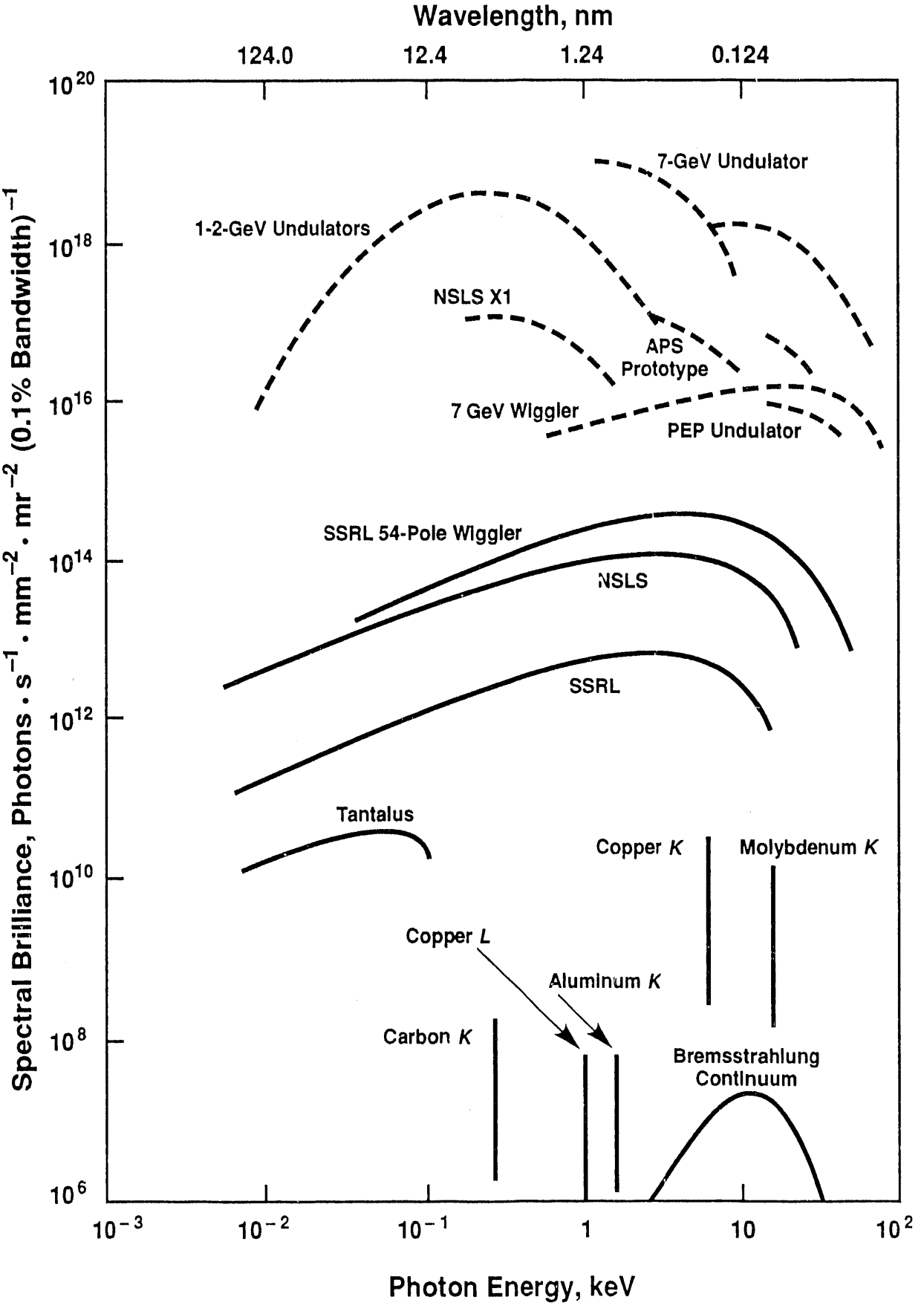

ADVANCED PHOTON SOURCE

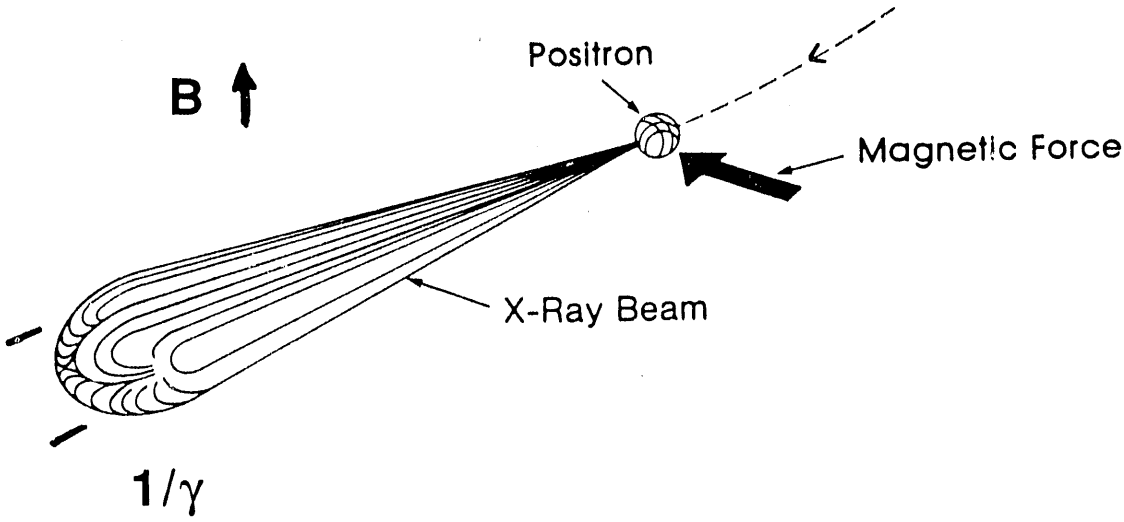

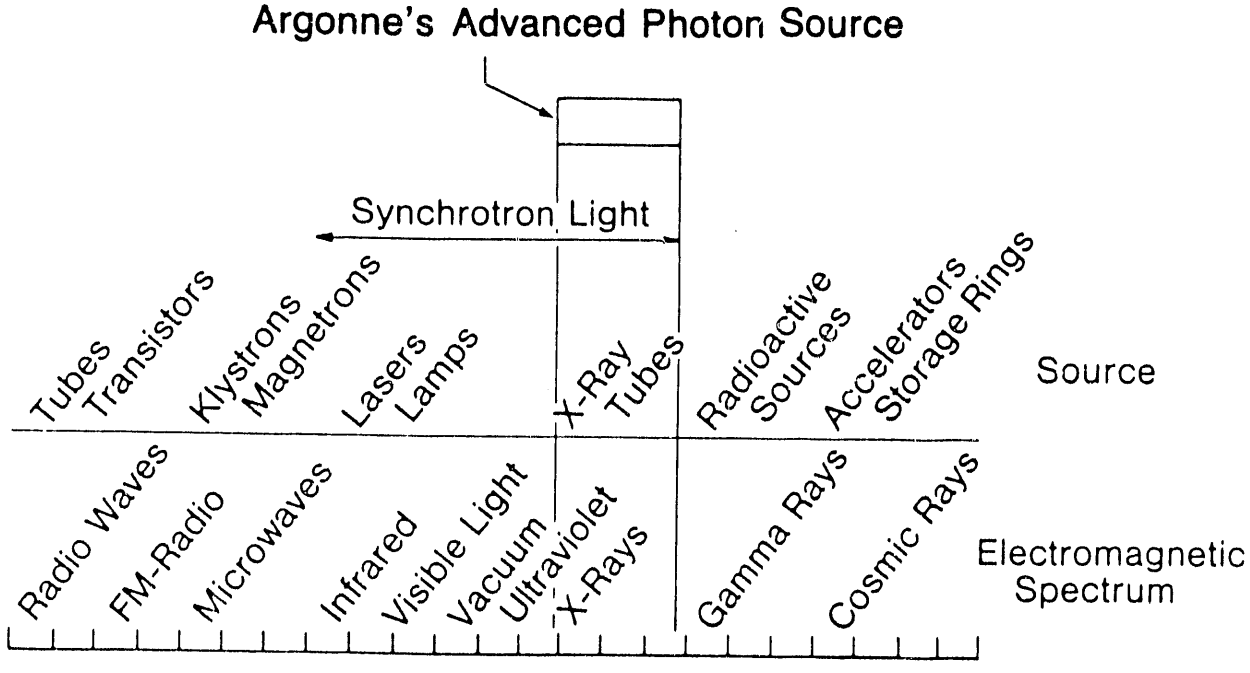

BEND MAGNET

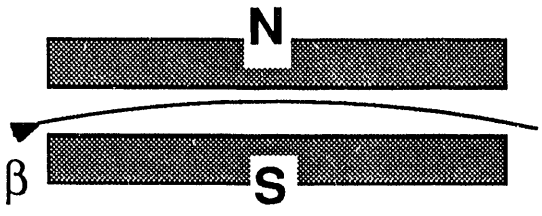

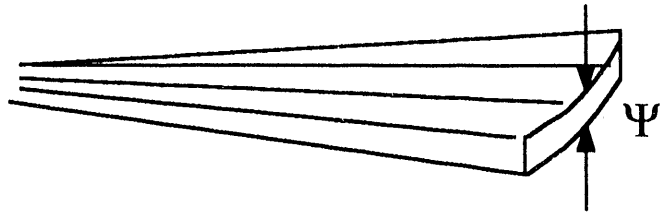

Vertical Opening Angle $\Psi = \sim 1/\gamma$

$\gamma = 1957\ E_R$ $\gamma = \sqrt{1 / (1 - \beta^2)}$

At 7 Gev, $1/\gamma \sim$ 0.07 mrad

Beam Height ~ 4 mm at 50 m

FREQUENCY DISTRIBUTION

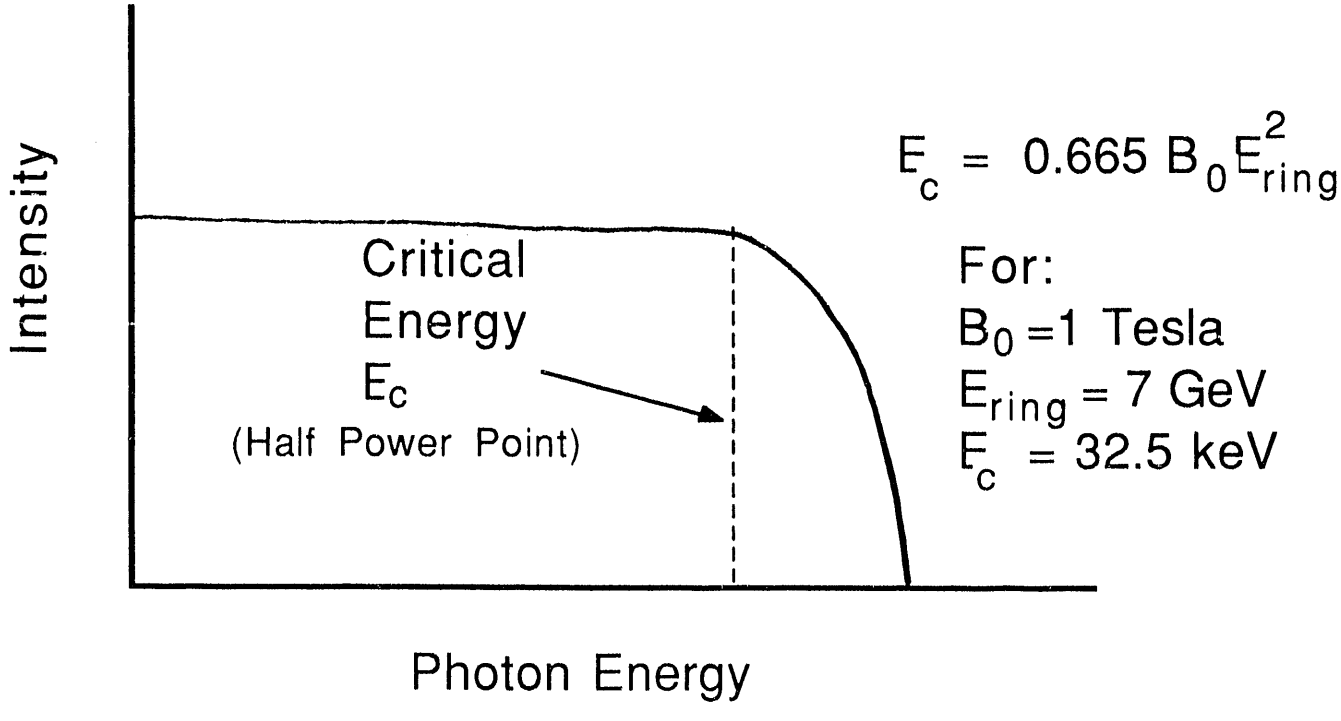

APS BEND MAGNET

E_c = 19.5 keV

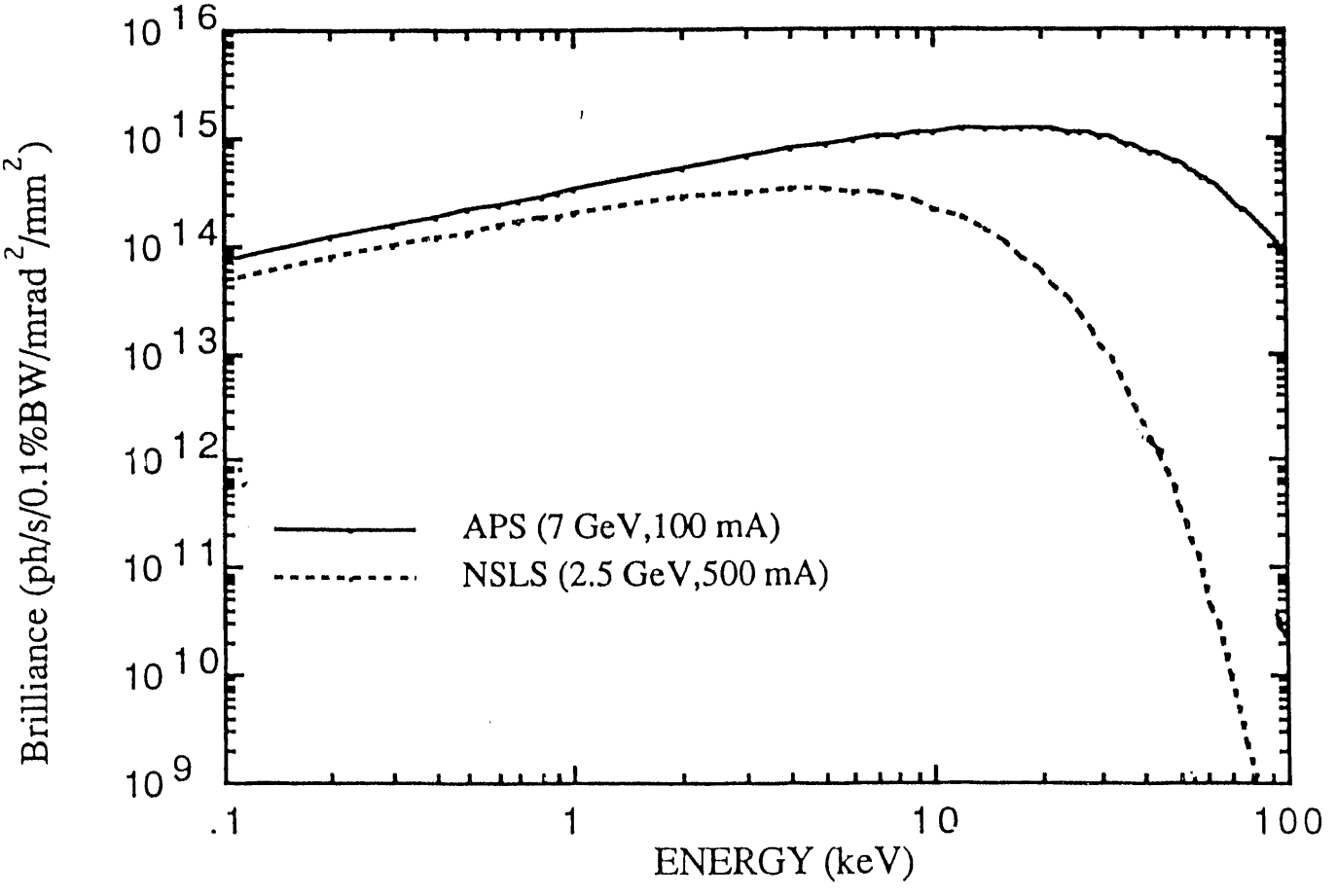

Brilliance of Bending-Magnet Radiation from Various Synchrotron Sources

ADVANCED PHOTON SOURCE

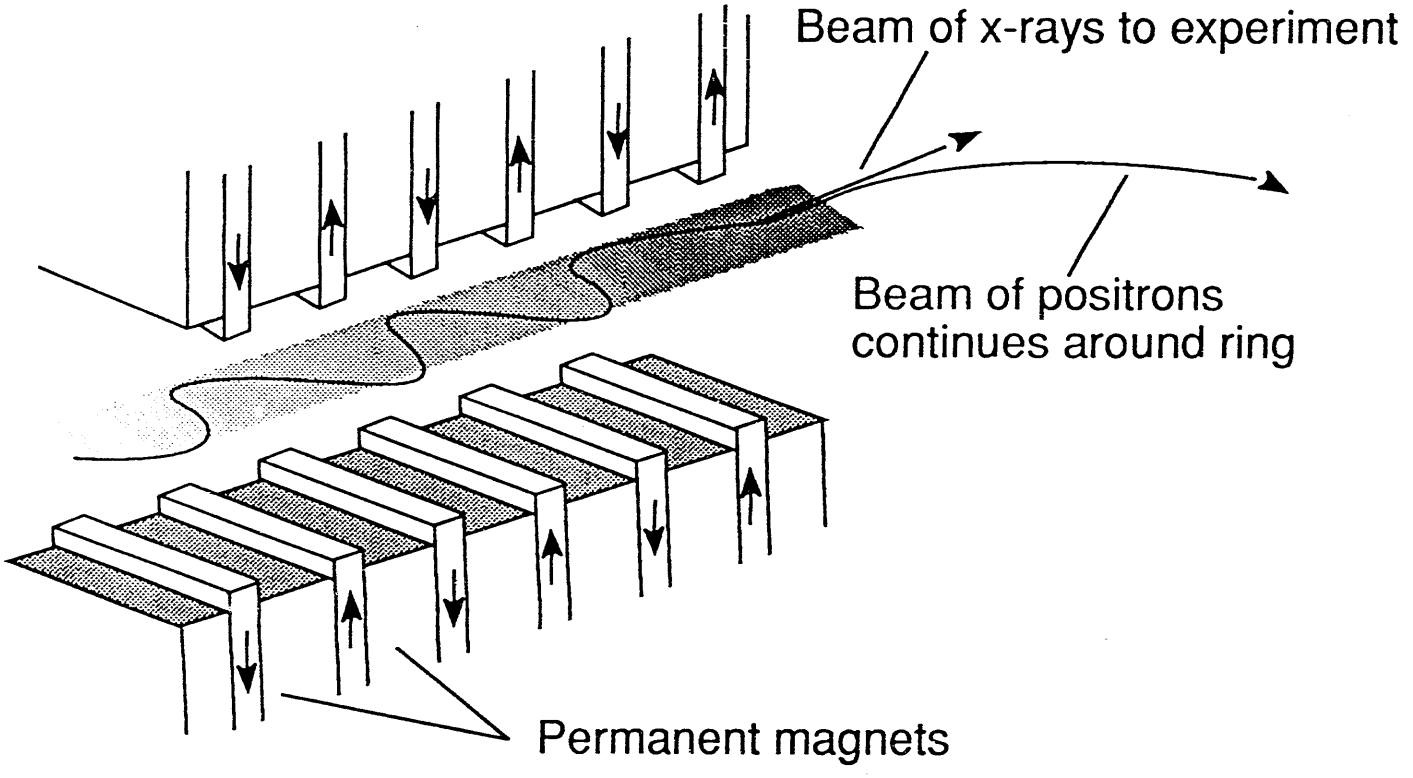

ADVANCED PHOTON SOURCE

BRIEF HISTORY OF IDs

- FIRST UNDULATOR, H. MOTZ ~**1953**

1970's

- EARLY 1970'S UNDULATOR DEVELOPMENT IN THE USSR
- FIRST SYNCHROTRON WIGGLER (EM) ~1979 SSRL (Alive and well at CHESS/CESR)

1980's (K. Halbach Decade)

- SYNCHROTRON PERMANENT MAGNET INSERTION DEVICES IN THE 1980's

  DEVELOPMENT OF PURE PERMANENT MAGNET AND HYBRID DEVICES

  $SmCo_5$ and Nd-Fe-B MAGNET TECHNOLOGY LBL/SSRL

  First $SmCo_5$ permanent Magnet ID (SSRL) (Alive and well at SRC/Wisconsin)

- PREPARATION FOR 3RD GENERATION LOW EMITTANCE SYNCHROTRON FACILITIES

  PEP/UNDULATOR (DEC., 1986)
  APS/CHESS UNDULATOR (MAY, 1988)

PARTICLE BEAM TRAJECTORY

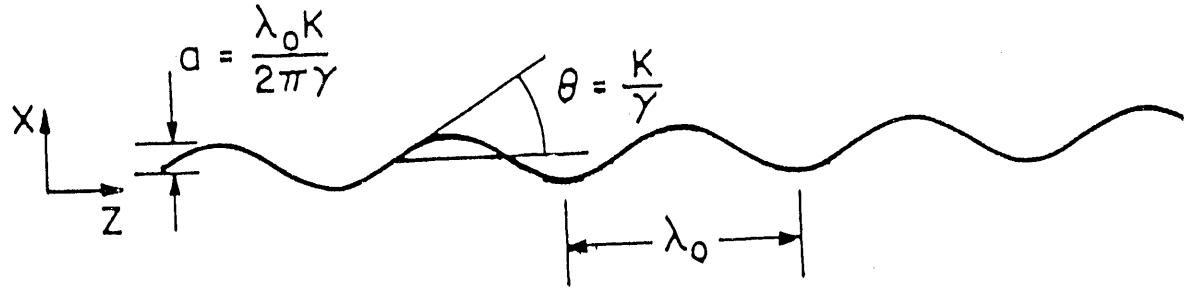

DEFLECTION PARAMETER K

$K = 0.934\ \lambda_0(cm)\ B_0(T)$

CENTRAL RADIATION CONE

ANGULAR WIDTH ~ $1/\gamma$

$\gamma = 1957\ E_R(GeV)$

WIGGLER REGIME

$K >> 1$

SUM INTENSITY FROM EACH POLE

UNDULATOR REGIME

$K \sim 1$

INTERFERENCE EFFECTS
WITHIN RADIATION CONE

UNDULATOR SOURCES

INTERFERENCE EFFECTS IN UNDULATOR REGIME CAUSE FREQUENCY AND SPATIAL 'BUNCHING'

EXAMPLE: APS@ 7GeV 100mA

ON-AXIS FREQUENCY DISTRIBUTION

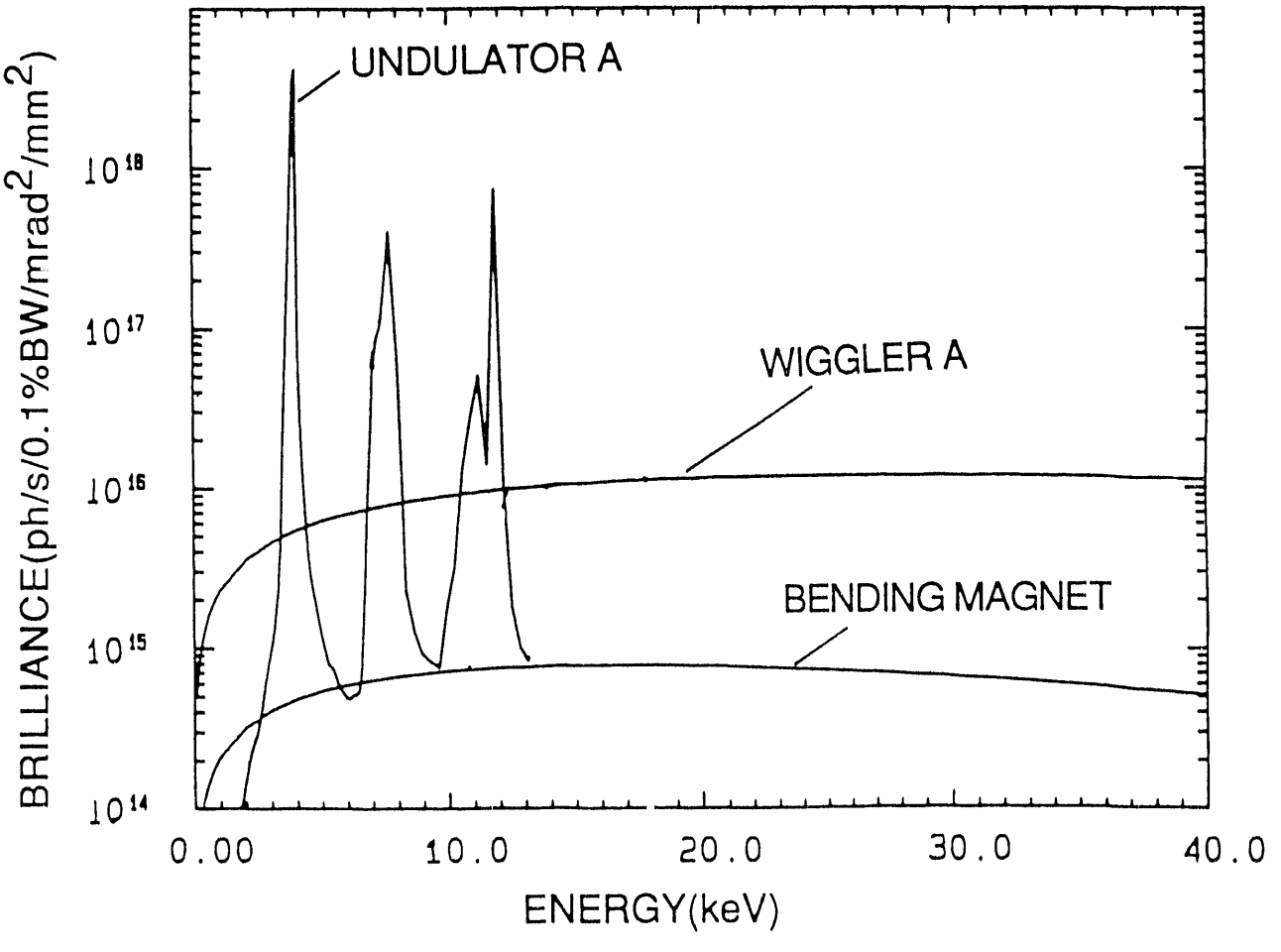

Angular Power Density Wig A

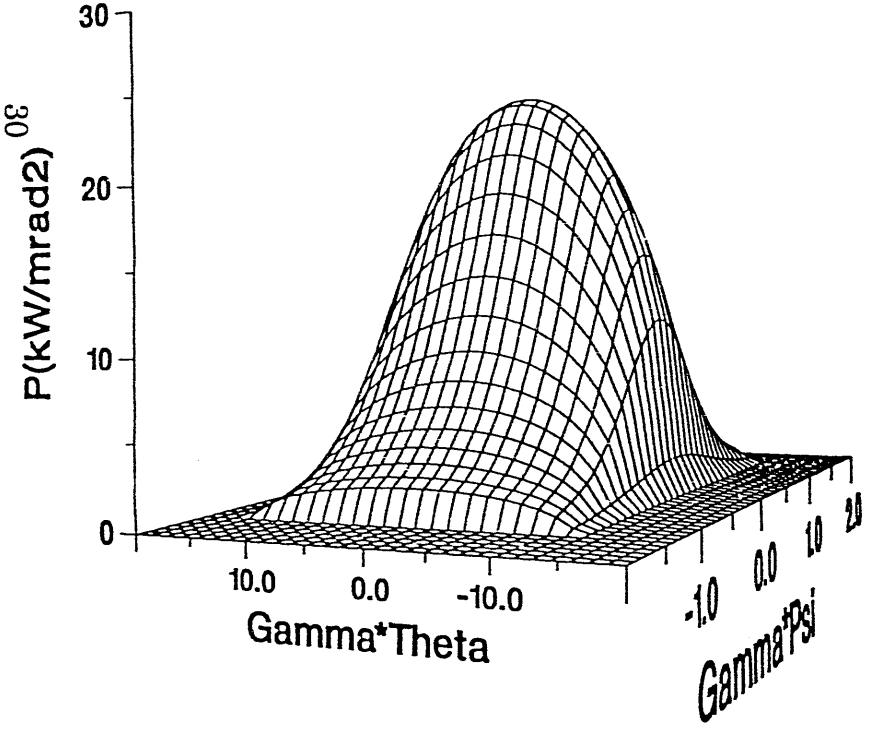

Angular Power Density Und A

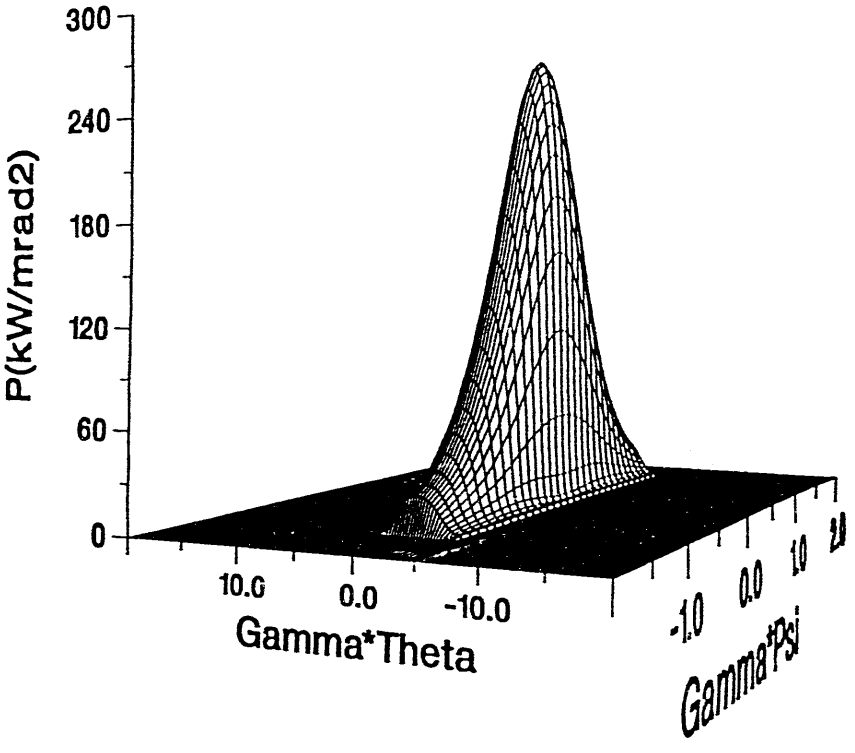

ADVANCED PHOTON SOURCE

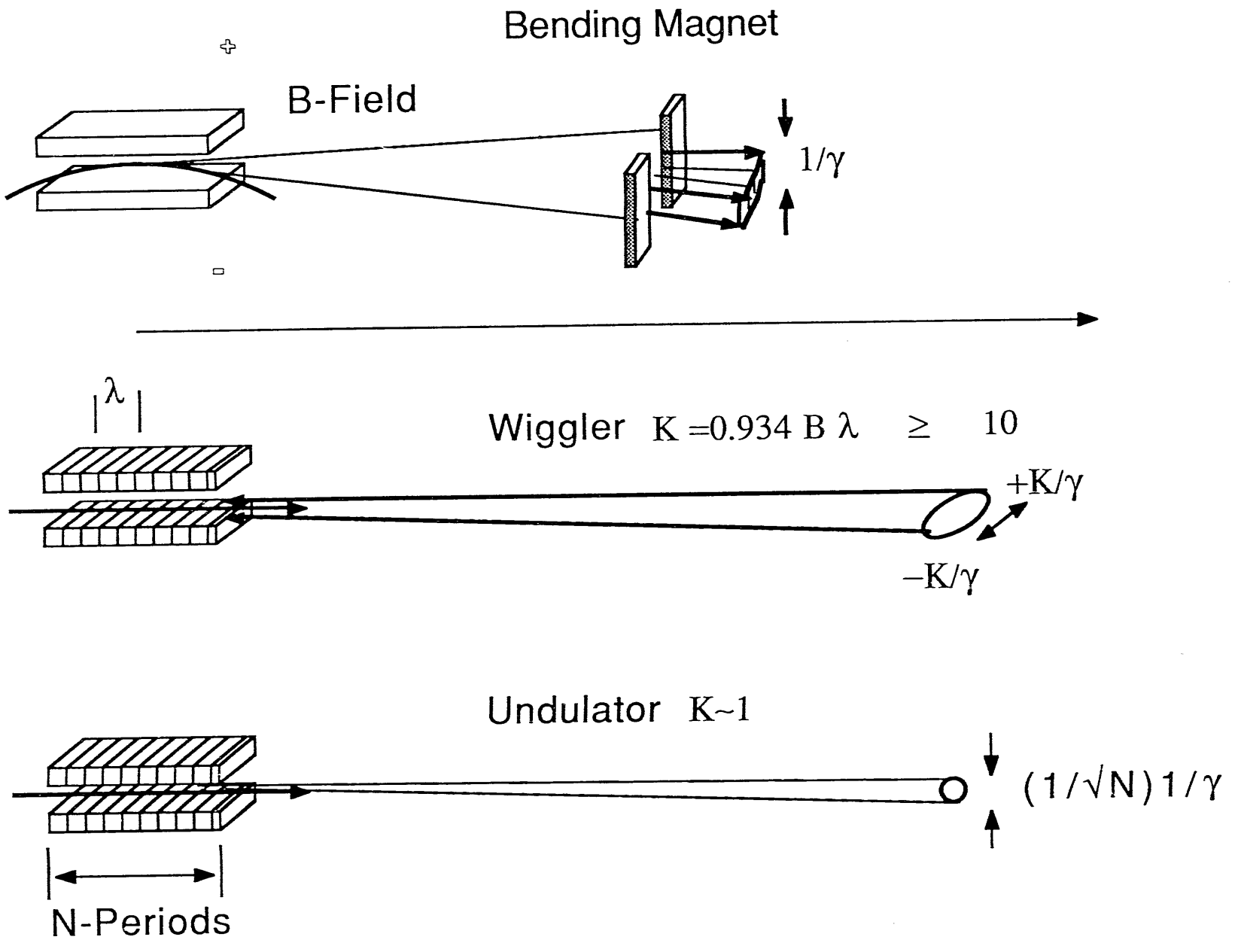

SOURCE BRILLIANCE

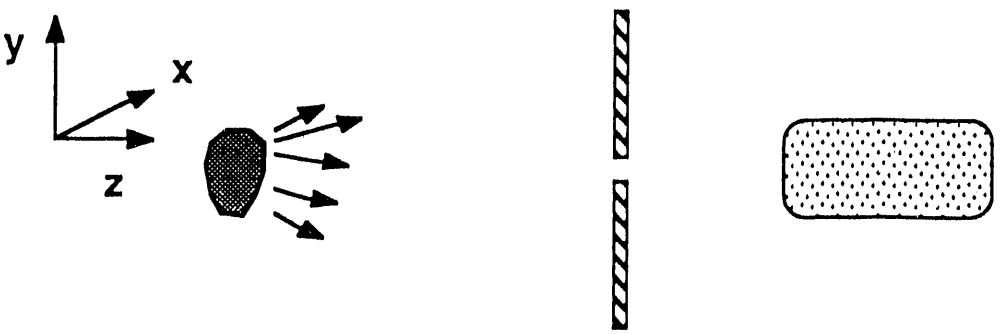

Extended Source | Pinhole | Detector

Flux Through Pinhole Depends on BOTH
Angular Divergence and
Spatial Distribution

Brilliance (Brightness): On Axis (Peak)

$$B \sim F/(\Sigma'_x \Sigma'_y \Sigma_x \Sigma_y) \qquad F=\text{Total Flux}$$

Angular Flux Density:

$$A \sim F/(\Sigma'_x \Sigma'_y)$$

APS Prototype Undulator at the U5 Straight Section at NSLS
6mm Pinhole (750 μrad) - 42 mm Magnet Gap

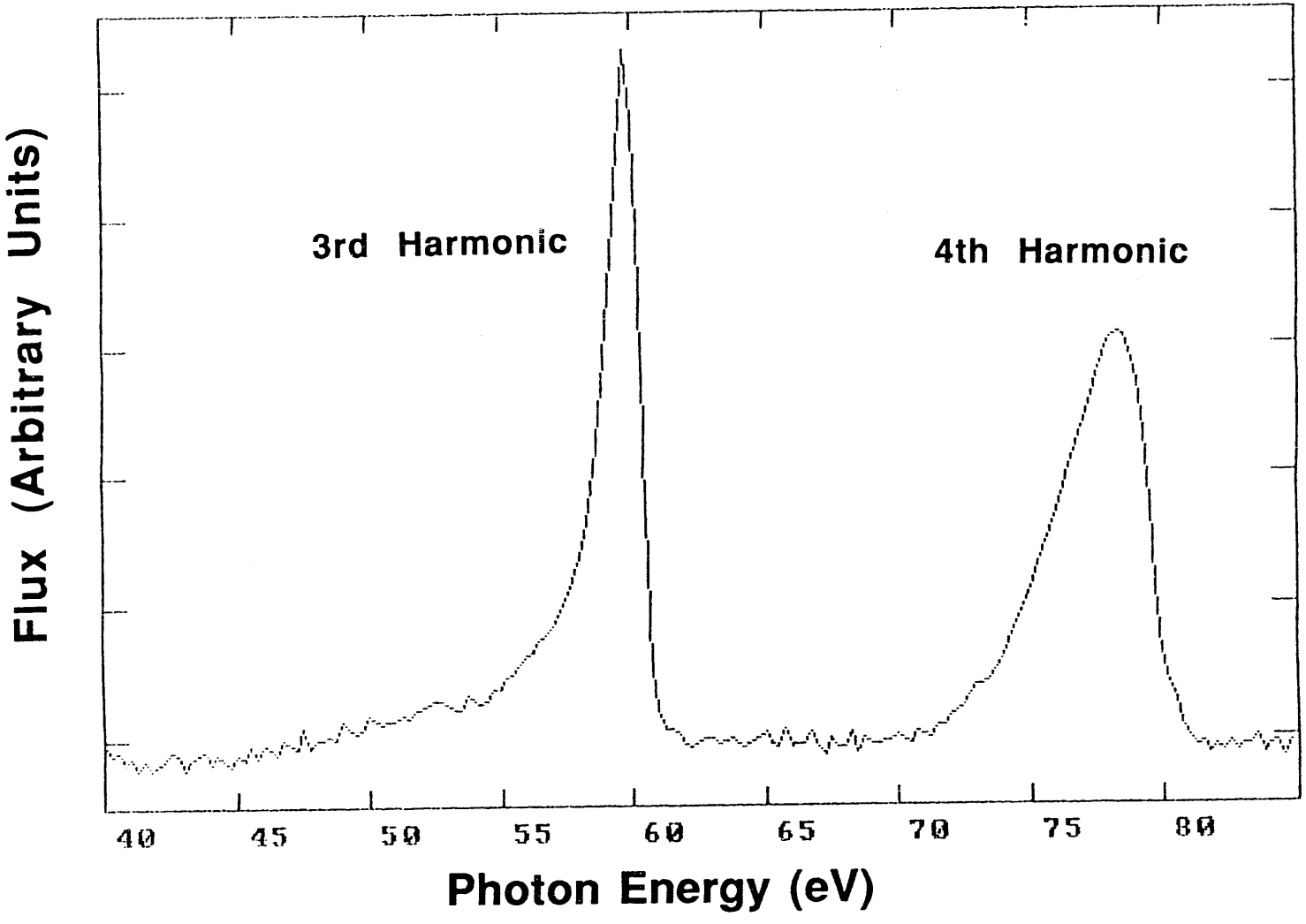

APS/CHESS PROTOTYPE UNDULATOR

FLUX THROUGH A 100μ X 100μ PINHOLE

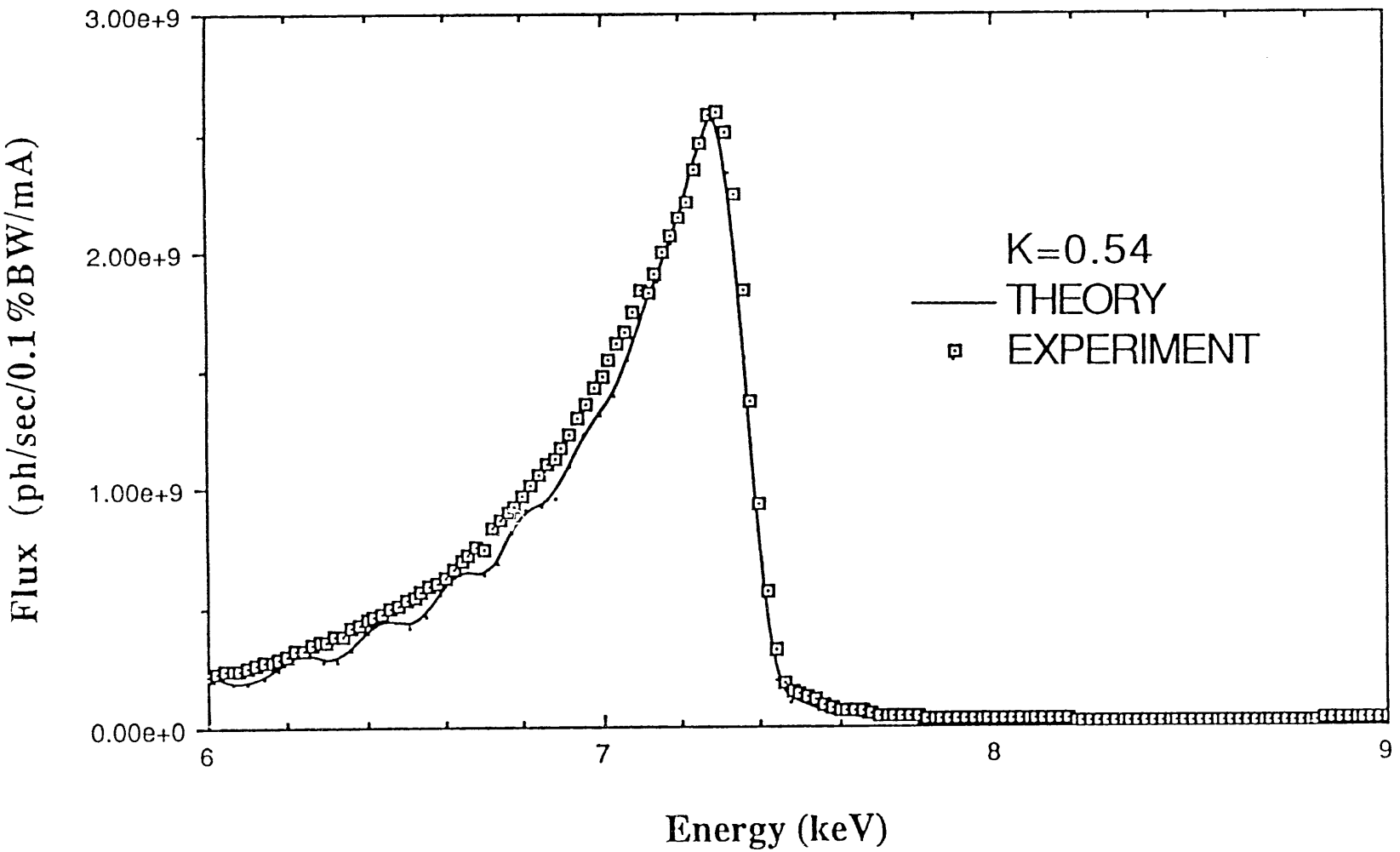

APS Undulator A (3.1 cm Period)
1st Harmonic Tunablity

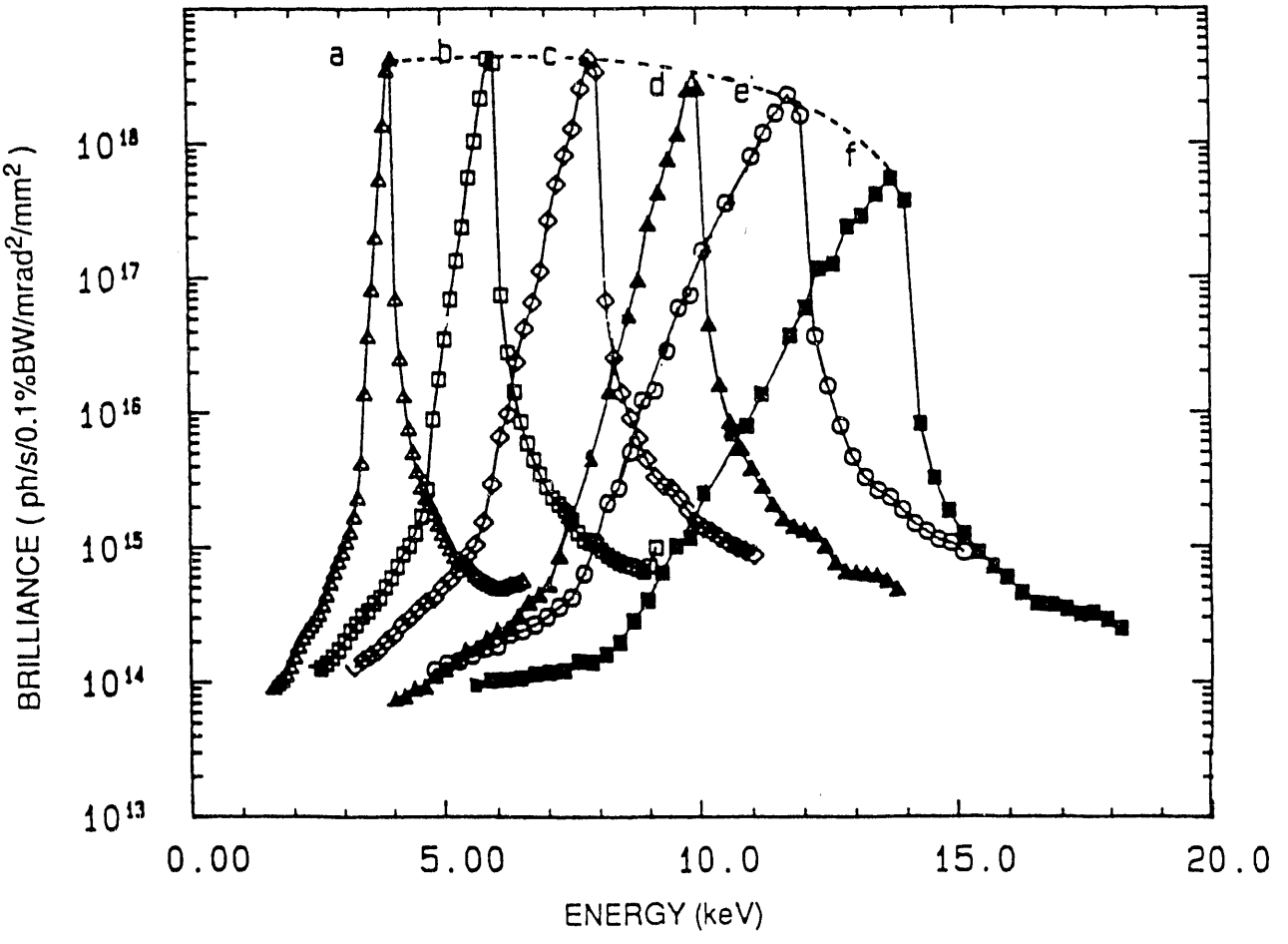

APS UNDULATORS A AND B -TUNABILITY

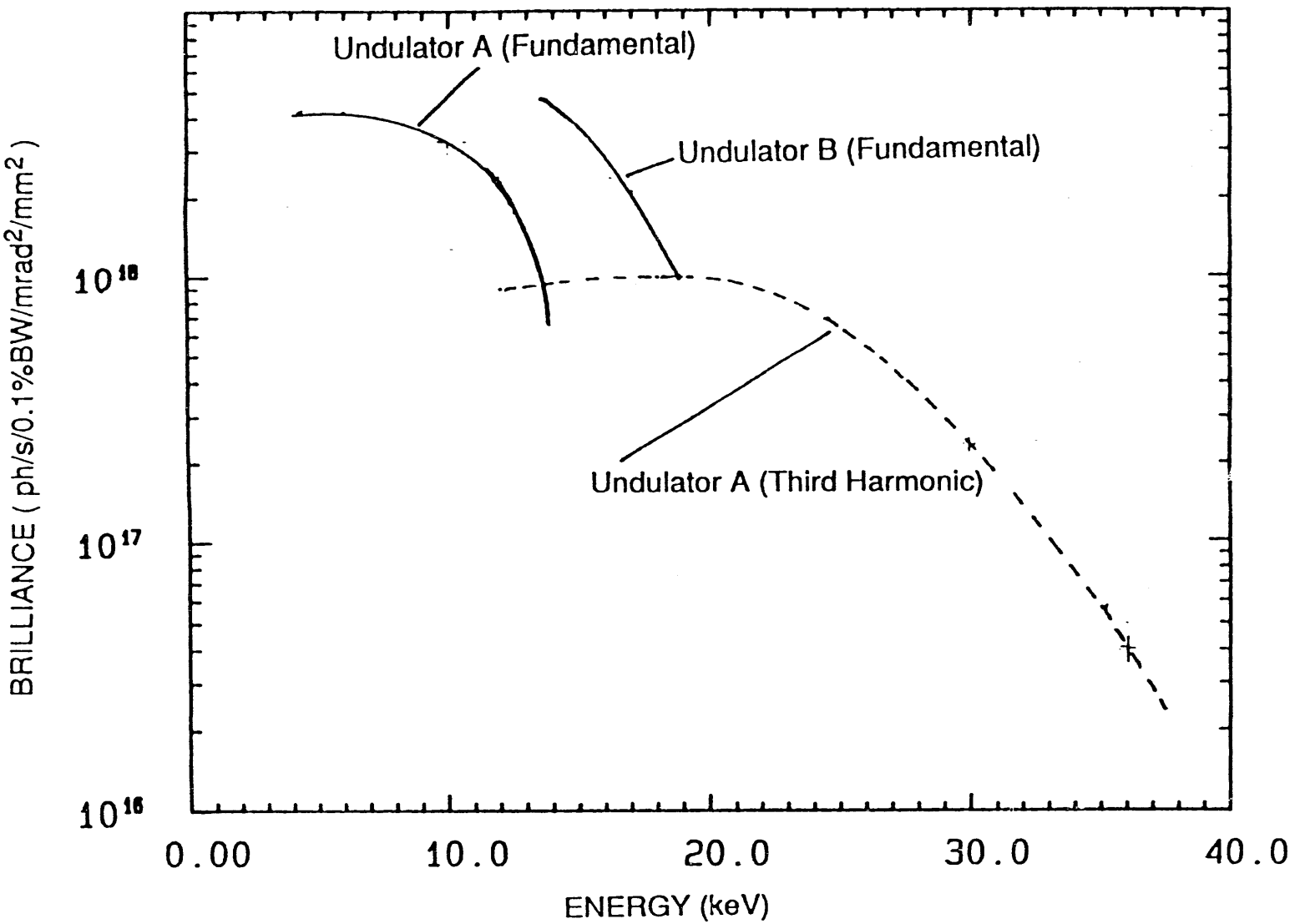

APS WIGGLERS A AND B

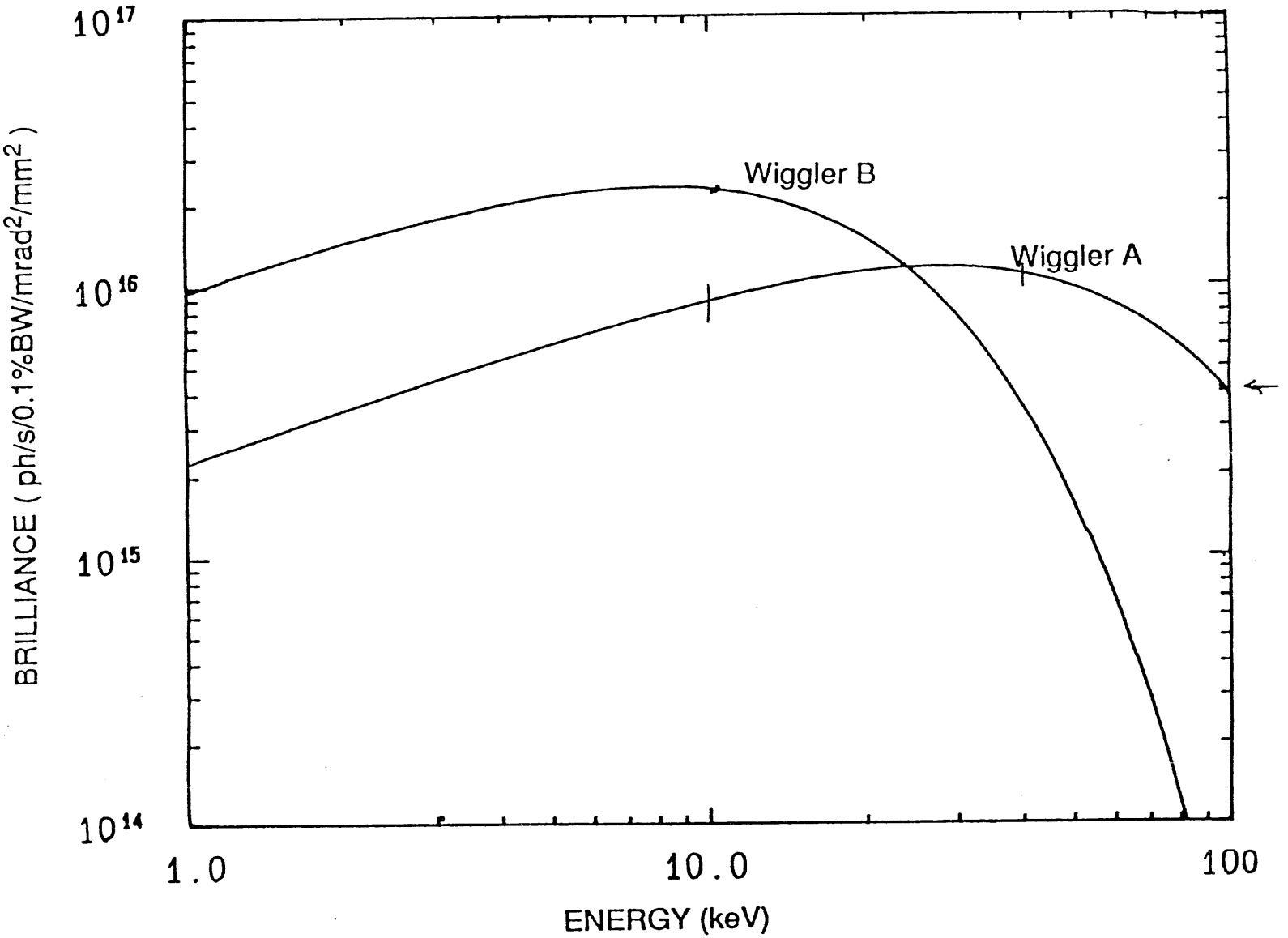

APS INSERTION DEVICE SUMMARY

	Undulators				Wigglers	
	A	B	C	D	A	B
Period (cm)	3.1	2.1	20	8	15	25
Length (m)	2.5	2.5	2.5	2.5	1.5	2.5
Undulator Fundamental:						
Min (keV)	4.5	13	0.5	1		
Max (keV)	14	20	1.5	3		
Wiggler Critical Energy:						
E_c(keV)				32	32.5	9.8
K_{max}	2.5	1.1	2.7	9	7	14

UND A , B, C, D, and WIG A:
Permanent Magnet (Nd-Fe-B) HYBRID DEVICES

UND D: Wiggler-Undulator

WIG B:
Electromagnet

Bending Magnet Radiation: Ec = 19.5 keV

POLARIZATION CHARACTERISTICS OF SYNCHROTRON X-RAY SOURCES

- **Bending Magnet**

  On-Axis: Plane Polarized (σ) in Horizontal On-Axis Plane

  Off-Axis: Both σ and π

- **Planar Wiggler**

  Positive and Negative Lobes of Trajectory Cancel π Component.

  Plane Polarized

- **Planar Undulator**

  On-Axis: Plane Polarized (σ) in Horizontal On-Axis Plane

  Off-Axis: Both σ and π (Complex)

BENDING MAGNET POLARIZATION

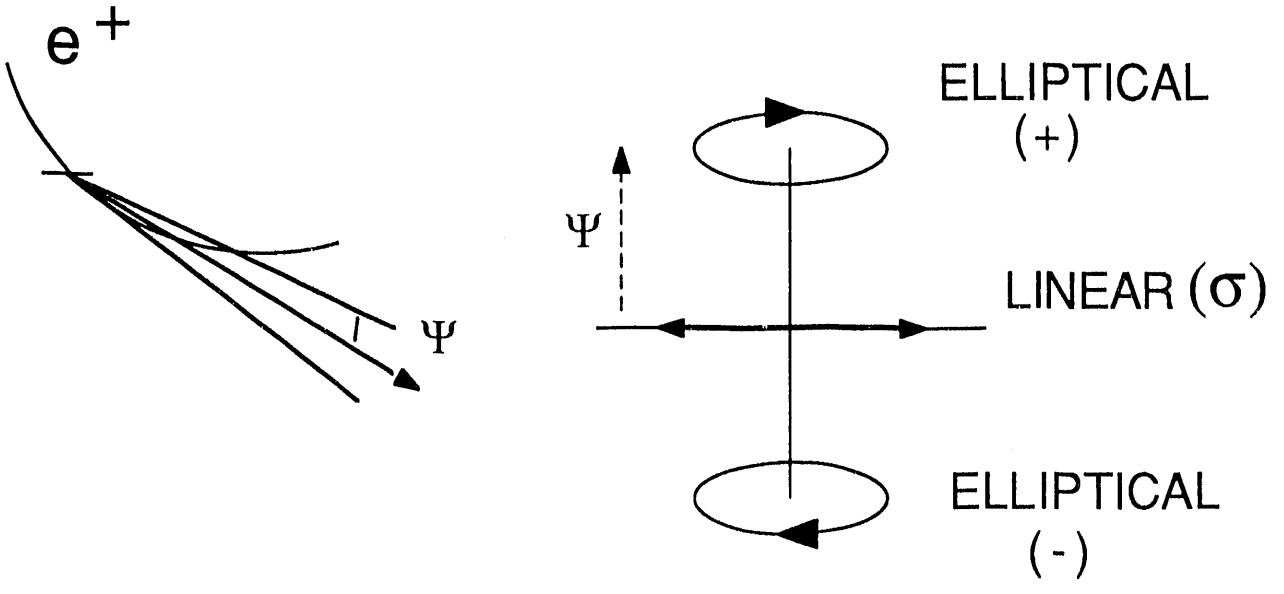

PLANAR WIGGLER OR UNDULATOR

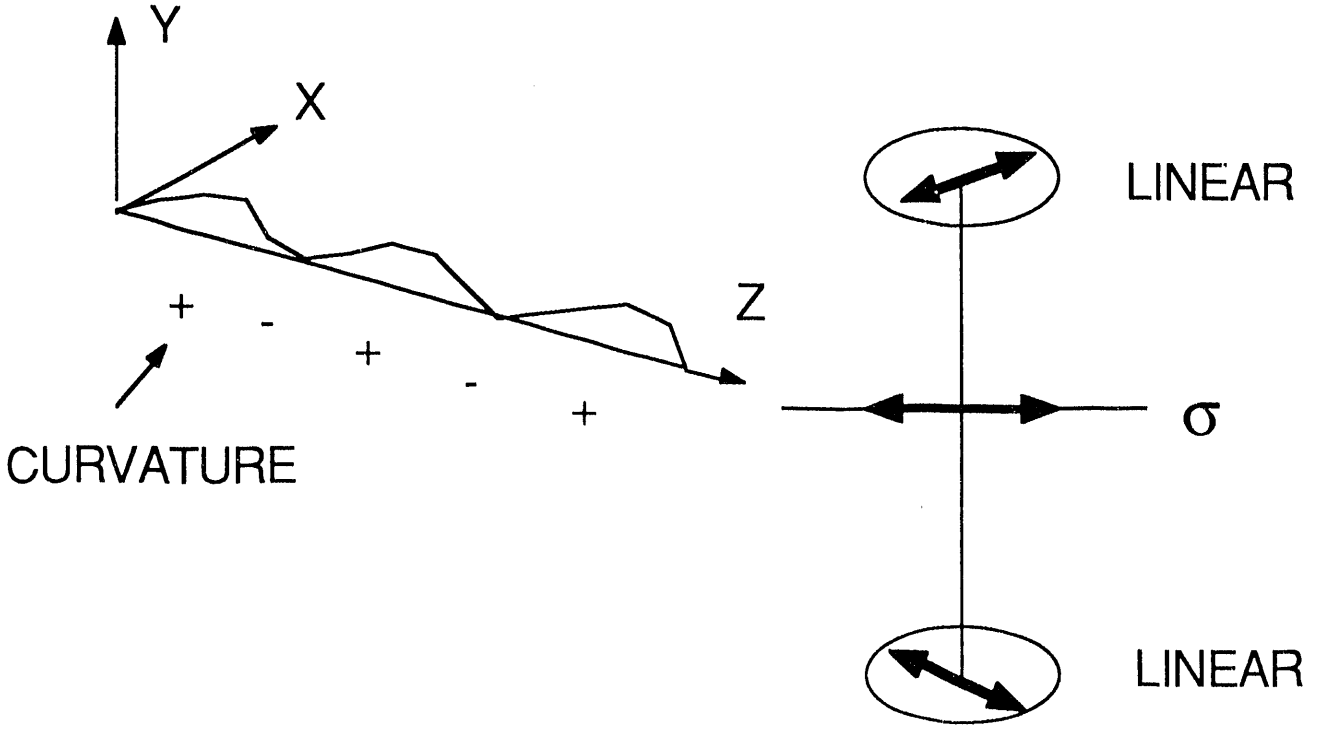

Undulator Polarization Properties (Zero-Emittance Case)

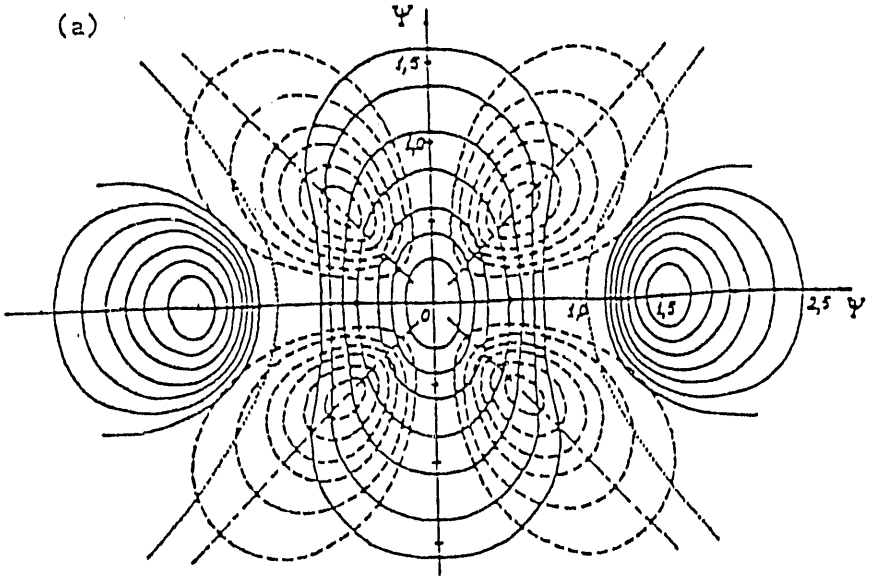

1st Harmonic

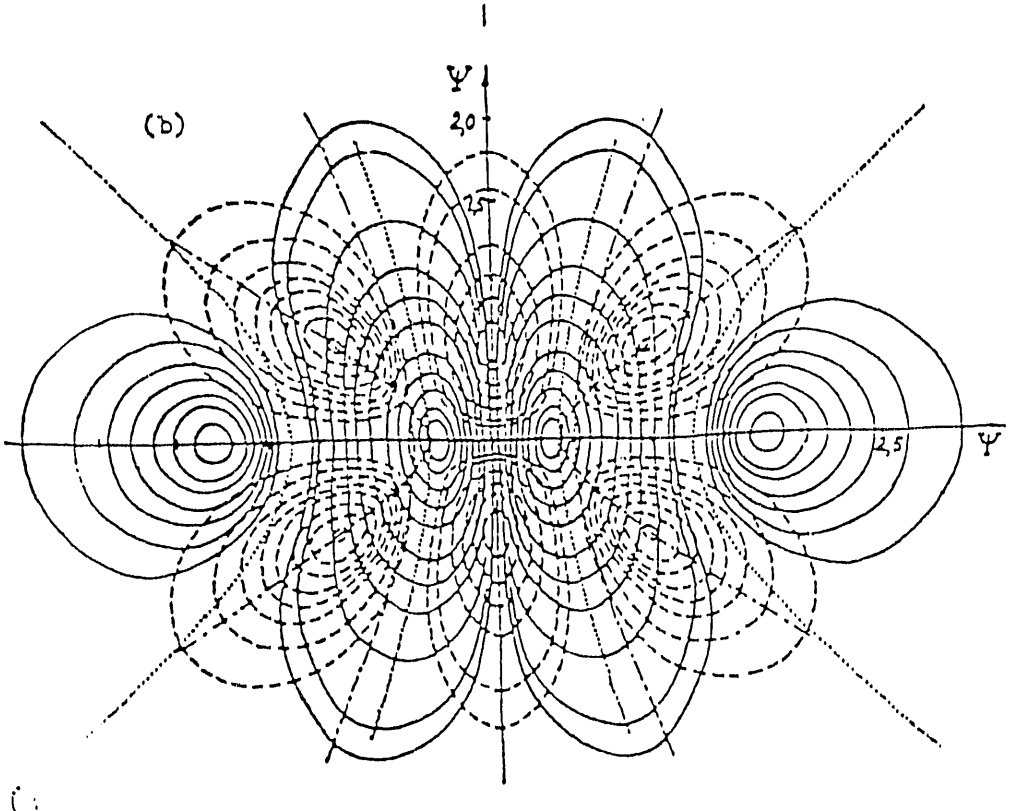

2nd Harmonic

Undulator Polarization Properties (APS-Emittance Case) 1st Harmonic

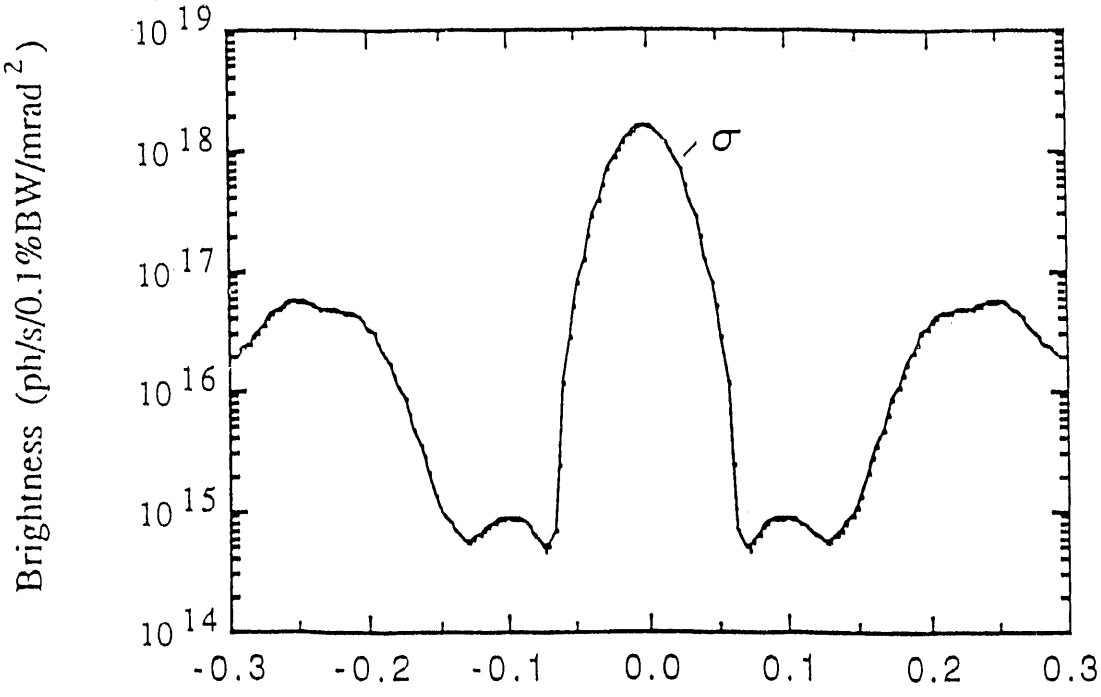

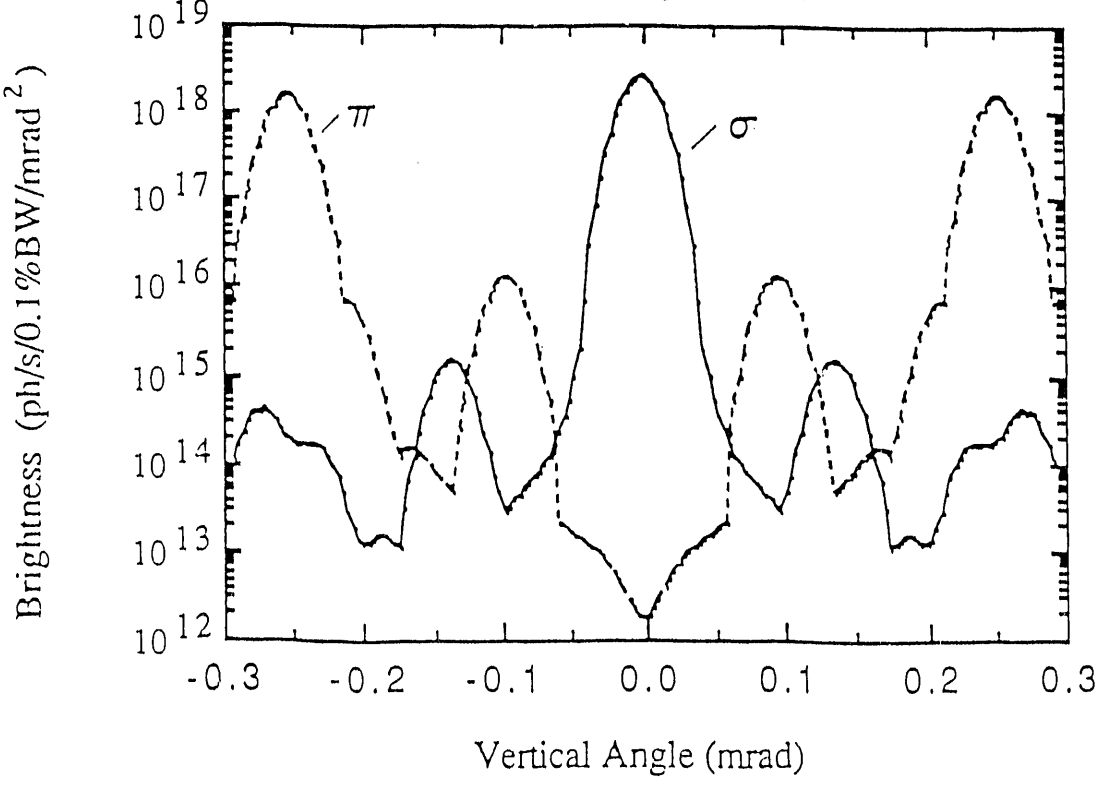

ELLIPTICAL WIGGLER

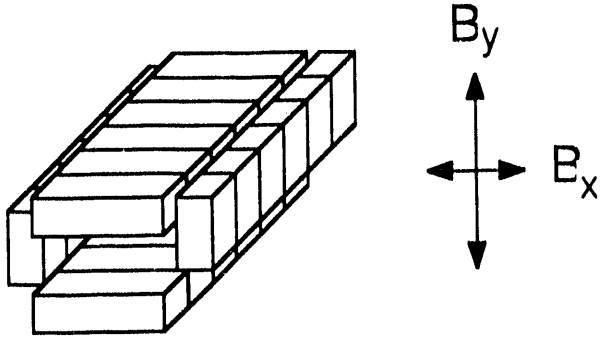

Elliptical
Trajectory

Depends on Phase of
Bx and By

Trajectory

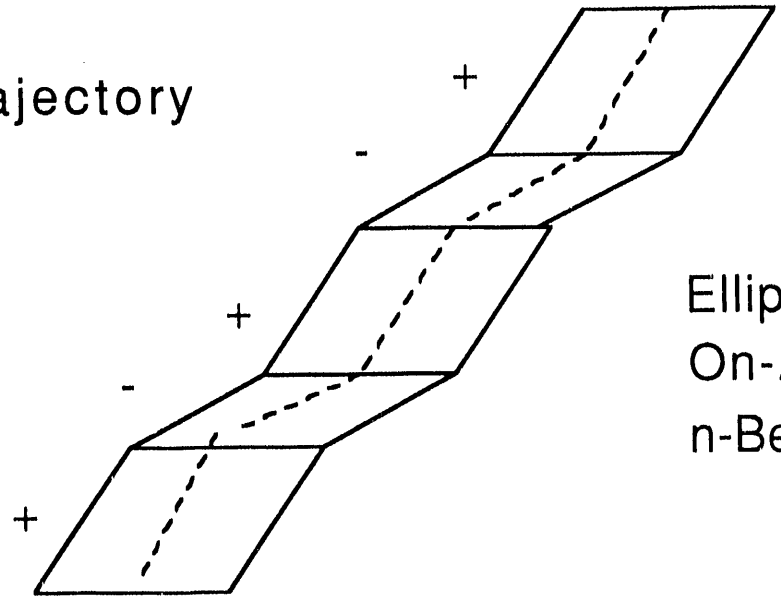

Elliptical Polarization
On-Axis
n-Bending Magnets

Change Phase by Shifting Bx with respect to By

ELLIPTICAL MULTIPOLE WIGGLER

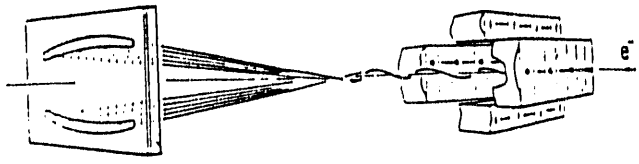

Cu Attenuator Wiggler

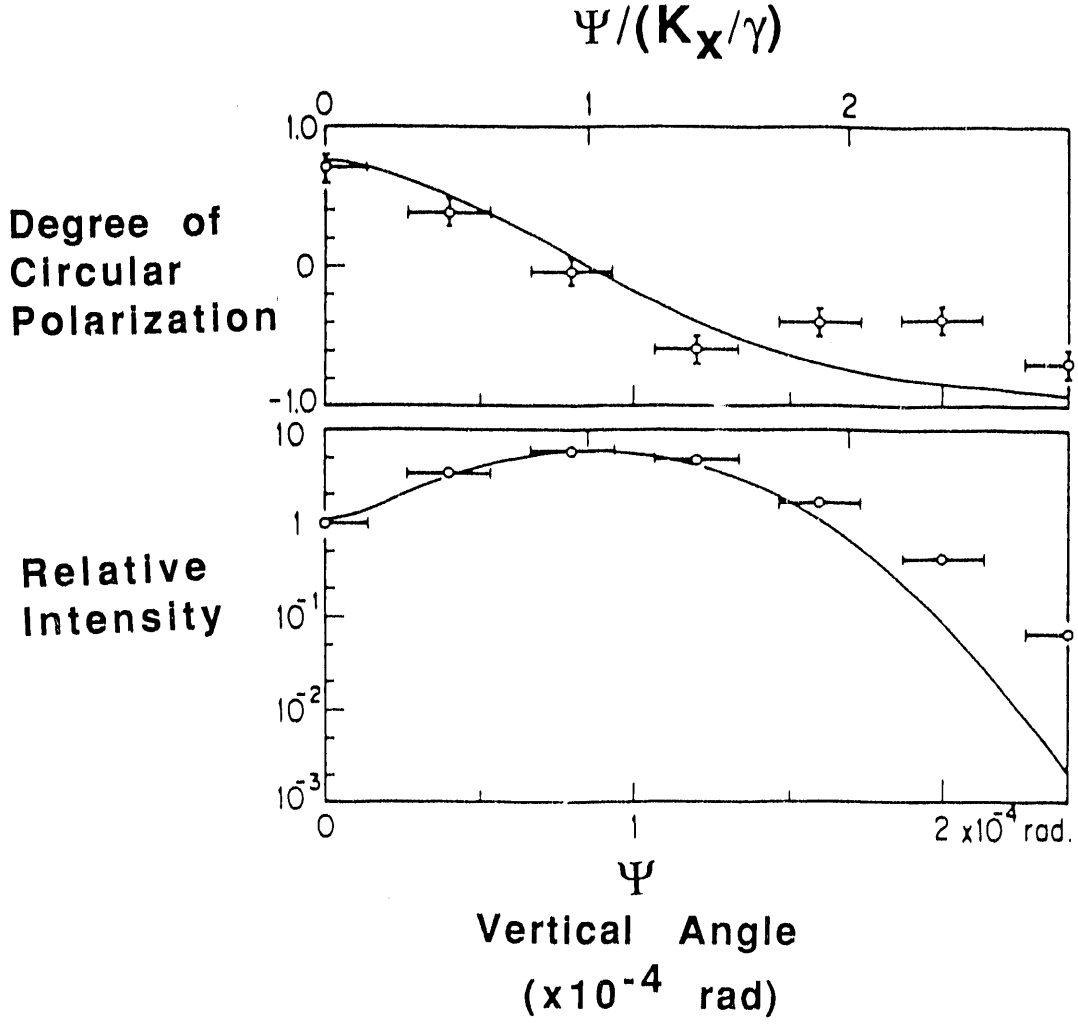

Adapted from S. YAMAMOTO et al.
Phys. Rev. Lett. **62**, 2672 (1989)

APS STORAGE RING TIME STRUCTURE

- Ring Circumference: 1104 m
  Orbit Period: 3683 ns
  Number of Bunches 1-60
  Bunch Duration 50-100 ps

- Flux (Number Of Photons) Per Bunch
  7 GeV, 100 mA
  20 Bunches Circulating

Source	Flux (x-rays/0.1%BW)
Bend	1.7×10^6 /mradθ
Wig A	4.0×10^7 /mradθ
Und A	2.1×10^8

Bend and Wig at Ec
Und A At 1st Harmonic

AN OVERVIEW OF SYNCHROTRON RADIATION UTILIZATION

Arthur Bienenstock
Stanford Synchrotron Radiation Laboratory
Bin 69, P.O. Box 4349
Stanford, CA 94305

1. Introduction

Over the past decade and a half, the availability of synchrotron radiation has become a very important asset for chemical engineering research. As more experimental stations and brighter radiation become available, its use will spread even further. Its value arises presently from the very considerable capabilities it makes possible in the following areas:

Structure Determination
Electronic State Determination
Chemical Analysis
Imaging
Spectroscopy
X-Ray Lithography

The first four of these areas are discussed in this article. All six are pursued in more detail in the papers which follow.

2. Structure Determination Techniques

With its extremely high intensity, controllable polarization and "tunable" white radiation spectrum, synchrotron radiation has had a dramatic impact on our ability to determine atomic arrangements in crystalline, poorly crystallized and amorphous materials. The techniques affected are listed below:

<u>X-Ray Diffraction</u>
Crystallography
- Anomalous Scattering
- Rotation
- Laue

Powder Diffraction
Amorphous Materials
Two-Dimensional Systems
Surfaces and Surface Layers
Small-Angle Scattering

<u>X-Ray Absorption Spectroscopy</u>
EXAFS
- Bulk
- Fluorescence
- Surface
- Photon Induced Desorption

Near Edge Structure (XANES)

As these techniques are developed, they are being applied increasingly to study transformation and reaction kinetics. This development will make them even more valuable to chemical engineering in the years to come. Examples of such kinetic studies are contained in a number of papers in this volume.

2.1 Anomalous X-Ray Scattering

The tunability of synchrotron radiation makes it possible to exploit the phenomenon of anomalous x-ray scattering in a number of different arenas. Here, the phenomenon is explained more extensively than other approachs, since it is not covered elserwhere in this volume.

As long as multiple scattering is not as an important phenomenon, the intensity of x-ray scattering, I(k), where k is the normal scattering vector, can be written as

$$I(\underline{k}) \propto |F(\underline{k})|^2, \qquad (1)$$

where the structure factor, F(k), is given by the equation

$$F(\underline{k}) = \sum_j f_j \exp(i\underline{k} \cdot \underline{r}_j). \qquad (2)$$

Here, fj is the atomic scattering factor and rj is the positional coordinate of the j-th atom. At photon energies which are high compared to any atomic excitation energies of the system, fj is merely the Fourier transform of j-th atom's electron density, foj. At photon energies close to an absorption edge of the j-th atom, however, there are both real and imaginary shifts so that fj is given by the equation

$$f_j = f_{oj} + f_j' + if_j''. \qquad (3)$$

fj" is simply proportional to the x-ray absorption coefficient. Hence, it decreases slowly with increasing photon energy until the x-ray absorption edge is reached. There, it jumps markedly and then decreases slowly with further increases of the photon energy. fj' is negative and is sharply negatively peaked at the x-ray absorption edge. For an atom like germanium with an atomic number of 32, fj' reaches values of -8 at the edge. Its magnitude is even larger at the L-edges of some transition elements.

The importance of anomalous scattering in protein crystallography arises from its ability to either supplement or replace the method of isomorphous replacement in the solution of the classic phase problem. That is, in order to determine the phases needed to reconstruct the electron density from the measured intensities,

one needs three different protein crystals in the method of isomorphous replacement. These are assumed to have identical structures except for the replacement of a specific element by two other elements. In a very large number of cases, it is our inability to grow the three different types of crystals which prevents the determination of the protein or macromolecular structure. This problem can be circumvented with anomalous scattering because one can vary the photon energy and make a single atom look like two different atoms by changing its atomic scattering factor. The resulting Multiwavelength Anomalous Dispersion (MAD) method[1] has found increasing utilization since its development approximately half a decade ago.

Anomalous scattering has also been used[2] to enhance the effectiveness of crystal structure determination by means of Rietveld analysis of powder diffraction data.

Similarly, the classical radial distribution function (RDF) structure determination technique often yields ambiguous results for amorphous materials containing more than one atomic species. The RDF yields the probability of finding two electrons separated by distance R, but from a system in which all the electrons of each atom are located at its center. Thus, it has peaks at the sample's common interatomic distances and the peak areas provide information about the coordination numbers. The ambiguity arises because one cannot tell which pair of atomic species are contributing to each interatomic distance peak.

This ambiguity is decreased markedly through employment of the Differential Distribution Function technique.[3,4] By utilizing two different sets of intensity measurements at two different photon energies close to the absorption edge of a specific atomic species, one gets a distribution function in which that specific species must be at least one of the participants in each interatomic distance pair. That is, all the pairs which do not involve that species are eliminated from the distribution function. This technique is particularly powerful when combined with the EXAFS technique described below.

Anomalous small-angle x-ray scattering is also become increasingly valuable for studying phenomena like phase separation, spinodal decomposition and voids in crystalline[5] and amorphous[6] alloys. The method is particularly valuable for amorphous thin films, where it was usually extremely difficult to determine whether small-angle x-ray scattering arose from voids, other defects or phase separation. With differential anomalous scattering, one can separate out the density fluctuations associated with each atomic species and distinguish between defects and phase separation. This technique can be made even more powerful through complementary utilization of the XANES discussed below.

2.2 The Rotation Method

One of the simplest synchrotron radiation crystal structure determination techniques[7] is built around the classical rotation camera. As employed now, one uses the extreme intensity of synchrotron radiation to take the rotation or oscillation picture very rapidly. The value of the method arises from the fact that radiation damage is not simply proportional to photon dose, but requires time as well since it is a two step process with some transport involved. With synchrotron radiation, therefore, much more data can be acquired from a crystal before it is severely damaged by the radiation then can be acquired with classical x-ray tubes. The lifetime of the crystal is even further enhanced by reducing its temperature to those of liquid nitrogen or helium.

2.3 The Laue Technique

In the Laue technique[7] for acquiring single crystal x-ray diffraction data, a white radiation beam is incident upon the sample so that many different sets of crystalline planes are in reflecting positions. With the extreme synchrotron radiation white radiation intensity's, data from protein crystals can often be acquired in fractions of a second. Thus, the approach provides a second method for avoiding radiation damage while obtaining protein diffraction data. In addition, atomic arrangements in excited or transition states can be examined.

2.4 Powder Diffractometry

In addition to the Rietveld Method discussed in Sec. 2.1, the extremely low divergence of synchrotron radiation can be valuable in the solution of very difficult powder diffraction problems.[8] For example, the normal use of powder diffractometry to identify crystalline phases in some complex materials is often difficult to apply when there are a number of phases whose diffraction lines overlap when examined with a normal x-ray system. With the very highly collimated synchrotron radiation that can be used readily in powder diffractometry, these peaks can often be resolved and identified separately. Similarly, the instrumental contribution to line broadening can be made very small, so that crystalline size and strain contributions can be determined more readily.

2.5 Two Dimensional Systems, Surfaces and Surface Layers

With the advent of synchrotron radiation, it has become possible to examine systems which are just a molecule or two thick, the surfaces of materials, or surface layers ranging in thickness from a few angstroms to a few microns.

In the most straight forward of these approaches, the extreme intensity and collimation is used to obtain diffraction patterns

from two-dimensional layers of liquid crystals and similar materials employing normal x-ray diffraction transmission or reflection procedures. As a result, it has been possible to study structural arrangements during phase transformations in these materials.

To achieve variable depth sensitivity when studying surfaces or surface layers, the technique of Grazing Incidence X-ray Scattering (GIXS)[9] is employed. In this technique, the x-ray beam is incident on the sample at an angle close to the critical angle for total reflection (a few tenths of a degree). By varying the angle of incidence, the penetration depth can be varied from about 20 Å to many microns. Portions of the beam which penetrates into the sample are diffracted with normal processes. From the resulting diffraction pattern, considerable information about the structure at the surface or in the surface layer can be obtained.

GIXS is proving to be, quite valuable in the study of thin amorphous films, reconstructed surfaces, phase transitions in adsorbed monolayers and surface layers of polymers and photoresists. We may expect it to be employed in the study of corrosion, oxidation, wear, polishing and surface chemical treatments.

Finally, the x-ray standing wave technique discussed by Bedzyk in this volume can be employed to obtained information about surface layers.

3. X-Ray Absorption Spectroscopy

3.1 EXAFS

The utilization of Extended X-Ray Absorption Fine Structure (EXAFS)[10] for structure analysis is discussed by many authors in this volume. EXAFS is used to determine the average coordinations of specific atomic species in complex materials which need not be crystalline. In this technique, one measures the x-ray absorption coefficient as a function of photon energy from immediately below the absorption edge to energies approximately 1000 eV above the edge. The absorption coefficient, like fj", decreases with increasing photon energy above the edge, then increases markedly at the absorption edge and then shows an overall decrease with increasing photon energy above the edge. Superimposed on the overall decrease above the edge are some sharp oscillations at very small energies above the edge and then a series of broader oscillations. It is the broad, or lower frequency, oscillations which are the EXAFS.

The oscillations arise in the following manner. The electron excited in the photoelectron absorption process may be perceived as a spherical wave. As that wave propagates outward, it hits the atoms surrounding the absorbing atom and is reflected back. In

the matrix element which governs the transition of the photoelectron from its highly localized initialed state to this final state, the final state wave function is effectively sampled at the absorbing nucleus. In this sampling process, the interference between the outgoing spherical wave and the back-scattered wave yields the oscillations as the photon energy is increased.

Thus, the EXAFS arise from a diffraction process in the final state wave function. As a result, one can use the EXAFS to determine the distance to near and further neighbors, get an idea of the number of those neighbors and, often, identify the species of those neighbors.

Since the EXAFS process is entirely local, it may be employed on amorphous materials as well as crystalline. Because each element has an identifiable absorption edge energy, EXAFS can be used to determine the average environment of each atomic species in a complex material. Thus, for example, it may be employed to determine atomic arrangements of very finely distributed catalyst material on a support or the environment of each atomic species in commercial complex glass or amorphous film.

3.1.1 Fluorescence EXAFS

As indicated above, the EXAFS is linked directly to the probability of exciting an electron from a core state to the continuum. As a result, any process which is directly coupled to that excitation will also show the fine structure as a function of photon energy above the absorption edge of a constituent atom. If that constituent atom is present at very low concentrations, it is usually advantageous to study its contribution to the x-ray fluorescence, rather than its contribution to the absorption coefficient. While its contribution to the absorption coefficient may be negligible because of the low concentration, it is likely to be the only element emitting at its fundamental fluorescent energies. Thus, a detector capable of photon energy analysis will yield a very high increase in signal to noise. With this technique, the surroundings of atoms present at concentrations as low as one part in 10^5 have been determined.

A beautiful utilization of the fluorescence technique is to determine how the surroundings of metal atoms in metalloproteins or metalloenzymes change as those proteins or enzymes go through their biological functions. Thus, for example, the surroundings of Fe atoms in hemoglobin have been determined in the oxidized and deoxidized states. Similarly, the surrourdings of sulfur in coal have been studied.

3.1.2 Electron Yield EXAFS

Surfaces may be studied by measuring photoelectron yield as a function of photon energy, since the electrons reaching the detector usually come from within a few angstroms of the surface. One may utilize this technique, for example, to study the poisoning of a catalyst by sulfur.

3.1.3 Photon Desorption EXAFS

One may even study the environments of metallic atoms next to oxygen atoms on partially oxidized surfaces using the technique of photon induced desorption EXAFS. Similarly, one can find the environments of metal atoms adjacent to sulfur atoms in partially poisoned catalyst surfaces.

3.2 Photoemission and Photoelectron Diffraction

Although it is widely regarded as a technique for studying electronic states, photoemission can be used to study the geometry of adsorbates on surfaces (Reference) and photoelectron diffraction is also used as a surface structure technique

4. Electronic State Determination Techniques

The determination of electronic states via synchrotron radiation is less relevant to this meeting, since they are not usually the focus of chemical engineers. Here, though, some of the techniques are listed and references are provided:

Photoemission
- Band Structure Analysis
- Densities of States
- Surface and Interface States

Compton Scattering
X-Ray/VUV Spectroscopy

Photoemission is a "classical" technique[11] for the determination of electronic densities of states. Monochromatic light incidence upon a sample yields photoemitted electrons. By subtracting the kinetic energy of the photoelectrons from the photon energy, the binding energy can be obtained. The number of photoemitted electrons as a function of kinetic energy then yields a distorted density of electronic states in the material. With angle resolution as well as energy resolution, the band structures of crystalline materials can be determined.

In addition, surface and bulk states can be distinguished using synchrotron radiation. This is achieved by varying the incident photon energy. For almost all materials, the electron meanfree??? path is only about five angstroms when the photoelectron energy is about 100 eV above the Fermi level. Thus, virtually all electrons reaching the detector come from a thin surface layer. If the

photon energy is increased so that the kinetic energy is of the order of 1,000 eV, the meanfree???? path increases markedly so that bulk states may be examined. Compton Scattering is a means of measuring electron momentum distributions in solids. These are used primarily to check theoretical calculations of electronic states.

5. Chemical Analysis Techniques

Two types of chemical analysis techniques are utilized synchrotron radiation:

X-Ray Fluorescence Analysis
X-Ray Absorption Spectroscopy

5.1 X-Ray Fluorescence Analysis

X-Ray fluorescence analysis is commonly employed in laboratories for chemical analysis, utilizing standard x-ray generators. Synchrotron radiation is employed when there are very special demands or, as discussed in the imaging section, when images based on chemical composition are to be constructed. An example of the former is the search by Sparks et al.[12] for super-heavy atoms in some ores. These workers showed that the sensitivity to $5X10^8$ super-heavy atoms per sample could be achieved utilizing tunable monochromatized synchrotron radiation and solid state, energy sensitive detector.

5.2 X-Ray Absorption Spectroscopy

As indicated in the EXAFS section, each element provides an absorption edge signal when the x-ray absorption coefficient is measured as a function of photon energy. This array of absorption edges provides the means by which the chemical analysis of a thin film may be performed[13].

6. Synchrotron Radiation Imaging Techniques

A variety of techniques have been developed for imaging, among which are:

X-ray topography
X-ray tomography
Non-invasive angiography
Photoelectron microscopy
X-ray microprobe
X-ray microscopy

6.1 X-Ray Topography

X-ray topography is used to image defects or strain fields in nearly perfect single crystals. In this technique the image is formed by mapping the intensity of a Bragg reflection over an area or volume of the diffracting crystal. Contrast arises from the changes in intensity resulting from the presence of defects and/or strain. Synchrotron radiation is valuable because a beam of very high intensity and low divergence can be achieved. In recent years, the technique has been employed to examine the relationship between properties of thin films[14] and those of the substrates as well as to examine strain fields[15] resulting from standard semiconductor processing processes.

6.2 X-Ray Tomography

Similarly, synchrotron radiation versions of three-dimensional x-ray tomography[16] have been developed. With the extremely high x-ray intensities and low angular divergences, coupled to two-dimensional detectors developed specifically for the purpose, one micron resolution has been obtained. In addition, concentrations of specific elements can be obtained by performing the x-ray tomography at photon energies which are somewhat above and somewhat below the absorption edge energies of the element of interest.

6.3 Non-Invasive Angiography

The procedure of obtaining images above and below absorption edge energies has also been employed in the development of a procedure to image the coronary arteries[17]. The goal of this work is to develop a diagnostic procedure which avoids the arterial catheterization and heavy iodine doses of the standard angiographic procedure. Low concentrations of iodine are introduced through the jugular vein into the coronary arteries. The contrast is obtained by taking pictures in rapid succession above and below the iodine absorption edge and then subtracting the two digitally.

6.4 Photoelectron Microscopy

Photoelectron microscopy[18] obtains images by "viewing" the electrons emitted from a very small area of a sample and then scanning that area over the surface. The small areas are obtained by either focusing the "light" or by utilizing detection schemes which detect the electrons from a small area. All the standard photoelectron spectroscopy techniques can be coupled to provide different types of images.

6.5 X-Ray Microprobe

X-ray microprobe images[19] employ standard x-ray fluorescence analysis techniques, but with beams which are focused to small areas. Again, the area of the sample is scanned to obtain the image.

6.6 X-Ray Microscopy

In x-ray microscopy[20], the beam is focused to a very small area and the image is obtained by measuring the sample's transmissivity. Elemental sensitivity can be obtained by imaging at photon energies above and below absorption edges.

7. References

1. See, e.g., J.M. Guss, E.A. Merritt, R.P. Phizackerley, B. Hedman, M. Murata, K.O. Hodgson and H.C. Freeman, Phase Determination by Multiple-Wavelength X-ray Diffraction: Crystal Structure of a Basic "Blue" Copper Protein from Cucumbers, *Science*, 241, 806 (1988).

2. G.H. Kwei, R.B. Von Dreele, A. Williams, J.A. Goldstone, A.C. Lawson and W.K. Warburton, Structure and Valence from Complementary Anomalous X-ray annd Neutron Powder Diffraction, *J. Molecular Structure*, 223, 383 (1990).

3. P.H. Fuoss, P. Eisenberger, W.K. Warburton and A. Bienenstock, Application of Differential Anomalous X-ray Scattering to Structural Studies of Amorphous Materials, *Phys. Rev. Letters* 46, 1537 (1981).

4. J. Kortright and A. Bienenstock, X-Ray Structural Study of Amorphous Mo-Ge Films", *Phys. Rev. B* 37, 2979 (1988).

5. See, e.g., J.P. Simon and O. Lyon, A determination of partial structure factors in an unmixed CuNiFe alloy by anomalous small-angle X-ray scattering, *Phil. Mag. Letters*, 55, 75 (1987).

6. See, e.g., P. Goudeau, A. Naudon, A. Chamberod, B. Rodmacq and C.E. Williams, On the Nature of the Heterogeneities in a Hydrogenated CuTi Amorphous Alloy: an ASAXS Study, *Europhys. Lett.*, 3, 269 (1987).

7. C. Nave, Protein Crystallography on a Synchrotron, *Synchrotron Radiation News*2, 24 (1989).

8. See, e.g., W. Parrish and M. Hart, Parallel Beam and Focusing X-ray Powder Diffractometry in *Advanced X-Ray Analysis, Vol. 32* (Plenum Press, 1989) p. 481.

9. See, e.g., S. Brennan and A. Bienenstock, Grazing Incidence X-ray Scattering, *Res. & Dev.* 31, 52, December, 1989.

10. See, e.g., *EXAFS and Near Edge Structure III*, eds. K.O. Hodgson, B. Hedman and J.E. Penner-Hahn (Springer-Verlag, 1984).

11. See, e.g., *Handbook on Synchrotron Radiation 2*, ed. G.V. Marr (North Holland, 1987).

12. C.J. Sparks, S. Raman, H.L. Yakel, R.V. Gentry and M.O. Krause, *Phys. Rev. Letts.* 38, 205 (1977).

13. L.C. Wilson, Atomic Arrangements in Short Period Molybdenum/Germanium Multilayers, Ph.D. Thesis, Stanford University, unpublished.

14. M. Kaminska, E. Weber, Z. Lilental-Weber and Z.U. Rek, Stoichiometry-Related Defects in GaAs Grown by Molecular Beam Epitaxy at Low-Temperatures, *J. Vac. Sci. & Tech. B* 7, 710 (1989).

15. S.R. Stock, Y.C. Chung and Z.U. Rek, A Multiple Slit Collimator for Synchrotron White Beam Section Topography, *J. Appl. Cryst.* 22, 70 (1989).

16. See, e.g., J.H. Kinney, S.R. Stock, M.C. Nichols, U. Bonse, T.M. Breunig, R.A. Saroyan, R. Nusshardt, Q.C. Johnson, F. Busch and S.D. Antolovich, Nondestructure Investigation of Damage in Composites Using X-ray Tomographic Microscopy (XTM), *J. Mater. Res.* 5, 1123 (1990).

17. A.C. Thompson, J.D. Zeman, E. Rubenstein, J.N. Otis, R. Hofstadter, G.S. Brown, D.C. Harrison, R.S. Kernoff, J.C. Giacomini, H.J. Gordon and W. Thomlinson, Coronary Angiography using Synchrotron Radiation, *Rev. Sci. Instrum.*, 60, 1674 (1989).

18. See, e.g., P. Pianetta, I. Lindau, P.L. King, M. Keenlyside, G. Knapp and R. Browning, Core Level Photoelectron Microscopy with Synchrotron Radiation, *J. Electron. Spectros. Rel. Phen.*, 52, 797 (1990).

19. See, e.g., A.C. Thompson, J.H. Underwood, U. Wu, R.D. Giauque, M.L. Rivers and R. Futernick, X-ray Microprobe Studies Using Multilayer Focussing Optics, *Adv. X-ray Analysis*, 32, 149 (1989).

20. See, e.g., *X-Ray Microscopy*, eds. G. Schmahl and D. Rudolph (Springer-Verlag, 1984).

STATUS REPORT ON THE ADVANCED PHOTON SOURCE

by

David E. Moncton
Associate Laboratory Director for the Advanced Photon Source
Argonne National Laboratory
Argonne, Illinois 60439 U.S.A.

Introduction

It is my pleasure to bring you up to date on the progress of construction for the Advanced Photon Source (APS) here at Argonne National Laboratory (ANL). Eight years have passed since an *ad hoc* committee on "future opportunities and technical needs for synchrotron-radiation-based research" was formed by the Department of Energy's Office of Basic Energy Sciences. That committee, chaired by P. Eisenberger and M. Knotek, proposed that the highest priority be given to construction of a high-energy storage ring designed to provide fundamental undulator radiation in the hard x-ray region of the spectrum.[1] In reaching that conclusion, the committee consulted with members of the U.S. synchrotron-radiation-research community as to their future needs. That example was followed in the planning and design for a facility to meet the requirements set down by the Eisenberger-Knotek committee. Prospective users from industry, universities, and national laboratories have been a sought-after and important source of counsel and inspiration for APS planners. As a result, the facility that is beginning to rise at Argonne is truly a national user facility.

The APS will have 68 beamlines for research, with that number divided evenly between insertion device and bending magnet beamlines. X-ray beams emanating from the insertion devices situated in the APS storage ring lattice will achieve unprecedented levels of brilliance. Research and development in support of that goal began well before ground was broken for construction at the APS site. We are now seeing significant gains in the technologies that will make possible forefront research at the APS. Synchrotron radiation sources have traditionally supported research across a broad range of disciplines. The APS will not deviate from that tradition, as evidenced by the proposals to form Collaborative Access Teams (CAT) at the APS.

Project Status

Facility modifications

Some significant conceptual changes have been made to the APS Experiment Hall (Fig. 1). Previously, radio-frequency (rf) apparatus had been housed in two buildings located on the storage ring. The effect of this configuration was to create two separate "shadow" areas in the Experiment Hall where no beamlines could be used for

synchrotron radiation research. The rf buildings have now been eliminated. The rf cavities and their associated power supplies and klystrons have been consolidated near the 12 o'clock position on the Experiment Hall. As a result, the two shadow areas are now combined in one location. The injector facilities, while not altered technically, have been relocated slightly counterclockwise on the Experiment Hall infield. Taken together, these modifications have created five straight sections in a row where there are no insertion devices. That shadow area of some 30,000 ft^2 can be used for a variety of other activities. The first use has given that space its name: the Early Assembly Area (EAA). Here the magnets, power supplies, and vacuum system components, which will be constructed in various buildings away from the APS site, will be brought together and assembled on storage ring girders, thus expediting completion of the accelerator system.

Additionally, the Control Center, the Central Laboratory/Office Building (CLO), and the Multi-Functional Building have been reconfigured and now lie in the path of the shadow area. This change will assure that there is absolutely no radiation in that area that would require non-radiation workers to have film badges. Access to office buildings, conference rooms, and libraries will be completely open.

Conventional facilities construction

The current forecast for construction expenditures is consistent with the original $456 M total estimated cost. APS has spent $52 M to date, with $343 M estimated for completion. The difference of $61 M resides in the contingency account. Overall, procurement of construction subcontracts is running at or under budget, due in part to the current buyer's market. Additionally, APS planners have made the facility designs more cost effective. The detailed design phase for almost all technical buildings (with the exception of the CLO and the user modules around the periphery of the ring) is nearly complete. Conventional facility construction began in July 1990 following ground breaking in June 1990. Site preparation activities were conducted in the late summer and early fall of that year. Contracts totalling nearly $40 million are to be awarded during FY1991. In April, work began on the Utility Building, the first structure to be erected on the site, with completion scheduled for spring 1992. Also in April, a subcontractor began pouring the 274 concrete caissons that are the support footings for the Experiment Hall. Other subcontracts recently awarded include those for the cooling tower, site grading, and site utilities. Work will begin soon on the Linac/Injection Wing structure, the first step in construction of the technical facilities. Beneficial occupancy is to occur in April of 1992. Fiscal year 1992 will also see beneficial occupancy of the synchrotron building (December 1992). Having the storage ring available for commissioning in June of 1995 will allow some early user beams. Various beamlines will come on over time, with the official completion of the project scheduled for late 1996.

Technical components

1. Accelerator Systems Division

The R&D program for APS technical components has benefitted from early and careful planning and design. As a result, the program is very well advanced, with many items in the prototype stage and some hardware for operations already procured. In FY1991, the detailed design for critical storage ring components such as the rf cavities, the vacuum system, the storage ring quadrupole magnet system, and the beam position monitors (BPM) will be completed.

A. Vacuum system

A vacuum system prototype comprising five extruded-aluminum 6063T5 alloy vacuum chamber segments connected by bellows and conflat flanges has been assembled. The prototype, which is equivalent to a full sector (1/40th) of the APS storage ring, permits complete testing of the manufacturing process, the vacuum integrity, the bakeout process, and the alignment of the chambers. This last factor is critical, as the chambers will carry the beam position monitors (BPM), which must be capable of detecting the particle beam position to better than ± 0.1 mm in order to assure the required beam stability. When a chamber is baked out, the BPMs move with the expansion and contraction of the chamber material and then must return to their original locations within very demanding tolerances.

B. Magnets

The APS storage ring magnets are crucial to successful operations, particularly the more than 400 storage ring quadrupole magnets, which have very precise magnetic-field tolerances. A second prototype storage-ring quadrupole has now been completed and tested, and indicated changes are being incorporated into the final design. A magnet test facility, to consist of four test stands (one dipole and three multipole), has been established in order to assure that all APS magnets achieve magnetic field requirements.

C. Girders

The girders that will support magnets, vacuum systems, and power supplies are central to the performance of the APS storage ring, which will have a low emittance and heavy tolerances. A resonant dynamical response by the girder to ground vibrations could lead to an amplified deflection of the stored beam. A girder has been loaded with a prototype storage ring magnet together with concrete blocks to simulate the weight of the other magnets on the girder, and three-dimensional dynamical testing of the girder assembly has been done. Lessons learned from this exercise will be applied to the girder design, leading to greater stability.

D. Linac

Procurement of the linac has been gratifyingly successful in that linac components have been obtained under budget and on schedule to date. The first of these components, led by the electron-gun assembly, are beginning to arrive. The gun is expected to be operational shortly, and we hope to have electrons accelerated to 60 MeV by fall of this year.

E. Radio-frequency systems

Mindful that radio-frequency systems have historically been a major challenge for storage rings and synchrotron facilities, the APS staff began very early in the project to develop an rf acceleration cavity prototype that could be run at high power. Due to this lead time, the prototype storage ring copper cavity arrived at Argonne on schedule in spite of earlier subcontractor delays. The cavity has met all performance requirements and is now undergoing "hot" tests on the rf test stand. This stand consists of a 250-kW klystron and an rf waveguide to provide power to the cavity. Synchrotron rf acceleration cavities are being fabricated by Interatom G.m.b.H., of Germany; delivery of the first cavity is expected in the fall of 1991.

2. Experimental Facilities Division

Insertion devices (ID), high heat-load optics, front-end engineering, and a variety of associated novel techniques are being addressed by the Experimental Facilities Division (XFD).

A. Insertion devices

A 3.3-cm-period undulator was designed in collaboration with staff from the Cornell High Energy Synchrotron Source and installed on the Cornell storage ring, CESR, three years ago, where it had a very successful run. We are on the verge of a several-weeks-long run of that device beginning in June. In tests at the U-5 port of the vacuum ultraviolet ring on the National Synchrotron Light Source (NSLS), the second prototype APS ID has confirmed our choice of materials and the constructability of the design. These tests have also demonstrated industry's ability to successfully construct insertion devices. Attention is now turning to tapered undulators, devices to produce circular polarization, and other novel ID techniques.

B. Optics cooling

Optical beamline elements at the APS will be required to accommodate intense heat from x-ray beams. The next-generation light sources now being constructed in Europe (European Synchrotron Radiation Facility) and Japan (SPring-8) are also challenged by this problem. Researchers at ANL have settled on liquid gallium as an optimal coolant for monochromating crystals. Liquid-Ga is being delivered efficiently by an APS-designed induction pump. The first version of this pump has been modified, resulting in a factor-of-five increase in flow rate. New concepts are

being devised for the monochromating crystals. Combining these advances has resulted in the ability to move further into the power densities that are appropriate for these new-generation machines. Power densities in the few tens of watts per square millimeter, approaching 100 W/mm^2, will be manageable. That would permit the APS to achieve brilliance levels of 10^{18} (photons • s^{-1} • mm^{-2} • mr^{-2} [0.1% bandwidth]$^{-1}$), corresponding to 5 or 10 mA stored in the storage ring. The full 100-mA current would afford brilliance of 10^{19} with a few hundred watts per square millimeter. Attaining that final level of brilliance is the focus of ongoing R&D.

C. Optics

In collaboration with R. Bionta of Lawrence Berkeley Laboratory, APS staff members have been making circular Fresnel jelly-roll structures measuring a few tenths of a millimeter in diameter to be used as hard x-ray zone plates. These zone plates have been used successfully at the NSLS to focus hard x-rays into spots of a micron or so. As work on these novel techniques progresses, one can expect to see a number of new instruments and new optical devices become available to the user community.

Project staffing

There are currently 265 staff members at APS, ahead of the scheduled recruiting pace. Emphasis has been on adding technical staff in the Accelerator Systems (ASD) and the Experimental Facilities (XFD) Divisions. It is particularly gratifying to have John Galayda as Division Director of the ASD. His appointment places that Division in the hands of someone who has had the experience of designing, constructing, commissioning, and operating the NSLS, experience that is critical to the APS.

User Issues

Collaborative Access Teams

Nineteen proposals to form Collaborative Access Teams, requesting use of 44 beamlines, were received for screening by the APS Proposal Evaluation Board (PEB). These proposals represent more than 400 principal investigators from 18 industries, 77 universities, 7 medical schools, and 19 research institutions (national labs and others). There have been 12 requests for APS standard undulators, 4 each for two types of wigglers, and 4 other devices have been requested. Scientific disciplines represented in the proposals include structural biology, materials science, geoscience, chemical science, soil/environmental science, medical imaging, biophysics, and basic energy science.

Scientific Review Panels

The PEB is now commissioning four panels for the scientific review of proposals to form CATs. This review process will include an effort to think through the standardization of beamline components. The objective is to assemble the most

reliable beamlines for the lowest possible cost, and to put as much engineering as possible into the fewest devices required. This review process is to be complete by October 15, 1991.

Independent Investigators

Each sector on the ring will be managed by a Collaborative Access Team (CAT), which will make at least 25% of its beam time available to independent investigators. A number of proposed CATs are structuring themselves so as to afford considerably more than 25% of their beam time to outside users. That is particularly the case with proposals put forth by the ANL's programmatic divisions. The Basic Energy Sciences Synchrotron Radiation Center that is being supported by the ANL Materials Sciences, Chemistry, and Physics Divisions is planning to provide 50% of its beam time to investigators from outside ANL. Plans for the proposed Structural Biology Center call for allotting a major share of beam time to the external research community.

Collaborative Research Program

A new Collaborative Research Program has been instituted to further cooperation between the APS and outside users who have an interest in a particular instrumentation development idea. Users will be invited to present formal written proposals, which will be reviewed by members of the XFD staff and the APS Users Organization Steering Committee. Accepted proposals will receive expertise and support, such as engineering, from the APS to complement resources brought by users.

User housing facility

A new, on-site, 240-bed housing unit to accommodate APS users without a residence in the Chicago area has long been a goal. A vacant parcel of land within walking distance of the facility has been selected and is the subject of environmental studies required for construction approval. Insights gained through consultation with user administrators at other synchrotron facilities have contribute greatly to a conceptual design,which is now well advanced. Discussions with the State of Illinois on this idea began in 1986 and led to a commitment by then Governor James R. Thompson to provide State financing for such a facility. Five years later, Illinois' financial situation is more austere, but we believe the State will honor its commitment.

Reference

1. "Planning Study for Advanced National Synchrotron-Radiation Facilities," P. Eisenberger and M. L. Knotek, Chairmen, Sandia National Laboratory Report (March 1984).

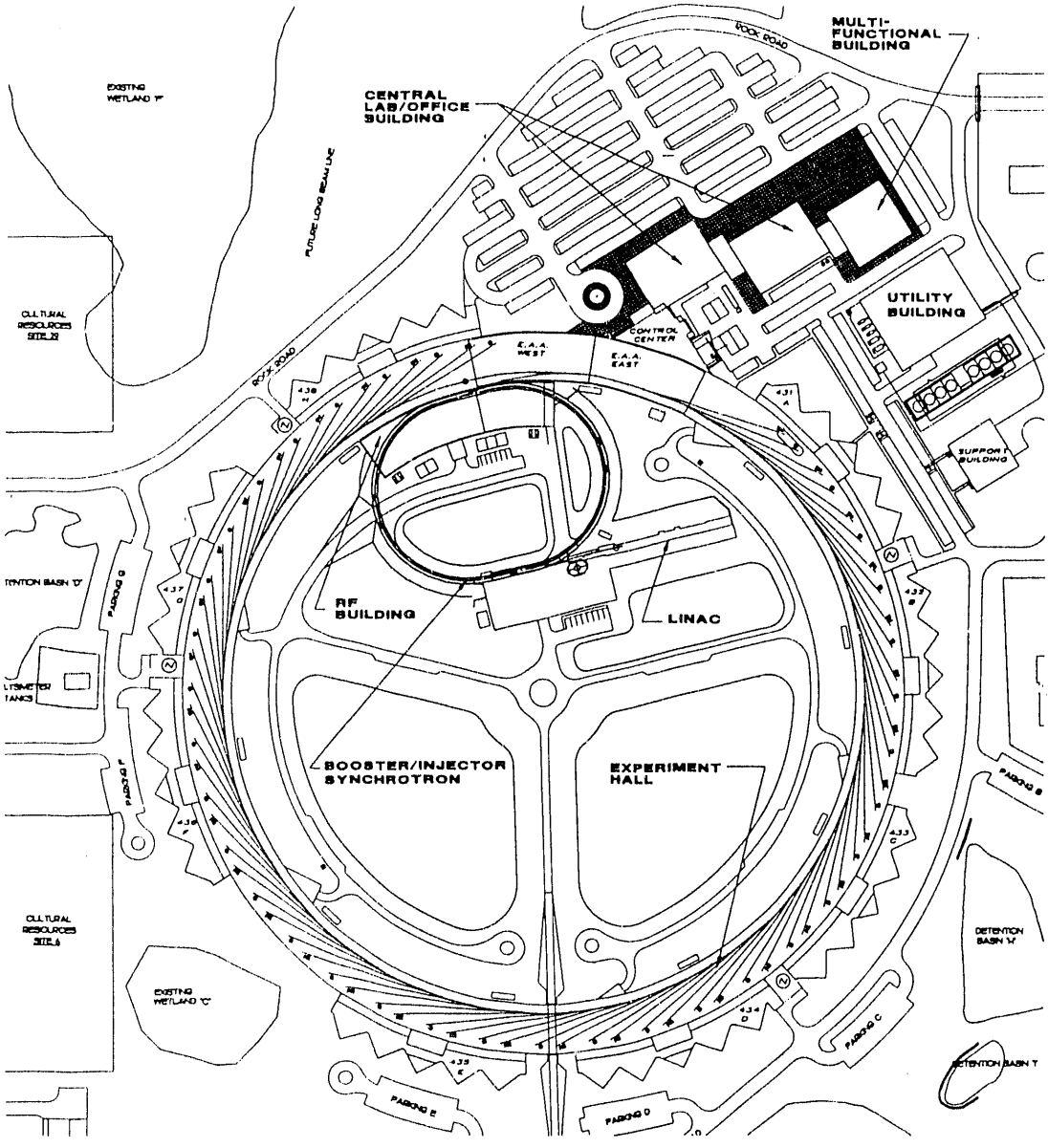

Fig. 1. Plan view of the Advanced Photon Source

PART II: TECHNICAL PRESENTATIONS

INVESTIGATION OF THE STRUCTURE AND CHEMISTRY OF SURFACE LAYERS ON METALS BY X-RAY ABSORPTION SPECTROSCOPY

Farrel W. Lytle and Robert B. Greegor
The Boeing Company, Seattle, WA 98124

1. Introduction

Most structural metals are very active chemically and without a passivating or protective layer would soon oxidize or corrode. The history of the industry is an attempt to minimize this process. The problem is becoming more acute, particularly in the aerospace industry, where the frames of many older airplanes are lasting longer than their outer skins. A more esoteric effect is the corrosion of metal surfaces in earth orbit by atomic oxygen. This paper is concerned with the structural and chemical characterization by x-ray absorption spectroscopy (XAS) of surface layers on aluminum alloys exposed to salt spray testing and with iron-based A-286 superalloy bolts exposed to atomic oxygen in a low earth orbit.

2. The Chromium-Conversion Surface on Aluminum

We describe some preliminary data on the chromium-conversion surface layer before and after salt spray testing on aluminum alloys (1). Some initial efforts of the characterization by XAS of fresh surfaces of this type have been reported (2,3). The use of this type of surface treatment is wide-spread in the industry, but is being phased out, because it is necessary to use a solution containing Cr^{6+}, a potent carcinogen, to prepare it. Consequently, there is a large effort to develop alternative surface treatments and to understand the present system. The role of Cr^{6+} in the surface is to react with any exposed bare Al with the resulting formation of a hydrated Cr^{3+} oxide which covers the Al and prevents further corrosion. The intent of this investigation was to determine the initial chemistry and structure around the Cr atoms and the change, if any, after exposure to salt spray. The aluminum alloy samples examined were of two types (compositions given as wt. pct.). Alloy **2024** contained 4.5 Cu, 1.5 Mg, 0.6 Mn, 0.3 Fe, 0. 15 Zn, 0.12 Si, 0.02 Ti, 0.02 Cr and the balance Al; alloy **7075** contained 6.0 Zn, 2.7 Mg, 1.6 Cu, 0.3 Fe, 0.2 Cr, 0.08 Si, 0.04 Mn, 0.03 Ti and the balance Al. These amounts are noted in order to give a perspective as to the kind of data obtainable from real samples. Satisfactory fluorescent x-ray data easily were obtained to about the 0.1% level.

The samples consisted of flat plates (2 x 3 x 0.1 cm) and were prepared by a deoxidizer cleaning and 1 or 3 minute immersion in an Alodine 1200S bath (4) followed by thorough rinsing and air drying. The samples were initially characterized by XPS, which is sensitive to the top 10-20 Å of the surface, and Auger analysis while sputtering in order to determine the approximate depth and composition of the surface layer. The thickness ranged from 2000-10,000 Å. These results are summarized in Fig. 1. The freshly prepared surface layer, which totally covered the sample, contained

only O, Cr, C, N, and Fe as noted. All of these elements were components from the Alodine bath used to prepare the surfaces. After salt spray testing (168 hrs. at 35 °C in a fine mist of 0.9 M NaCl) approximately 500 Å of the surface eroded away and some elements from the original alloy were uncovered. This was apparent in the depth profiling data and in the decrease in XAS Cr edge jump.

The XAS data were obtained using Si(220) crystals detuned 50% to reject harmonics with a combined electron yield and fluorescent EXAFS detector in order to sample both the near surface and bulk of the samples. The fluorescent x-rays of Cu, Cr, Fe and Zn have a range in Al of ~ 2-4 μm so they sample both the surface and bulk whereas the electron yield signal is due primarily to the KLL Auger electrons (5,6) which have a range of ~ 1000 Å so they sample 1/2 to 1/5 of the surface layer. An initial attempt at controlling the sampling depth by reflection was unsuccessful because of the inherent roughness of the surfaces. The electron yield and fluorescent x-ray XANES for Cr, Cu, Fe and Zn are compared in Figs. 2-3. Note that there are variations in the Cr XANES between the surface and the bulk particularly after salt spray testing, while there were few differences for Cu and Zn. ***As a preliminary conclusion Cu and Zn must be present in the surface in the same intermetallic compounds as in the bulk. They were not altered chemically by the reaction of Al with the Alodine bath.*** There is a large difference between the Fe XANES in the bulk and on the surface. By comparison to reference spectra it was noted that the surface Fe was present as $Fe(CN)_6^{3-}$ which was the Fe coordination in the original Alodine solution.

Both the XANES and EXAFS of the Cr spectra were analyzed. The sensitivity of the Cr 3d peak to valence and coordination environment is well known (7). In the centrosymmetric octahedral symmetry of Cr^{3+} compounds the 1s to 3d transition is dipole forbidden and found to be small as shown in Fig. 4, bottom. In non-centrosymmetric coordination, orbitals from the oxygen ligands mix with the Cr 3d orbitals to produce empty, anti-bonding orbitals for which the intense dipole transition is allowed. This is evident in the chromate solution spectra in Fig. 4, top. These spectra from 0.1 M Cr^{6+} and Cr^{3+} solutions turned out to be better models of the Cr in the surface layer than various solid reference compounds, particularly in the detailed shape of the peaks at the top of the edge. This is evident in the comparative plots in Fig. 5 of reference data from, top to bottom, Cr_2O_3, $CuCr_2O_4$ (a spinel with Cr^{3+} in the octahedral site), Cr^{3+} solution, a salt spray tested sample and a summed spectrum which fits it. The observation that simple sums of the data from solutions fit the Cr spectra from the surface layer was consistent with FTIR data from the surface layers which showed large hydration peaks. The summed spectra depicted in Fig. 4, center, covered the range of data from the samples and consequently could be used to infer the Cr^{3+}/Cr^{6+} ratio in the spectra from samples. The fraction of hexavalent Cr determined in this way is listed for each sample in Table 1. The Cr EXAFS data were also analyzed by Fourier transform with a Cr-O phase shift and are shown in Fig. 6 in comparison with other reference compounds. Note that both Cr_2O_3 and $CuCr_2O_4$ have intense 2nd neighbor peaks at ~ 3 Å whereas the solution and Alodine surfaces have much smaller peaks indicating a lack of long range order. Also note the decrease in the short 1st neighbor component, the Cr^{6+}-O bond, after salt spray testing, bottom. The Fourier filtered function $X(K)\cdot K^3$ was fit with a two shell model

while varying E_0 (the inner potential), R(4), R(6), N(4) and N(6) where R is the bond distance, N is the number of bonds and (4) or (6) refers to the Cr in tetrahedral or octahedral coordination, respectively. The disorder term was calibrated by first fitting to Cr_2O_3 and K_2CrO4, examples of Cr in octahedral and tetrahedral coordination, and then held constant, appropriately, during the fit. The fits were of excellent quality and the data are summarized in Table 1. The **surface** column is the fit to the electron yield EXAFS from the top ~ 1000 Å, the **total** column is the fit to the fluorescent x-ray EXAFS which sampled both the surface and the bulk. Also shown are the **edge jump** for each type of data from which the amount present could be determined, hence the thickness of the surface layer containing Cr. Statistical analysis of all the fits listed in Table 1 indicated that in the fresh Alodine surface 23 ± 2% of the Cr was hexavalent, balance Cr^{3+}, with average coordination of 1.2 ± 0.3 O atoms at 1.71 ± 0.03 Å and 4.1 ±1.0 atoms at 1.99 ± 0.01 Å. The valence determination from the XANES and the structure from the EXAFS were compatible within experimental error. After salt spray testing a large proportion, down to 7% in some cases, of the Cr^{6+} was reduced to Cr^{3+} with appropriate change in the coordination. This is the way the chromium-conversion effect is supposed to work and signals the ultimate failure of the layer when all of the Cr^{6+} is gone with continued exposure to salt spray.

3. Corrosion of A-286 Superalloy by Atomic Oxygen

This iron-based alloy contains (wt. pct.) 0.003 B, 0.05 C, 0.2 Al, 0.2 Mn, 0.3 V, 0.7 Si, 1.25 Mo, 2.15 Ti, 15.0 Cr, 25.0 Ni and balance Fe. The structure is austenite or fcc. It is commonly used in jet turbine engines with excellent oxidation resistance to 750 °C. Bolts made from this alloy were tested in space to determine the effects of atomic oxygen and the space environment. Casual inspection showed varying degrees of discoloration, etching and, in a few instances, flaking scale. The bolts were examined as described above with a combination of fluorescent x-ray and electron yield detection in order to discriminate between the bulk and near surface environments of the elements of interest. Spectra were obtained at the K edges of Cr, Fe and Ni. The results showed that only the Cr atoms reacted appreciably. This is illustrated in Fig. 7 which shows the XANES spectra of Cr_2O_3 and bolt C3 from the electron yield (surface) and fluorescent x-ray (bulk) signals. The fluorescent x-ray signal is typical of a transition metal K edge in a fcc structure and was approximately the same for Cr, Fe and Ni. By inspection, it can be seen that the electron yield signal is predominantly from Cr_2O_3 with some contribution from the underlying bulk metal, i. e. the Cr_2O_3 layer is less than ~ 1000 Å thick. This is shown more clearly by the presence of the more distant radial structure peaks in the EXAFS Fourier transforms shown in Fig. 8. The spectra of Ni and Fe were the same in electron yield and fluorescent x-ray and similar to that shown in Figs. 7 and 8, bottom. This example clearly shows the important role of Cr in the corrosion protection of this alloy.

These two examples show the utility of XAS using simple techniques on real samples to characterize common examples of corrosion at the level of atomic structure and chemistry of individual atomic species . The combination of electron yield and fluorescent x-ray data allowed an examination of the near surface region in contrast to the bulk. In principle it is possible to control the sampling depth to the top ~ 20 Å by x-ray reflection techniques. However, we found that routine samples, as described above, are too rough for this technique. The desired specular reflection was

destroyed. It will be necessary to first polish the samples and then form the desired surface structure with much shorter reaction times so that an acceptable degree of smoothness may be retained.

4. Acknowledgement

We are grateful to SSRL and NSLS for beam time. The work of Greegor was supported in part by the DOE, Basic Energy Sciences, Grant No. DE-FG06-84ER45121.

5. References

1. F. W. Lytle, G. L. Bibbins, K. Y. Blohowiak, R. B. Greegor, R. E. Smith and G. D. Tuss, "Investigation of the Structure and Chemistry of a Chromium-Conversion Surface Layer on Aluminum", submitted to Corrosion Sci.

2. J. K. Hawkins, H. S. Isaacs, S. M. Heald, J. Tranquada, G. E. Thompson and G. C. Wood, Corros. Sci. 27, 391 (1987).

3. J. S. Wainright, O. J. Murphy and M. R. Antonio, "Oxidation State and Coordination Environment of Cr in a Sealed Anodic Aluminum Oxide Film by XAS", Corros. Sci., accepted.

4. Manufactured by Parker-Chem, Henkel Corp., 32100 Stephenson Highway, Madison Heights, MI 48071. The Material Safey Data Sheet for Alodine 1200S indicates a 9 g/l solution of 50-60% CrO_3, 20-30% KBF_4, 10-15% $K_3Fe(CN)_6$, 5-10% K_2ZrF_6 and 5-10% NaF by weight which is approximately 0.065 M in Cr.

5. A. Erbil, G. S. Cargill, R. Frahm and R. F. Boehme, *Phys. Rev.* **B37**, 2450 (1988).

6. W. T. Elam, J. P. Kirkland, R. A. Neiser and P. D. Wolf, *Phys. Rev.* **B38**, 26, (1988).

7. F. W. Kutzler, R. A. Scott, J. M. Berg, K. O. Hodgson, S. Doniach, S. P. Cramer and C. H. Chang, *J. Am. Chem. Soc.* **103**, 6083 (1981).

Table 1. Compilation of Cr Data.

Samples	Time	Salt Spray	Hex Cr Fraction		Edge Jump		Surface				Total			
			Surface	Total	Surface	Total	N(4)	R(4), Å	N(6)	R(6), Å	N(4)	R(4), Å	N(6)	R(6), Å
7075#1	1	no	0.22	0.24	0.36	0.49								
7075#11	1	no	0.22	0.21	0.21	0.50	0.80	1.69	4.75	2.02	1.38	1.70	3.94	1.99
7075#6	1	no	0.21	0.22	0.26	0.51	1.42	1.69	3.88	1.98				
7075#6	1	yes	0.07	0.07	0.22	0.44	0.77	1.78	4.85	2.00				
7075#15	1	yes	0.14	0.14	0.22	0.32								
7075#8	3	no	0.25	0.26	0.25	0.90								
7075#13	3	no	0.24	0.24	0.33	0.83	1.20	1.70	4.20	2.01	1.27	1.70	4.10	2.02
7075#3	3	yes	0.24	0.26	0.27	0.88	1.45	1.67	3.83	1.97	1.52	1.69	3.73	1.98
2024#49	1	yes	0.15	0.16	0.22	0.29	0.92	1.67	4.62	1.97	1.55	1.66	3.69	1.94
2024#P1-1	1	yes	0.07	0.08	0.28	0.34	0.80	1.79	4.81	1.99				
2024#FT1-1	1	yes	0.24	0.27	0.29	0.54								
2024#PM-1	1	yes	0.20	0.20	0.24	0.35								
2024#F1-1	1	yes	0.25	0.27	0.27	0.40								
2024#4	3	no	0.22	0.24	0.26	0.42	1.40	1.72	3.89	2.00	1.04	1.68	4.45	2.01
2024#7	3	no	0.21	0.22	0.26	0.40	1.33	1.74	4.01	2.01	1.43	1.70	3.86	1.99
2024#10	3	no	0.21	0.24	0.28	0.39								
2024#6	3	yes	0.18	0.19	0.24	0.37	1.03	1.87	4.46	2.03	1.32	1.70	4.02	1.98
2024#P3-1	3	yes	0.16	0.20	0.27	0.83								

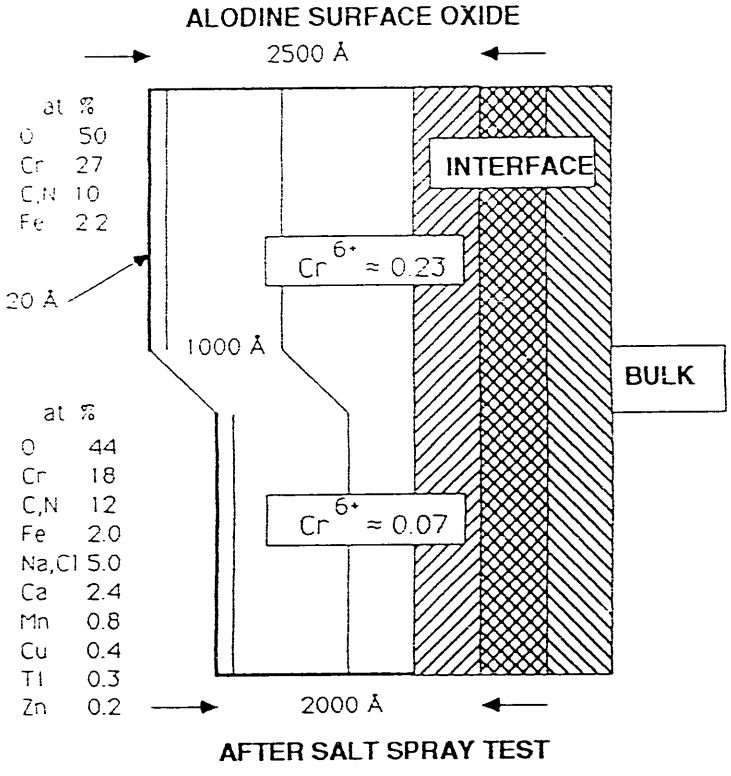

Fig. 1 Schematic illustration of the composition and profile of an Alodine surface oxide layer before and after salt spray testing.

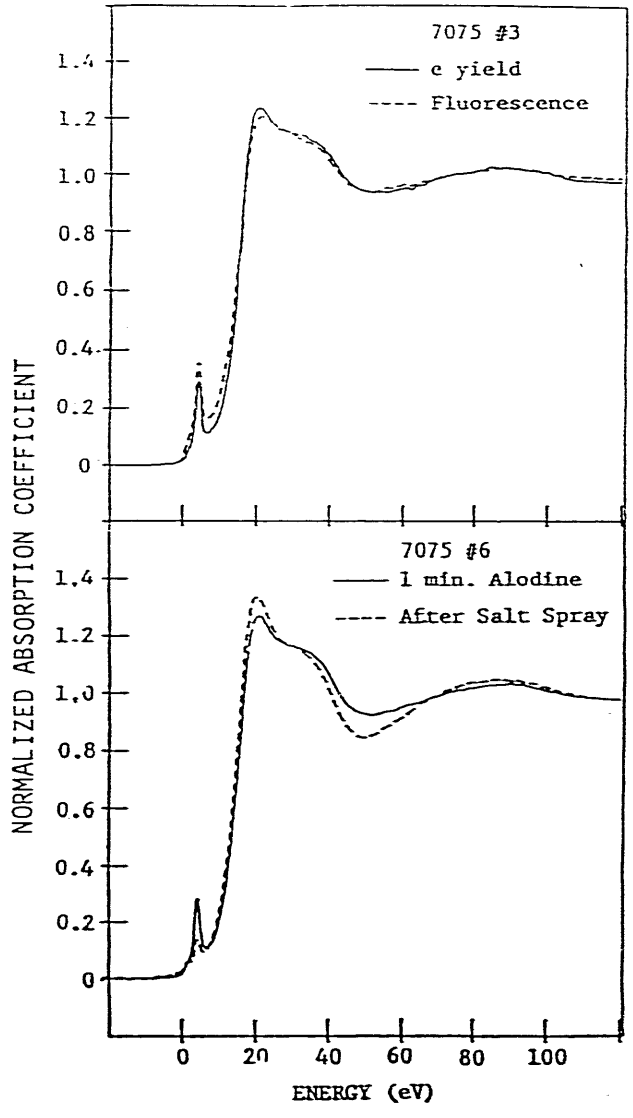

Fig. 2 Top, examples of XANES electron yield and fluorescence from the same sample indicating a non-uniform depth distribution of Cr^{6+}. Bottom, Cr XANES before and after salt spray testing showing the reduction of Cr^{6+} to Cr^{3+}.

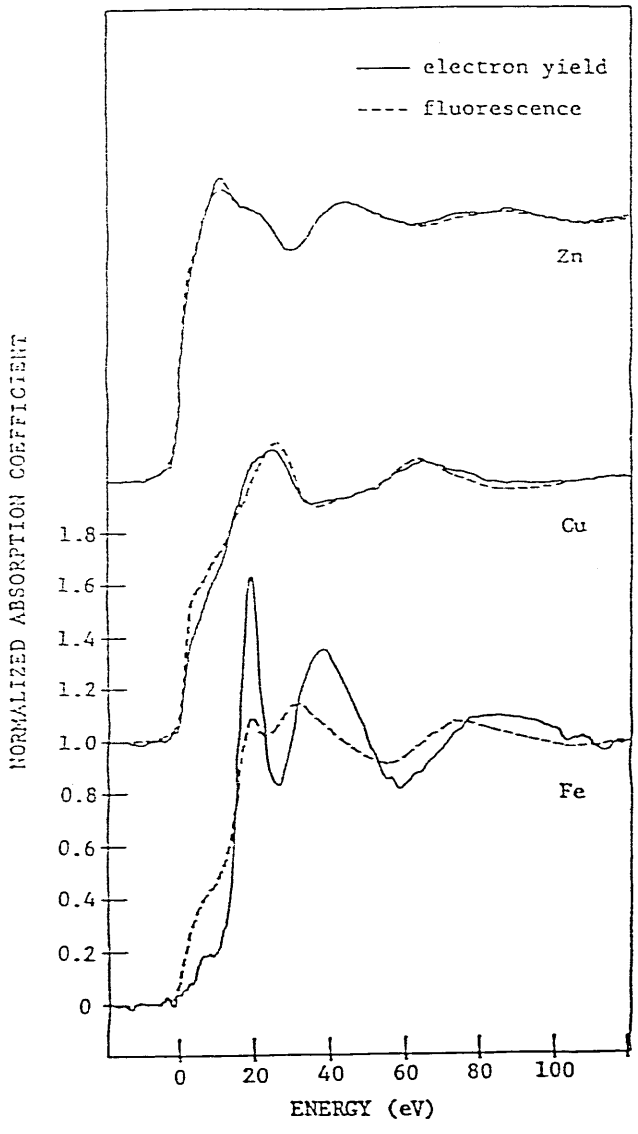

Fig. 3 Comparison of the electron yield (surface 1000 Å) and fluorescence (bulk alloy) XANES spectra for the Fe, Cu and Zn components of the Alodine layer.

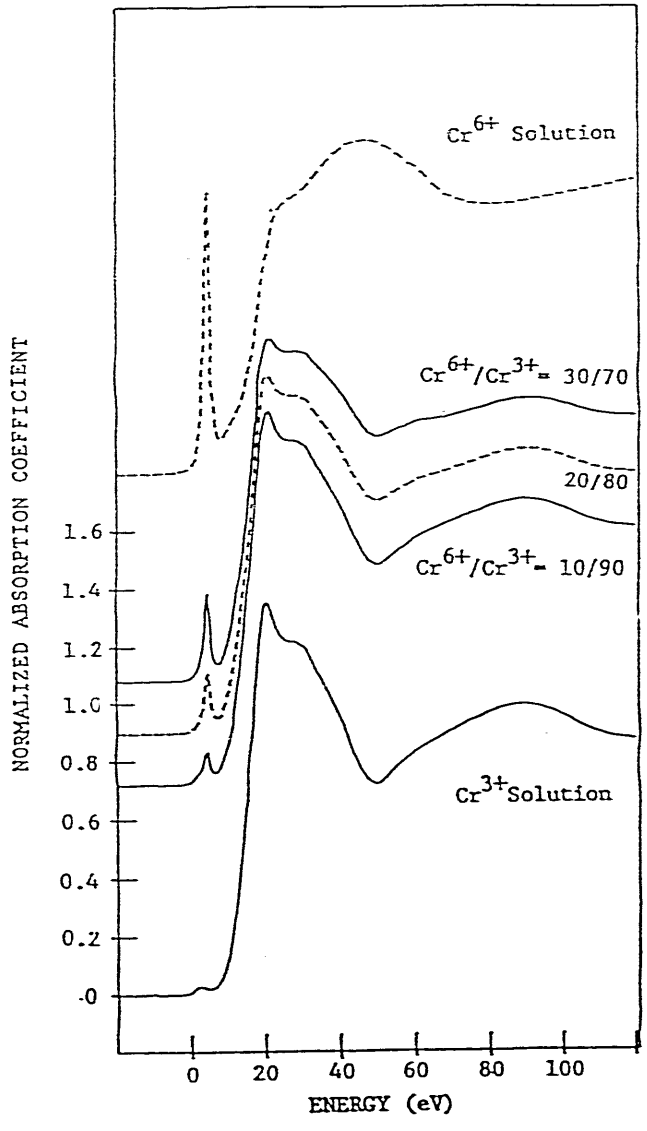

Fig. 4 Cr K edge XANES reference spectra from solutions of 0.1 M $(CrO_4)^{2-}$, top, and $Cr(H_2O)_6^{3+}$, bottom. The plots in the center are sums of the top and bottom spectra in the proportions indicated.

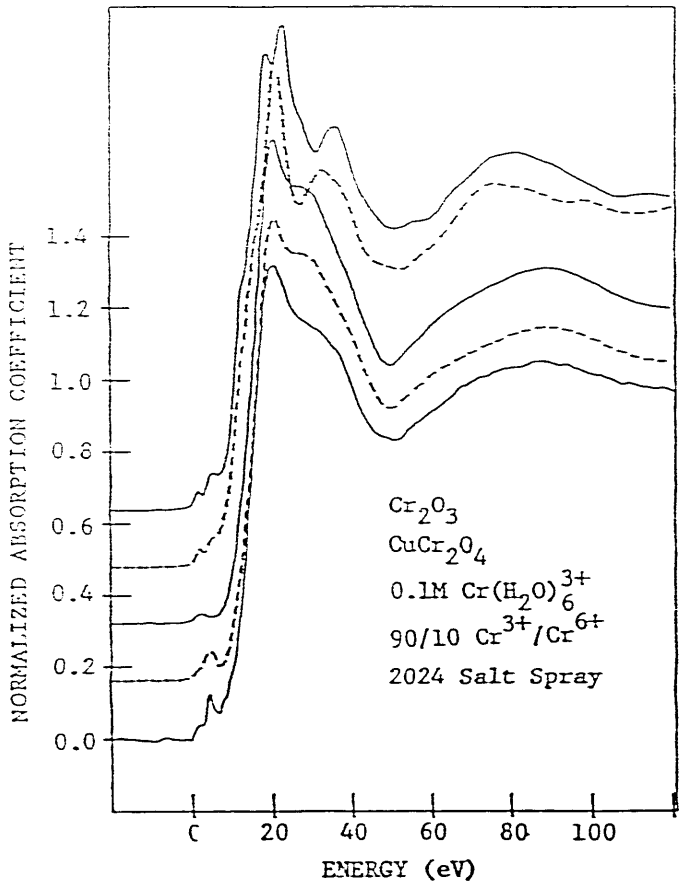

Fig. 5 Examples of Cr XANES spectra from reference coupounds and a salt spray sample. Note the match between the 90/10 sum and the salt spray sample.

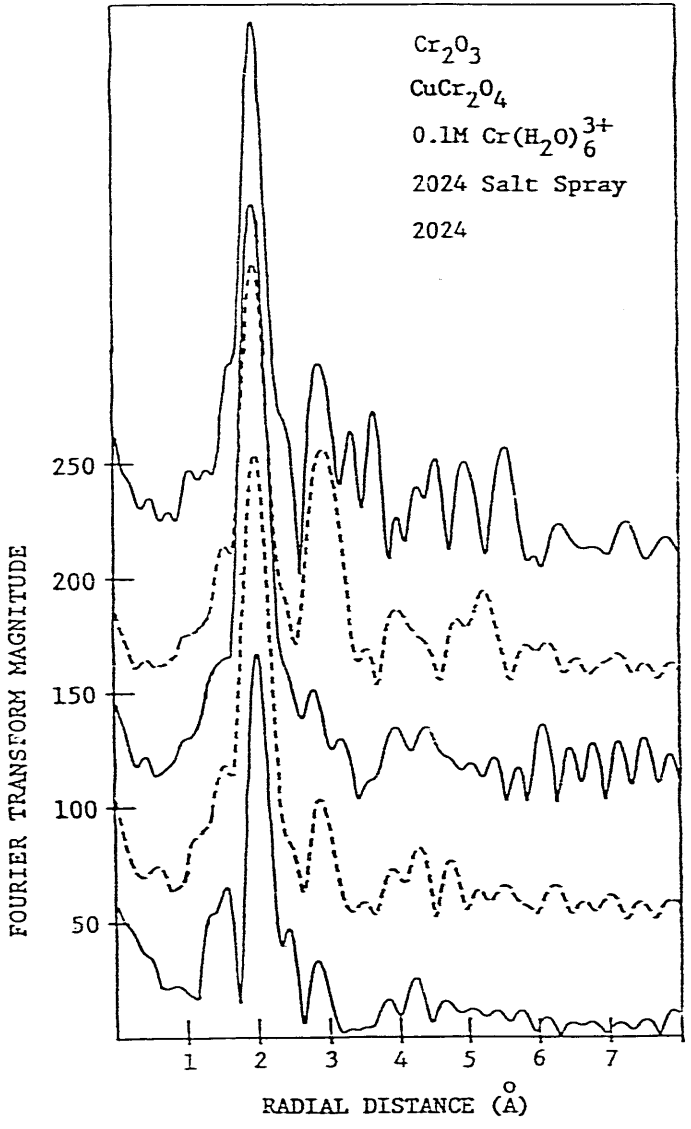

Fig. 6. K2, Cr-O phase corrected Fourier transforms of Cr K edge spectra for reference compounds and typical samples.

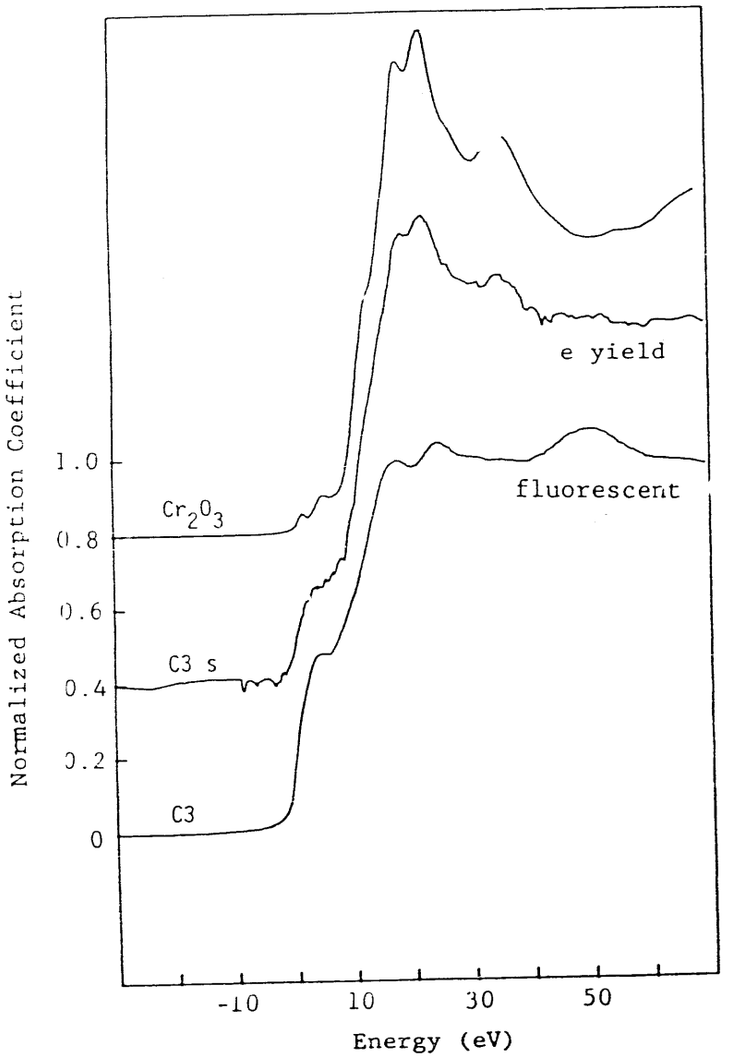

Fig. 7 Comparison of the Cr K edge in A-286 measured in e yield and fluorescent x-ray mode with Cr_2O_3.

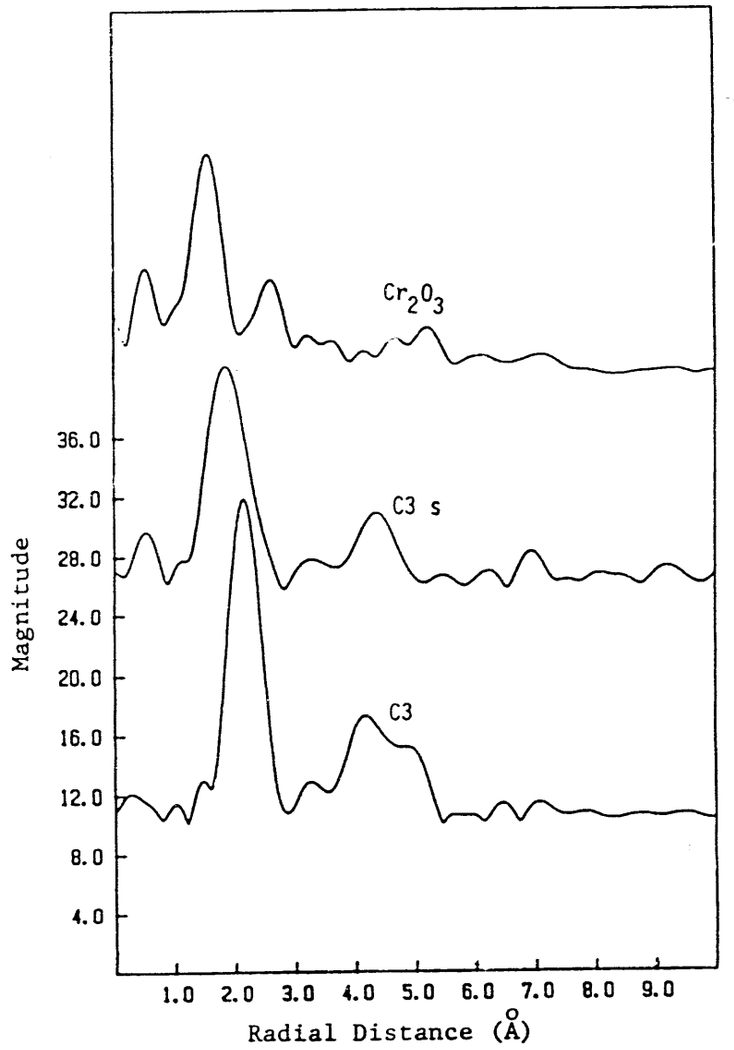

Fig. 8 Fourier transforms of the EXAFS of the samples in Fig. 7.

MEASURING THE DIFUSE DOUBLE LAYER AT AN ELECTROCHEMICAL INTERFACE WITH LONG PERIOD X-RAY STANDING WAVES

Michael J. Bedzyk*

Cornell High Energy Synchrotron Source (CHESS)**
Cornell University, Ithaca, NY 14853 USA

When an x-ray beam impinges on a boundary separating two materials that have different indices of refraction, part of the energy in the traveling wave is reflected and the remainder is transmitted (or refracted). Since the index of refraction (n) is less than unity for x-rays in matter, x-rays undergo total external reflection, when the incident angle θ is less than the critical angle θ_c. The index of refraction is expressed as $n = 1-\delta-i\beta$, where $\delta = N_e r_e \lambda^2/2\pi$ and $\beta = \mu\lambda/4\pi$. Using Snell's law, $\theta_c = (2\delta)^{1/2}$, which is typically between 1 and 10 mrad, depending on the wavelength λ and effective electron density N_e.

During total external reflection, the interference between the incident and specular reflected x-ray plane waves produces an x-ray standing above the mirror surface. [1-4] As shown in Fig.1, the antinodal planes of this periodic E-field intensity pattern are parallel to the surface and have a period of $D = \lambda/2\sin\theta$. Since the total external reflection condition occurs between $\theta = 0$ and $\theta = \theta_c$, the period of the standing wave varies from $D = \infty$ to $D = D_c$. The critical period, $D_c = \lambda/2\theta_c$, is 80 Å for a gold mirror and 200 Å for a silicon mirror. In general, the standing wave period at the critical angle is $D_c = [\pi/(4N_e r_e)]^{1/2}$.

The phase of the standing wave relative to the mirror surface can be determined by using Fresnel theory which describes the magnitude and phase v of the E-field amplitude ratio $E_R/E_O = |E_R/E_O|\exp(iv)$. The θ dependence of the reflectivity $R = |E_R/E_O|^2$ and phase v are shown in Fig. 2a. The phase at the mirror surface decreases from π to 0, as the mirror is tilted through the total reflection condition. Thus, at the mirror surface, the reflected plane wave is completely out of phase with the incident plane wave at $\theta = 0$ and completely in phase at $\theta = \theta_c$. Therefore, at $\theta = 0$ a standing wave node is at the mirror surface and the first antinode is at infinity, and as θ is increased the first antinode moves toward the mirror surface, until, it coincides with the mirror surface at $\theta = \theta_c$. As θ increases the second, third, fourth, . . . antinodes of the standing wave also move inward, since the period is decreasing as θ increases. The E-field intensity above the mirror surface is express as

$$I(\theta,z) = |\,\varepsilon_O + \varepsilon_R\,|^2 \;=\; |E_O|^2\,[1 + R + 2\sqrt{R}\cos(v - 2\pi Qz)]\,,$$

where $Q = 2\sin\theta/\lambda = 1/D$ is the magnitude of the wave-vector transfer $\mathbf{Q} = \mathbf{k_R} - \mathbf{k_O}$. (Notice that the E-field intensity is simply the total E-field times its complex conjugate, where the total E-field is expressed as the sum of the incident and reflected plane waves ε_O and ε_R, respectively.) The θ dependence of the intensity $I(\theta, z)$ at $z = 0$ (the mirror surface) and at $z = 2D_C$ is illustrated in Fig. 2b.

Since the photoelectric-effect cross section is proportional to the E-field intensity at the center of an atom, one can determine the position z of an atom layer above the reflecting surface by monitoring the fluorescence yield from that atom layer as the mirror is tilted through the reflection. If the marker layer of atoms is contained in a plane at $z= 2D_C$, the fluorescence yield will have a modulation like that is shown in Fig. 2b. In general, if an atom layer is at $z = XD_C$, then $X+1/2$ modulations will occur between $\theta = 0$ and $\theta = \theta_C$. Such a modulated fluorescence yield was recently observed for the first time . [3] This was for Zn atom layer embedded in the top arachadate bilayer of a Langmuir-Blodgett multilayer which was deposited on the surface of a gold mirror. As shown in Fig. 3b, three full oscillations in the Zn fluorescence yield occur before reaching the gold critical angle, indicating that the Zn layer is at $z = 2.5D_C = 200$ Å . This was more precisely determined to be 218 Å by using a χ^2 fit of the data to theoretical yields based on a layered model. From this fit, we also determined that the 2σ thickness of the Zn layer was 24 Å .

Since the standing wave samples the selected atom distribution with a variable period D, we are in effect measuring the Fourier transform of that distribution over a continous range in $Q = 1/D$. With a variable period ranging from 10's of angstroms to 100's of angstroms, this new x-ray standing wave probe is ideally suited to measure surface and interface layered structures which have natural length scales in the 10 to 1000 Å regime. The prior mentioned case of studying the layered structure within an ultra-thin organic film is just such a structure.

Another such structure is the diffuse-double layer at a charged surface/aqueous interface. Recently, we have directly measured the ionic distribution profile in an electrolyte in contact with a charged phospholipid membrane with long-period x-ray standing waves. [4] As schematically depicted in Fig. 4, the 27 Å thick membrane was supported from below by a silicon/tungsten layered-synthetic-microstructure (LSM). The x-ray standing waves were generated by total external reflection from the surface of the Si/W LSM and by Bragg diffraction from the 35 Å periodic structure of the LSM. The top of the membrane formed a negatively charged sheet of phosphate ions in contact with a very dilute $ZnCl_2$ aqueous solution. The coverage of the condensed Zn layer (which partially neutralized the phosphate layer) and the Debye length of the electrostatically attracted diffuse Zn ion layer were measured with x-ray standing waves at various

pH levels.

The incident x-ray beam, which was tuned to 9.8 keV for optimally exciting Zn K fluorescence,was produced by the 123-pole APS/CHESS undulator at the Cornell Electron Storage Ring (CESR). The experimental setup for this measurement is depicted in Fig. 5. The data collection consists of recording the reflected intensity with an ion chamber and the fluorescence spectrum with a solid-state detector as a function of angle θ. The simultaneously collected reflectivity and Zn Kα fluorescence data for the initial scan at pH 6.8 are shown in Fig. 6, a and b , respectively. The drop in reflectivity for $\theta < 0.8$ mrad is due to the 20 μm incident beam height oversubtending the 25 mm length of the sample. The drop off in reflectivity at 1.8 mrad corresponds to the critical angle for polypropylene and water at 9.8 keV (both materials have the same electron density). The drop off in reflectivity at 4.5 mrad corresponds to θ_c for the 3:1 Si/W mixture of the LSM. Since the polypropylene film is not perfectly flat, the maximum reflectivity from the polypropylene is only 60 percent. The reflectivity at 3 mrad is only 32 percent owing to the attenuation of both the incident and reflected beams by the 6 μm thick polypropylene film and 2 μm thick water layer. We were able to use this measured attenuation to determine the thickness of the trapped water layer.

The small Zn Kα count rate shown in Fig. 6b below $\theta = 1.8$ mrad is due to the beam being reflected away by the polypropylene film and not being allowed to penetrate into the solution. Keeping in mind that the first XSW antinode moves inward toward the Si/W mirror surface as θ approaches the Si/W critical angle, notice that the first XSW antinode passes over the maximum of the Zn density before the Si/W critical angle is reached. This indicates that a concentrated layer of Zn exists at some displaced distance above the Si/W surface (see Fig. 4).

Unlike the pH 6.8 data, the pH 4.4 and pH 2.0 Zn fluorescence yield curves shown in Fig. 6, c and d, do have a significar.. count rate below the polypropylene critical angle. This is due to a small amount of Zn^{2+} passing into the partially hydrolized polypropylene.

The solid line curves in Fig. 6b-d correspond to a χ^2 fit of the data above 2 mrad to a theoretical yield curve which assumes that the Zn^{2+} ions have an exponential decay distribution. The two parameters determined by the fit are the Zn^{2+} concentration in the condensed layer N_c and the Debye length L' of the exponential decay. We were able to show that changing the pH from 6.8 to 4.4 to 2.0 caused the Debye length to decrease from 58 Å to 8 Å to 3 Å. This represents a weakening of the electrostatic attraction of the charged interface due protonation of the phosphate head groups of the lipid membrane. Over this same change in pH, N_c went from 0.31 M to 0.31 M to 0.18 M.

Conclusion

These results, which are more extensively described in Ref. 4, represent the first detailed structural measurement of the diffuse-double layer. The crucial x-ray properties that made this break-through possible are; (1) the capability of x-rays to penetrate through low-Z materials, such as water, and (2) the capability of using angstrom wavelength x-rays to generate x-ray standing waves with periods ranging from 70 to 1000 Å.

Acknowledgements:

My collaborators were Mark Bommarito and Don Bilderback of Cornell University, Martin Caffrey of the Ohio State University, and Jay Schildkraut and Tom Penner of the Eastman Kodak Company.

* Present addresses: Dept. of Materials Science and Engineering, Northwestern University, Evanston, IL 60208-3100 and Materials Science Division, Argonne National Laboratory

** This Material is based upon work conducted at CHESS, supported by the National Science Foundation under award No. DMR 90-21700. This work was also supported in part by a grant from the Eastman Kodak Company.

[1] M.J. Bedzyk, New Trends in X-ray Standing Waves, Nucl. Instr. and Meth. **A266**, 679 (1988).

[2] M.J Bedzyk, D. H. Bilderback, G. M..Bommarito, M. Caffrey, and J. S. Schildkraut, X-ray Standing Waves: A Molecular Yardstick for Biological Membranes, Science **241**, 1788 (1988).

[3] M. J. Bedzyk, G. M. Bommarito, and J. S. Schildkraut, X-ray Standing Waves at a Reflecting Mirror Surface, Phys. Rev. Lett. **62**, 1376 (1989).

[4] M. J. Bedzyk, G. M. Bommarito, M. Caffrey, and T. L. Penner, Diffuse-Double Layer at a Membrane-Aqueous Interface Measured with X-ray Standing Waves, Science **248**, 52 (1990).

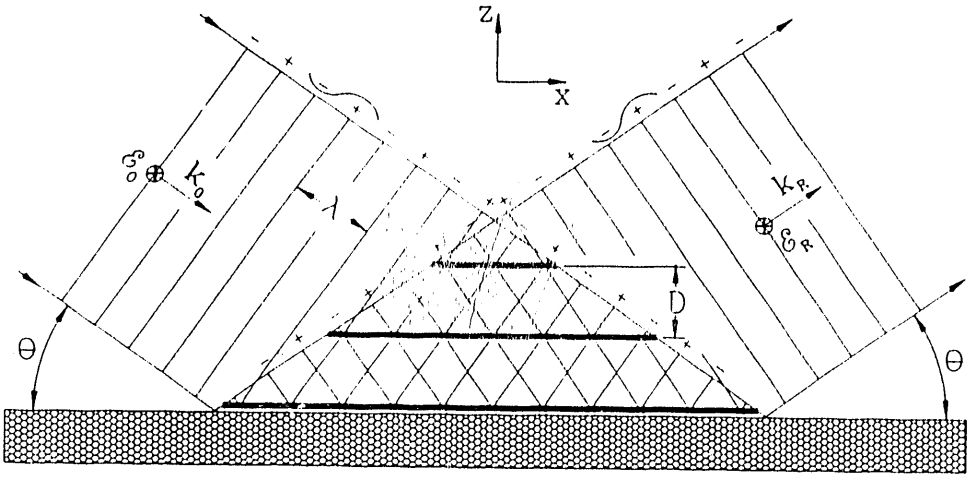

Fig. 1 Illustration of the x-ray standing wave field formed by the interference between the incident and specular-reflected plane waves above a mirror surface. (From Ref. 3 .)

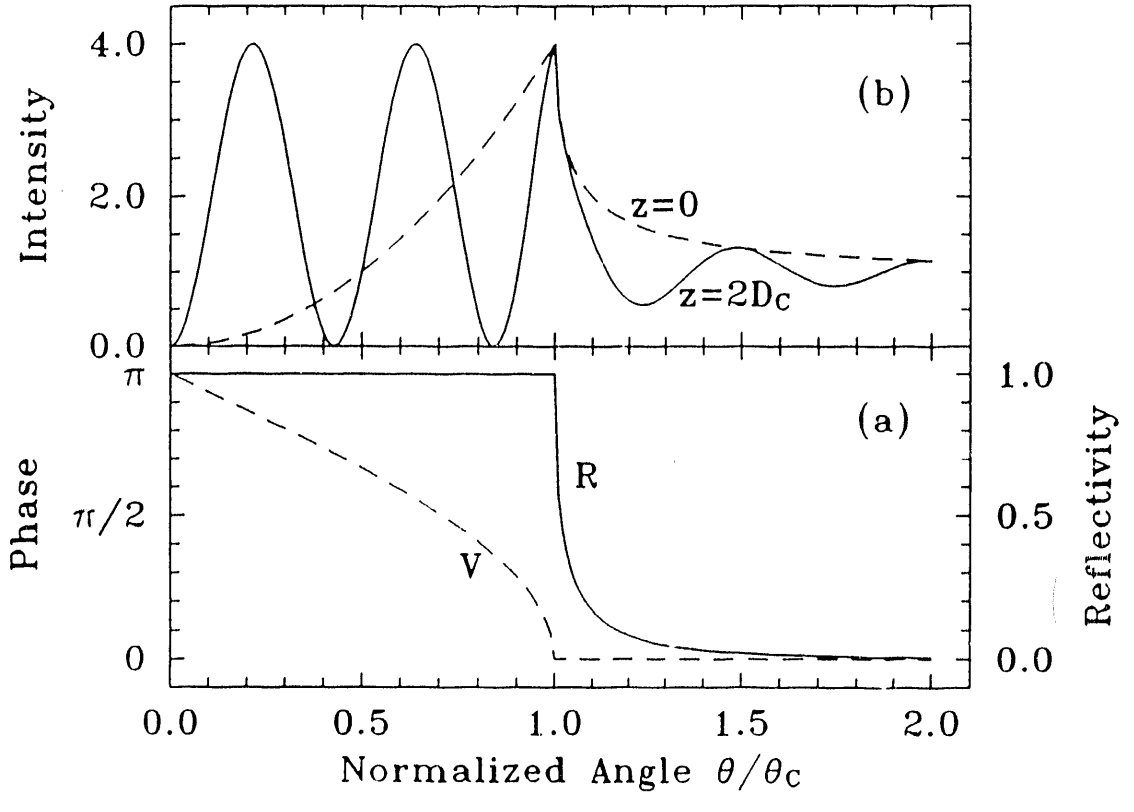

Fig. 2 For $\beta = 0$. (a) The angular dependence of the reflectivity R and relative phase v of the reflected plane wave. (b) The angular dependence of the E-field intensity at $z = 0$ and $z = 2D_C$ for $|E_0| = 1$. (From Ref. 3 .)

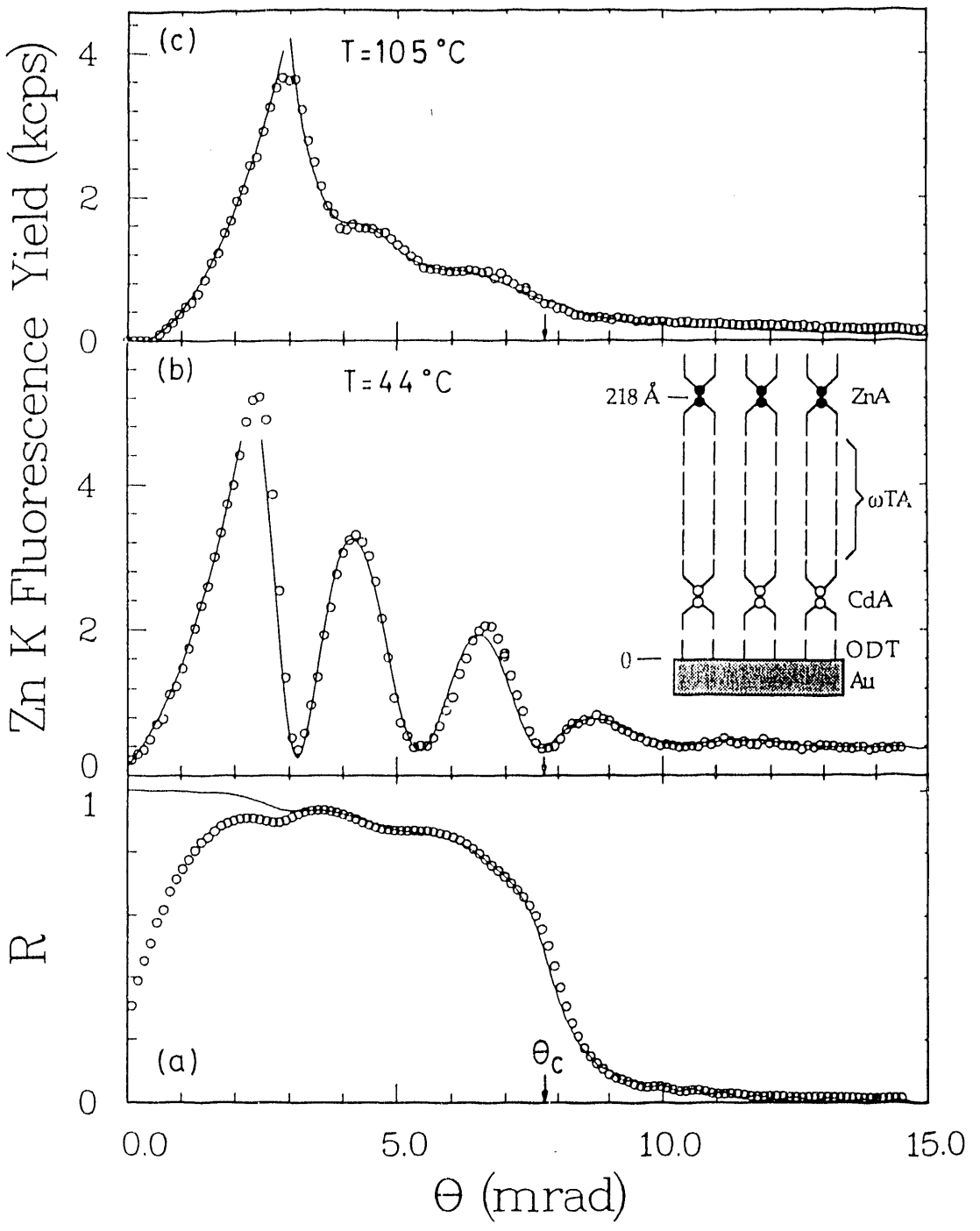

Fig. 3 (a) The angular dependence of the reflectivity at 9.8 keV for the LB film/ Au mirror schematically depicted in the inset. (b) The angular dependence of the Zn Kα fluorescence count rate at T = 44° C, and (c) at T = 105° C. Inset: Circles represent heavy atoms and vertical line segments represent hydrocarbon chains, The LB bilayers are zinc arachadate (ZnA), w-tricosanoic acid (wTA), and cadmium arachadate (CdA). Octadecyl thiol (ODT) was adsorbed onto the gold surface to make it uniformly hydrophobic for the subsequent LB depositions. (From Ref. 3 .)

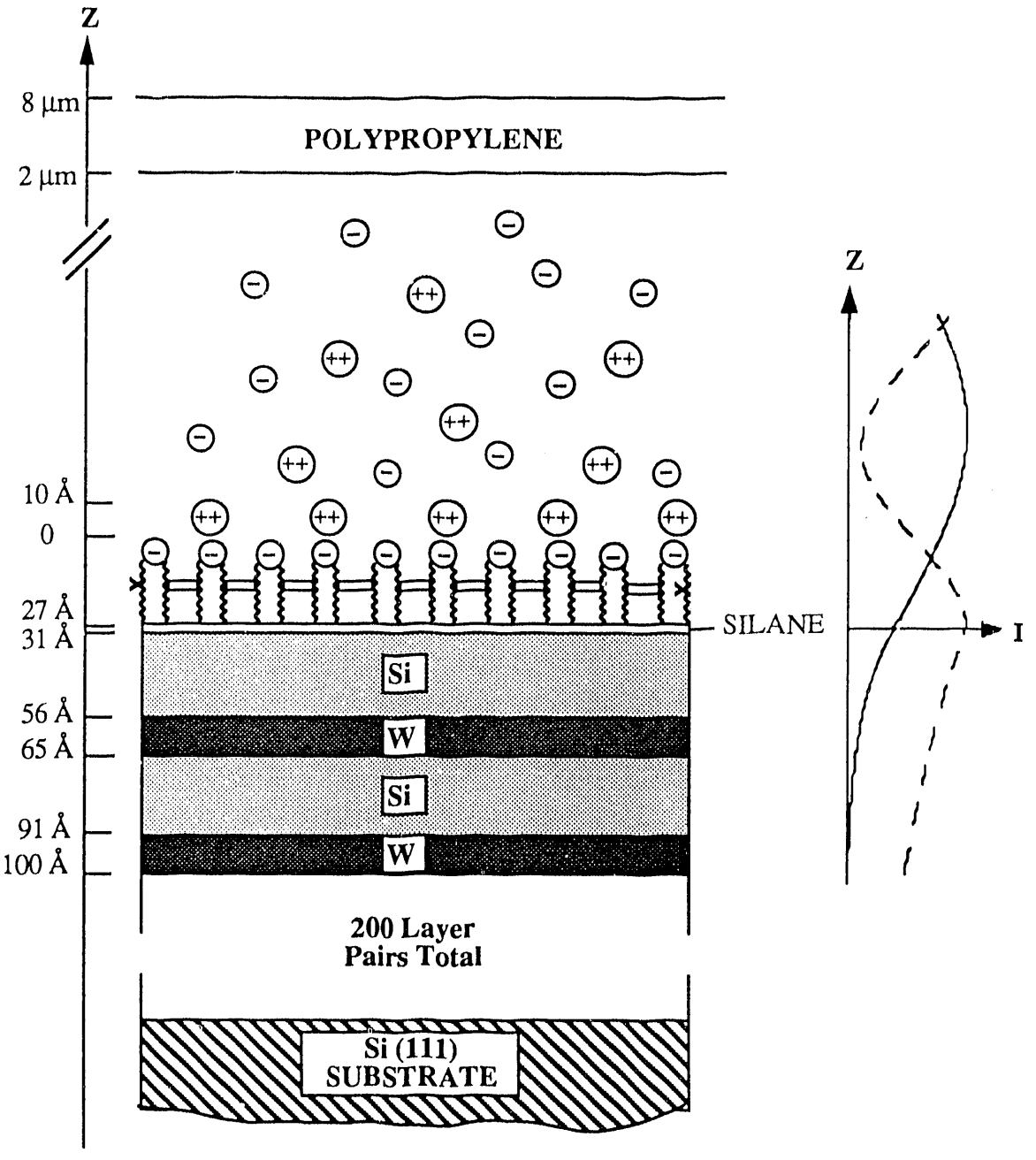

Fig. 4 Schematic showing a cross-linked phospholipid membrane deposited on a silanated Si/W LSM. The top of the lipid contains a PO_4^- headgroup which attracts Zn^{2+} ions in the 0.1mM aqueous solution. The encapsulating 6 μm thick polypropylene film traps a 2 μm thick water layer by capillary action between the film and the lipid. Along the right side is shown the E-field intensity at E_γ = 9.8 keV for $\theta = 2.5$ mrad (solid curve) and $\theta = \theta_c = 4.5$ mrad (dashed curve). When $\theta < \theta_c$ an x-ray standing wave exists above the reflecting surface and an evanescent wave exists below. [From Bedzyk et al., *Science* **248**, 52-56 (1990). Copyright 1989 by the AAAS.]

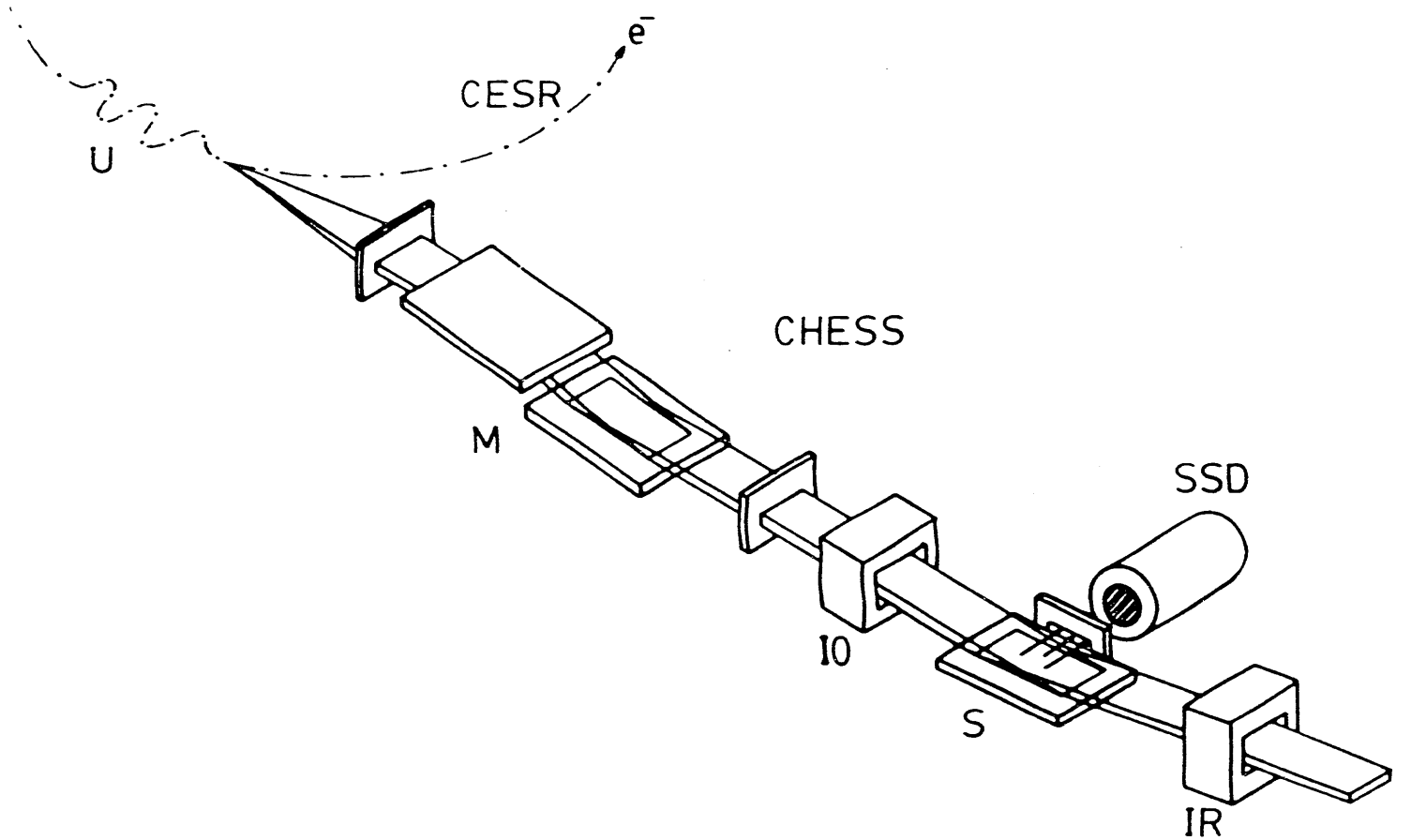

Fig. 5 Experimental setup for collecting x-ray standing wave data. The x-ray radiation from the undulator (U) passes through a Si(111) monochromator (M) and is then reflected by the sample (S). As we scan in θ, we simultaneously collect x-ray fluorescence spectra with a solid-state detector (SSD) and reflectivity with an ion chamber (IR). [From Bedzyk et al., *Science* **248**, 52-56 (1990). Copyright 1989 by the AAAS.]

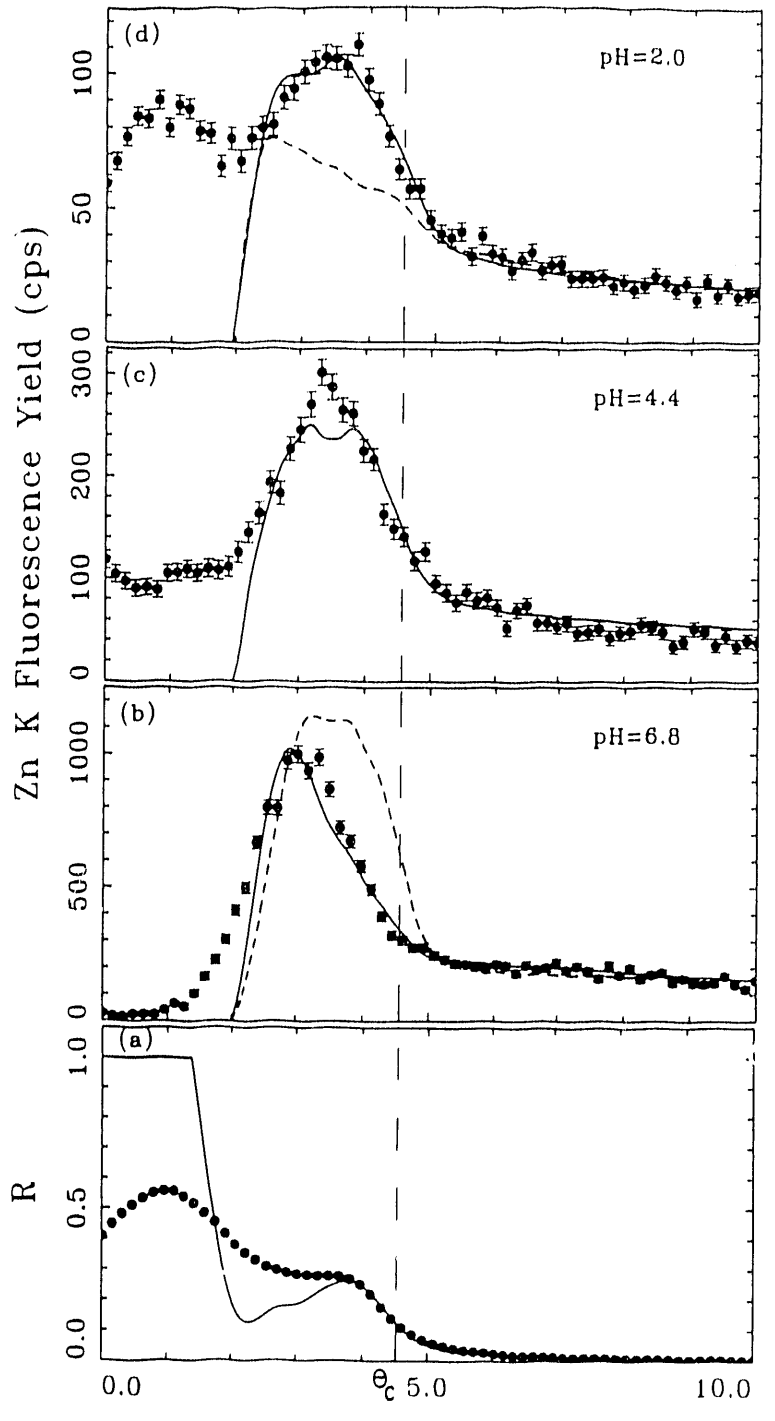

Fig. 6 The experimental (circles) and theoretical (solid lines) angular dependence at $E_\gamma = 9.8$ keV of (a) the specular reflectivity and (b-d) the Zn Kα fluorescence yield for (b) pH 6.8, (c) pH 4.4, and (d) pH 2.0. The solid curves in (b-d) are the χ^2 fit yields for a Zn^{2+} ion distribution which exponentially decays away from the interface. The dashed curve in (b) corresponds to the yield for a discrete Zn^{2+} inner Helmholtz layer at 2 Å above the phosphate headgroup layer. The dashed curve in (d) corresponds to the yield for a flat Zn^{2+} distribution.

STUDIES OF CORROSION USING A COMBINATION OF X-RAY SCATTERING AND ELECTROCHEMICAL TECHNIQUES

Victor A. Maroni[†‡], Hoydoo You[†], Carlos A. Melendres[†‡], and Zoltan Nagy[†‡]
[†]Materials Science Division
and
[‡]Chemical Technology Division
Argonne National Laboratory
Argonne, IL 60439

A panel report to the National Materials Advisory Board published in 1985 [1] highlighted the potential utility of techniques based on X-rays for in situ characterization of electrode/electrolyte interfaces. From the years just prior to 1985 up to the present there has been a growing number of publications reporting successful applications of X-ray-based techniques in the study of immersed electrochemical interfaces [2-19]. This research has (as examples) included (1) determinations of oxidation states of elements in corrosion layers and on electrode surfaces by near-edge X-ray absorption techniques [4,5]; (2) measurements of interatomic distances and coordination numbers for ordered, nanocrystalline, and amorphous corrosion films by extended X-ray absorption fine structure (EXAFS) techniques[6-10]; (3) studies of underpotential deposited monolayers [11,12], the liquid mercury electrode interface [13], electrochemically induced crystal surface reconstruction [14], and passive film growth behavior (thickness and roughness) [15-17] by X-ray scattering methods; and (4) exploration of ion concentration profiles and electrolyte structure in the electrical double layer region by X-ray standing wave methods [3,18] and X-ray excited electron spectroscopy [19]. When one adds to this the potential for conducting in situ microscopy and microprobe analysis of electrochemical interfaces with X-rays, and further considers that the prospects for doing detailed time dependent studies with the various techniques already mentioned will be greatly enhanced by the coming generation of synchrotron light sources, the vistas for interrogating electrochemical interfaces appear unlimited. To appreciate the significance of these possibilities, it is important to realize that the type of information gained from the variety of accessible X-ray methods can either not be obtained by other instrumental techniques or can not be obtained as easily or effectively.

A majority of the research on electrochemical interfaces has involved the use of the EXAFS technique, but the number of scattering (e.g., reflectivity and diffraction) and standing wave studies is growing. While this lecture summary is directed mainly to reflectivity-type studies, it is noteworthy that the characteristics of the experimental embodiments (and the attendant complexities) for combined X-ray and electrochemical measurements on immersed electrodes have many similarities for EXAFS, scattering, and standing wave investigations. The embodiments used for most studies reported in recent years fall into two configurational geometries, the "reflection" geometry and the "transmission" geometry. The general features of these two geometries are presented in Figs 1 and 2. Figure 1 shows the configuration of key components that are required for combined electrochemical measurements and X-ray interrogation. For the reflection geometry the working, counter, and reference electrodes are deployed in a coaxial arrangement, and the X-ray path through the electrolyte is defined

(and constrained) by a thin, X-ray transmissive membrane that is pulled taut over the surface of the electrode ensemble such that the remaining electrolyte film is typically ≤ 50 μm. For more details and examples of applications of reflection-type cells the reader is referred to references [9,12,14].

With the transmission geometry, the working, counter, and reference electrodes have a more conventional deployment for electrochemical measurements in that the counter electrode faces the working electrode and the reference electrode is located in very close proximity to the working electrode surface. The X-ray path length in the electrolyte is defined by the width of the working electrode (t in Fig. 2) and the electrolyte is contained by the two thin, X-ray transmissive, parallel membranes shown in Fig. 1. Additional details and examples of applications of transmission geometry cells can be found in references [2,8,13,15-17].

There are advantages and disadvantages to each type of cell geometry. As shown in Fig. 2, the X-ray path through the electrolyte is relatively constant for the transmission geometry but can vary over a wide range for the reflection geometry in the course of scattering measurements. This has two consequences, one of which is that the transmission geometry has superior transmission properties at small angle (up to 2 or 3°), while the reflection cell has a shorter path at higher angles. The second consequence is that reflectivities measured in the transmission geometry require little or no correction for absorption because the path length is nearly constant over the angular range of interest in glancing incidence studies and in most of the other types of scattering experiments. Furthermore, because the membrane boundaries are perpendicular to the working electrode surface for the transmission geometry, spurious reflections from the membrane/air and membrane/electrolyte interfaces are directed away from the path of the transmitted X-ray beam. These same spurious reflections will tend to propagate in parallel with the reflected beam when the reflection geometry is used.

Additional advantage/disadvantage factors are that the counter electrode positioning for the transmission cell facilitates a more uniform current distribution over the working electrode surface than can be achieved with the reflection cell. This permits electrochemical manipulations involving current flow to be carried out during X-ray measurements. The reflection geometry allows probing of larger electrode areas and is much more amenable to studies at high incidence angles.

Major experimental challenges that must be overcome with either type of cell include: (1) obtaining/preparing nearly atomically smooth working electrode surfaces (± 5 Å root-mean-square roughness); (2) establishing/maintaining an impurity-free environment in the cell interior, in the incoming electrolyte, and in any cover gas regions; and (3) avoiding radiation damage to cell parts (particularly the thin membranes) and to the working electrode surface. Surfaces that are sufficiently smooth for most types of X-ray scattering studies have been prepared by polishing single crystals (e.g., Ag, Au, Pt, Si) [11,12,14-17], from cleaved or polished glasses and ceramics (e.g., quartz, borosilicate glass, and mica) [15], and by magnetron sputtering or thermal evaporation of metals onto smooth substrates [3,18]. Finally, the choice of beamline can also be very important to success [3], in that high brilliance and X-ray energies in the range where adsorption by water is minimal are advantageous for most types of X-ray scattering measurements.

An X-ray/electrochemical cell (XEC) based on the transmission geometry has been constructed in our laboratory and used successfully to study the corrosion of thin film silver and copper working electrodes supported on single crystal substrates. A cross section view of the cell embodiment and two alternative center section designs are shown in Figs. 3 and 4, respectively. The XEC has a sandwich configuration, consisting of a Teflon center piece that houses the electrodes and defines the shape of the electrolyte cavity. The center piece is surrounded on both sides by thin Teflon or Teflon-coated Kapton membranes. (The Teflon-coated Kapton has proven to be more resistant to radiation damage by the incident X-rays than Teflon alone.) The membranes are held flat against the center piece by a pair of inner Teflon frames, which, in turn, are supported by a pair of outer metal frames. The entire assembly is compressed and held together by four bolts that pass through the holes in each corner of the outer frame pieces. The press fit of the membranes to the center piece provides a seal that is leak tight regardless of the positioning angle of the cell in the beam line spectrometer. The alternative center piece designs in Fig. 4 are more difficult to construct than the one shown in Fig. 3, but they simplify cell assembly in the field and have tended to provide a better seal around the electrolyte cavity. The experimental arrangement of the XEC at the synchrotron beam line facility is shown in Fig. 5. Additional details concerning the construction and operation of the XEC are given in reference [15].

A variety of X-ray scattering experiments have been performed at the National Synchrotron Light Source using the XEC. Figure 6 shows the results of reflectivity measurements made on a borosilicate glass substrate coated with ~70 Å of vapor deposited chromium followed by ~1000 Å of vapor deposited nickel. The upper reflectivity curve, taken on a nitrogen purged cell, and the lower curve, taken on a cell filled with 0.1 M NaOH, show the attenuation in reflected beam intensity due to the electrolyte. The magnitude of the attenuation is exactly that expected from absorption by water, and indeed no other corrections are needed to interpret the differences between the two curves in Fig. 6. The high frequency oscillations in the reflectivity curves arise from interference effects associated with the total film thickness (Ni + Cr), while the low frequency oscillations are generated by the chromium layer. The results for this duplex film show how X-ray reflectivity can be used to monitor film thickness even in multi-layered film structures.

Figure 7 presents reflectivity data for a ~250 Å silver film supported on a silicon (100) crystal in an XEC containing borate buffer solution at pH 8.4. The upper curve in Fig. 7, recorded at a reducing potential of −0.8 V, should represent a condition where there is only a very thin (at best) oxide layer on the silver surface. The same condition should also obtain at 0 V, and the middle curve tends to support this view by virture of its similarity to the upper curve. The curve at +0.5 V constitutes a potential regime where significant oxidation of the silver is expected to occur. The obvious differences in reflectivity between the lower curve and the two above it illustrate the sensitivity of the X-ray reflectivity technique to changes in surface morphology and composition.

Figure 8 contains cyclic voltammetry and corresponding reflectivity data from an experiment performed with a working electrode consisting of a ~250 Å copper film supported on a silicon (111) single crystal. In this experiment the potential was cycled from an open circuit value of −0.12 V (curve A) to a reducing condition of −0.8 V (curve B), to an oxidizing condition of +0.4 V (curve C), then back to the reducing potential of −0.8 V. Notice in Fig.

8b how the anticipated transformations in surface morphology (as the reduced metal surface is oxidized then reduced again) affect the reflectivity pattern. Oscillations for the reduced metal are sharper and continue to higher Q values when compared to those for the oxidized metal. Analysis of these data [16,17] reveals that the initially "flat" surface of the reduced metal roughens by as much as 30 Å in root mean square fluctuation, but reversibly recovers to nearly the same degree of flatness that existed following the first reduction (curve A). The results of this study show how X-ray reflectivity can be used to track the morphological effects of cyclic electrochemical oxidation and reduction reactions, such as those that occur on the surface of battery electrodes and in many types of corrosion processes. Also, the increasing appearance of in situ X-ray scattering information for surfaces that are undergoing various types of morphological or roughening transitions has required that new theories and models be developed to permit meaningful analysis of the data. Examples of such developments are given in references [20-22].

Acknowledgements

The authors wish to acknowledge their collaboration with Wenbing Yun in several aspects of the research reviewed in this abstract. This work was sponsored by the U. S. Department of Energy/Office of Basic Energy, Energy Sciences under Contract W-31-109-ENG-38.

References

1. In Situ Characterization of Electrochemical Processes, Publication NMAB 438-3 (National Academy Press, Washington D.C., 1987) p. 33.
2. J. Robinson, in Spectroelectrochemistry, R. J. Gale, Ed. (Plenum Press, New York, 1988) p. 9.
3. H. D. Abrũna, in Modern Aspects of Electrochemistry, J. O'M. Bockris, R. E. White, B. E. Conway, Eds. (Plenum Press, New York, 1989) p. 265.
4. A. J. Davenport, H. S. Isaacs, and M. W. Kendig, Corrosion Science 32, 653 (1991).
5. A. J. Davenport, H. S. Isaacs, G. S. Frankel, A. G. Schrott, C. V. Jahnes, and M. A. Russac, J. Electrochem. Soc. 138, 337 (1991).
6. J. McBreen, W. E. O'Grady, G. Tourillon, E. Dantyge, A. Fontaine, and K. I. Pandya, J. Phys. Chem. 93, 6308 (1989).
7. M. E. Kordesch and R. W. Hoffman, Nuclear Instruments and Methods in Physics Research 222, 347 (1984).
8. L. Bosio, R. Cortes, and M. Froment, in Proceedings of the Third International EXAFS Conference, (Springer Verlag, Berlin, 1984) p. 484; L. Bosio, R. Cortes, A. Defrain, and M. Froment, J. Electroanal. Chem. 180, 265 (1984).
9. J. Kruger and G. G. Long, in Critical Issues in Reducing the Corrosion of Steels, H. Leidheiser and S. Haruyama, Eds (National Association of Corrosion Engineers, 1986) p. 284.
10. K. I. Pandya, R. W. Hoffman, J. McBreen, and W. E. O'Grady, J. Electrochem. Soc. 137, 383 (1990).

11. M. R. Toney, J. G. Gordon, M. G. Samant, G. L. Borges, O. R. Melroy, L.-S. Kau, D. G. Wiesler, D. Yee, and L. B. Sorensen, Phys. Rev. B42, 5594 (1990).

12. M. G. Samant, M. F. Toney, G. L. Borges, L. Blum, and O. R. Melroy, J. Phys. Chem. 92, 220 (1988).

13. L. Bosio, R. Cortes, M. Denoziere, and G. Folcher, Colloque de Physique 50, C7-23 (1989).

14. B. M. Ocho, J. Wang, A. Davenport, and H. Isaacs, Phys. Rev. Lett 65, 1466 (1990).

15. Z. Nagy, H. You, R. M. Yonco, C. A. Melendres, W. Yun, and V. A. Maroni, Electrochim. Acta 36, 209 (1991).

16. C. A. Melendres, H. You, V. A. Maroni, Z. Nagy, and W. Yun, J. Electroanal. Chem. Interfacial Electrochem. 297, 549 (1991).

17. H. You, C. A. Melendres, Z. Nagy, V. A. Maroni, W. Yun, and R. M. Yonco, Phys. Rev. B (submitted).

18. M. J. Bedzyk, G. M. Bommarito, M. Caffrey, and T. L. Penner, Science 248, 52 (1990).

19. R. Moberg, F. Bökman, O. Bohman, and H. O. G. Siegbahn, J. Chem. Phys. 94, 5226 (1991).

20. R. Cowley and T. W. Ryan, J. Phys. D: Appl. Phys. 20, 61 (1987).

21. S. K. Sinha, E. B. Sirota, S. Garoff, and H. B. Stanley, Phys. Rev. B38, 2297 (1988).

22. I. M. Tidswell, B. M. Ocko, P. S. Pershan, S. R. Wasserman, G. M. Whitesides, and J. D. Axe, Phys. Rev. B41, 1111 (1990).

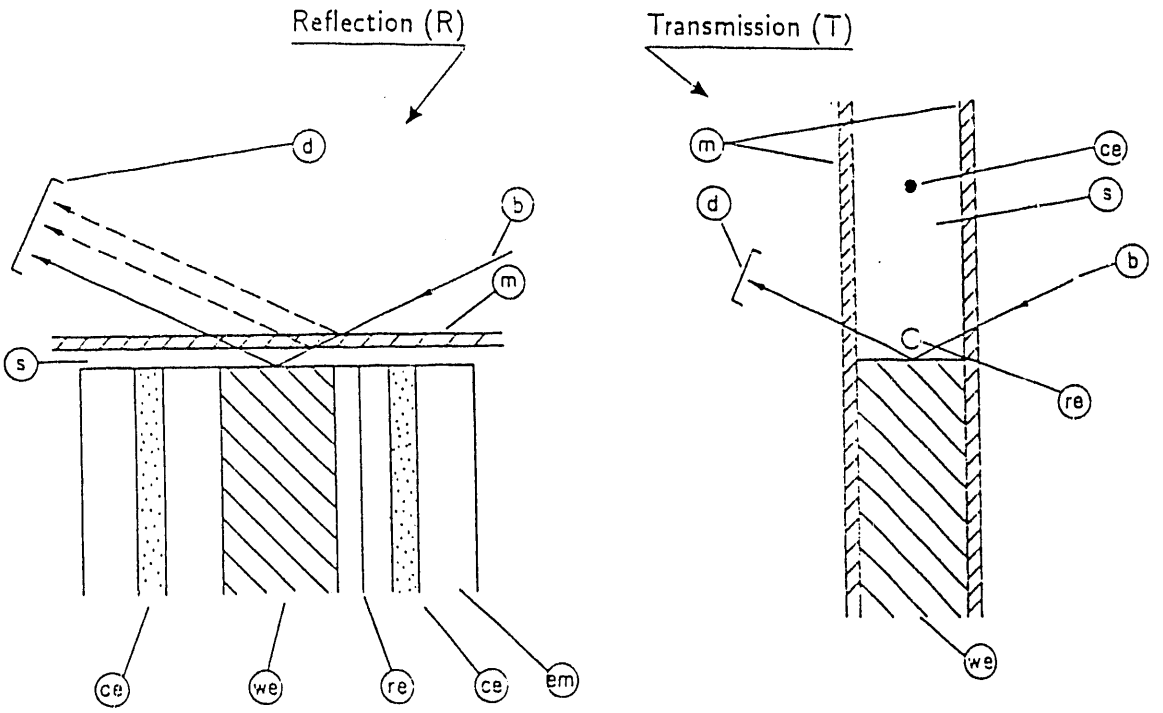

Figure 1. Schematic, cross-sectional representation of (left) the reflection geometry and (right) the transmission geometry X-ray/electrochemical cell. b: X-ray beam, ce: counter electrode, d: detector, em: electrode mounting, m: membrane, re: reference electrode, s: solution, we: working electrode.

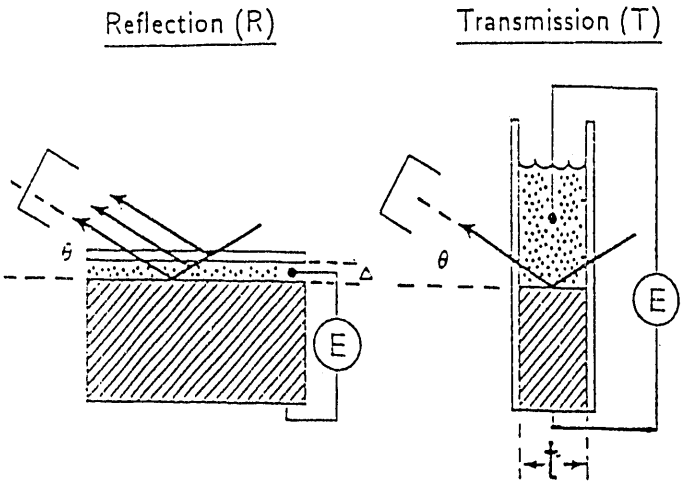

$\text{Path}_R = 2\Delta/\sin\theta$ $\qquad$ $\text{Path}_T = t/\cos\theta$

$\text{Path}_R/\text{Path}_T = 2\Delta \cdot \cos\theta/t \cdot \sin\theta$

For $\Delta = 0.05$ mm and $t = 2$ mm ⇓

θ	$\text{Path}_R/\text{Path}_T$
0.05°	~60
0.5°	~6
3°	~1
5°	~0.6
10°	~0.3

Figure 2. Effect of electrolyte path length for transmission and reflection geometry.

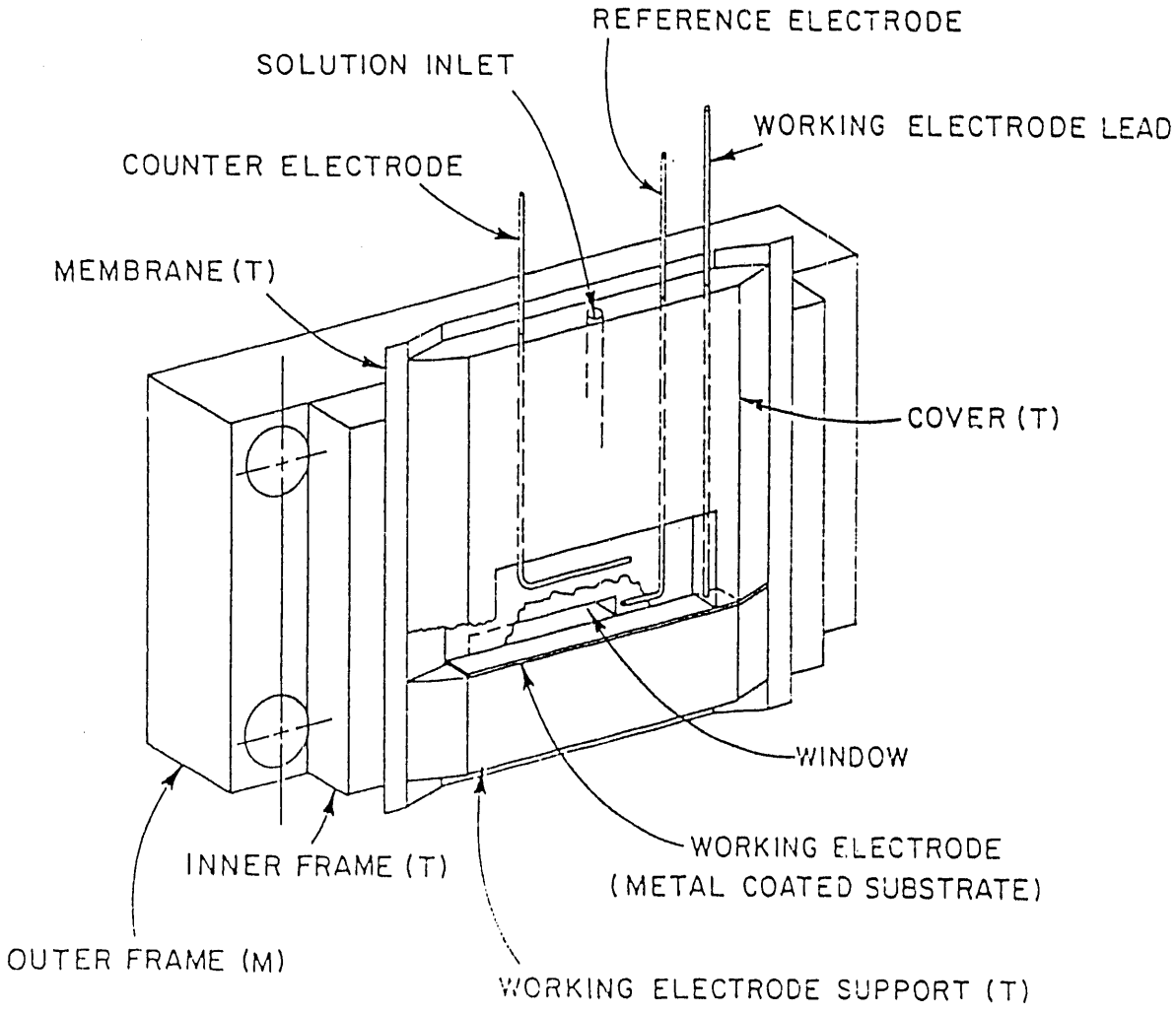

Figure 3. Transmission-type X-ray/electrochemical cell used by Nagy et al. [15-17]. T=Teflon, M=metal.

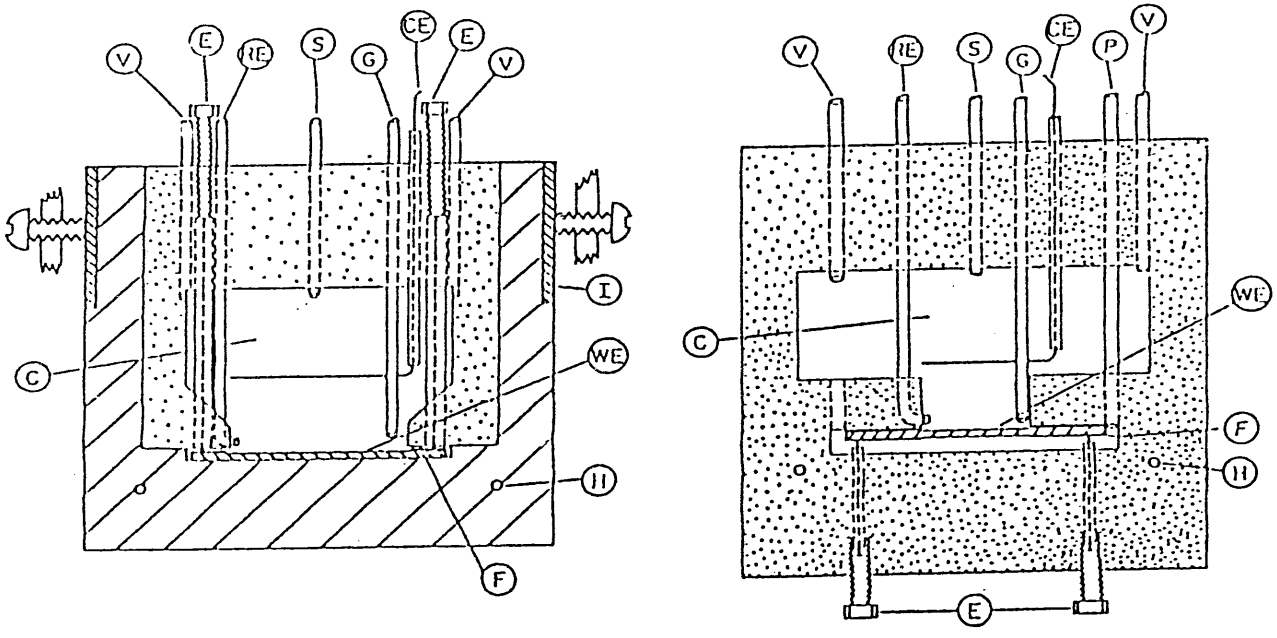

Figure 4. Alternative center sections for transmission-geometry X-ray/electrochemical cell. (Left) two-piece center section. (Right) one-piece center section. C: solution cavity, CE: counter electrode, E: working electrode lead, F: metal foil, G: gas inlet, H: positioning hole, I: metal insert, P: purge hole, RE: reference electrode, S: solution inlet, V:vent, WE: working electrode. (Overall size: 6.5x6.0x0.32 cm.)

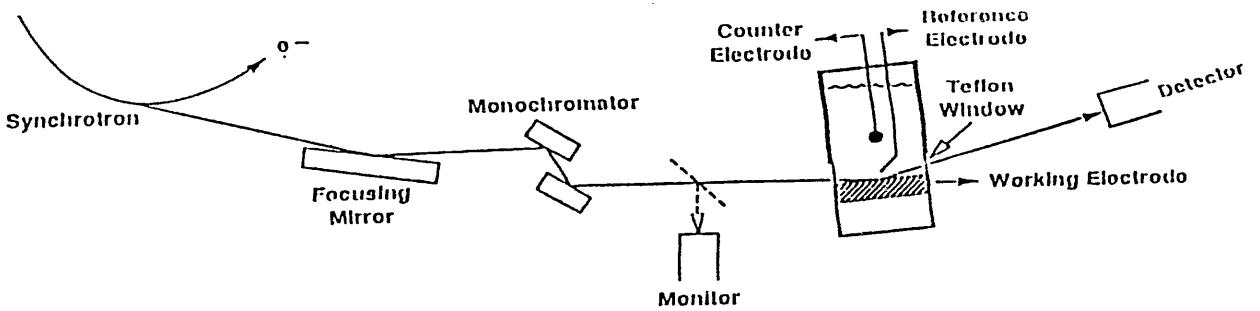

Figure 5. Experimental arrangement used with the XEC at the synchrotron.

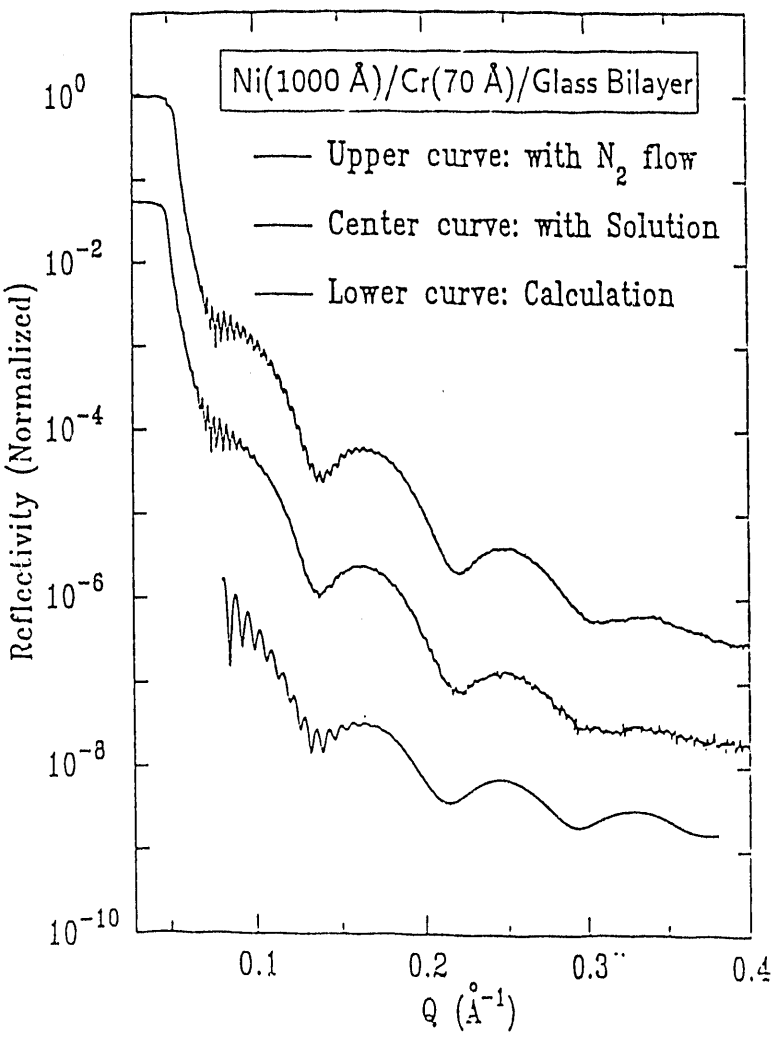

Figure 6. X-ray reflectivity data for a Ni(1000 Å)/Cr(70 Å)/borosillicate glass multilayered metal film electrode.

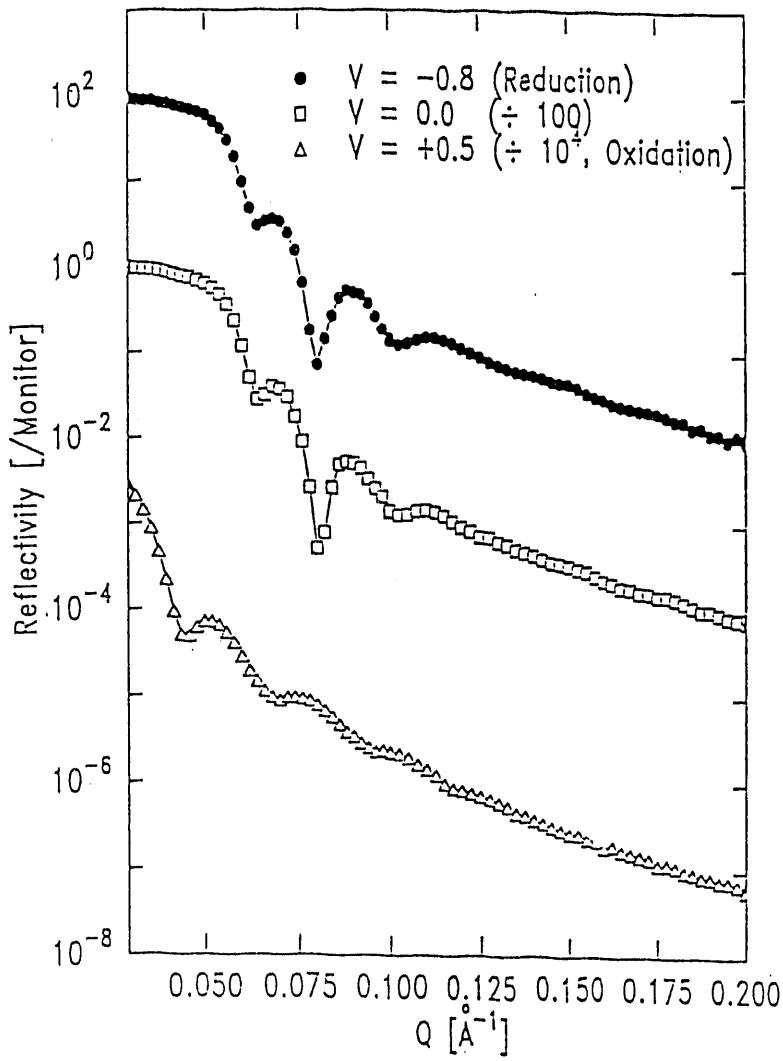

Figure 7. Reflectivity curves for a silver film on a silicon single crystal substrate at various potentials versus Ag/AgCl reference.

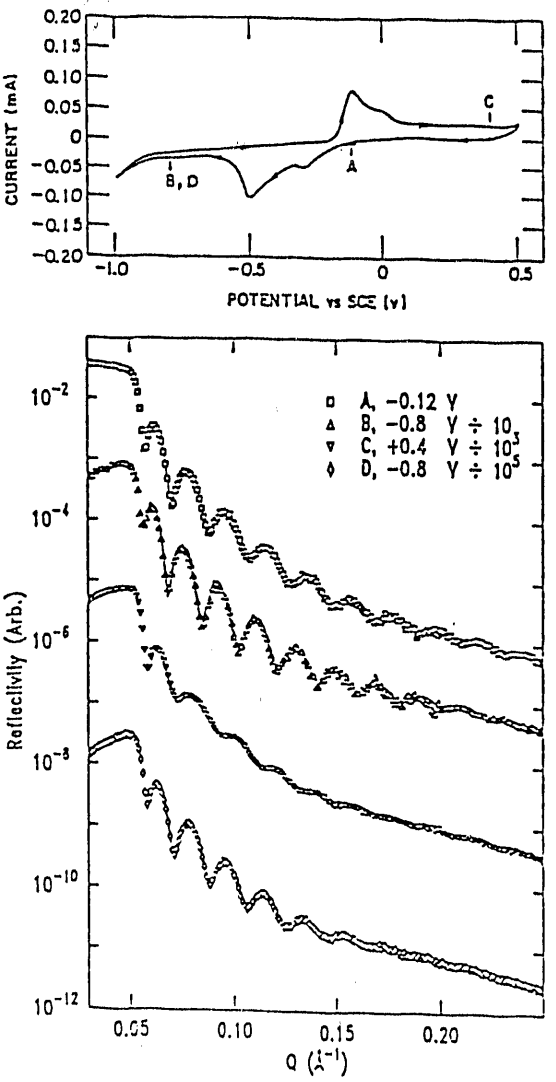

Figure 8. Cyclic voltammetry curve (inset a) and reflectivity data (inset b) at selected potentials for a ~250 Å copper film on a Si (111) single crystal.

SYNCHROTRON RADIATION STUDIES OF SUPPORTED METAL CATALYSTS

G.H. Via, G. Meitzner, F.W. Lytle* and J.H. Sinfelt
Corporate Research Laboratory
Exxon Research and Engineering Company
Annandale, New Jersey 08801

1. Introduction

Metallic clusters supported on refractory oxides have been used extensively for several decades in the production of chemicals and petroleum derived transportation fuels. These materials typically have surface areas of several hundred square meters per gram, and the metal clusters are often less than 20 Å in diameter. Metal clusters in this size range are characterized by having a high fraction of the total number of atoms in the surface of the cluster. The ratio of surface metal atoms to total metal atoms in the catalyst is defined as the dispersion, and in many catalytic systems the dispersion approaches unity. The composition of these catalytic materials is generally on the order of 1 weight percent metal or less.

Catalysts containing more than one metal component are of particular interest since the addition of a second metal provides a method of controlling the selectivity of the catalyst. That is, the second metal can alter the rates of competing reactions in a complex reaction sequence and thus alter the final product distribution of the reaction. This is illustrated in ***Figure 1*** by the early work of Sinfelt[1] with model catalyst systems. In this work the reactions of cyclohexane in hydrogen over silica supported ruthenium and osmium catalysts were studied. The two principal reaction pathways are, 1) dehydrogenation of cyclohexane to form benzene, and 2) hydrogenolysis of cyclohexane for form methane. It was found that when the catalysts were prepared with varying amounts of a second non-reactive metal (copper), the dehydrogenation rates remained essentially constant while the hydrogenolysis rates decreased by about an order of magnitude as the amount of copper was increased to form a 1:1 atomic ratio with the primary metal (Ru or Os) in the supported catalyst. Thus, the selectivity of the catalysts as defined by the ratio of the dehydrogenation to hydrogenolysis reaction rates increased significantly with the addition of the second metal. An interesting feature of these particular metal pairs is that in the bulk, copper is completely immiscible with ruthenium or osmium so that we would not necessarily anticipate alloy formation in the small metal clusters. Bimetallic catalysts therefore represent an important class of materials that are of interest both scientifically and technologically.[2]

Despite the importance and long-standing use of supported metal catalysts, detailed information on the structure of the metal clusters has been difficult to obtain. The factors contributing to this difficulty include the low concentration of the metal(s) in the system, the small size of the clusters, and the high dispersion which makes the structure very sensitive to the cluster environment. The development of x-ray absorption spectroscopy[3] with the increasing availability of synchrotron radiation, however, has provided a powerful and versatile tool for studying the structure of these complex systems. Using the Extended X-ray Absorption Fine Structure (EXAFS) technique, it is possible to obtain information on the local atomic structure of supported monometallic catalytic metals[4] and their interaction with the support[5]. In the discussion that follows we will focus on results that have been obtained on the structure of supported bimetallic cluster catalysts.

*The Boeing Company, Seattle, Washington

2. EXAFS Technique

EXAFS refers to the oscillations in x-ray absorption coefficient that occur on the high energy side of x-ray absorption edges. These oscillations can be thought of as arising form the interference between electron waves resulting from the ejection of a core electron due to absorption of an x-ray photon and the electron waves after they are backscattered by atoms surrounding the absorber atom. The oscillation in absorption coefficient is defined by the expression

$$\chi(K) = (\mu - \mu_o)/\mu_o \qquad (1)$$

where μ and μ_o are the atomic absorption coefficients of the absorber atom in the material of interest and in the free state. The energy dependent wave vector, K, is defined by

$$K = (8mE\pi^2)^{1/2}/h \qquad (2)$$

where m is the mass of the electron, h is Planck's constant, and E is the kinetic energy of the electron. The energy E is the difference between the x-ray photon energy and a threshold energy associated with the ejection of the core electron. The contribution to the total EXAFS function of a particular type of atom at a specific interatomic distance, R, from the absorber atom is given by

$$\chi(K) = (N/KR^2)F(K)\exp(-2K^2\sigma^2)\sin\,[2KR + 2\delta(K)] \qquad (3)$$

where N is the total number of those particular atoms at the distance R, F(K) is an element specific function which accounts for electron backscattering and inelastic scattering, σ is the root mean square deviation in the interatomic distance R due to thermal vibrations or structural disorder, and 2δ is the phase shift term which contains contributions from both the absorber atom and the backscattering atom. In general, the experimentally observed EXAFS function of a particular element would be the sum of a number of terms given by equation (3). Furthermore, in dilute or poorly order systems we are often only interested in structural information concerning the first coordination shell of an element. The term first coordination shell usually refers to those atoms directly bonded to a particular element. Even in this simple case, however, we may still have several contributions to the EXAFS function.

The conceptual process of analysis of EXAFS data to determine structural information is depicted in ***Figure 2***. The steps involve extraction of the total EXAFS function from the experimentally measured x-ray absorption spectrum, transformation of the extracted data from energy to wave vector space, fourier transformation of the total EXAFS function to produce a radial structure function (similar to XRD radial distribution function), isolation of that portion of the radial structure function in distance space that is of interest followed by inverse fourier transformation to yield a 'simplified' EXAFS function (fourier filtering), and finally analysis of this 'simplified' spectrum to obtain structural information. This final analysis step generally proceeds by modeling of the data using non-linear regression techniques[6] with theoretical or experimental functions (from reference compounds) for phase shifts and backscattering amplitudes. The structural information derived from this process includes coordination number, N, interatomic distance, R, and disorder term, σ, for each different atom type in the first coordination shell. Since backscattering amplitudes and phase shifts are dependent on the chemical identity of the backscattering element, it is usually possible to distinguish between chemically probable choices of backscattering elements if the difference in atomic number between the various choices is several units.

3. The Bimetallic Structure Problem

X-ray absorption edges are generally well separated in energy so that for supported bimetallic clusters composed of metals **a** and **b**, the absorption spectrum for each component can be measured separately without interference from the other component. In cases where this cannot be done due to elements being adjacent in the periodic table, alternative approaches based on data analysis techniques[7] or energy dispersive detection schemes[8] have been devised to deal with the problem. In any event, independent absorption measurements of the environment of each component is assumed.

Figure 3 summarizes the general features of the bimetallic EXAFS problem. In general, each metallic component will have first shell near-neighbors of each type, **a** and **b**. If we ignore contributions to the EXAFS function from support interactions, the EXAFS function for each edge will contain contributions from backscatterers of type **a** and **b**. There will, therefore, be four possible combinations of absorber and backscattering atoms, **aa**, **bb**, **ab**, and **ba**. Edge **a** contains contributions from **aa** and **ab** while edge **b** contains contributions from **bb** and **ba**. Each contribution is characterized by a coordination number, an interatomic distance, and a disorder term.

One approach to the solution of this problem involves analyzing the data from each edge separately. We have developed such an approach which includes the use of data on appropriate reference materials and an iterative least squares procedure for determining best fit values of the various structural parameters[9,10]. This procedure makes use of the structure independent relationship

$$R_{ab} = R_{ba} \tag{4}$$

to guide the overall solution to the problem even though each edge analysis is carried out separately. That is, the **ab** interatomic distance determined from each independent data set (edge) should agree regardless of the specific cluster structure or structures formed. Details of this procedure are discussed elsewhere[10,11]. This approach has been used to study the structure of a wide variety of supported bimetallic cluster catalysts[10,12,13,14,15,16].

Equation (4) describes one structure independent relationship that must be satisfied in the solution to the bimetallic problem. There are, however, two additional relationships which must also be satisfied.

$$\sigma_{ab} = \sigma_{ba} \tag{5}$$

and,

$$N_{ab} = (X_b/X_a)N_{ba} \tag{6}$$

where X_a and X_b are the atomic fractions of **a** and **b** in the bimetallic cluster catalysts. That is, all of the information on structural parameters (interatomic distance, root mean square relative displacement in distance, and coordination number) related to intermetal bonding is contained in the data form each edge. Furthermore, relationships describing this redundancy can be written which are completely independent of the structure(s) formed by the clusters. It is possible, therefore, to use these relationships to reduce the number of unknown parameters in a problem and thus improve the quality of the derived information. We have recently developed a comprehensive multi-edge data analysis procedure which implements all relevant parameter constraints and applied it to much of our previously published data[17,18].

4. Results on Supported Bimetallic Cluster Catalysts

Figure 4 summarizes the bimetallic pairs which we have examined by x-ray absorption spectroscopy and groups them according to bulk solubility[19]. We distinguish between four classes of materials - pairs which are completely immiscible in the bulk, pairs which exhibit low but finite miscibility, pairs which exhibit intermediate miscibility, and pairs which are completely miscible in the bulk. In the latter category, some of the pairs such as Pt-Cu or Pt-Sn are also capable of forming ordered solid solutions at one or more atomic ratios. It should be noted that the bulk solubility classification applies strictly to metallurgical (generally high temperature) preparations, whereas the catalytic systems we are dealing with are prepared very differently. Typical preparation conditions for most of the catalysts involved aqueous co-impregnation of the porous regions of the oxide support with soluble salts of the metals, followed by air drying and reduction in hydrogen at approximately 675K. These materials, therefore, have never been exposed to the high temperatures typical of metallurgical preparations. Furthermore, the clusters formed in catalytic preparations are generally very small (less than 30 Å) and contain a high fraction of surface atoms. We anticipate ,therefore, that surface effects and support interactions will play an important role in determining the kinds of cluster structures formed.

In addition to variations in bulk solubility, our studies have also included some materials in which the preparation procedure, the nature of the support, or the cluster composition has been varied. In the discussion that follows we will use experimental results on the structure of bimetallic clusters to examine the importance of these various influences on structure. For this purpose we will focus on the composition of the first coordination shell of the bimetal clusters. That is, we will not discuss or examine the systematics of interatomic distance variation. It should also be pointed out that the experimental results summarized below are based on measurements carried out primarily at 100K on catalysts that had been reduced in the range of 675-775K in flowing hydrogen. In most cases the gas environment for the catalysts during measurement was also hydrogen, although in the case of palladium the hydrogen was exchanged for helium to avoid the complication of hydride formation.

4.1 Surface Segregation

Figure 5 summarized information on the structure of a number of silica supported copper containing, 1:1 atomic ratio, bimetallic pairs as a function of bulk solubility. The structural information in this figure, as well as others, is presented in the form of a stacked bar graph in which the height of a bar corresponds to a coordination number. That is, the total coordination number for each component of a pair is represented by the total height of the bar associated with that element. This total coordination number is the sum of the number of copper near-neighbors (light colored bar in the figure) and the number of other metal near-neighbors (dark bar). For each metal pair there are two bars corresponding to the coordination environment for each component in the pair. For 1:1 atomic ratio clusters the average total coordination number of the clusters is the average of the total coordination number of each of the metal components. The average cluster coordination number for clusters which are not 1:1 in atomic ratio are calculated by taking the elemental composition into consideration.

All of the metals involved in our studies are either fcc or hcp in the bulk so that for the bulk or large metal clusters the maximum coordination in the first shell is 12. The errors typically associated with the analysis of coordination number from EXAFS data is 1-2 coordination units[4]. An examination of the data in ***Figure 5*** shows several interesting features. In all cases the metal clusters contain both elements regardless of the bulk miscibility of the pair. While there will almost certainly be a distribution of cluster compositions in any particular system, there appears to be a strong tendency to form bimetal clusters rather than isolated monometallic clusters. In addition, with the exception of the Cu-Au pair, the average cluster coordination number for all of the

systems appears to be significantly less than 12, although there does not appear to be any systematic variation with bulk solubility. This would indicate that in most cases the clusters are quite small. A striking feature of all of the cluster data is that the total coordination number of one of the components is usually significantly less than the total coordination number of the other component. Furthermore, the first shell near-neighbors of each component tend to be dominated by atoms of the same element so that the compositions are not uniform. This means that the clusters are characterized by a high degree of surface segregation where the component with the highest coordination number is at the center or core of the cluster and the other component resides primarily in the surface of the cluster. It should also be noted that with the exception of the Cu-Re pair, the component in the surface (copper) is in all cases the most volatile component and the one we would expect on the basis of energetics to be the surface segregated species.

Rhenium appears to be the exception to this rule. In ***Figure 6*** we summarize data on three different 1:1 atomic ratio rhenium cluster pairs along with data on 1:1 Cu-Ag on silica. In all three of the rhenium cases we find that the total rhenium coordination number is smaller than that of the other component indicating that the surface segregated species is rhenium. In each case we would anticipate that the other metal would be the surface rich component. We conclude, therefore, that other factors such as strong support interactions may be important in controlling the nature of rhenium clusters. It should also be noted that Liang[20], et. al. have carried out anomalous diffraction studies on high loading Pt-Re/silica catalysts and found that the Re crystallizes predominantly in an fcc phase rather than in the normal hcp form. This suggests that platinum acts as a crystallization template for the rhenium, which could occur if platinum reduces at a lower temperature than rhenium during cluster formation. In any event, these findings at high loading levels are consistent with our results at low loading. With regard to the Cu-Ag pair, the silver coordination number is slightly lower than that of copper suggesting that silver is the surface segregated phase. In this case silver is the most volatile component so this result is expected.

4.2 Bulk Solubility

The influence of bulk miscibility on cluster structure appears to be rather subtle. In ***Figure 5*** we saw that there was no obvious trend in structure with solubility. In ***Figure 7***, however, we compare data on copper-Group VIII metal clusters from the second and third rows of the periodic table. In each case we compare clusters exhibiting widely different bulk miscibility characteristics, but with approximately the same overall coordination number. We see that with each pair (Cu-Os vs. Cu-Pt and Cu-Ru vs. Cu-Rh) the cluster with the highest degree of bulk solubility shows the greatest extent of interaction between metals in the cluster. For example, in the Os-Pt comparison, the fraction of platinum atoms coordinated with copper exceeds the osmium fraction with copper, and the fraction of copper atoms coordinated with platinum exceeds the copper fraction with osmium. The Cu-Os pair are completely immiscible in the bulk while the Cu-Pt pair are miscible in all proportions. Bulk miscibility does, therefore, appear to promote increased interaction between the bimetal pair. It should also be noted that in the case of copper the metals which exhibit the lowest bulk solubility have hcp crystal structures (Os and Ru in this case) while those with the highest bulk solubility have fcc structures (Pt and Rh above). Copper, of course, also crystallizes in the fcc form.

4.3 Cluster Size

The effect of cluster size on the degree of interaction between the two metals in a cluster is much more important than the bulk solubility properties. This can be seen in ***Figure 8*** where we compare data on three cluster pairs with approximately the same solubility characteristics, but with significantly different cluster sizes as determined by their overall coordination number. We see that as the clusters get smaller the extent of interaction between the two metals increases. In the limit of extremely small 1:1 clusters the composition of the first coordination shells of the two metals can

approach a homogeneous distribution due to the limited number of possible atomic arrangements. This effect can be seen in the data on the Cu-Re pair where the interaction between the two metals is high despite the fact that the bulk metals are completely immiscible. The influence of surface segregation, however, can even be seen to operate in these extremely small clusters (coordination number = 4) in that the coordination numbers for the two components are not equal. As the clusters get larger, the surface segregation factor causes the average interaction between the two components to decrease since the atomic mixing occurs primarily in the region of the metal-metal interface. In the limit of very large clusters (small surface area) the average degree of interaction tends to zero.

Many factors such as preparation technique and nature of the support will influence cluster size. In ***Figure 9*** we illustrate some of these effects by comparing structural data on clusters with the same overall composition which have been produced in different ways. We compare, for example, 1:3 atomic ratio clusters of copper and ruthenium deposited on a high surface area silica support by co-impregnation of soluble salts and by deposition of the bimetallic carbidocarbonyl cluster bis(acetonitrilecuprio)carbidohexadecacarbonylhexaruthenium, $[(CH_3CN)_2Cu_2Ru_6C(CO)_{16}]$.[21] The insert in ***Figure 9*** is a model showing the metal positions in the cluster precursor. The metal core consists of a distorted octahedron of ruthenium atoms encapsulating a carbon atom with two adjacent capping copper atoms. We see that the reduced bimetallic cluster formed from the carbidocarbonyl cluster compound has a lower total coordination number than clusters of the same composition formed by the traditional co-impregnation technique. We also see that because of the smaller average cluster size in the case of the carbidocarbonyl cluster preparation, the degree of interaction of copper with ruthenium and ruthenium with copper is higher. This is consistent with the trends seen in ***Figure 8***.

In ***Figure 9*** we also compare 1:1 atomic ratio rhodium-iridium clusters prepared by co-impregnation of high surface area silica and alumina supports. The average cluster size is smaller in the alumina supported material than in the silica supported material. The degree of interaction of rhodium with iridium and iridium with rhodium is also somewhat higher for the alumina supported material, which is again consistent with the trends seen in our other results. The effect, however, is much less pronounced in this case. The Rh-Ir pair is interesting from the point of view that in both the alumina and silica supported materials the composition of the clusters is rather uniform and the total coordination number of the first near-neighbor shell of each metal is essentially indistinguishable. That is, surface segregation is not a very important factor for this bimetal pair even thought our results suggest that there is a slight tendency for rhodium to concentrate in the surface of the clusters. This is no doubt due to the fact that these two metals are very similar. They are completely miscible in the bulk, they both crystallize in the fcc phase, and their atomic volumes are very similar. The nearest neighbor interatomic distance for iridium metal is 2.714 Å and the value for rhodium is 2.690 Å[13]. These materials represent some of the most homogeneous clusters that we have investigated.

The data in ***Figure 10*** address the issue of the influence of cluster composition on cluster size or dispersion. We compare structural information on Cu-Ru clusters prepared on a high surface area silica support by co-impregnation of different atomic ratios of copper to ruthenium. The EXAFS results show that as the ratio of Cu:Ru increases the average total cluster coordination number decreases. This indicates that the copper somehow plays a role in either anchoring small ruthenium clusters to the support or in preventing cluster agglomeration because of surface modification. These EXAFS results on Cu-Ru are consistent with electron microscopy data[22] shown in the right field of ***Figure 10*** which compares the cluster size distribution for a pure ruthenium catalyst with that of the 1:1 atomic ratio Cu-Ru catalyst used in the EXAFS measurements. This shows that the distribution functions are rather similar except in the high end. The pure material shows an extended distribution of sizes with some clusters as large as 100 Å whereas the bimetallic catalyst has no clusters larger than about 60 Å. Since a large fraction of the metal atoms in the system will

be in the largest clusters, the average cluster diameter for the bimetallic system will be significantly smaller than that of the pure material. Control of cluster composition can thus be an important tool in controlling cluster dispersion in supported catalytic systems.

5. Summary

X-ray absorption spectroscopy has proven to be an extremely powerful tool for providing structural information on supported metal catalysts. In the case of bimetallic cluster catalysts a number of important trends regarding structure have been deduced as a result of these studies. We find that bulk miscibility is not a good indication of cluster formation in small, supported clusters. Bimetallic clusters rather than phase separated monometallic clusters form under all miscibility conditions. Surface segregation of the most volatile component in a pair tends to occur in most cases, although exceptions to this have been observed in rhenium containing bimetallic clusters. We find that cluster size is influenced by many factors such as preparation technique, support, and cluster composition. We also find that cluster size is a major factor in determining the extent to which the two metals interact with unlike neighbors in the clusters.

6. References

[1]J.H. Sinfelt, *J. Catal.* **29**, 308 (1973).

[2]J.H. Sinfelt, *Bimetallic Catalysts: Discoveries, Concepts, and Applications* (John Wiley and Sons, New York, 1983).

[3]D.E. Sayers, F.W. Lytle and E.A. Stern, *Phys. Rev. Lett.* **27**, 1204 (1971).

[4]G.H. Via, J.H. Sinfelt and F.W. Lytle, *J. Chem. Phys.* **71**, 690 (1979).

[5]F.W. Lytle, G.H. Via and J.H. Sinfelt, in: *Synchrotron Radiation Research*, eds. H. Winick and S. Doniach, Ch. 12, pp. 401-424 (Plenum Publishing Corporation, New York, 1980).

[6]K. Levenberg, *Quart. Appl. Math.* **2**, 164 (1944); D.W. Marquart, *SIAM J. Appl. Math.* **11**, 431 (1963); J.J. More, B.S. Garbow and K.E. Hillstrom,*User Guide to MINPACK-1*, Argonne National Laboratory Report ANL-80-74 (1980).

[7]J.H. Sinfelt, G.H. Via and F.W. Lytle, *J. Chem. Phys.* **76**, 2779 (1982).

[8]G.N. George, G.H. Via and M. Sansone, *National Synchrotron Light Source Annual Report*, 233 (1990).

[9]J.H. Sinfelt, G.H. Via and F.W. Lytle, *J. Chem. Phys.* **72**, 4832 (1980).

[10]J.H. Sinfelt, G.H. Via, F.W. Lytle and R.B. Greegor, *J. Chem. Phys.* **75**, 5527 (1981).

[11]J.H. Sinfelt, G.H. Via and F.W. Lytle, *Catalysis Reviews-Science and Engineering* **26**, 81 (1984).

[12]G. Meitzner, G.H. Via, F.W. Lytle and J.H. Sinfelt, *J. Chem. Phys.* **78**, 882 (1983).

[13]G. Meitzner, G.H. Via, F.W. Lytle and J.H. Sinfelt, *J. Chem. Phys.* **78**, 2533 (1983).

[14]G. Meitzner, G.H. Via, F.W. Lytle and J.H. Sinfelt, *J. Chem. Phys.* **83**, 353 (1985).

[15]G. Meitzner, G.H. Via, F.W. Lytle and J.H. Sinfelt, *J. Chem. Phys.* **83**, 4793 (1985).

[16]G. Meitzner, G.H. Via, F.W. Lytle and J.H. Sinfelt, *J. Chem. Phys.* **87**, 6354 (1987).

[17]G.H. Via, J.H. Sinfelt, G. Meitzner and F.W. Lytle, *Mat. Res. Soc. Symp. Proc.* **143**, 111 (1989).

[18]G.H. Via, K.F. Drake, Jr., G. Meitzner, F.W. Lytle and J.H. Sinfelt, *Catal. Lett.* **5**, 25 (1990).

[19]M. Hansen, *Constitution of Binary Alloys*, 2nd ed. (McGraw-Hill, New York, 1958).

[20]K.S. Liang, G.J. Hughes and J.H. Sinfelt, *Physica B* **158**, 135 (1989).

[21]J.S. Bradley, R.L. Pruett, E. Hill, G.B. Ansell, M.E. Leonowicz and M.A. Modrick, *Organometallics* **1**, 748 (1982).

[22]E.B. Prestridge, G.H. Via and J.H. Sinfelt, *J. Catal.* **50**, 115 (1977).

Cu ENHANCES CYCLOHEXANE DEHYDROGENATION SELECTIVITY OF Ru and Os

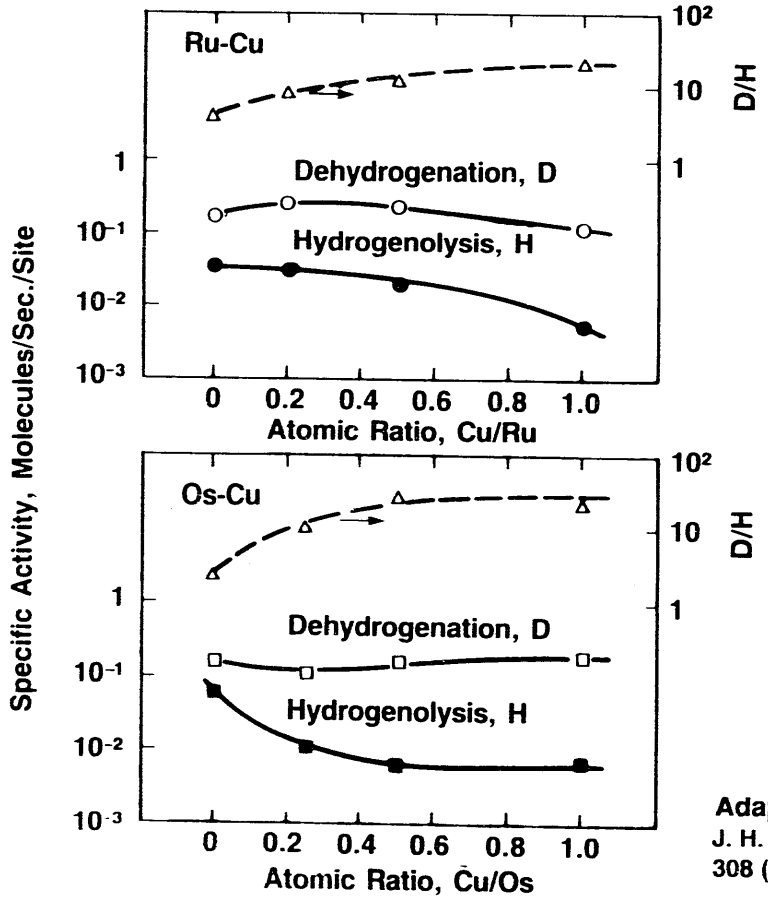

Adapted from
J. H. Sinfelt, J. Catal. 29, 308 (1973).

Figure 1

EXAFS Provides Physical and Chemical Information On Local Environment

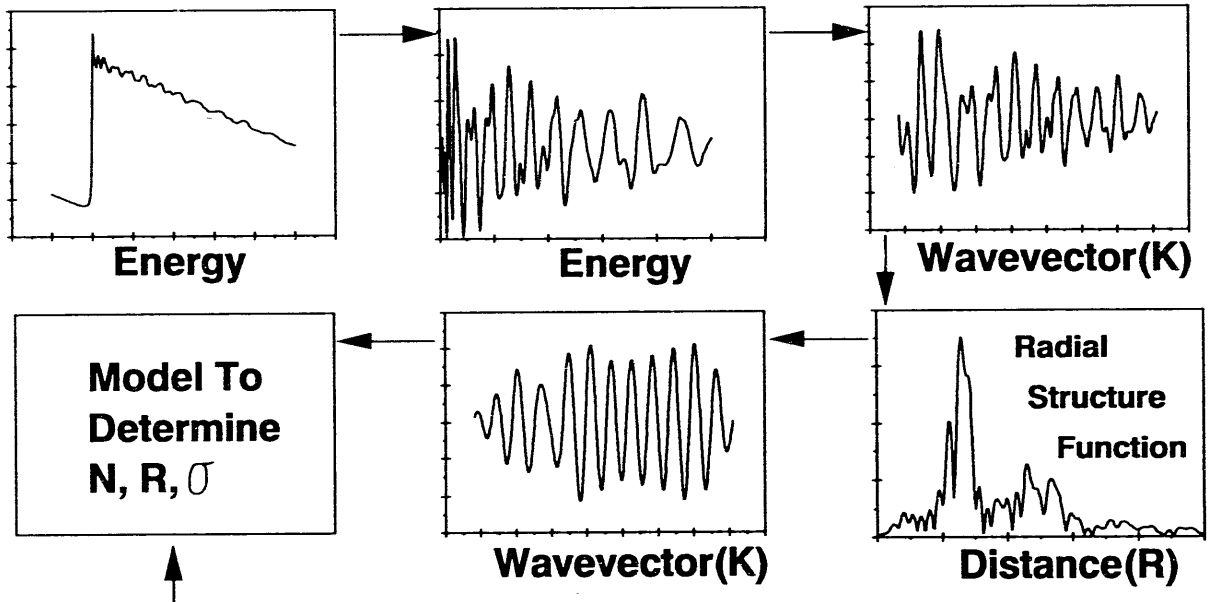

$$K\chi(K)=\sum_i (N_i/R_i^2)\,F_i(K)\exp(-2K^2\sigma_i^2)\sin(2KR_i+\varphi_i(K))$$

Figure 2

EXAFS MEASURES AVERAGE LOCAL STRUCTURE OF EACH ATOM TYPE

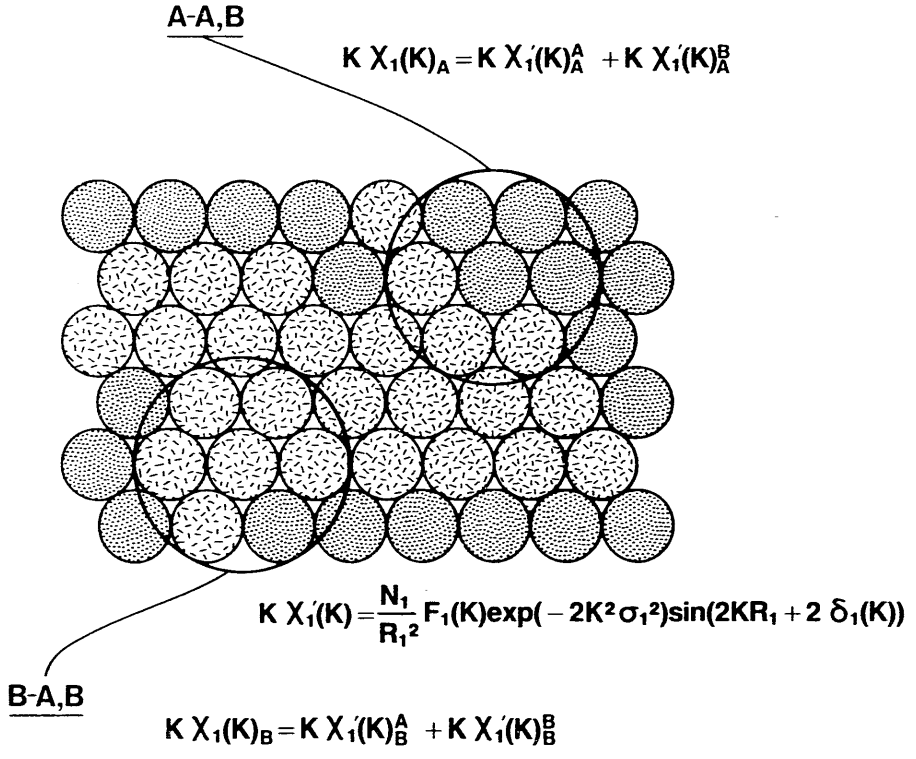

Figure 3

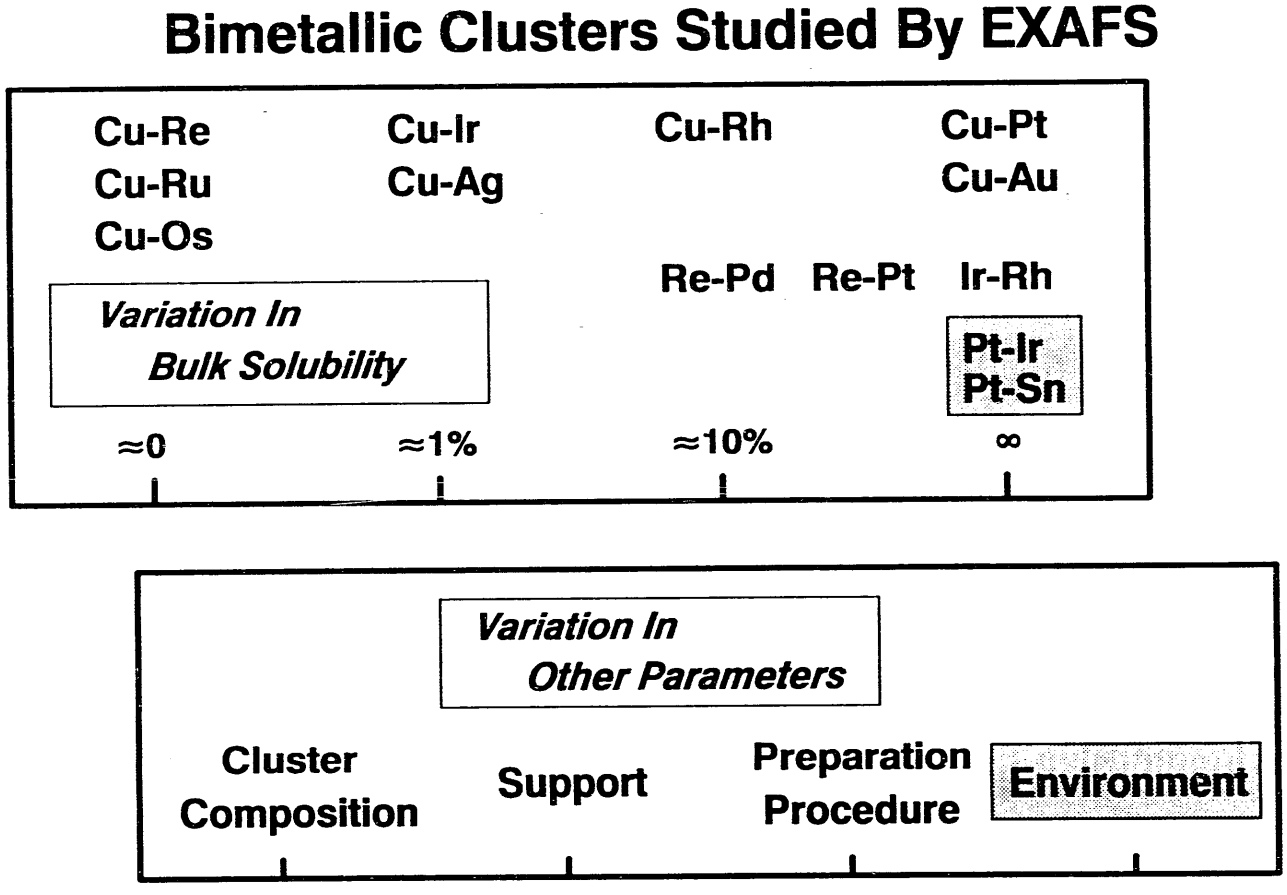
Bimetallic Clusters Studied By EXAFS
Cu-Re
Cu-Ru
Cu-Os
Cu-Ir
Cu-Ag
Cu-Rh
Cu-Pt
Cu-Au
Re-Pd
Re-Pt
Ir-Rh
Pt-Ir
Pt-Sn
Variation In
Bulk Solubility
≈0
≈1%
≈10%
∞
Variation In
Other Parameters
Cluster
Composition
Support
Preparation
Procedure
Environment

Figure 4

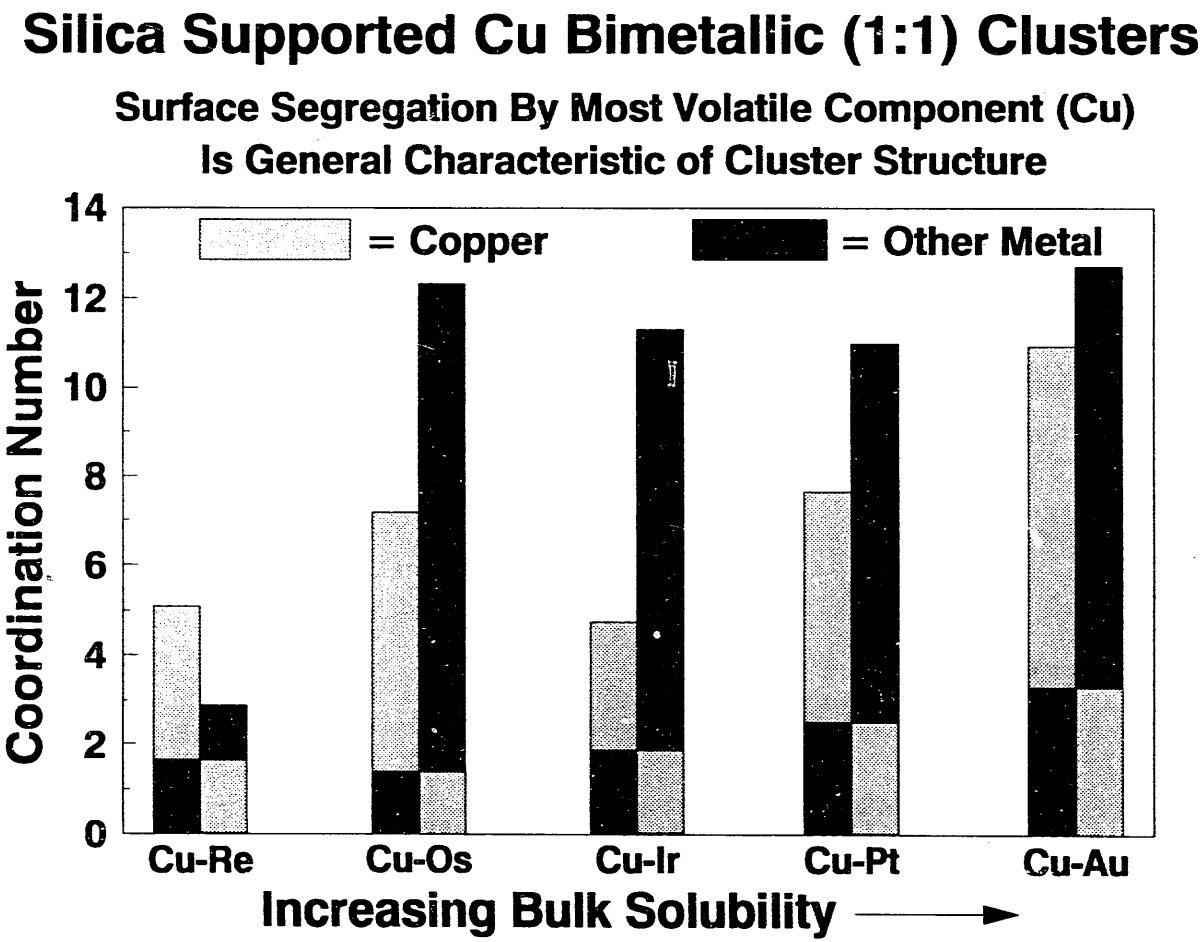
Silica Supported Cu Bimetallic (1:1) Clusters
Surface Segregation By Most Volatile Component (Cu)
Is General Characteristic of Cluster Structure
= Copper
= Other Metal
Coordination Number
0
2
4
6
8
10
12
14
Cu-Re
Cu-Os
Cu-Ir
Cu-Pt
Cu-Au
Increasing Bulk Solubility

Figure 5

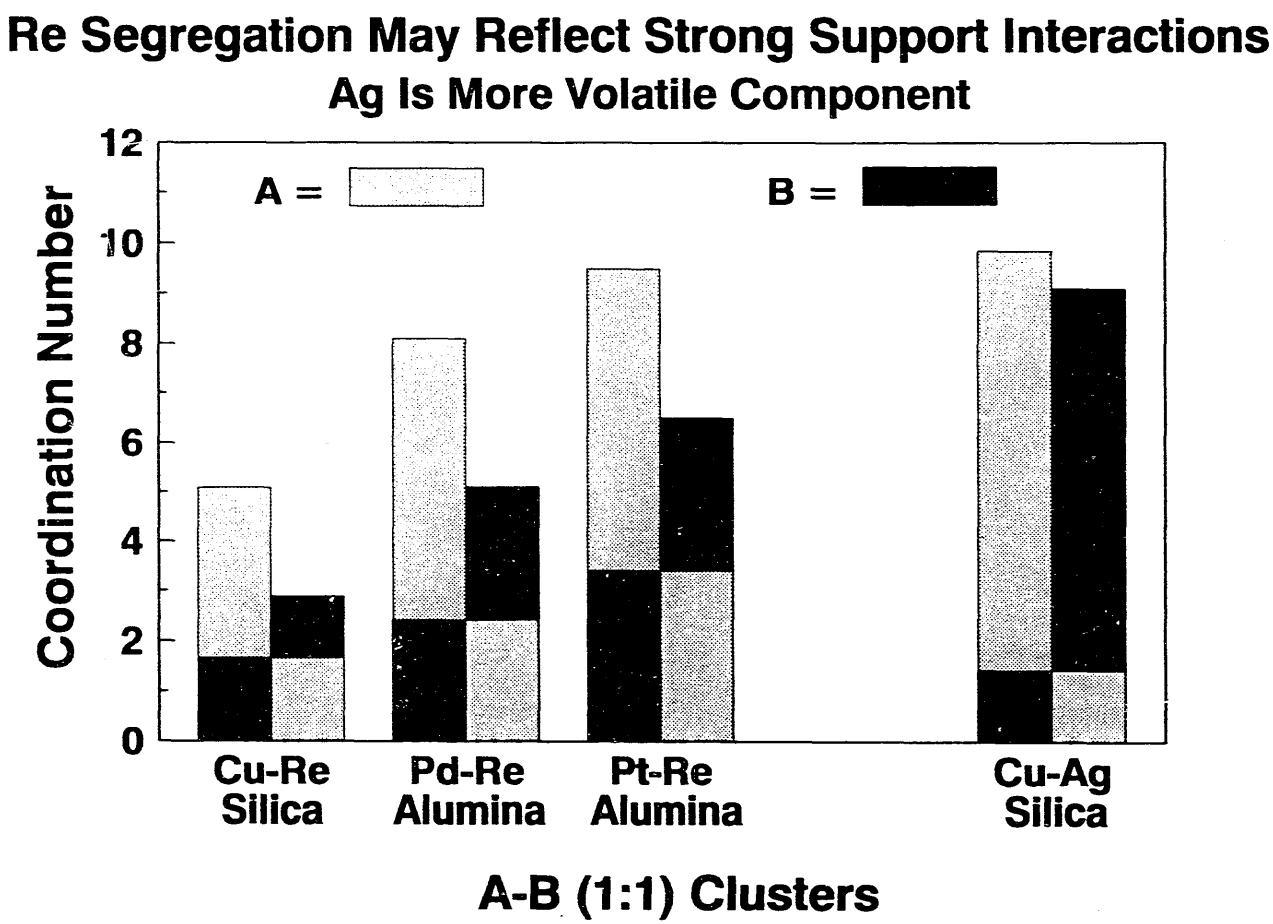
Re Segregation May Reflect Strong Support Interactions
Ag Is More Volatile Component
Coordination Number
12
10
8
6
4
2
0
A =
B =
Cu-Re Silica
Pd-Re Alumina
Pt-Re Alumina
Cu-Ag Silica
A-B (1:1) Clusters

Figure 6

Bulk Solubility Has An Influence On The Structure Of Bimetallic Clusters

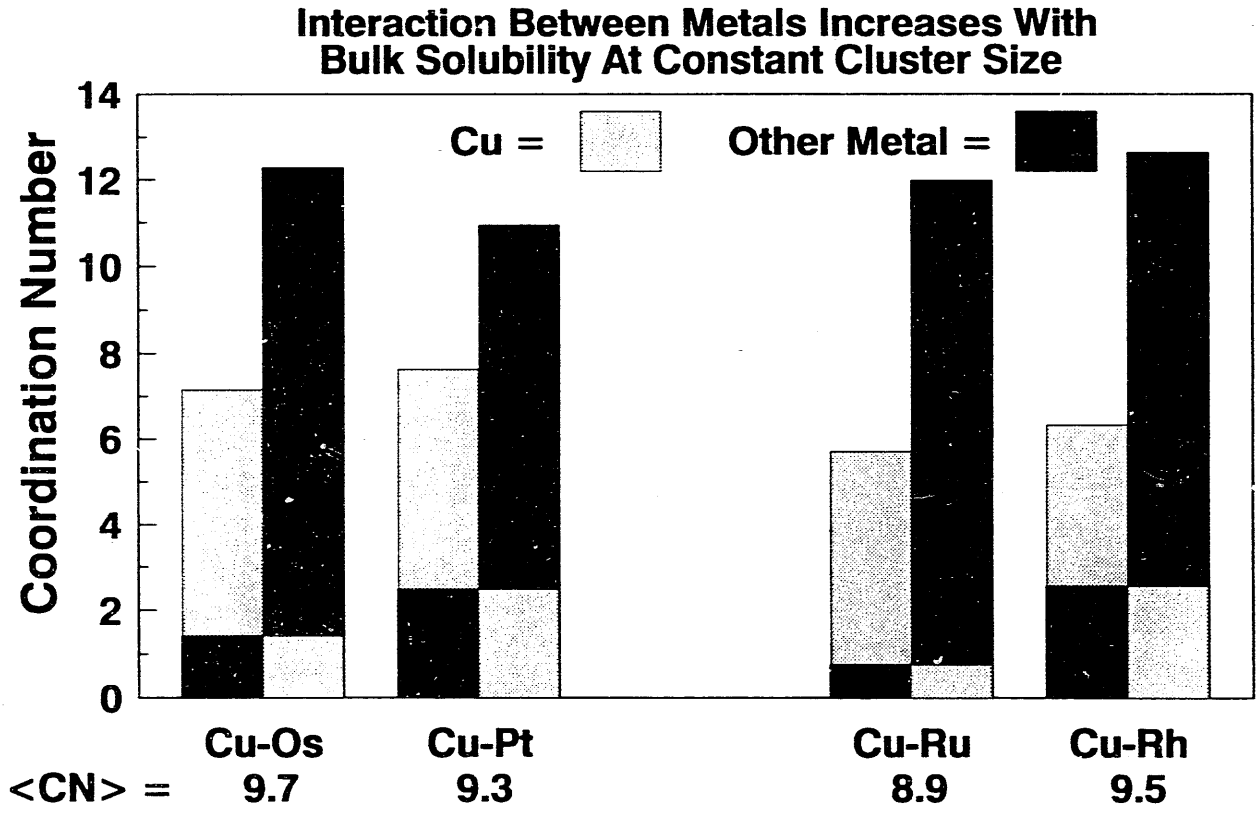

Figure 7

The Effect of Cluster Size Can Obscure The Effect of Solubility On Structure

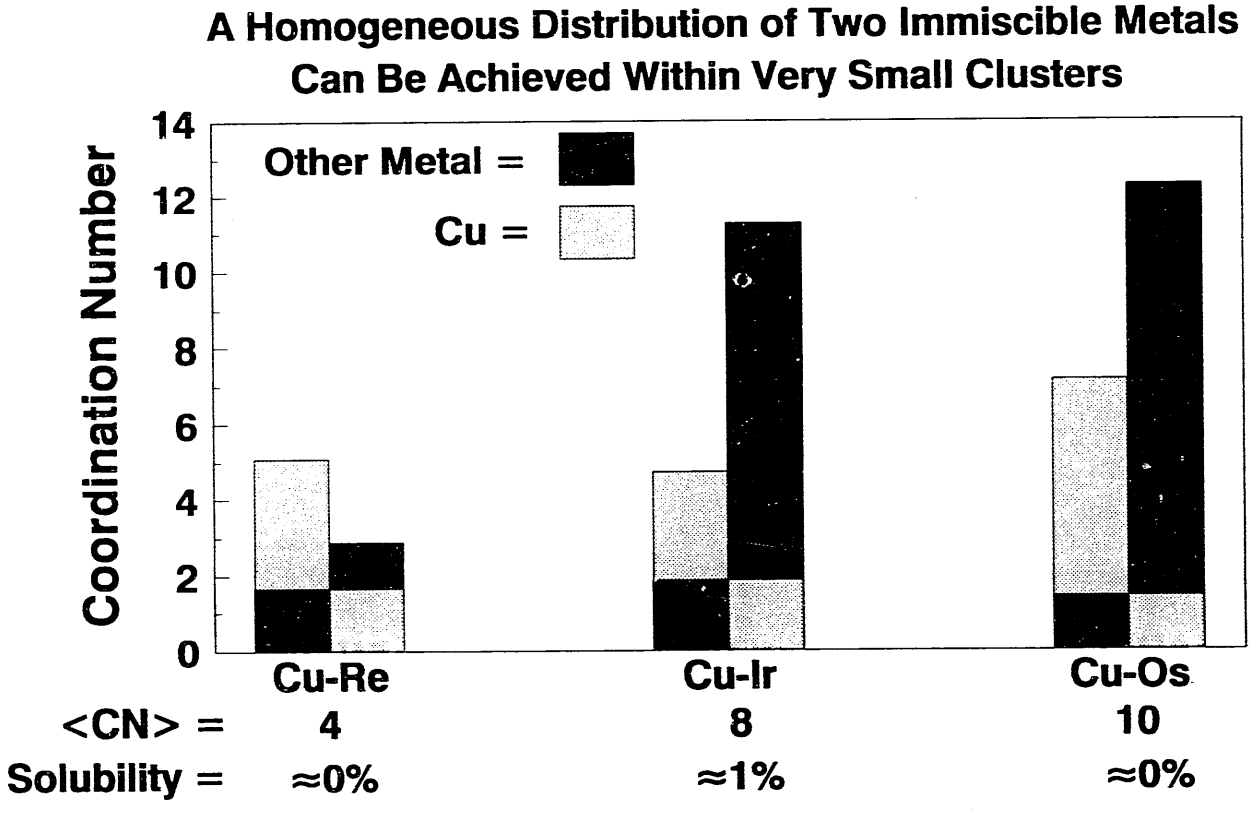

Figure 8

Method of Preparation and Support Influence Cluster Structure

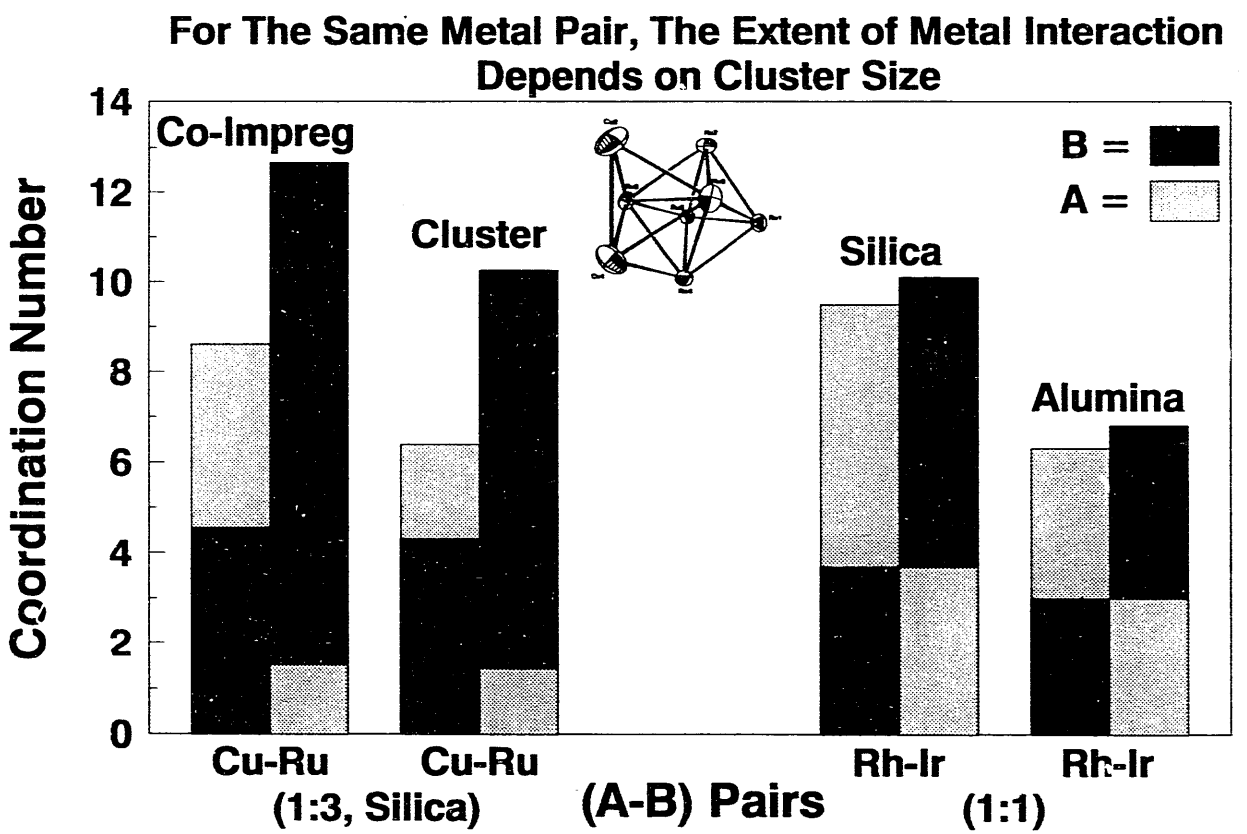

Figure 9

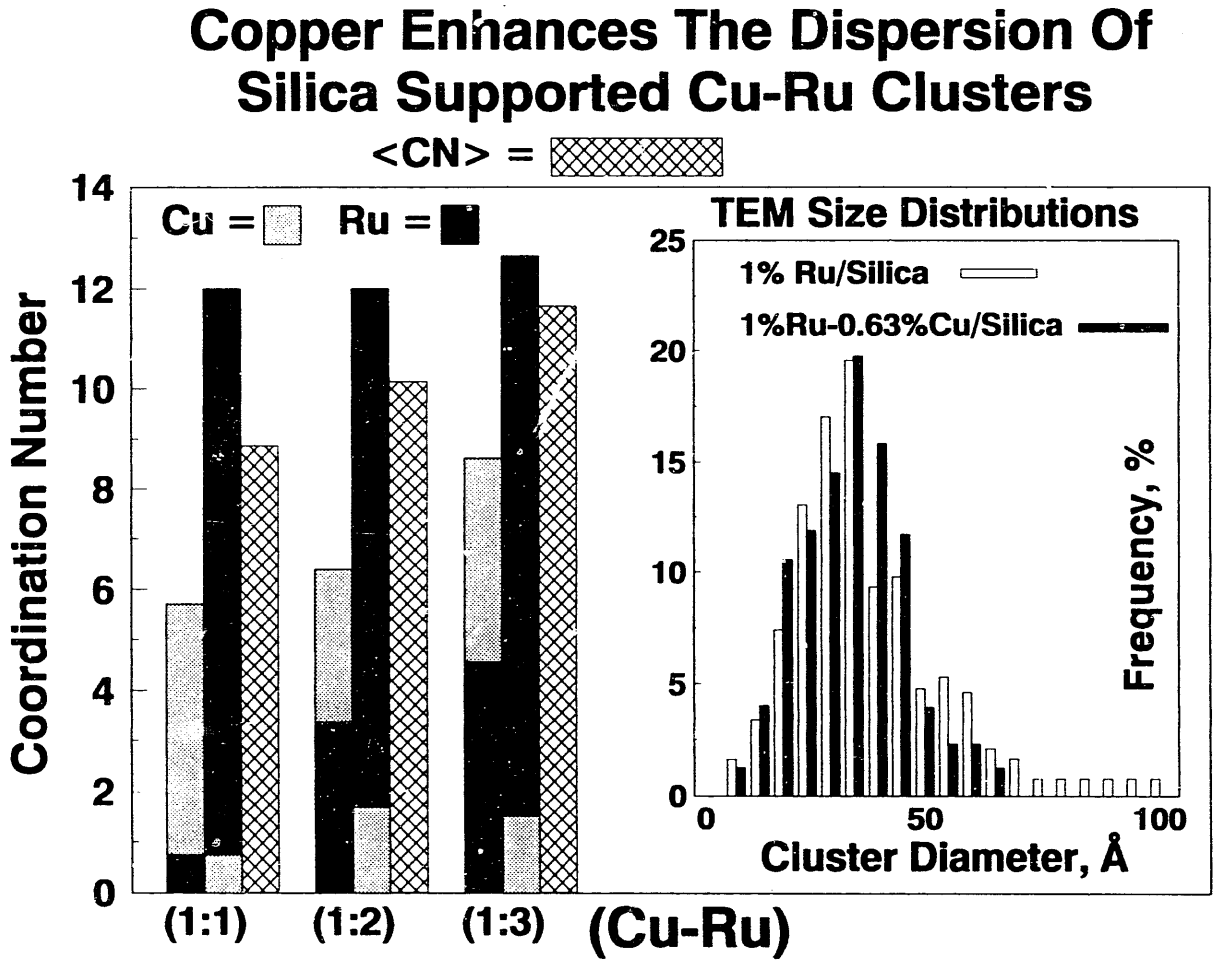
Copper Enhances The Dispersion Of Silica Supported Cu-Ru Clusters
<CN> =
Cu =
Ru =
Coordination Number
14
12
10
8
6
4
2
0
(1:1)
(1:2)
(1:3)
(Cu-Ru)
TEM Size Distributions
1% Ru/Silica
1%Ru-0.63%Cu/Silica
25
20
15
10
5
0
0
50
100
Cluster Diameter, Å
Frequency, %

Figure 10

EXAFS CHARACTERIZATION OF SUPPORTED METAL CATALYSTS IN CHEMICALLY DYNAMIC ENVIRONMENTS

Heinz J. Robota
Allied-Signal Research and Technology
50 E. Algonquin Road, Box 5016
Des Plaines, IL 60017-5016

1. Introduction

Characterization of catalysts focusses on the identification of an "active site" responsible for accelerating desirable chemical reactions. The identification, characterization, and selective modification of such sites is fundamental to the development of structure-function relationships. Unfortunately, this goal is far from realized in nearly all catalysts, and particularly in catalysts comprised of small supported metal particles. X-ray absorption spectroscopy (XAS) has had a dramatic effect on our understanding of supported metal particles in their resting state. Information on changes in the electronic structure of the active species is often available through near edge structure and information on particle composition, size, etc. can typically be extracted from the extended fine structure. However, the performance of a catalyst can not be assessed from such simple resting state measurements. Numerous factors affect performance, and an appreciation for the chemical consequences of these additional factors must be developed as we strive to develop a comprehensive understanding of operating catalysts. Among the factors which influence catalyst performance are the exact catalyst composition, including the support and any modifiers; particle size; catalyst finishing and pretreatment conditions; pressure, composition, and temperature of the operating environment; time. Gaining an understanding of how the structure of a catalytic site can change with such an array of variables requires that we begin to develop measurement methods which are effective under chemically dynamic conditions.

Ideally, it should be possible to obtain a full X-ray absorption spectrum of each element thought to have a causal relationship with observed catalyst properties. From these spectra, we can optimally extract only a relatively limited amount of information which we must then piece together with information derived from other characterization methods and intuition to arrive at a hypothetical structure of the operating catalyst. Important chemical contacts or bonds can be extracted from observed backscattering amplitudes and phase shifts. Similarly, bond lengths or distances among components can be extracted. However, as the number of contacting constituents increases, our ability to extract reliable information decreases. Also, there remain unresolved questions as to exactly what types of peripheral neighbors one can expect to detect by XAS. This is particularly true when atom pairs may only be separated by a few Å but not bonded to one another. Also related to the chemical structure of the active site are the relative coordinations of atoms about one another which can also be extracted from the fine structure data. Information about crystallinity, homogeneity, and general disorder can be obtained from the Debye-Waller factor. Finally, through analogy with known compounds, the electronic structure of the active atoms can be inferred from near edge absorption features.

Clearly, we are faced with reconstructing a complex system from a very limited amount of information. The challenge to the experimentalist is further heightened by the practical considerations of a chemically dynamic environment. Reactors in which reasonable samples in a meaningful form can be exposed to reactive gases under appropriate reaction conditions (pressure, temperature, flow rates) while still remaining compatible with the constraints of X-ray absorption measurements are a clear requirement. The already constrained XAS information is further diluted through thermal motion of correlated atoms at elevated temperatures. This is potentially amplified by reconstruction or reorganization of the active centers as reactive gases adsorb, react, and again desorb. Sample homogeneity will also likely be affected as reactant/product concentrations vary throughout the sample. Adding to these difficulties is the potentially different time scales of the chemical reactions and the time required to obtain meaningful data.

With such a list of caveats, it is not surprising that the number of experiments reported under chemically dynamic conditions is limited. Nevertheless, simple chemical interactions have been investigated for some time, and interest in using XAS to characterize these interactions appears to be growing. Also, there is slow progress being made in conducting XAS measurements on catalysts under operating conditions. In an effort to point out the value of examining catalysts under such chemically dynamic conditions, I will present several examples beginning with relatively simple effects of single adsorbates, through the action of surface reactions, on to full operating conditions, with a final description of a system allowing measurements under "real time" continuous conditions.

2. Examples of Measurements Under Chemically Dynamic Conditions

The Effects of CO Adsorption

In situ infrared spectroscopic (IR) measurements following adsorption of CO onto ultra-dispersed $Rh/\gamma\text{-}Al_2O_3$ catalysts had been shown to produce $Rh\text{-}(CO)_2$ species which were characterized as isolated species. This interpretation suggested that either the Rh was initially present as isolated atoms or that the action of CO on ultra-small Rh particles led to the disruption of the particles with the production of the species observed by IR. In the early 1980s, Koningsberger, Prins, and co-workers applied XAS to investigate this question[1,2]. Examination of the freshly prepared ultra-dispersed $Rh/\gamma\text{-}Al_2O_3$ catalyst clearly revealed the presence of small metallic Rh crystallites. Thus, the notion that individual Rh atoms might be present initially was clearly demonstrated to be incorrect. Upon exposure of the catalyst to CO at 100 kPa at room temperature, a distinct change in the EXAFS is observed. The characteristic oscillations at values of $k > 5$ Å^{-1} are sharply reduced in amplitude, suggesting the loss of Rh-Rh correlations. These initial qualitative assessments were indeed borne out by a detailed quantitative analysis. Severe disruption of the ultra-small Rh particles had indeed taken place, with new features due to the C and O atoms of adsorbed CO. Even at room temperature, CO was shown able to break up the Rh particles. This disruption allowed for a consistent interpretation of the end product, the geminal dicarbonyl species observed by IR.

While adsorption at room temperature was able to disrupt most of the Rh

particles, some Rh-Rh correlation remained. Adsorption at 523 K however, led to complete loss of the residual Rh-Rh correlation, suggesting complete disruption of the particles. Exactly how far removed from one another the Rh atoms are after such a disruption is unfortunately not available from the EXAFS result. Once the correlations are lost, we lose all information about the mutual interactions of the surface species. However, upon exposing the disrupted catalyst to H_2 at 523 K, not only did Rh particles reform, but reformed with sizes much greater than were initially present. This, sintering of the particles took place, even under thermally mild conditions. These results clearly demonstrate how chemically dynamic conditions can lead to states of a catalyst not produced by simple preparative procedures.

In an interesting follow-up to the work of Koningsberger and Prins, Johnston *et al.*[3] recently reported results for a $Rh/\gamma\text{-}Al_2O_3$ catalyst under a combined H_2/CO gas mixture typical of those used in Fishcer-Tropsch synthesis. As a control, they initially checked the effects of CO alone, and obtained results in agreement with those of Koningsberger, Prins and co-workers. However, upon exposing the catalyst to the mixed gas stream at 373 K, only metallic Rh particles are observed. Under the conditions used, catalytic conversion of the gases was not taking place. However, it is interesting to note that the simultaneous presence of CO and H_2 appears to prevent the particle disruption induced by CO alone.

Prompted by the effects of CO on highly dispersed Rh catalysts (which are observed for other supports in addition to $\gamma\text{-}Al_2O_3$), Sachtler and co-workers investigated the influence of CO on the structure of ultra-small Pd particles in a Y-zeolite matrix[4]. As for the freshly prepared Rh catalysts discussed above, the fresh Pd/Y-zeolite catalyst exhibited EXAFS characteristic of very small Pd particles. However, following exposure to 100 kPa of CO at room temperature, unambiguous evidence for considerable particle growth is observed. Previous IR results on this system had led to the suggestion that a Pd_{13} carbonyl cluster is formed following the CO treatment. While the EXAFS can not confirm this result, an increase in particle nuclearity is unambiguously observed. Unlike the CO/Rh case, no evidence for C and O coordination was reported. This may be due to only weak CO adsorption in this system, resulting in proportionately low CO/Pd coverage following the He purge prior to EXAFS measurements. Clearly, measurements in a fully *in situ* experiment would contribute to our understanding of the behavior of Pd under these chemically dynamic conditions.

Titration of Adsorbed O by H_2 on Highly Dispersed $Pt/\gamma\text{-}Al_2O_3$

Exposure of highly dispersed precious metal catalysts to O_2 at room temperature is known to result in surfaces covered with chemisorbed O atoms. Further, the metallic character of the particles, demonstrated by strong metal atom pair correlations is disrupted somewhat. These findings are in some ways similar to the action of CO on highly dispersed Rh catalysts, where both metal-adsorbate and metal-metal coordination are detectable by EXAFS. This is demonstrated for a 0.38% $Pt/\gamma\text{-}Al_2O_3$ catalyst following a one minute exposure to air at room temperature in Figure 1. Prior to air exposure, the phase and amplitude corrected transform exhibits a single peak characteristic of Pt-Pt nearest neighbor interactions. Following air exposure, the Pt-Pt intensity is reduced and a shoulder at shorter distance can be identified as Pt-O coordination. Similar results were reported previously for Pt/SiO_2 catalysts[5].

Removal of these chemisorbed O atoms by H_2 is one basis for making dispersion determinations. Following brief exposure of the O covered catalyst to a H_2 stream, still at room temperature, not only is the O removed, but the metal particles undergo an apparent severe reorganization[6]. This is shown in Figure 2 where the Fourier transforms of the initially prepared and room temperature titrated EXAFS measurements are shown. Following titration, not only has the nearest neighbor Pt-Pt correlation increased, but clear evidence for more distant coordination shells is also seen.

These results are suggestive of the sintering observed in the $Rh/\gamma\text{-}Al_2O_3$ case following removal of CO by H_2. However, elevated temperatures were required in the Rh case. Also, this particle reorganization appears to be reversible. Upon heating the titrated catalyst to 500°C in only a H_2 stream, the EXAFS returns to that of the fresh catalyst. Higher shells disappear and the nearest neighbor signal again diminishes. Rather than particle sintering, these results are suggestive of order-disorder transformations, probably driven by metal-support interactions and the very high surface free energy of very small metal particles. By sacrificing order in the metal particle, the Pt atoms may increase their contact with the support, thus lowering their degree of coordinative unsaturation. Upon exposure to O_2, stronger chemisorption bonds are formed, weakening the interaction with the substrate. Following titration, the particles remain covered with H atoms. However, upon heating, the adsorbed atoms can desorb and sufficient thermal energy is available to allow the atoms within the particle to again establish contacts with the support. Unfortunately, attempts to detect the metal atom-support contacts have thus far been unfruitful.

These observations of particle reorganization have potential impact on questions concerning the nature of reactive sites on highly dispersed metal catalysts. If changes in particle morphology occur under reaction conditions, in effect creating the important site only in the presence of the reactants, then no amount of characterization under static conditions will reveal these critical structures.

$Pt/\gamma\text{-}Al_2O_3$ under Reaction Conditions: CO Oxidation

Thus far, examples have dealt with the effects of individual adsorbates or stoichiometric reactions on the properties of supported metal catalysts. However, under full catalytic operation, the catalyst is simultaneously exposed to multiple gases. Also, while single step reaction measurements allow one to cool the sample after each step so as to improve the EXAFS signal quality, most relevant catalytic processes require temperatures above ambient. We have recently been investigating the properties of Pt particles engaged in the oxidation of CO to CO_2 by O_2 under fully *in situ* conditions[7]. Surface sensitivity is afforded through small particles demonstrated by a dispersion of 85%.

It is instructive to compare the structure of the catalyst under several reference conditions, as shown in Figure 3, with other previous measurements. As received, the catalyst is under ambient conditions and has been exposed to air for several years. The EXAFS and Fourier transforms under these conditions bears little similarity to a reduced catalyst exposed briefly to O_2. Rather, the dominant signal is due to Pt-O coordination. Essentially no evidence remains for Pt-Pt correlations. These results are again similar to

the observations following CO adsorption on Rh. However, the absence of Pt-Pt correlation does not coincide with complete disruption of the small particles. This is demonstrated by TEM observations which reveal a multitude of particles with diameters between 9 and 15Å. Thus, the absence of Pt-Pt features appears more likely due to a broad distribution of Pt-Pt distances and poor correlation of Pt-Pt positions, effectively quenching the EXAFS and limiting the amount of information we can derive.

Following treatment in H_2, measurement at 100°C clearly reveals the re-establishment of metallic Pt particles. Similarly, treatment of either an as received catalyst with only a CO/He stream at elevated temperature or exposing a H_2 treated catalyst to this stream results in a catalyst state with EXAFS which differs little from the simple reduced state. This is despite the fact that CO must now completely cover the catalyst particles. Note that neither particle disruption nor particle growth takes place on these catalysts under these CO containing atmospheres. Finally, if the reduced catalyst is treated in a stream of O_2/He at 200°C, a catalyst state essentially indistinguishable from the as received state results.

With these reference measurements as guides, we can now turn our attention to measurements made during actual catalyst operation. Despite the simplicity of the reaction, much has yet to be learned about the microscopic details which control net reaction rates. A wide range of CO/O_2 ratios was examined while trying to keep the net CO conversion level around 30%, so as to not deplete all of the reactants. This required changing both the O_2 concentration and temperature while holding the CO flow rate constant. Roughly speaking, kinetic analyses of CO oxidation by O_2 indicate a first order dependence in O_2 partial pressure and an inhibitory negative first order dependence on CO. This would suggest that CO covers the catalyst surface and that the rate of reaction is controlled by the ease with which O_2 can get onto the surface. IR measurements are generally in agreement with such a description. Thus, we might anticipate a mixture of metallic looking and O covered Pt particles.

Results of the *in situ* measurements under full operating conditions are shown in Figure 4. By comparing with the reference states of the catalyst, it appears that under most of the conditions employed, the Pt surface is covered by O. This is revealed in EXAFS and Fourier transforms which are quite similar to those obtained on the as received catalyst or following treatment in O_2 only. Only when the CO/O_2 ratio becomes strictly stoichiometric does the catalyst exhibit CO covered Pt particle EXAFS. However, the interpretation of these results may not be so simple and transparent. Just as in the case of the as received catalyst or following O_2 treatment, the quantitative fit of the observable EXAFS to Pt-O coordination is not satisfactory. Poor fit quality, low coordination number, and high disorder factors are found for all of these measurements. As noted above, this may be indicative of "hidden" Pt-Pt coordination which the structure of the particles prevents us from revealing by EXAFS. Clearly, further work in this emerging area will need to be done to resolve these questions. Nevertheless, these initial results are encouraging in that they demonstrate that meaningful measurements can be made under moderately severe operating conditions.

Real Time XAS Measurements

Even when operating under chemically dynamic conditions, most catalysts face a steady stream of reactants converting to products at some fixed temperature. The dynamics of the system are embodied in the chemical conversions which take place on very short time scales distributed throughout the catalyst bed. However, some chemical systems have an intrinsic temporal element which the steady-state measurements described thus far can not address. For example, conditions can be established which will cause the oxidation of CO to undergo oscillatory behavior with periods ranging from less than one second to minutes. In order to probe whether catalyst changes during such oscillatory oxidation are cause or effect, it would be ideal to obtain a full EXAFS spectrum on a time scale shorter than the chemical oscillation period. Similarly, when catalysts are treated during their preparation, rejuvenation, or as they respond to changes in operating conditions, fully time resolved chemical and structural information would potentially provide greater insight into how the microscopic changes affect a catalyst's macroscopic properties.

Development of beamlines capable of providing this type of information has been in progress for some time[8]. These time resolved XAS instruments are based on the combined dispersive and focussing properties of bent monochromator crystals. By using a triangularly shaped, thin single crystal, an optical element of appropriate curvature can be produced by holding the long side of the triangle fixed while pushing behind the point. A broad white X-ray beam striking the surface of such a bent crystal encounters a slowly changing angle of incidence causing diffraction of slightly different energies at each point along the crystal. These individual rays come to somewhat of a focus where the sample is placed. After the focus, the linear dispersion of wavelengths is converted to an energy spectrum by using a digital detector with finely divided spatial resolution which translates into spectral resolution. By gating the collection system at fixed intervals, complete spectra can be obtained with variable time resolution down to the cycle time of the electronic collection system.

Currently operating systems are limited to a total energy range of roughly 400 eV which makes their applicability to systems requiring full EXAFS scans limited. However, they are ideally suited to examining XANES of systems undergoing oxidation state changes or changes in morphology which are reflected in electronic structure changes. With a time resolution on the order of several ms, spectra can be collected quite rapidly and changes to catalyst properties mapped out as reactions proceed. While a full EXAFS spectrum would be required for any sort of semi-quantitative analysis, qualitative information may still be available from changes to the EXAFS observable at lower energies. For example, in the oscillatory CO oxidation case, the change from O covered surfaces to metallic particles is clearly revealed by the presence or absence of a well defined cleft at roughly 50 eV above the edge. This type of fingerprint could be followed as the operating conditions are adjusted to give oscillatory conversions with varying amplitudes and time scales. Whereas we are currently limited to averaging over these periods, more profound structural or chemical variations in the catalyst particles may be revealed as both reactor and operating conditions are adjusted to more explicitly probe such temporal changes during operation.

Changes in electronic properties of catalytically active atoms may be only subtly revealed by changes in the XANES region of the spectrum. Shifts in edge position can be determined with very high precision, roughly 10 meV, which exceeds our current ability to interpret. However, even without rigorous identification of the structures, either physical or electronic, which give rise to specific spectral changes, it may be possible to qualitatively correlate such observations with changes in catalyst operating characteristics. While far from ideal, such correlations are at the heart of current practice in catalyst development and may open new insights into how one system differs from another under the demanding conditions of actual operation.

3. Conclusions

Attempts to correlate simple static measurements with catalyst properties under demanding operating conditions may not be fruitful as revealed by the often dramatic changes in metallic particles when exposed to even the most benign environments containing active gases. Conclusions based on exposures to single reaction components may not hold when the full complement of reactants are present. The rigor with which chemical and structural information can be obtained under chemically dynamic conditions is compromised by the explicit violation of underpinning assumptions in making quantitative EXAFS analyses. However, the compromise of rigor in favor of qualitative correlation under the more realistic conditions strongly favors the latter. Chemically dynamic environments reveal properties of supported metal catalysts which are not detected by simple static measurements, thus enhancing our overall understanding of these complex systems. Finally, development of new sources and new approaches to making XAS measurements should allow catalyst scientists to more closely tailor their reactors and measurements to obtain specific information under ever more realistic operating conditions. The ambiguity in interpretation, limited rigor, and increased complexity in the composite experimental arrangement are outweighed by the new insights obtainable only under such demanding conditions.

4. References

1) H.F.J. Van't Blik, J.B.A.D. Van Zon, T. Huizinga, J.C. Vis, D.C. Koningsberger, and R. Prins, J. Phys. Chem. 1983, *87*, 2264

2) H.F.J. Van't Blik, J.B.A.D. Van Zon, D.C. Koningsberger, and R. Prins, J. Mol. Catalysis, 1984, *25*, 379

3) P. Johnston, R.W. Joyner, and P.D.A. Pudney, J. Phys.: Condens. Matter 1989, *1*, SB171

4) Z. Zhang, H. Chen, L.-L. Sheu, and W.M.H. Sachtler, J. Catal. 1991, *127*, 213

5) F.W. Lytle, R.B. Greegor, E.C. Marques, D.R. Sandstrom, G.H. Via, and J.H. Sinfelt, J. Catal. 1985, *95*, 546

6) H.J. Robota, M.J. Cohn, A.Z. Ringwelski, and R.A. Eades, Mat. Res. Soc. Symp. Proc. Vol. 111, 1988, 201

7) H.J. Robota, D.J. Liu, S.P. Greiner, R.D. Gonzalez, and Y. Xiong, unpublished results

8) G. Tourillon, E. Dartyge, A. Fontaine, and A. Jucha, Phys. Rev. Lett. 1986, *57*, 603

Phase and Amplitude Corrected Fourier Transforms for Clean and O Covered Pt Catalyst Particles

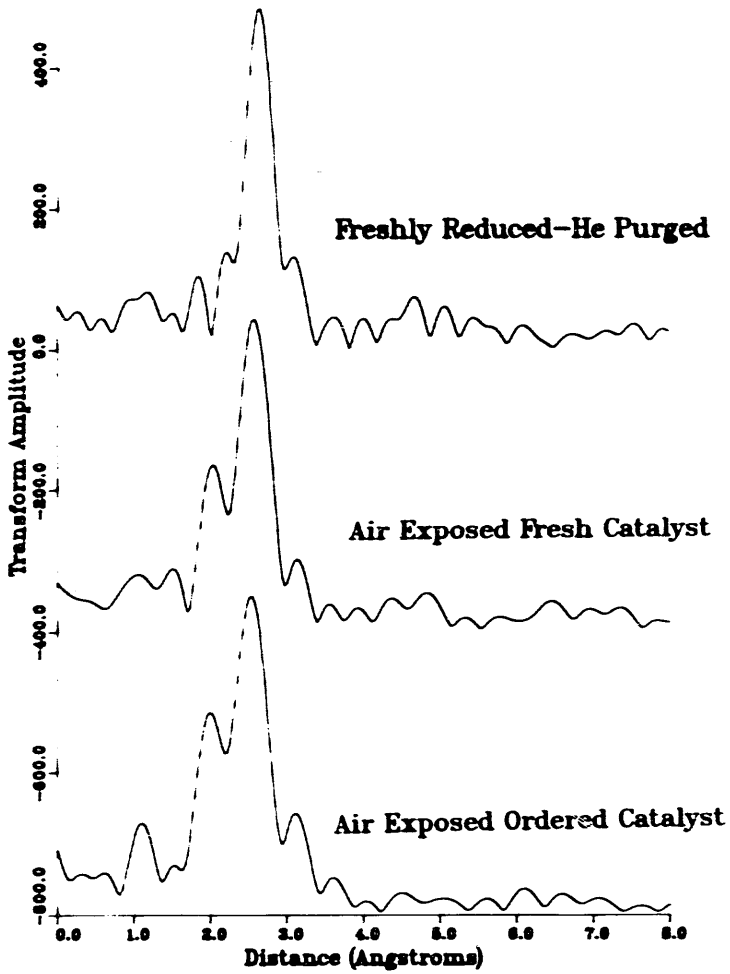

Figure 1

Fourier Transforms (k**3 Weighted) of the Pt Catalyst Following the Different Gas Treatments

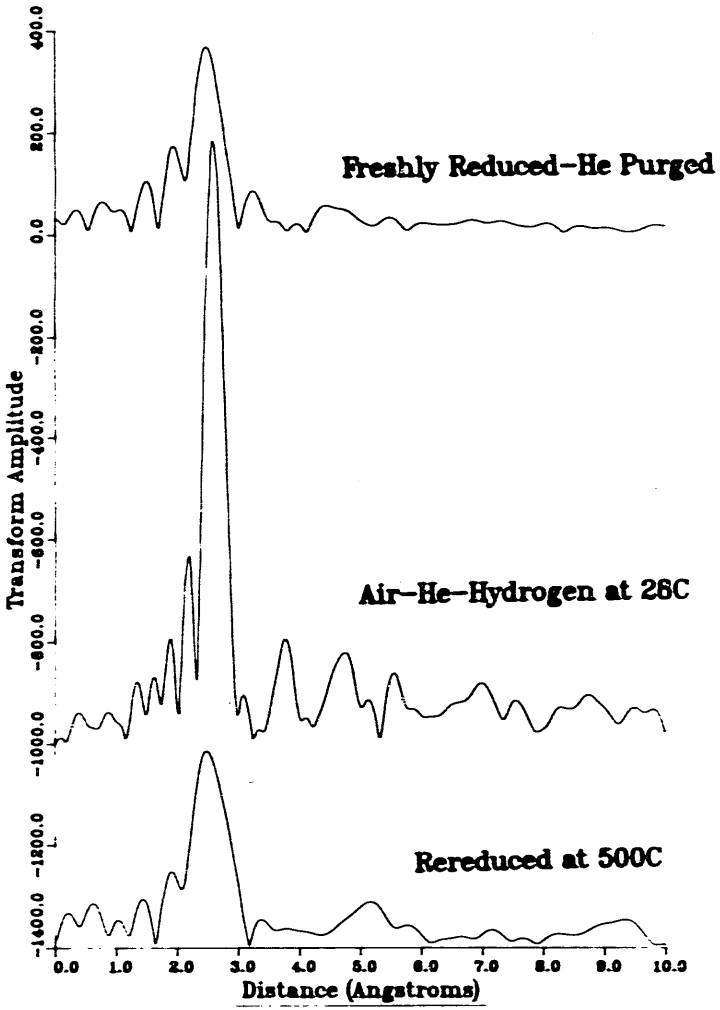

Figure 2

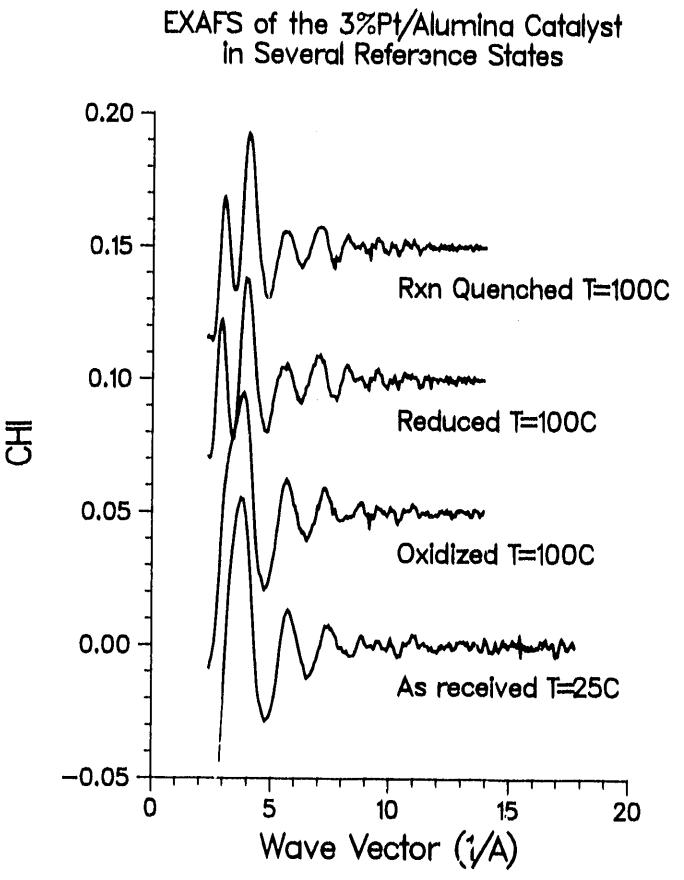
EXAFS of the 3%Pt/Alumina Catalyst
In Several Reference States
0.20
0.15
0.10
0.05
0.00
−0.05
CHI
Rxn Quenched T=100C
Reduced T=100C
Oxidized T=100C
As received T=25C
0
5
10
15
20
Wave Vector (1/A)

Figure 3

A

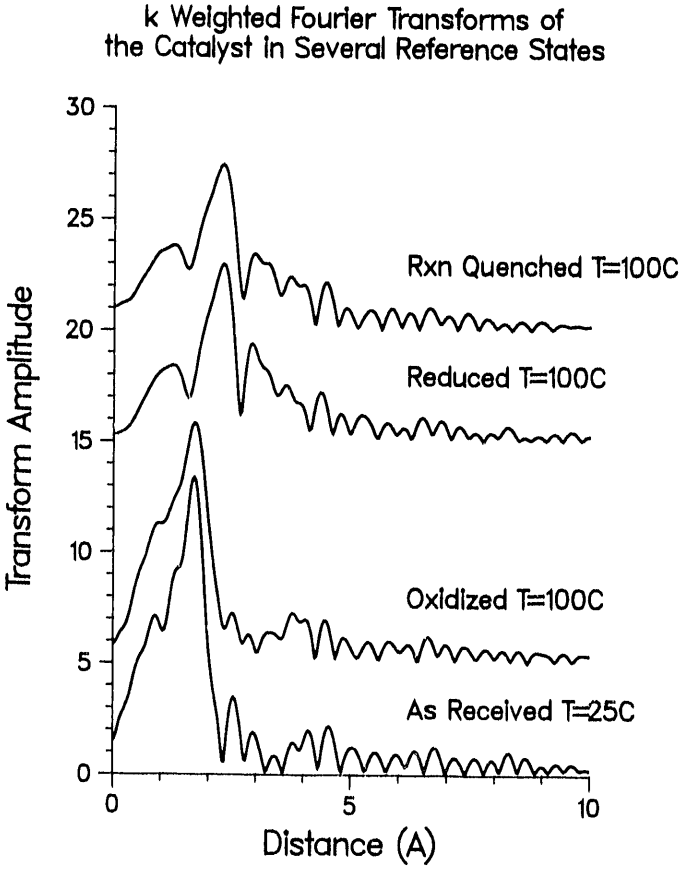
k Weighted Fourier Transforms of
the Catalyst in Several Reference States
30
25
20
15
10
5
0
Transform Amplitude
Rxn Quenched T=100C
Reduced T=100C
Oxidized T=100C
As Received T=25C
0
5
10
Distance (A)

B

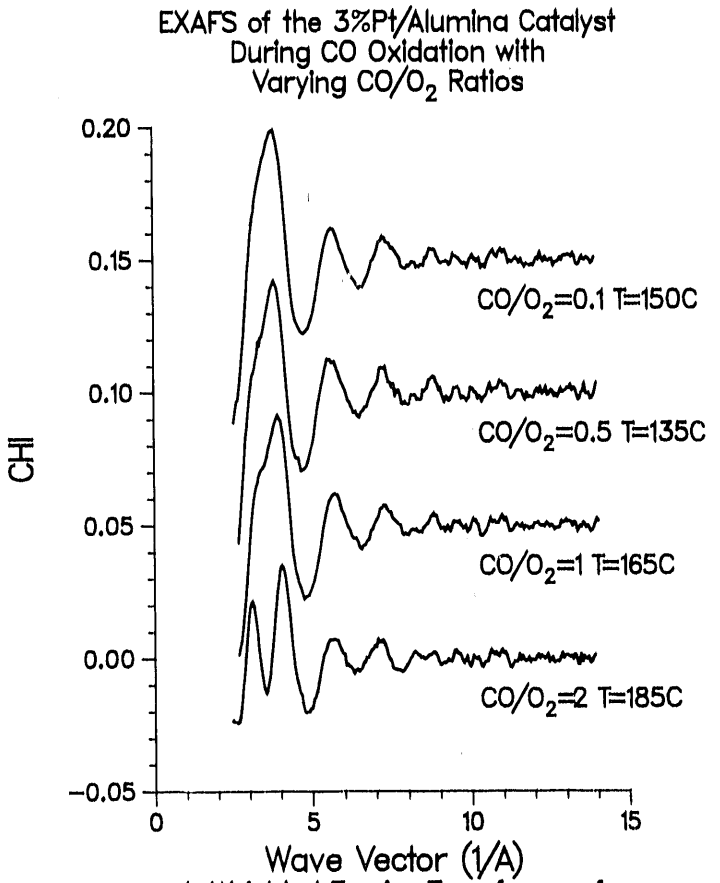
EXAFS of the 3%Pt/Alumina Catalyst
During CO Oxidation with
Varying CO/O2 Ratios
CHI
0.20
0.15
0.10
0.05
0.00
-0.05
0
5
10
15
Wave Vector (1/A)
CO/O2=0.1 T=150C
CO/O2=0.5 T=135C
CO/O2=1 T=165C
CO/O2=2 T=185C

Figure 4

A

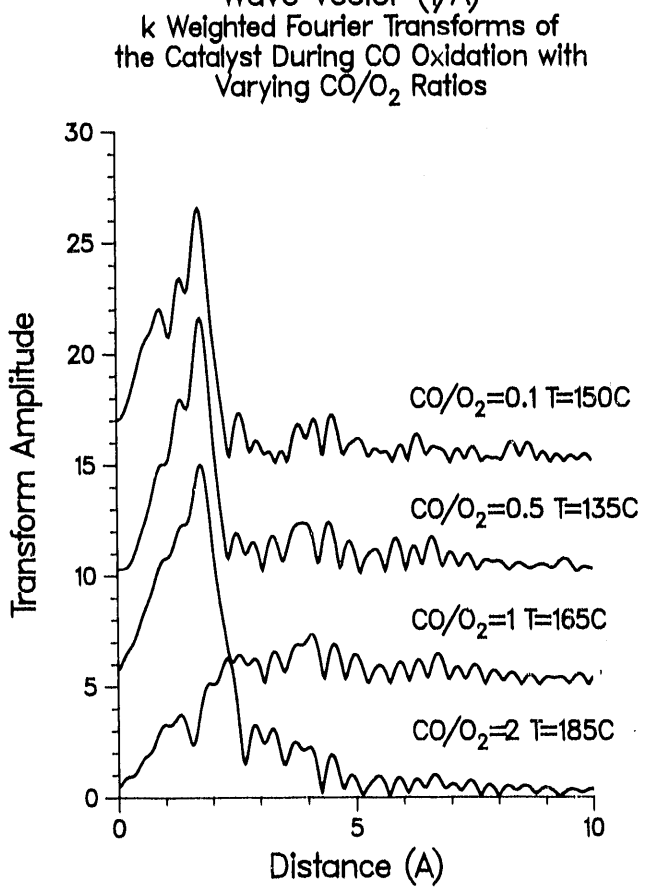
k Weighted Fourier Transforms of
the Catalyst During CO Oxidation with
Varying CO/O2 Ratios
Transform Amplitude
30
25
20
15
10
5
0
0
5
10
Distance (A)
CO/O2=0.1 T=150C
CO/O2=0.5 T=135C
CO/O2=1 T=165C
CO/O2=2 T=185C

B

DEEP-UV AND X-RAY MICROLITHOGRAPHY

Michael P. Bohrer
AT&T Bell Laboratories
Murray Hill, New Jersey 07974

1. Introduction To Microlithography

Remarkable progress has been achieved in the miniaturization of electronic devices since the invention of the point contact transistor in 1947. Although the overall size of integrated circuit chips has not changed significantly over the years, the number of interconnected active components (transistors, diodes, etc.) in a single silicon device have grown from 250 in 1965 to over 32,000,000 by 1990. This improvement has come about through a decrease in the size of the circuit elements. Device feature sizes have decreased from >20 μm in 1963 to <0.6 μm at the present. Figure 1 shows the minimum feature size versus year commercialized for MOS circuits.

The three dimensional circuit elements are fabricated by a series of processes collectively known as "lithography". A silicon device wafer is first coated with a thin polymeric film known as a resist. A pattern is generated in this resist film by exposing it to a radiation source through a patterned mask. The radiation induces a chemical change in the resist such that in a subsequent step the exposed resist is either more soluble in some developing solvent than the unexposed areas (positive tone resist), or is less soluble (negative tone resist). Following the development step, the pattern is transferred, via techniques such as etching, ion implantation, and/or diffusion, to the underlying substrate. This process is shown schematically in Figure 2.

Although the minimum feature size achievable by a lithographic process is dependent on many factors, including the resist material properties, processing conditions, and hardware limitations, the fundamental resolution is limited by diffraction of the exposing radiation. Standard photolithography techniques, utilizing ultraviolet light in the wavelength region of 300-450 nm, are currently used to produce features as small as 0.6 μm. As diffraction limitations are reached, however, new lithographic strategies usin shorter wavelength radiation will be required to achieve the sub-half micron dimensions required for future generations of devices. As indicated in Figure 3, several strategies are being pursued, including deep-UV photolithography, electron beam lithography, and x-ray lithography. In this talk, I will discuss some of the current research activities and trends in the areas of deep-UV and x-ray lithography. The successful development of a new lithographic technology requires the collaborative efforts of researchers in the fields of of material science, process engineering, hardware design, and device design (Figure 4). Chemical engineering science often plays a key role in material synthesis (including scale-up) and processing of resist materials. The main focus of this talk will be on the development of new resist materials designed specifically to function with deep-UV or x-ray radiation. A characteristic resist development scheme is shown in Figure 5.

2. Deep-UV Microlithography

In recent years, deep-UV exposure tools have been designed and built using KrF excimer laser light sources that have a peak intensity at 248 nm. Conventional photoresists are not appropriate for use with these new deep-UV tools due to deficiencies in sensitivity and absorption properties of the materials. For most resists, the quantum yield is significantly less than 1, and since the new lithographic tools in general have low brightness sources, high sensitivity resists are required. In addition, the absorption of conventional photoresists is too high to allow uniform imaging through practical resist film thicknesses ($\sim$1 μm). Thus new resists and processes will be required after photolithography has reached its limits ($\sim$0.5 μm).

One approach to improving sensitivity involves the concept of chemical amplification pioneered by Ito and Willson[1] which employs the photogeneration of an acidic species that catalyzes many subsequent chemical events such as deblocking of a protecting group or crosslinking of a matrix polymer. The overall quantum efficiency of such reactions is thus effectively much higher than that for the initial acid generation. Researchers at AT&T[2] have developed a deep-UV chemically amplified resist (CAMP) based on poly(t-butoxycarbonyloxy-styrene sulfone) (PTBSS) and photoacid generators such as onium salts or nitrobenzyl esters. The structure of a dinitrobenzyl tosylate ester photoacid generator and the acid generation step are depicted in Figure 6. Following generation of the acid, heating the resist film causes deprotection of the PTBSS, forming an aqueous base soluble hydroxy-substituted polymer (Figure 7). The CAMP resist has demonstrated high sensitivity ($\sim$11 mJ/cm^2) and the capability of 0.35 μm resolution[3]. Current research which is focused on both lithographic process development and scale-up of the synthesis of the PTBSS will be discussed.

3. X-Ray Microlithography

In many laboratories x-ray lithography has been investigated as a possible replacement for photolithography. X-rays with a wavelength of a few angstroms have been used in a proximity exposure format to fabricate features that are $<$0.1 μm. Both synchrotron and laser-based x-ray sources are being actively investigated as candidates for x-ray lithographic production tools. Some of the key features of these types of sources are listed in Figure 8. Although significant advances both in resist chemistry and on the technological aspects associated with exposure hardware have been made, further developments in these areas are still required for x-ray lithography to become a commercial reality. The essential requirements for x-ray lithography as diagramed in Figure 9, include: 1) A mask consisting of a pattern made with an x-ray absorbing material on a thin x-ray transparent membrane, 2) an x-ray source of sufficient brightness in the wavelength range of interest to expose the resist through the mask, and 3) an x-ray sensitive resist material. Recent advances in x-ray resist materials will be the primary focus of this talk.

The conventional approach has been to use resists that were developed for electron beam lithography and use them for x-ray lithography. There is a strong correlation between the sensitivity of the resist system to electron beam radiation and their corresponding sensitivity to x-ray radiation. In general, however, the sensitivity of conventional electron beam resists is not sufficient for economic throughput in an x-ray lithographic system. One approach to increasing the sensitivity of an x-ray resist was recently reported by Novembre and coworkers[4]. They showed that copolymers of 4-t-butoxycarbonyloxy-styrene and sulfur dioxide (PTBSS, as described in Section 2) can be used as sensitive, single component, positive acting resists. It is proposed that x-ray radiation induces polymer main chain scission and that radical species are produced which in turn are responsible for the formation of acidic moieties. Heat treatment then converts the exposed polymer into poly(4-hydroxy-styrene sulfone) which is aqueous base soluble. The above scheme is presented in Figure 10. Lithographic evaluation has demonstrated 0.4 μm resolution using an x-ray dose of only 10 mJ/cm^2.

Alternative approaches for designing x-ray resists such as multi-level schemes and incorporation of atoms with a high absorption cross section for particular x-ray emissions will be described.

References

1. Ito, H. and C. G. Willson, Applications of Photoinitiators to the Design of Resists for Semiconductor Manufacturing, in *ACS Symposium Series* **242,** ed. T. Davidson (American Chemical Society, 1984).

2. Tarascon, R. G., E. Reichmanis, F. M. Houlihan, A. Shugard, and L. F. Thompson, Poly(t-BOC-Styrene Sulfone)-Based Chemically Amplified Resists for Deep-UV Lithography, *Polym. Eng. Sci.* **29,** 850, (1989).

3. Nalamasu, O., M. Cheng, J. M. Kometani, S. Vaidya, E. Reichmanis, and L. F. Thompson, Development of a Chemically Amplified Positive (CAMP) Resist Material for Single Layer Deep-UV Lithography, *Proc. SPIE* **1262,** 32, (1990).

4. Novembre, A. E., W. W. Tai, J. M. Kometani, J. E. Hanson, O. Nalamasu, G. N. Taylor, E. Reichmanis, and L. F. Thompson, Single Component-Chemically Amplified Resist Materials for Electron-beam and X-ray Lithography, *Proc. SPIE* **1466,** (1991).

Figure 1. Minimum feature size versus year of commercialization for MOS devices.

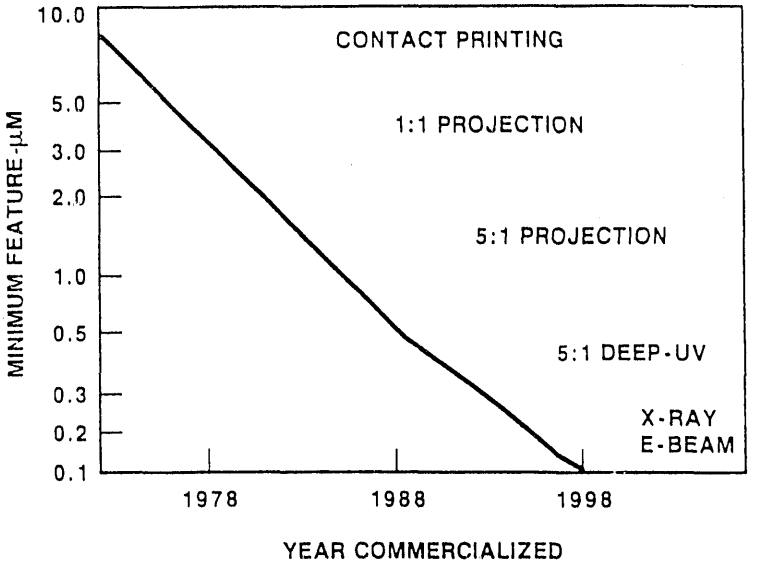

Figure 2. Schematic diagram showing the formation of a polymeric relief image using lithography. The resist pattern is used to subsequently modify the underlying substrate.

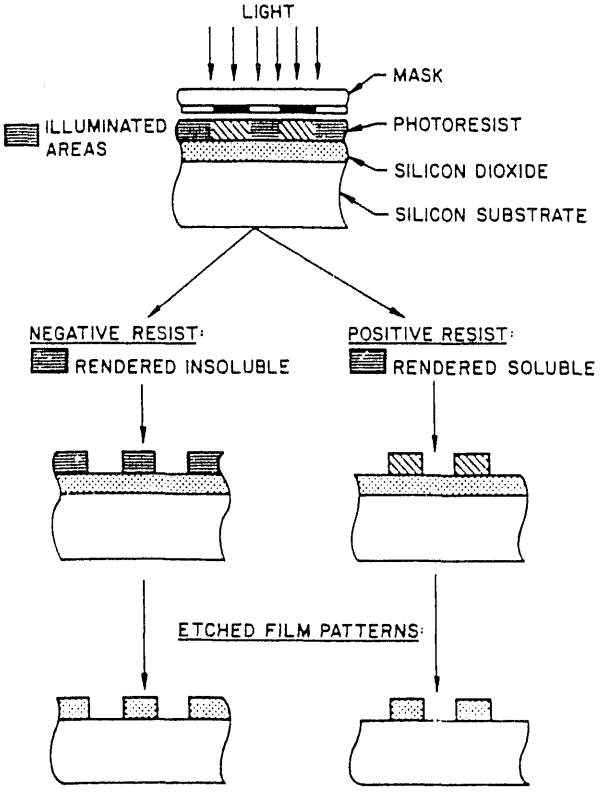

Figure 3. Diagram showing three possible alternatives to conventional photolithography.

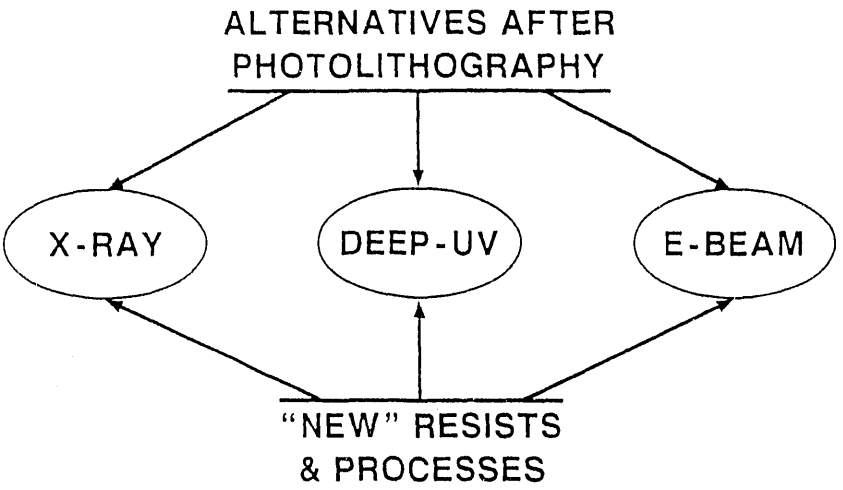

Figure 4. Schematic representation showing the interactions between material science, hardware development, process development, and device design that is required for the successful development of a new lithographic technology.

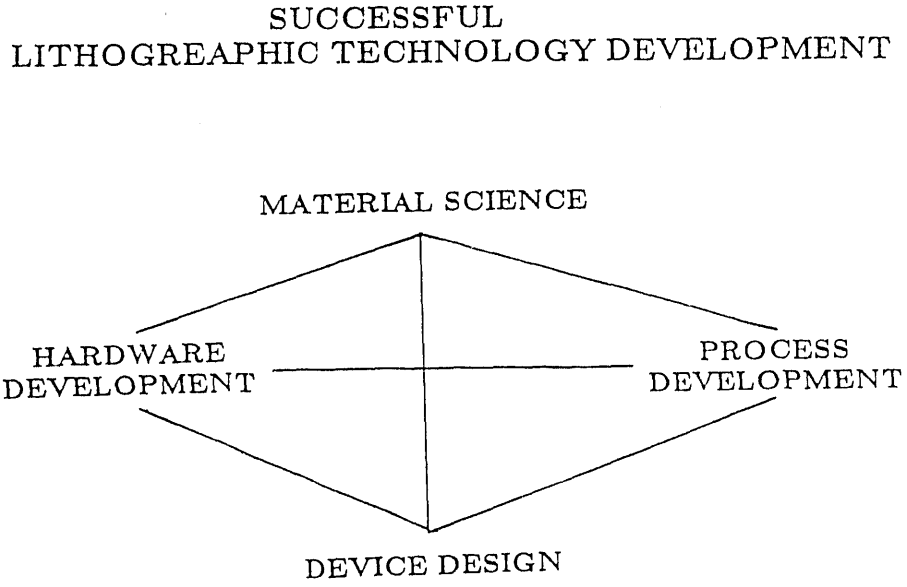

Figure 5. Flow diagram typically followed for the development and commercialization of a new resist material.

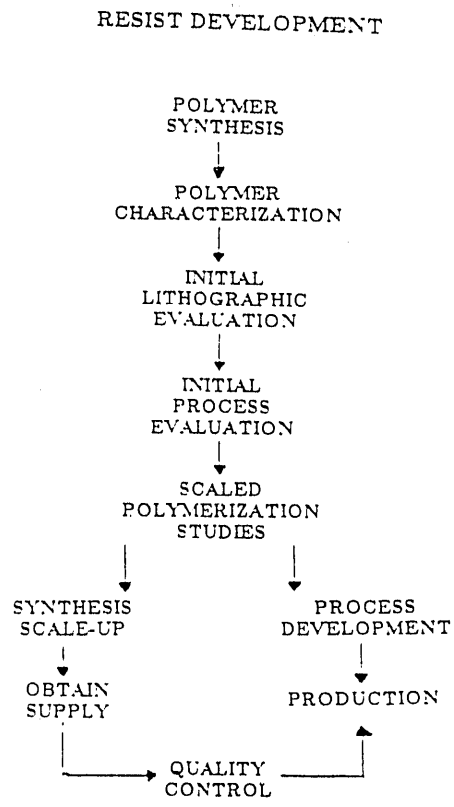

Figure 6. Structure of dinitrobenzyl tosylate ester and the photo-generated tosic acid initiator.

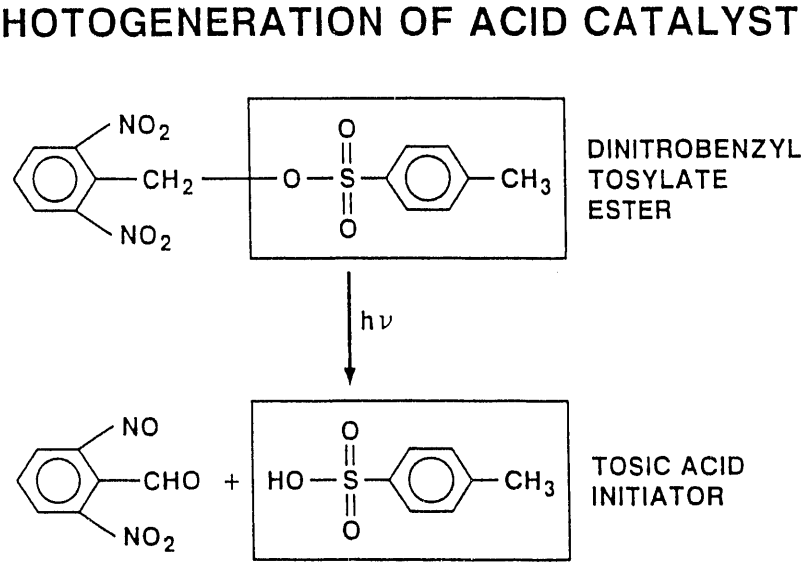

Figure 7. Acid catalyzed deprotection of poly(t-butoxycarbonyloxy-styrene) to form poly(hydroxy-styrene).

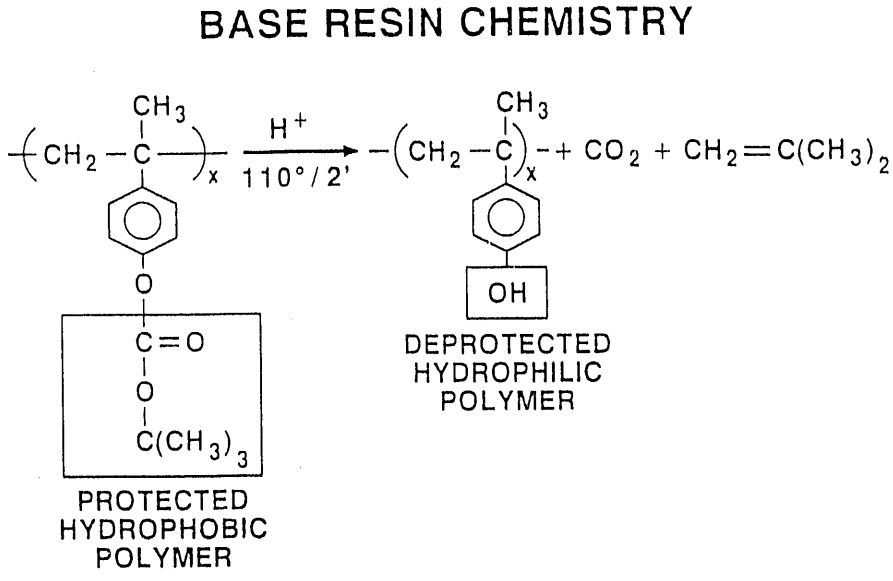

Figure 8. Comparison of synchrotron and laser based x-ray sources.

COMPARISON OF X-RAY SOURCES

PARAMETER	SYNCHROTRON STORAGE RING	LASER BASED X-RAY SOURCE
PEAK (Å)	9	14
ILLUMINATION INTENSITY (mW/cm^2)	50	5-15
COLLIMATION	WELL COLLIMATED	REQUIRES COLLIMATOR
SOURCE VACUUM (Torr)	10^{-8}-10^{-9}	10^{-2}
SYSTEM AVAILABILITY	1990 K. SUSS SUMITOMO	1988 HAMPSHIRE
COST ($M)	40 RING + 3M/STATION	2.5

Figure 9. Schematic diagram of an x-ray lithographic process based on proximity exposure with a collimated source.

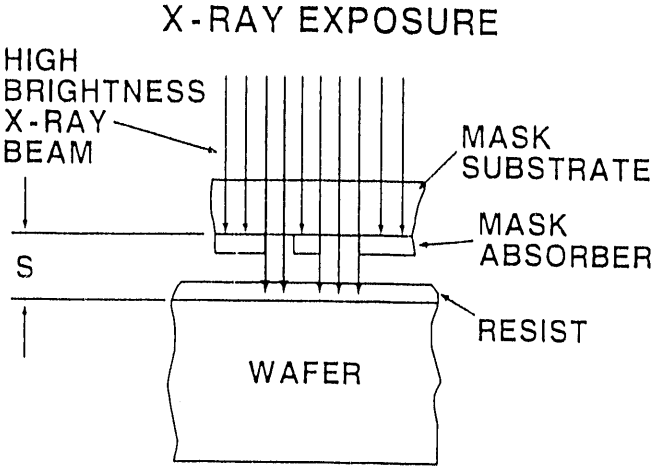

Figure 10. Proposed x-ray radiation induced reaction mechanism for a single component, chemically amplified resist.

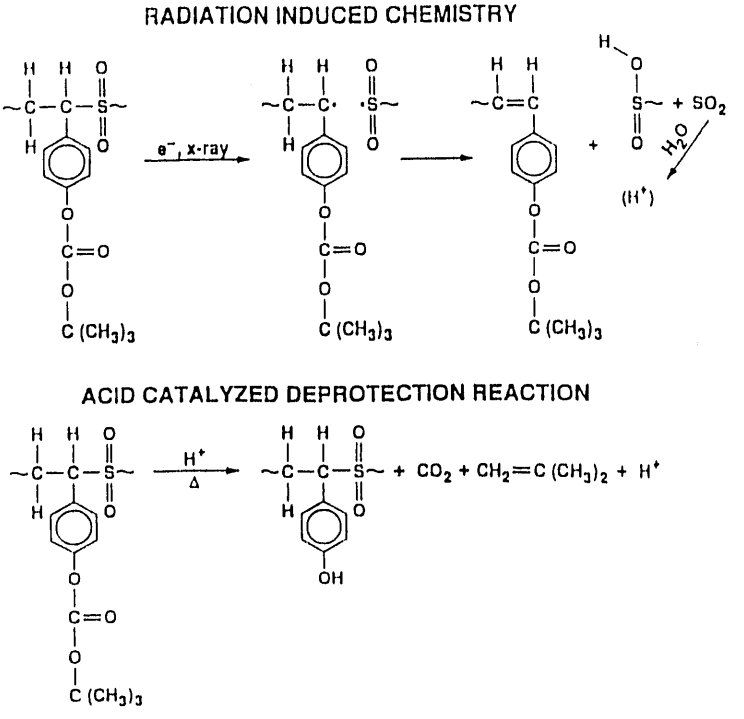

X-RAY MICROIMAGING OF ELEMENTAL COMPOSITION AND MICROSTRUCTURE FOR MATERIALS SCIENCE

Gene E. Ice and Cullie J. Sparks
Metals and Ceramics Division
Oak Ridge National Laboratory
Oak Ridge, TN 37831-6118

1. Abstract

X rays have many advantages over electrons and other charged particles for the microcharacterization of materials. X rays are more efficient in photoejecting inner shell electrons, which results in characteristic x-ray fluorescence. X rays also produce less Bremsstrahlung, which yields a far higher signal-to-background ratio than that obtained with electrons. Minimum detectable limits (MDL) for x-ray excited fluorescence can be a few parts per billion, 10^{-3} to 10^{-5} less than for electron excitation. The third generation synchrotron radiation sources, such as the Advanced Photon Source, will, for the first time, provide x-ray sources as brilliant as the most advanced electron probes. It will, therefore, soon be possible to develop a submicron x-ray probe with unprecedented low levels of detection in diffraction, EXAFS, Auger, photoelectron and fluorescence spectroscopies for structural and chemical characterization. Some applications to materials science are shown.

2. Advantages of an X-ray Probe

We are at the beginning of a revolution in our ability to microimage elemental composition and structure with x rays. This revolution is the result of vastly more brilliant x-ray sources, new developments in x-ray optics and rapidly improving image processing (Fig. 1). The superiority of x rays for imaging internal structure and elemental composition has long been recognized (Figs. 2-3), yet efforts to construct x-ray microprobes have been largely dormant for 30 years due to the overwhelming brightness of electron sources (Fig. 4). With the construction of third generation synchrotron radiation sources, we will, for the first time, have x-ray sources as brilliant as the most advanced electron sources. With simultaneous advances in x-ray optics, it will be possible to deliver the same flux of x rays to a 1 μm^2 spot as with electrons (Fig. 5). The fluorescent signal from each x ray on a sample is typically 10-100 times greater than that from electron or ion excitation (Fig. 6). Even more dramatic is the signal-to-noise ratio, which is typically four to five orders of magnitude greater for x rays than for electrons (Fig. 7). An x-ray microprobe will, therefore, deposit much less power into the sample for the same minimum detectable limit (Fig. 8). Conservative estimates for the detection limits with a 1 μm^2 x-ray microprobe having 10^{14} 8 keV photons/sec far exceed that possible with alternative probes (Fig. 9). An x-ray microprobe will also yield better spatial resolution for thick samples. The ultimate performance

for fluorescence detection will be achieved using crystal spectrometers (Fig. 10). An x-ray microprobe offers several other advantages compared to charged particle microprobes. The most important of these is the ability to make measurements in the presence of air, water, or other gases, and the ability to probe deep into a sample (Fig. 11).

3. Applications of an X-ray Microprobe to Materials Science

An x-ray microprobe on a third generation storage ring will have many important applications to materials science. The low MDL of an x-ray microprobe will be useful in mapping out trace element distributions in inhomogeneous samples. Microprobes using pinholes and solid state detectors are currently capable of detecting 100 ppb of metals in plastic with 10-60 μm diameter probe size (Fig. 12). The extended range of detectability of a third generation x-ray microprobe will be useful in mapping out the elemental distribution in microcircuits, particularly near junction contacts and at interfaces.

Information about elemental distributions near grain boundaries will help elucidate the role of microalloying in altering grain boundary brittle failure (Fig. 13). Similarly at 1 μm resolution, we will be able to study diffusion along interfaces and grain boundaries with remarkable sensitivity. Another interesting problem is the effect of microalloying on radiation-induced swelling.

An x-ray microprobe can be a valuable tool for nondestructive studies of microstructure in composite materials. Some possible applications are the radiographic or tomographic study of nuclear fuel particles (Figs. 14-15), and fiber reinforce composites. Tomographic studies using x-ray fluorescence will be particularly sensitive to trace element distributions.

An x-ray microprobe will be a valuable tool for studying the crystallographic structure at grain boundaries, interfaces, and at composite boundaries. Some early experiments have already demonstrated the usefulness of x rays for studying structure at and near boundaries (Figs. 16-17). Particularly intriguing is the ability to study not only the structure, but also the local strain near cracks, precipitates, flaws, and other features of importance to materials properties.

WE ARE AT THE BEGINNING OF A REVOLUTION IN OUR ABILITY TO MICROIMAGE ELEMENTAL COMPOSITION AND STRUCTURE.

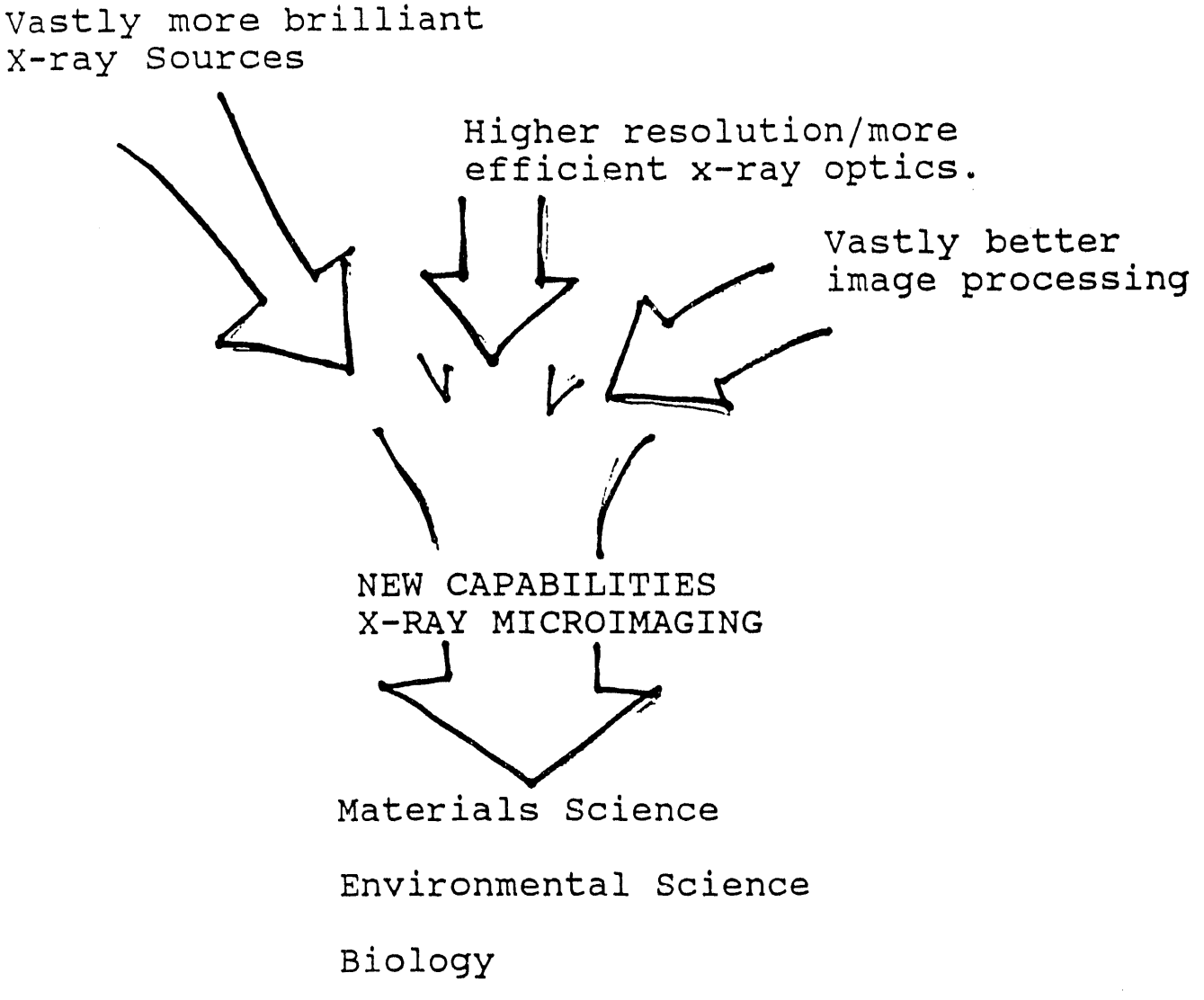

Figure 1

X RAYS ARE MOST DESIRED PROBE

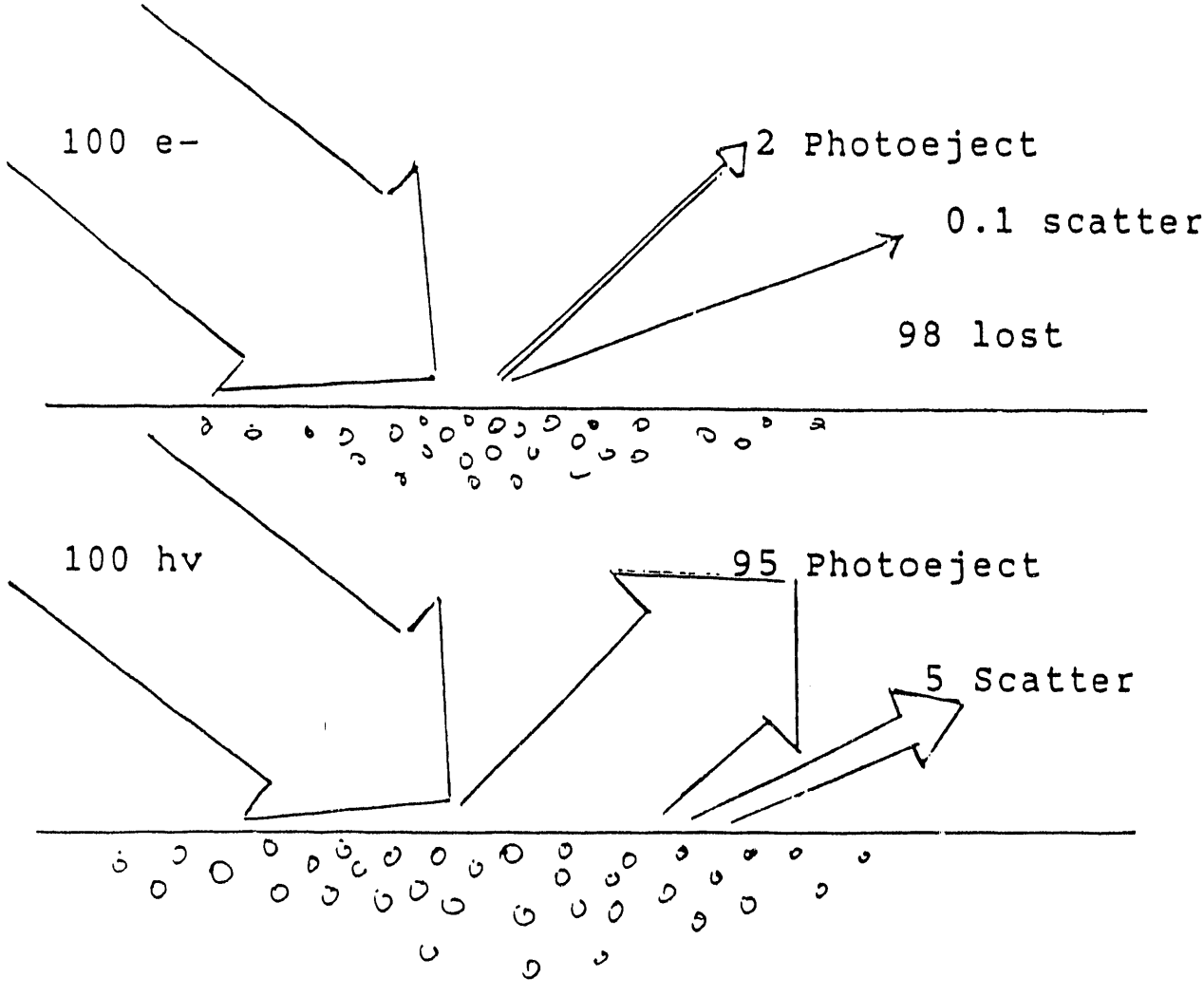

Figure 2

X RAYS: THEIR INTERACTIONS AND RADIATIONS FOR IMAGING

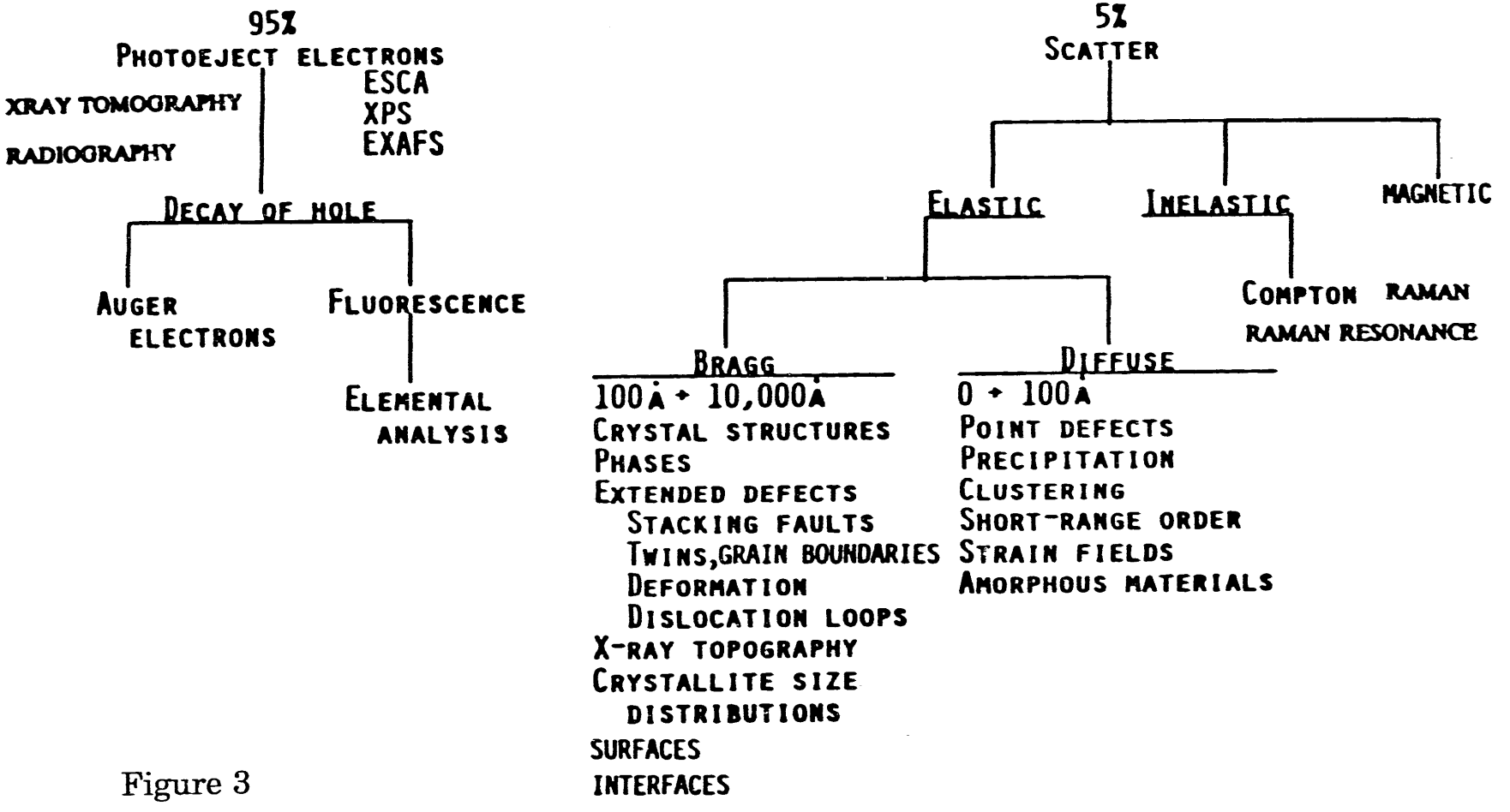

Figure 3

X RAY BRILLIANCE HAS BEEN DOUBLING EVERY 9 MONTHS FOR THE LAST 25 YEARS.

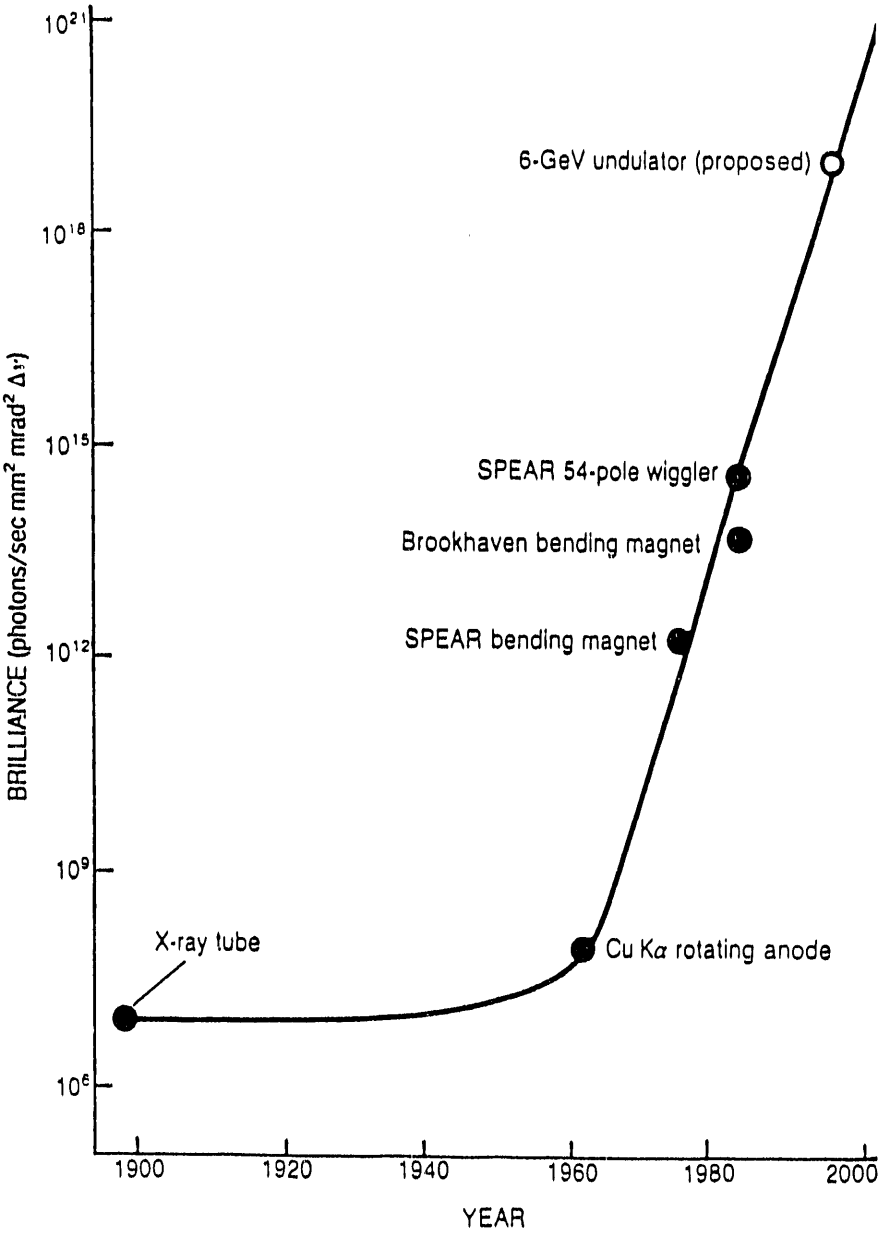

THE ORNL BEAMLINE AT THE NSLS
10^{12} X RAYS/SEC MM^2

APS 10^{15} X RAYS/SEC μM^2

Figure 4

X-RAY OPTICS ARE EVOLVING TO TAKE ADVANTAGE OF SR SOURCE PROPERTIES.

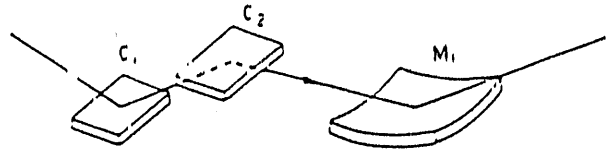

A. NONDISPERSIVE MULTILAYERS OR CRYSTALS FOLLOWED BY ELLIPSOIDAL MIRROR.

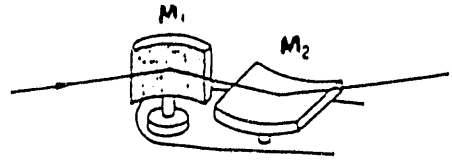

B. CROSSED ELLIPTICAL MIRRORS WITH MULTILAYER ON M_1.

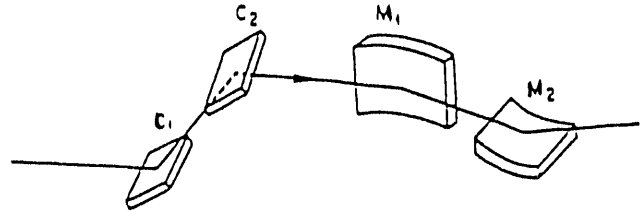

C. NONDISPERSIVE MULTILAYERS OR CRYSTALS FOLLED BY CROSSED ELLIPTICAL MIRRORS.

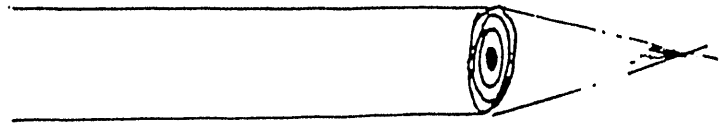

D. ZONE PLATES

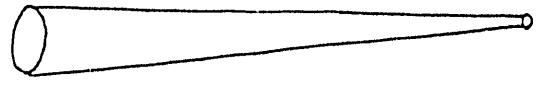

E. GLASS CAPILLARIES.

ANTICIPATE 10^{14} PHOTONS/μM^2/SEC

Figure 5

AN X RAY PRODUCES FROM 10 TO 100 TIMES THE FLUORESCENT SIGNAL PRODUCED BY AN ELECTRON

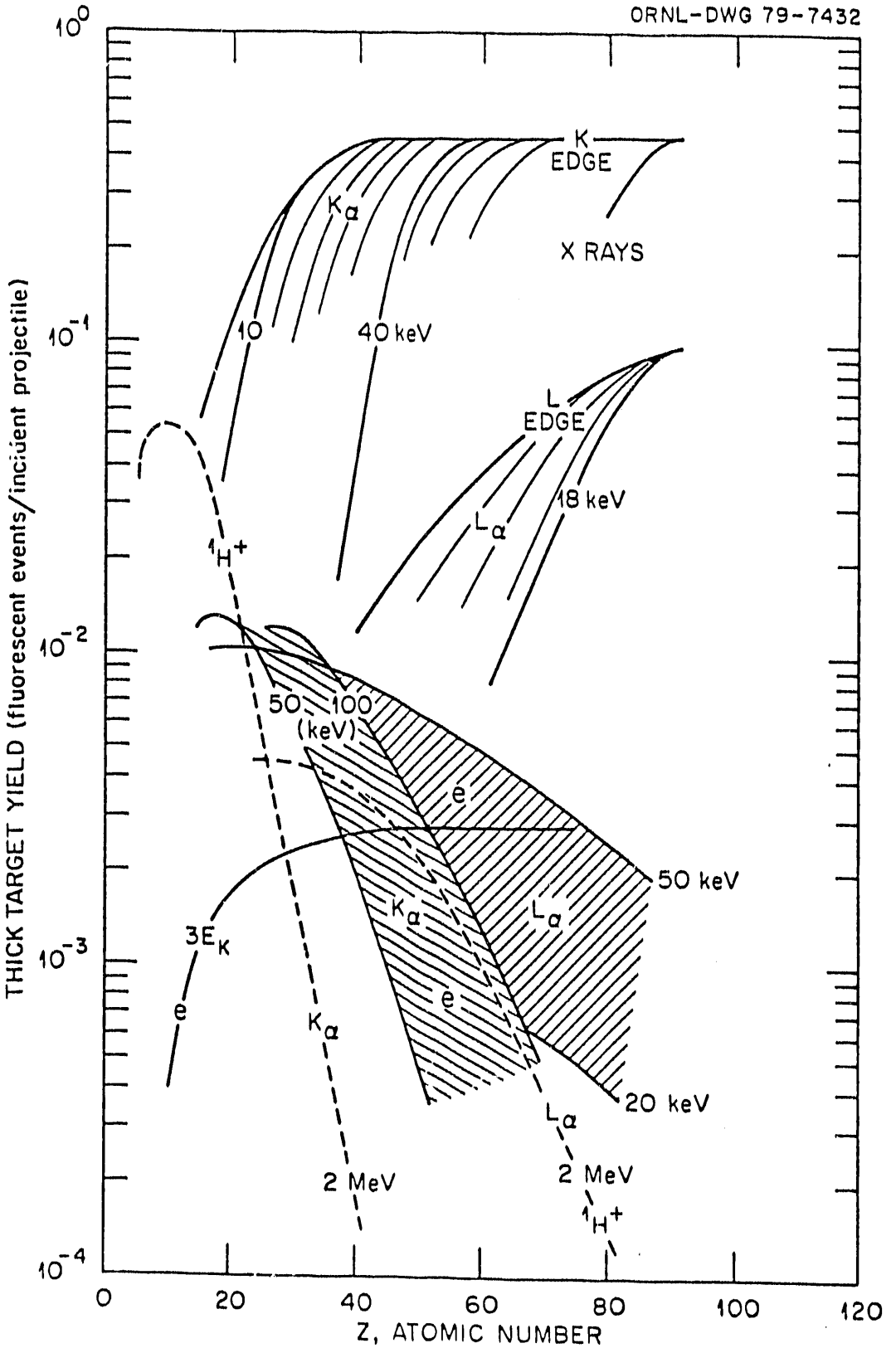

Figure 6

X-RAY PRODUCED FLUORESCENCE HAS 10^4 TO 10^5 GREATER SIGNAL TO BACKGROUND THAN FROM ELECTRONS

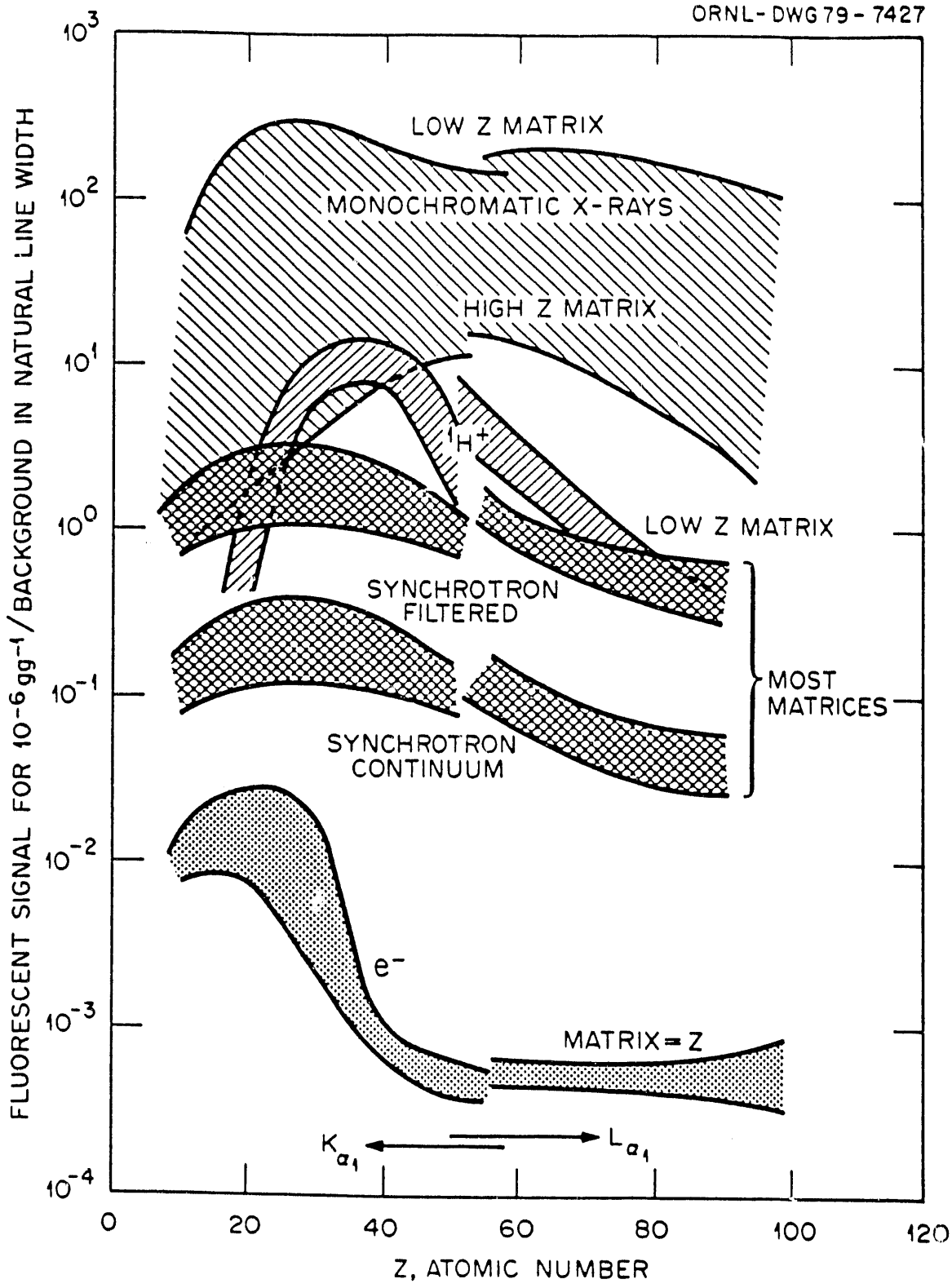

Figure 7

ULTIMATE LIMITATION TO MICROPROBE MDL IS THE POWER WHICH CAN BE ABSORBED BY THE SPECIMEN.

10^{14} 8 KeV/sec

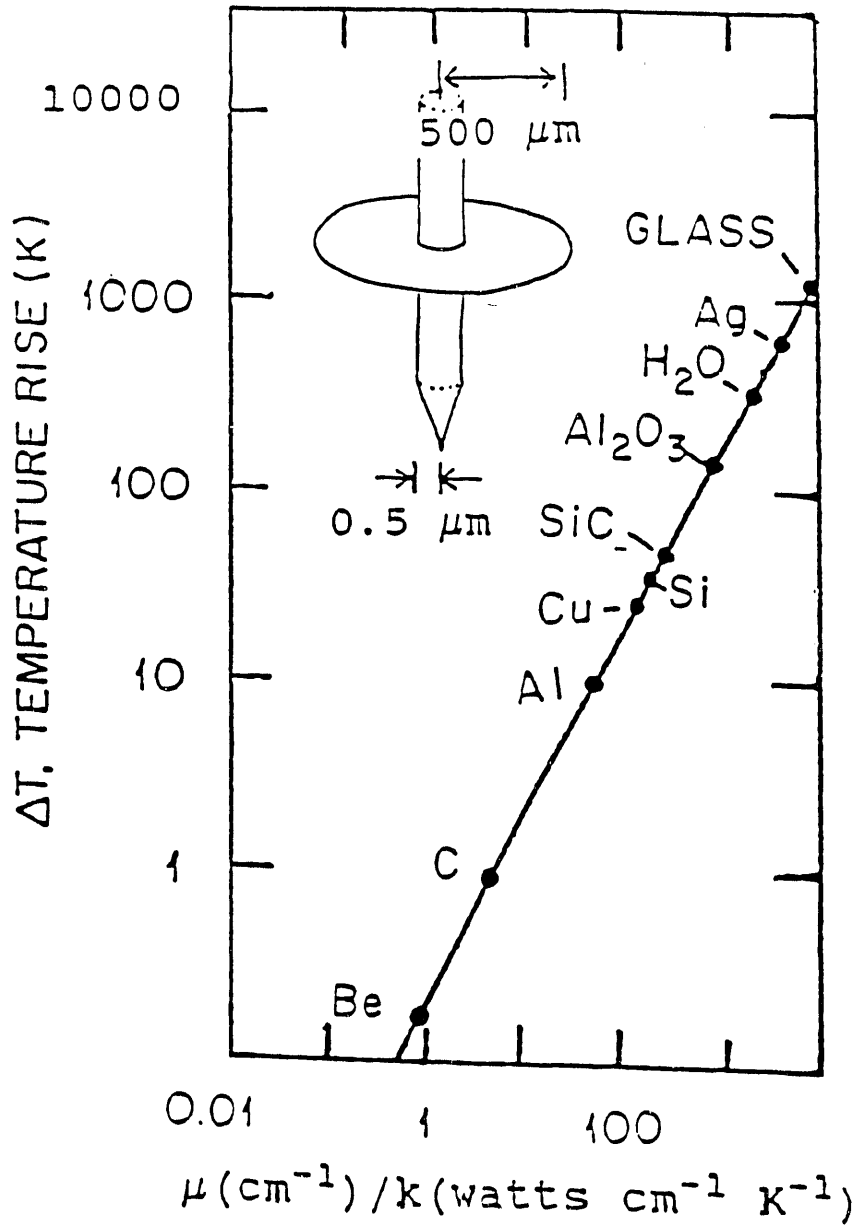

A MICROPROBE AT THE APS MAY APPROACH THIS LIMIT FOR SOME MATERIALS.- Can reduce power on the specimen by decreasing dE/E or by reducing divergence.

Figure 8

Conservative detection limits in fluorescence and diffraction for a 1-μm-diam X-ray microprobe based on counting times of 1 sec

Signal	Amounts detected
X-ray fluorescence	10^{8} atoms, embedded in a matrix, 10^{6} atoms, in organics 10^{3} atoms, free standing 10^{-9} weight per unit weight of sample 10^{-4} monolayer
X-ray diffraction	
Single crystal	10^{10} atoms, 10^{-12} g or 600-Å-diam particle 10^{-2} of a monolayer coverage
Polycrystalline	10^{14} atoms, 10^{-8} g or 1-μm-diam particle 1 part in 3000 parts of second phase 20 monolayers coverage

Figure 9

MOSAIC CRYSTAL SPECTROMETER COMBINES THE EFFICIENCY OF SSD WITH RESOLUTION OF A CRYSTAL SPECTROMETER.

- INTRINSIC RESOLUTION COMPARABLE TO PERFECT CRYSTAL SPECTROMETER.
- INTEGRATED REFLECTIVITY 10-1000 TIMES GREATER THAN A PERFECT CRYSTAL.

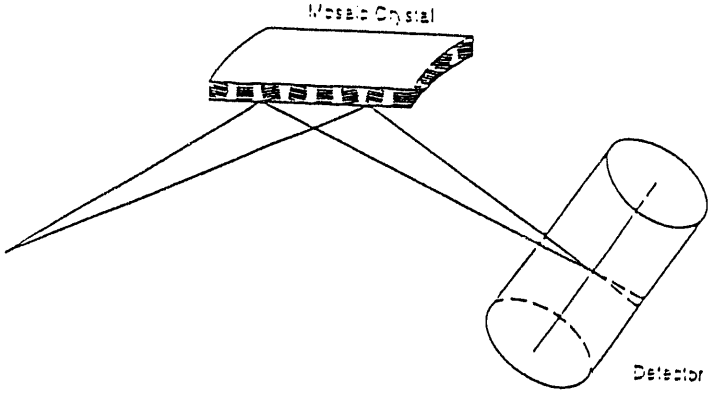

CURVED MOSAIC CRYSTAL EFFICIENTLY FOCUSES THE X-RAY BEAM TO COLLECT A LARGE SOLID ANGLE.

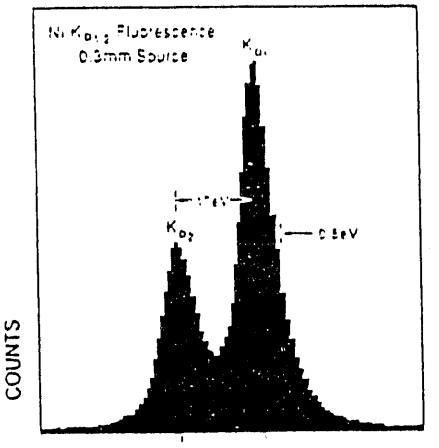

COMPARED TO A SOLID SATE DETECTOR (dE ~ 150 eV), MOSAIC SPECTROMETER HAS A RESOLUTION THAT IS 20 TIMES BETTER (dE ~ 8 eV).

- ALLOWS LOWER MDL
- AVOIDS SIGNAL FROM MATRIX SWAMPING DETECTOR.
- DISADVANTAGE: ONE SPECTROMETER/ELEMENT

Figure 10

ADVANTAGES OF AN X RAY EXCITED FLUORESCENCE MICROPROBE

I. LOWERING DETECTION LIMITS: BETTER CONTRAST

II. REDUCING HEAT AND RADIATION DAMAGE

III. IMPROVING ACCURACY OF QUANTITATIVE ANALYSIS

IV. IMPROVING SPATIAL RESOLUTION

V. REDUCING TIME FOR ANALYSIS

VI. EXTENDING MEASUREMENTS TO MANY KINDS OF SAMPLES

- A. IN PRESENCE OF AIR, OTHER GASES, WATER
- B. LARGE SPECIMEN CHAMBER

VII. NEGLIGIBLE CHARGE COLLECTION

Figure 11

DETECTABLE SIGNALS FROM METALS AT 100 ppb IN PLASTIC WITH MONOCHROMATIC EXCITATION RADIATION AND SOLID STATE DETECTORS

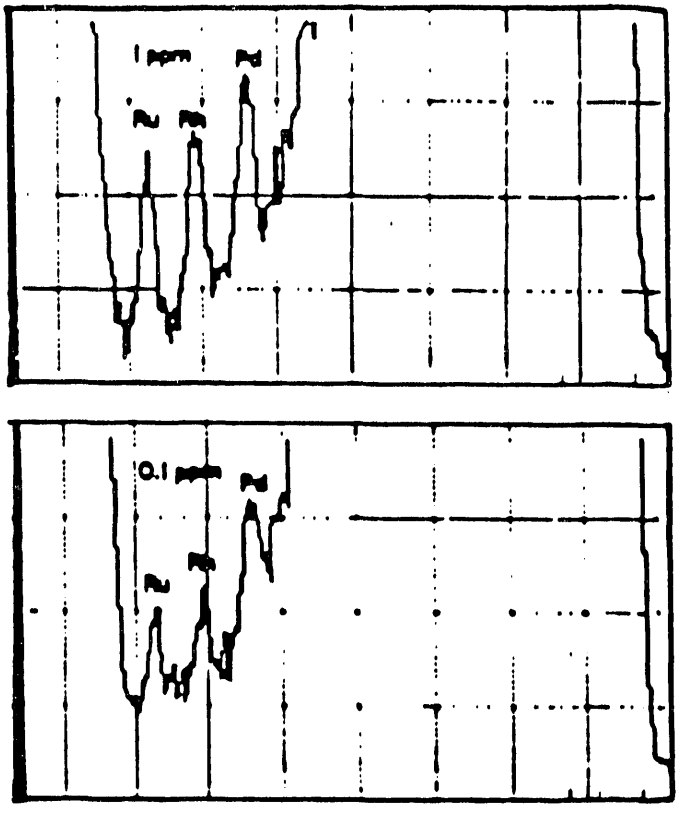

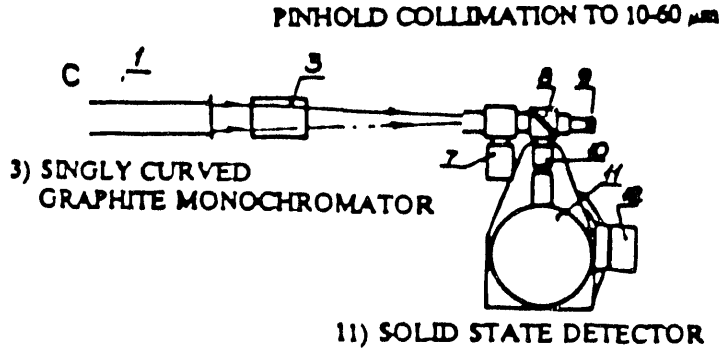

Figure 12

V. BARYSHEV, Y. KOLMOGOROV, G. KULIPANOV, AND A. SKRINSKY
VEPP-4, NOVOSIBIRSK, USSR
ADAPTED FROM NUCL. INSTR. METH. A246, 739 (1986)

STUDY EFFECTS OF MINOR ALLOYING ADDITIONS ON MATERIALS BEHAVIOR

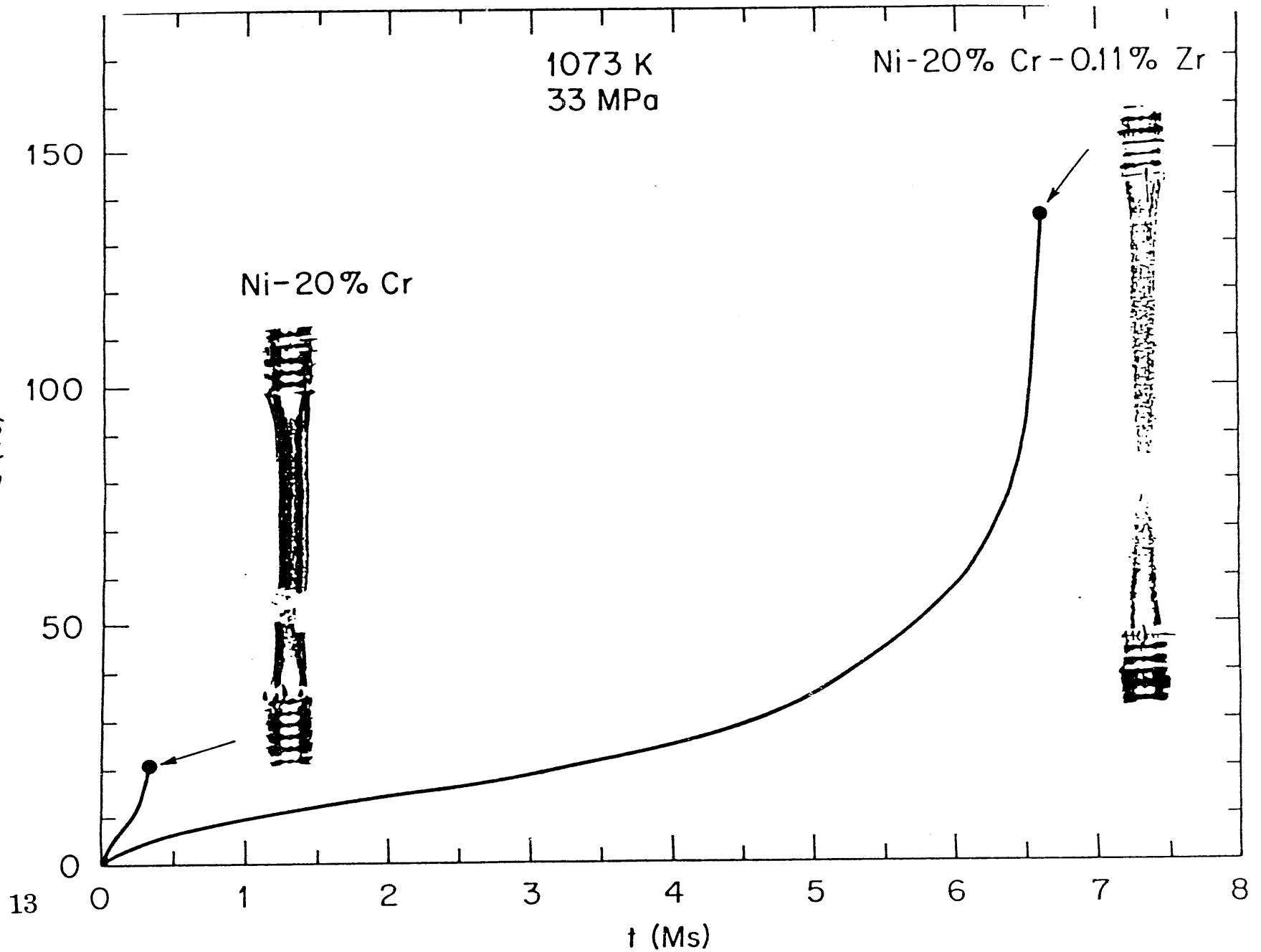

Figure 13

Fuel Sphere Characteristics

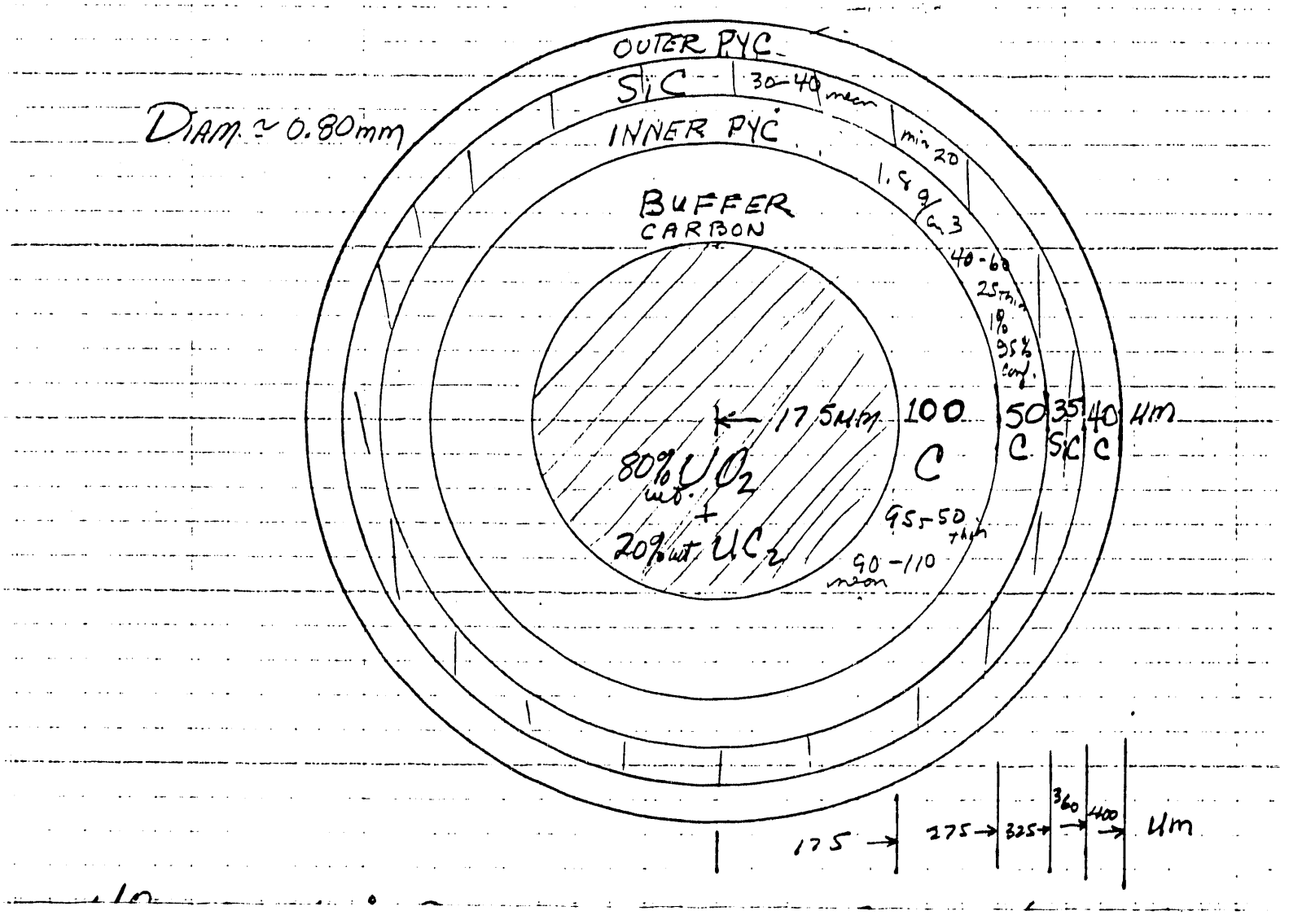

Figure 14

OPTICAL PHOTOMICROGRAPH OF COATED FUEL PARTICLE

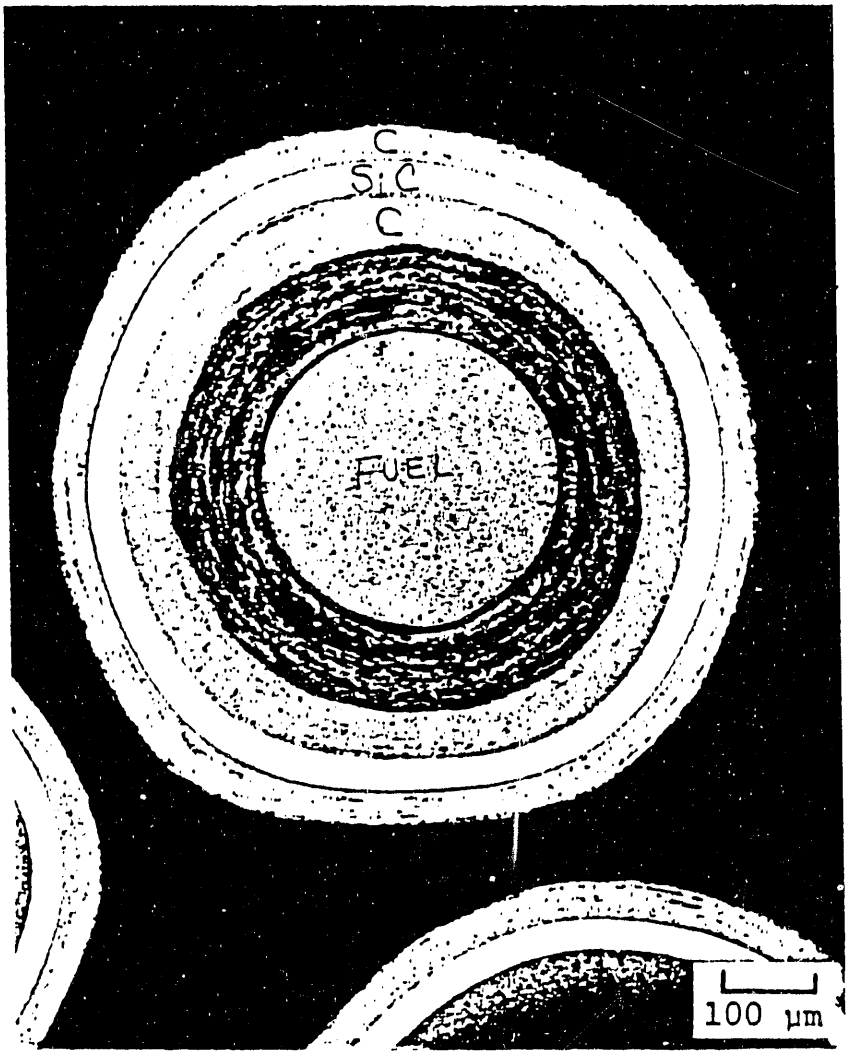

MP86003-2

Figure 15 Photomicrograph showing typical microstructure of a TRISO-coated, 500µm ThO_2 kernel, fuel particles from batch 8876-56.[2]

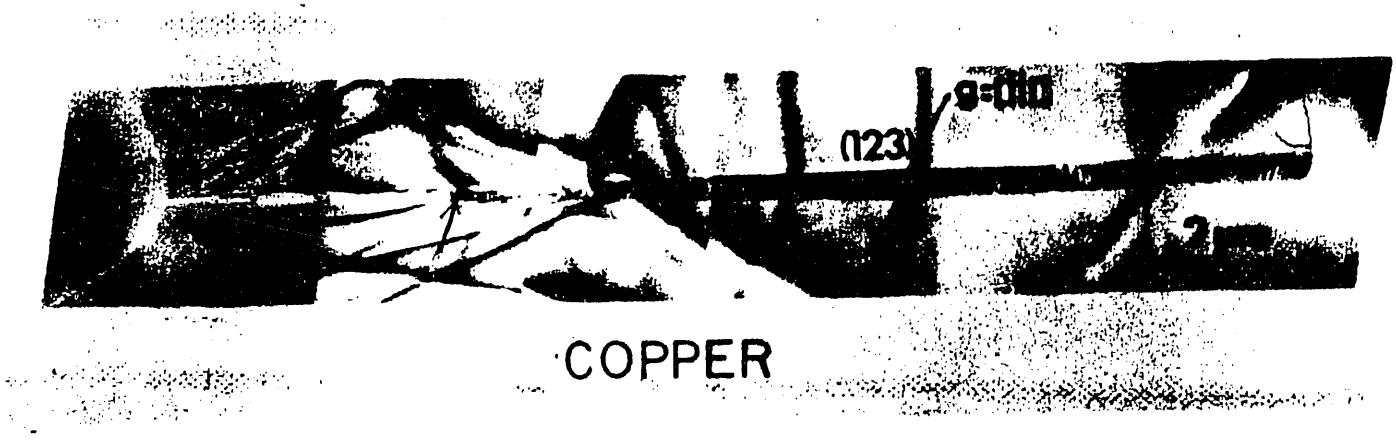

Figure 16

X-ray Microprobe allows study
of strain in imperfect crystals.

1. Extends topography to crystals
   with too many dislocations.

2. Separate lattice rotations
   from dilation.

3. Study purely local effects
   of free surfaces etc.

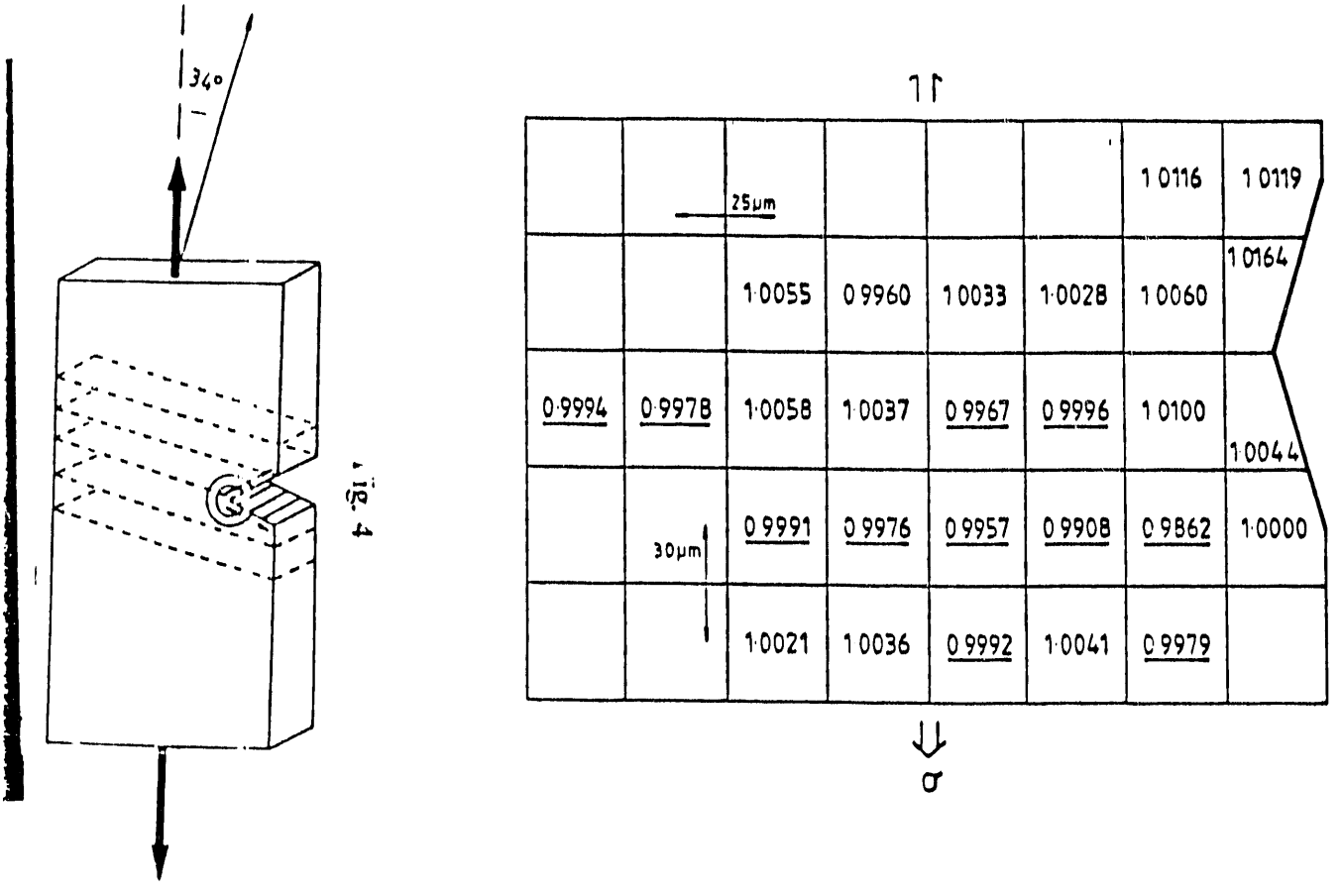

Figure 17

HIGH-ENERGY SYNCHROTRON RADIATION X-RAY MICROSCOPY: PRESENT STATUS AND FUTURE PROSPECTS*

K. W. Jones, B. M. Gordon, and P. Spanne
Brookhaven National Laboratory, Upton, New York 11973

M. L. Rivers and S. R. Sutton
University of Chicago, Chicago, Illinois 60637

1. Introduction

High-energy radiation synchrotron x-ray microscopy is used to characterize materials of importance to the chemical and materials sciences and chemical engineering. The x-ray microscope (XRM) forms images of elemental distributions fluorescent x rays or images of mass distributions by measurement of the linear attenuation coefficient of the material. Distributions of sections through materials are obtained non-destructively using the technique of computed microtomography (CMT). The energy range of the x rays used for the XRM ranges from a few keV at the minimum value to more than 100 keV, which is sufficient to excite the K-edge of all naturally occurring elements.

The work in progress at the Brookhaven NSLS X26 and X17 XRM is described in order to show the current status of the XRM. While there are many possible approaches to the XRM instrumentation, this instrument gives state-of-the-art performance in most respects and serves as a reasonable example of the present status of the instrumentation in terms of the spatial resolution and minimum detection limits (MDLs) obtainable.

The examples of applications cited give an idea of the types of research fields that are currently under investigation. They can be used to illustrate how the field of x-ray microscopy will benefit from the use of bending magnets and insertion devices at the Advanced Photon Source (APS).

2. X26 X-ray Microscope Apparatus

The X26 XRM at present is a simple device which uses a collimator to produce x-ray beam sizes down to 1 μm × 1 μm. X-ray fluxes that are sufficient for trace element microscopy can be obtained because of the high brightness of the NSLS x-ray ring and by use of the white beam rather than a monoenergetic beam.

*Research supported in part by the US Department of Energy, Office of Basic Energy Sciences, Division of Chemical Sciences, Contract No. DE-AC02-76CH00016 (KWJ, BMG, PS); NSF Grant No. EAR89-15699 (MLR); NASA Grant No. NAG 9-106 (SRS).

The XRM uses computer-controlled stepping motor stages to move a specimen through the x-ray beam. The specimen is positioned for analysis of particular areas by viewing it through an optical microscope placed at 135° to the incident photon beam. Fluorescent x rays are detected with an energy-dispersive Si(Li) x-ray detector placed at 90° to the incident beam. Beam attenuation by the specimen is determined by use of an ion chamber upstream of the specimen and a scintillation detector or ion chamber placed down stream from the specimen.

3. XRM Configurations

A number of different beam-line configurations are used for x-ray microscopy experiments so that conditions can be optimized for different experimental requirements. Some of the arrangements used or planned for use in the near future are as follows:

- Pinhole beam collimator. White light.
- Beam collimator, Kirkpatrick-Baez Microscope. (With A. Thompson, J. Underwood, R. Giauque, *et al.*, Center for X-ray Optics, LBL).
- Beam collimator, monochromator, zone-plate. (Wenbing Yun *et al.*, ANL; LLNL).
- Focussing mirror and pinhole collimator. White light.
- Broad-bandwidth monochromator, focussing mirror, pinhole collimator.
- High-resolution monochromator, focussing mirror, pinhole collimator. (Spatially resolved emission XANES and EXAFS).
- Pinhole collimator, specimen, high-resolution monochromator. (High spatial resolution and time-resolved absorption XANES and EXAFS).

4. XRM Performance

The performance of the XRM at the present time when used on the X26 NSLS bending magnet beam line is as follows (1-2):

- Spatial resolution as small as ~ 1 μm.
- Detection limits ~ 1-10 femtogram.
- Two-dimensional emission or absorption maps.
- Non-destructive sections using CMT in emission or absorption mode.
- Multielement detection.
- μXANES and μEXAFS analysis.
- μXRD analysis.
- Minimal sample preparation.
- Operation over a range of pressures and temperatures with solids, liquids, or gases.
- Minimal beam damage.

5. XRM Applications

The XRM has been employed in several experiments that are relevant to chemical engineering and related sciences. Several examples are cited in illustration of this point.

Work with both x-ray fluorescence (XRF) and CMT has been done on rare-earth exchanged zeolite fluid cracking catalysis (FCC) and hydrotreating catalysts (3) as well as polyethylene polymerization particles (4). A non-destructive CMT section of a polyethylene particle is shown in Figure 1. The tomogram shows the presence of small Si-Cr fragments and makes it possible to estimate the porosity of the pellet. Both results should be of importance in understanding the basic mechanisms involved in the polymerization process and could, ultimately, lead to improvements in the manufacturing process.

Examination of fly-ash particles using the XRM provides information on the trace element composition and distribution in the particle which cannot be easily obtained using electron microscopy or other techniques. Measurements on individual particles should be useful in understanding some of the details of the combustion mechanism in coal-fired power plants and in municipal waste incinerators. This knowledge should also be helpful in understanding the environmental effects caused by the dispersal of the particles in the atmosphere. The distribution of lead and zinc obtained for a 15 μm section of fly ash from an incinerator is shown in Figure 2. The pixel size is 5 μm $\times$ 5 μm. Both elements show a large enhancement of the concentration at the surface of the particle implying condensation on the substrate as the particle passes through a cooler region in the flame.

Orthopedic implants are widely used and represent a subject requiring a multidisciplinary approach. CMT can be used as one part of an experimental program designed to improve the performance of the implants. The base metal material is often prepared with a porous surface for the bone to grow into. The bone-implant region can be studied effectively with CMT since no specimen preparation is needed and, for animal studies, can be used for in-vivo measurements. Figure 3 (5) shows a tomogram obtained for a phantom fabricated with a rat femur and 1 mm stainless steel rod. The tomogram shows that high quality images free of artifacts can be obtained.

Finally, x-ray near-edge absorption spectroscopy (XANES) is often used to measure the oxidation state of trace quantities of elements in situ. The XRM has recently been used to determine the chromium oxidation state in specimens of pyroxene and olivine in lunar basalt 15555 and in rat kidney. High-sensitivity XRF measurements are needed since the chromium concentration is low and reasonable (sub-mm) spatial resolution is needed to distinguish different biological and geological structures. Figure 4 (6) shows the fluorescent XANES spectrum obtained with the XRM. The results indicate that the chromium is present in both 2^+ and 3^+ oxidation states in the olivine. Accumulation of further data will help to gain better understanding of the conditions under which the basalt was formed.

6. Improvements to the XRM

There is need to improve the performance of the XRM. The needs include reductions in the minimum detection limits and improvements in the spatial resolutions. Some of the points that are currently being investigated are:

- Improve mechanical collimators construction. What is the ultimate limit?
- Other types of collimators. Focussing capillaries?
- Utilize wavelength dispersive detectors for improved detection limits.
- Asymmetrically cut silicon demagnifiers and magnifiers.
- What methods can be used for work at resolutions below 1 μm? New focussing optics? Improved zone plates?

7. X-ray Microscopy at the Advanced Photon Source

The Advanced Photon Source will present stunning new opportunities for the improvement of the XRM. Our present work demonstrates the pressing need for improvements in the x-ray source brilliance and energy range. The APS will satisfy both requirements. The import for x-ray microscopy has been discussed recently by Sparks and Ice (7)

The XRM used with an APS undulator source will utilize beams which have roughly four orders of magnitude higher brilliance and brightness than the beams from the NSLS bending magnet source. A similar increase in the photon flux through a pinhole can be expected. This will bring the flux to a value comparable to those observed for electron beams in electron microscopes. The undulator can be tuned over a wide energy range and can produce K-x rays for elements to about Z = 60.

The higher energy range covered by high fluxes is necessary for CMT measurements of large samples and for critical energy absorption measurements. The possibility of forming images with K-x rays of the heavier elements will also be an important advance.

Beam-induced radiation damage is already becoming important for the current XRM instruments in some cases. It will be a factor of much more importance with the APS. A detailed study during the years before the APS becomes operational will be important.

Finally, it is amusing to speculate on the spatial resolution that might be obtained with the APS. Figure 5 (from Reference 8) shows the improvement in resolution as a function of time. Extrapolation of the curve shows a value of about 1 nm reached in another ten years. This is no doubt too optimistic, but resolution values well under 1 μm should be reached. Hence, the XRM should be an instrument with many scientific applications in chemical engineering, as well as for many other scientific and engineering areas.

8. References

1. K. W. Jones, B. M. Gordon, G. Schidlovsky, P. Spanne, Xue Dejun, R. S. Bockman, and A. J. Saubermann, Biomedical Elemental Analysis and Imaging Using Synchrotron X-Ray Microscopy, in *Microbeam Analysis-1990*, eds. D. B. Williams, P. Ingram, and J. R. Michael (San Francisco Press, Inc., 1990).

2. M. L. Rivers, S. R. Sutton, and K. W. Jones, X-Ray Fluorescence Microscopy, in *X-Ray Microscopy III* (Springer-Verlag, 1991), in press.

3. K. W. Jones, P. Spanne, S. W. Webb, W. C. Conner, R. A. Beyerlein, W. J. Reagan, and F. M. Dautzenberg, Catalyst Analysis Using Synchrotron X-Ray Microscopy. *Nucl. Instrum. and Methods* B56/57, 427 (1991).

4. W. C. Conner, S. W. Webb, P. Spanne, and K. W. Jones, The Use of X-Ray Microscopy and Synchrotron Microtomography to Characterize Polyethylene Polymerization Particles, *Macromolecules* 23, 4742 (1990).

5. K. W. Jones, G. Schidlovsky, P. Spanne, Xue Dejun, R. S. Bockman, M. B. Rabinowitz, P. B. Hammond, R. L. Bornschein, and D. A. Hoeltzel, Calcified-Tissue Investigations Using Synchrotron X-Ray Microscopy, in *X-Ray Microscopy III* (Springer-Verlag, 1991), in press.

6. S. R. Sutton, K. W. Jones, B. Gordon, M. L. Rivers, and J. V. Smith, Chromium Valency in Individual Lunar Olivine Grains Using X-Ray Absorption Near Edge Structure (XANES) Microanalysis, in *Proceedings of XXII Lunar and Planetary Science Conference, Houston, Texas, March 1991* (Lunar and Planetary Institute, 1991), in press.

7. C. J. Sparks and G. E. Ice, X-Ray Microprobe-Microscopy, in *Proceedings of 15th Intern. Conf. on X-Ray and Inner-Shell Processes, July 1990*, in press.

8. K. W. Jones, Synchrotron Radiation-Induced X-Ray Emission, in *Handbook on X-Ray Spectrometry: Methods and Techniques*, eds. R. Van Grieken and A. Markowicz (Marcel Dekker, Inc., 1991), to be published.

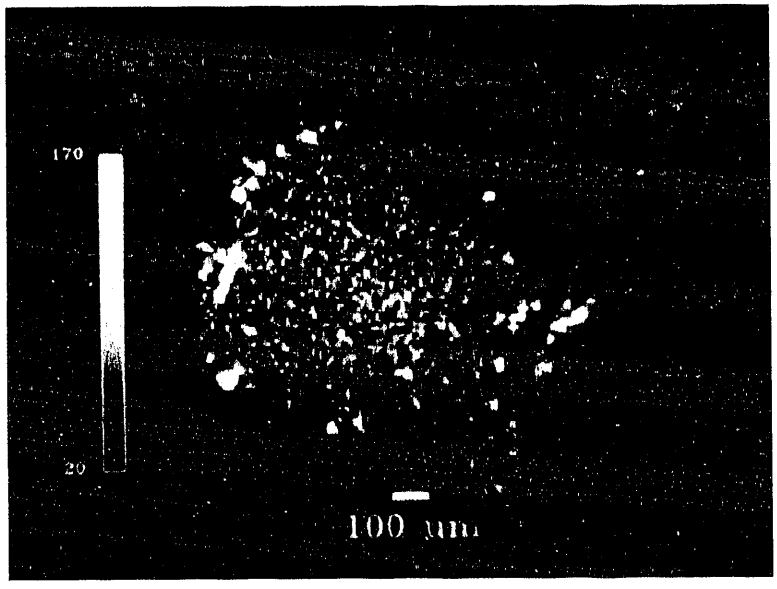

Figure 1. Tomogram of polyethylene polymerization particle. The beam size was 12 μm × 5 μm and a slice thickness of 5 μm. Catalyst particles are seen at the periphery of the particle.

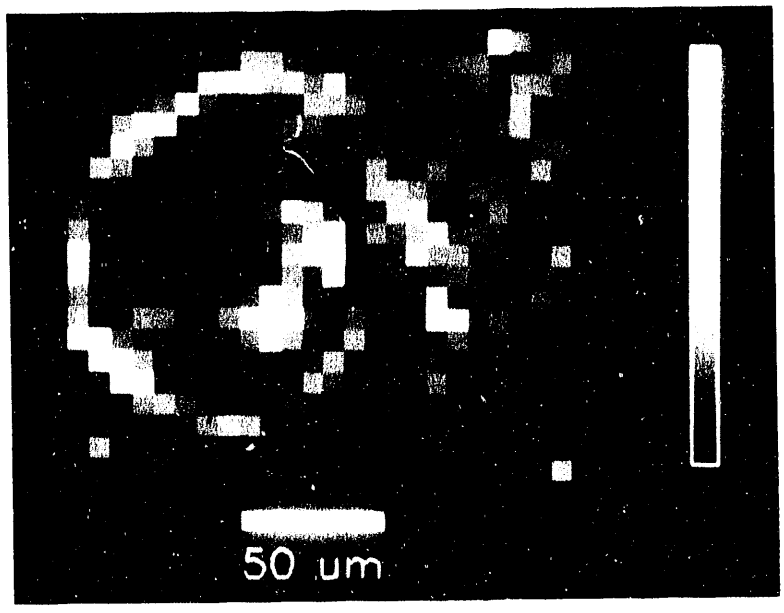

(A)

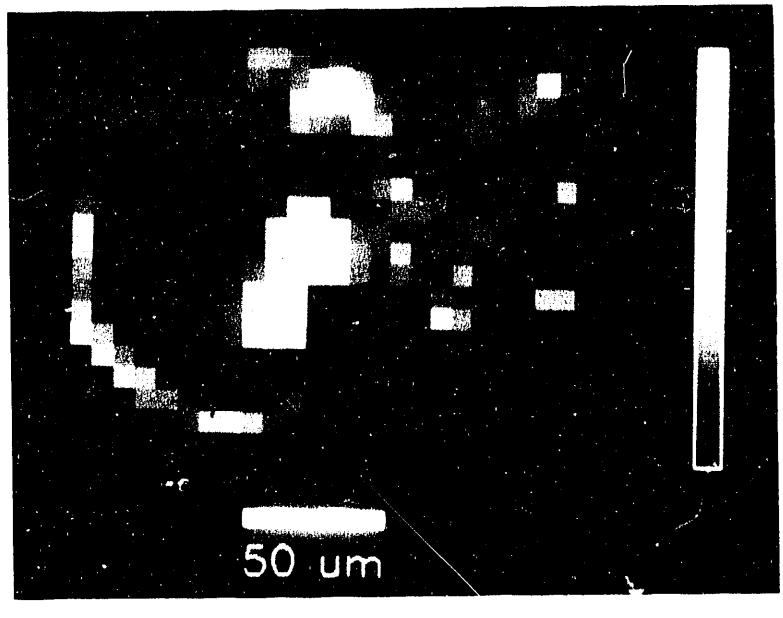

(B)

Figure 2. Distribution of lead (A) and zinc (B) in a 15-μm section of fly ash from an incinerator.

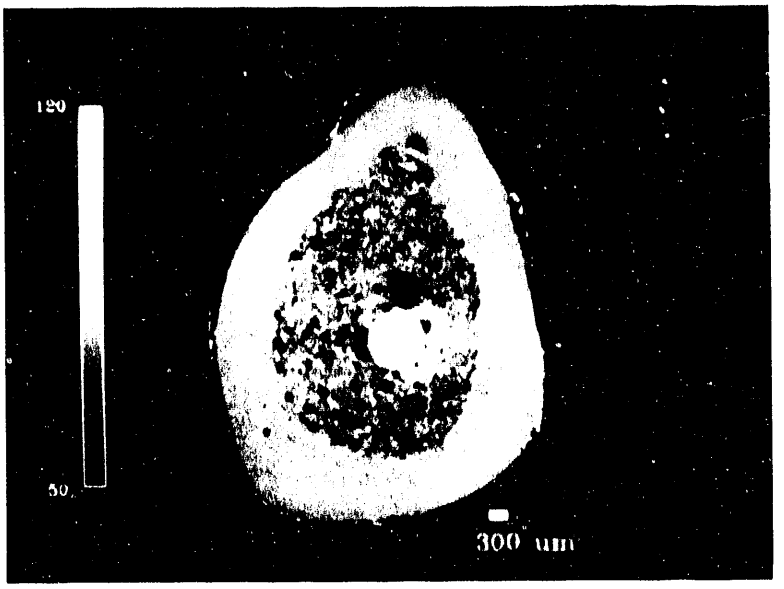

Figure 3. Tomogram of orthopedic implant phantom. This shows the feasibility of studying the bone growth in porous implants.

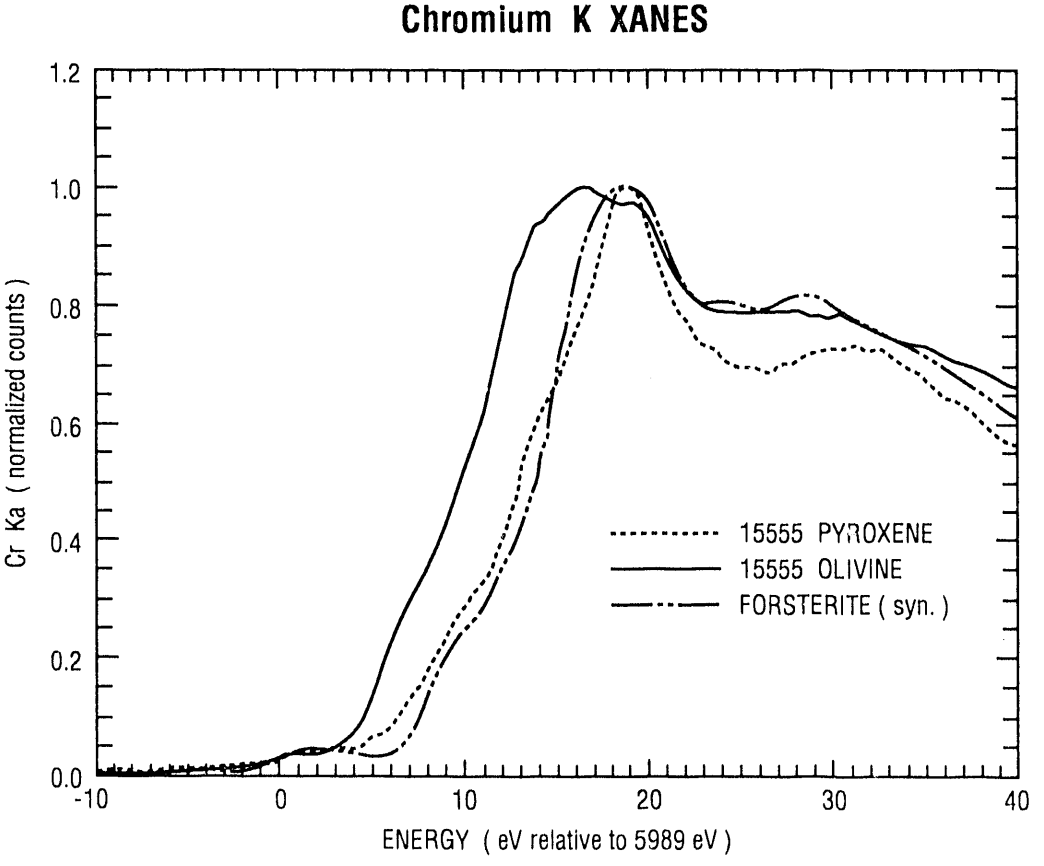

Figure 4. XANES spectrum obtained for pyroxene and olivine contained in a specimen of lunar basalt 15555.

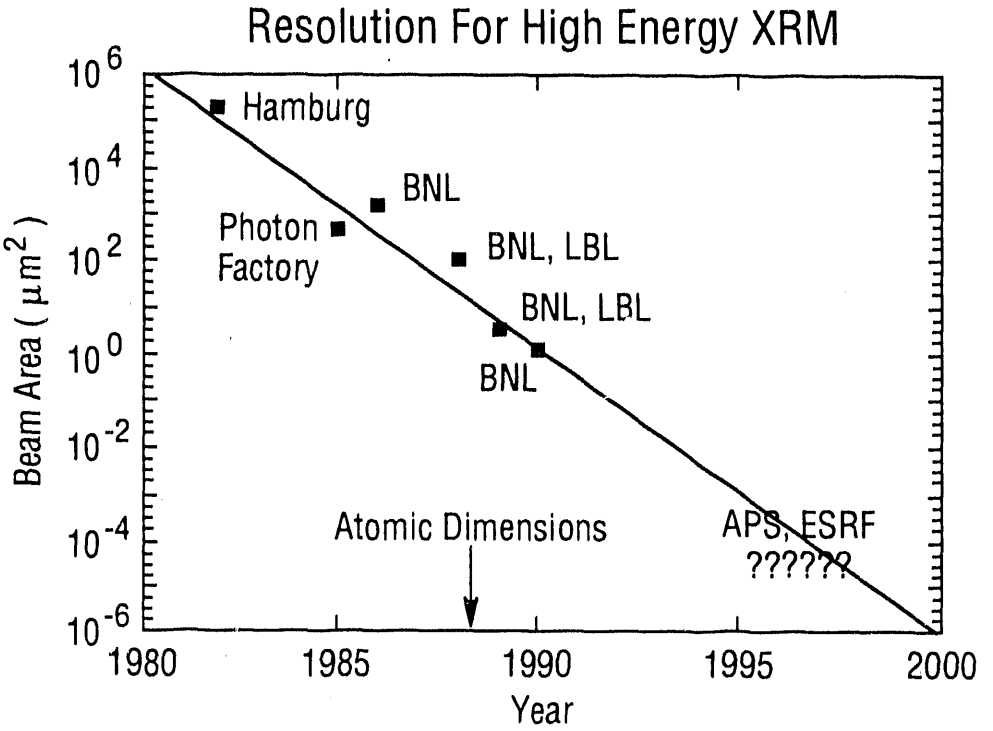

Figure 5. XRM spatial resolution plotted as a function of time.

PROGRAM

FINAL PROGRAM

Workshop on Applications of Synchrotron Radiation to Chemical Engineering Science

April 22-23, 1991

Argonne National Laboratory

Monday, April 22, 1991

Morning Session, Building 205 Auditorium (M. J. Steindler, Chairman)

8:00-8:45 a.m. Registration

8:45 a.m. Welcome and Introduction of Plenary Speaker by Dr. Alan Schriesheim, ANL Laboratory Director

9:00 a.m. Plenary Lecture by Dr. Keith McHenry, Amoco Corporation

"Energy and Environmental Challenges to Chemical Engineering"

9:50 a.m. Break

10:10 a.m. Session I: An Overview of Operational Aspects and Applications of Synchrotrons

- Dr. James P. Viccaro, Argonne National Laboratory
  "Insertion Device Radiation Sources"

- Dr. Arthur Bienenstock, Stanford Synchrotron Radiation Laboratory
  "Applications of Synchrotron Radiation to Science and Engineering Problems"

11:50 a.m. Lunch

Afternoon Session, Building 205 Auditorium (M. Blander, Chairman)

1:00 p.m. Status Report on the Advanced Photon Source

- Dr. David E. Moncton, Argonne National Laboratory

1:20 p.m. Session II: Applications of UV/X-ray Radiation in Electrochemical and Corrosion Research

- Dr. William O'Grady, Naval Research Laboratory
  "X-ray Absorption Spectroscopy in the Study of Electrochemical Interfaces"

- Dr. Farrel W. Lytle, The Boeing Company
  "Investigation of the Structure and Chemistry of the Surface Layer on Metals: The Chromium-Conversion Surface on Aluminum"

3:00 p.m. Break

3:15 p.m. Session II: (continued)

- Dr. Michael J. Bedzyk, Cornell University
  "Measuring the Diffuse Double Layer at an Electrochemical Interface with X-ray Standing Waves"

- Dr. Victor A. Maroni, Argonne National Laboratory
  "Studies of Corrosion Using a Combination of X-ray Scattering and Electrochemical Techniques"

5:00 p.m. Adjourn Session II/Begin Tour of APS Site

6:30 p.m. Banquet at Carriage Greens Country Club

Tuesday, April 23, 1991

Morning Sessions, Building 205 Auditorium (D. W. Green, Chairman)

8:30 a.m. Session III: Applications of UV/X-ray Radiation to Catalyst Development and Characterization

- Dr. Grayson Via, Exxon Research and Engineering Co.
  "Synchrotron Radiation Studies of Supported Metal Catalysts"

- Dr. Heinz J. Robota, Allied Signal, Inc.
  "Probing Catalyst Changes Under Dynamic Chemical Conditions by X-ray Absorption Spectroscopies"

10:15 a.m. Break

10:40 a.m. Session IV: Applications of UV/X-ray Radiation to Fluids

- Dr. Eric Sirota, Exxon Research and Engineering Co.
  "X-ray Synchrotron Scattering Studies of
  Complex Fluids Under Shear Flow"

11:30 a.m. Lunch

Afternoon Sessions, Building 205 Auditorium (D. W. Dees, Chairman)

12:50 p.m. Session V: Applications of UV/X-ray Radiation to Imaging and Lithography

- Dr. John H. Kinney, Lawrence Livermore National Laboratory
  "Three-dimensional X-ray Microscopy
  Using Synchrotron Radiation"
- Dr. Michael P. Bohrer, AT&T Bell Laboratories
  "Deep-UV and X-ray Microlithography"

2:30 p.m. Break

2:45 p.m. Session VI: Applications of UV/X-ray Radiation to Materials Analysis

- Dr. Gene E. Ice, Oak Ridge National Laboratory
  "X-ray Microimaging of Elemental Composition
  and Microstructure for Materials Science"
- Dr. Keith Jones, Brookhaven National Laboratory
  "High Energy X-ray Microscopy"

4:30 p.m. Adjourn Session VI

PROGRAM

Workshop on Applications of Synchrotron Radiation to Chemical Engineering Science

Round Table Discussion: Strategies for Gaining Access to APS

Wednesday, April 24, 1991
Building 205 - A059

8:30 a.m. Opening Remarks

- Shiu-Wing Tam, CMT

8:45 a.m. Current APS User Access Policy

- Gopal Shenoy, APS

9:15 a.m. APS Beamline Administrative Proposal: A Case Study

- Elane Streets, CMT/ACL

9:30 a.m. APS Beamline Technical Proposal: A Case Study

- Victor Maroni, CMT

9:45 a.m. Round Table Discussion

- Moderator: Shiu-Wing Tam, CMT

10:30 a.m. Break

10:45 a.m. Round Table Discussion

- Moderator: Shiu-Wing Tam, CMT

11:30 a.m. Adjourn Session

PARTICIPANTS

Susan H. Barr
Advanced Photon Source
Argonne National Laboratory
Building 360
9700 South Cass Avenue
Argonne, IL 60439
708-972-5981

Donald A. Becker
Analytical Division
Amoco Corporation
Box 3011
Naperville, IL 60566
708-420-5218

Michael J. Bedzyk
Wilson Laboratory
CHESS
Cornell University
Ithaca, NY 14853
607-255-0920

Arthur Bienenstock
Stanford Synchrotron Radiation Laboratory
P.O. Box 4349
Stanford, CA 94305
415-926-3153

Milton Blander
Chemical Technology Division
Argonne National Laboratory
Building 205
9700 South Cass Avenue
Argonne, IL 60439
708-972-4548

Michael P. Bohrer
Lithographic Materials and Chemical
Engineering Research
AT&T Bell Laboratories
600 Mountain Avenue
Murray Hill, NJ 07974
908-582-3054

Amrit Boparai
Chemical Technology Division
Argonne National Laboratory
Building 205
9700 South Cass Avenue
Argonne, IL 60439
708-972-7710

Michael K. Bowman
Chemistry Division
Argonne National Laboratory
Building 200
9700 South Cass Avenue
Argonne, IL 60439
708-972-3546

Kathleen A. Carrado
Chemistry Division
Argonne National Laboratory
Building 200
9700 South Cass Avenue
Argonne, IL 60439
708-972-7968

Ronald G. Cavell
Department of Chemistry
University of Alberta
Edmonton, ALTA T6G 2G2
CANADA
403-492-5310

Lin Chen
Chemistry Division
Argonne National Laboratory
Building 200
9700 South Cass Avenue
Argonne, IL 60439
708-972-3533

Shayao Chuang
Washington State University
Materials & Components Tech. Div./Bldg. 212
c/o Argonne National Laboratory
9700 South Cass Avenue
Argonne, IL 60439
708-972-6643

Cyrus Crowder
Department of Analytical Sciences
Dow Chemical Company
1897 Building
Midland, MI 48667
517-636-8692

Crystal E. Durr
Chicago State University
Biological & Medical Research Div./Bldg. 202
Argonne National Laboratory
9700 South Cass Avenue
Argonne, IL 60439
708-972-3862

Larry A. Curtiss
Chemical Technology Division
Argonne National Laboratory
Building 205
9700 South Cass Avenue
Argonne, IL 60439
708-972-7380

Deon G. Ettinger
Division of Educational Programs
Argonne National Laboratory
Building 223
9700 South Cass Avenue
Argonne, IL 60439
708-972-4272

Dennis W. Dees
Chemical Technology Division
Argonne National Laboratory
Building 205
9700 South Cass Avenue
Argonne, IL 60439
708-972-7349

John Faber
Amoco Research Center
Amoco Corporation
MS F-9
P.O. Box 3011
Naperville, IL 60566
708-961-6294

Roger J. Dejus
Advanced Photon Source
Argonne National Laboratory
Building 360
9700 South Cass Avenue
Argonne, IL 60439
708-972-5557

Patricia A. Finn
Chemical Technology Division
Argonne National Laboratory
Building 205
9700 South Cass Avenue
Argonne, IL 60439
708-972-4511

Michael J. Deveney
Analytical Division
Amoco Corporation
P.O. Box 3011
Naperville, IL 60566-7011
708-420-5527

Barrett L. Gady
Rochester Institute of Technology
c/o Argonne National Laboratory
Chemistry/Materials Science Divs./Bldg. 200
9700 South Cass Avenue
Argonne, IL 60439
708-972-3556

James D. Dudek
University of Wisconsin-Plattville
Materials Science/Chemistry Divs./Bldg. 200
c/o Argonne National Laboratory
9700 South Cass Avenue
Argonne, IL 60439
708-972-6674

Joseph L. Gambino
New York Institute of Technology
Materials & Components Tech. Div./Bldg. 308
c/o Argonne National Laboratory
9700 South Cass Avenue
Argonne, IL 60439
708-972-3377

Erik P. Geiss
Clarkson University
Physics Division/Building 203
c/o Argonne National Laboratory
9700 South Cass Avenue
Argonne, IL 60439

David W. Green
Chemical Technology Division
Argonne National Laboratory
Building 205
9700 South Cass Avenue
Argonne, IL 60439
708-972-4379

Dieter M. Gruen
Materials Science/Chemistry Divisions
Argonne National Laboratory
Building 200
9700 South Cass Avenue
Argonne, IL 60439
708-972-3513

Hyo Chol Ha
Virginia Commonwealth University
Energy Systems Div./Bldg. 362/Mail Box 3
c/o Argonne National Laboratory
9700 South Cass Avenue
Argonne, IL 60439
708-972-5706

Robert A. Holoboff
University of Florida
Materials Science Division/Building 223
c/o Argonne National Laboratory
9700 South Cass Avenue
Argonne, IL 60439
708-972-4108

Joseph C. Hutter
Chemical Technology Division
Argonne National Laboratory
Building 205
9700 South Cass Avenue
Argonne, IL 60439
708-972-6497

Gene E. Ice
Metals and Ceramics Division
Oak Ridge National Laboratory
Room A262, 4500S MS 6118
P.O. Box 2008
Oak Ridge, TN 37831
615-574-2744

Christopher E. Jones
University of Southern Mississippi
Materials Science Division
c/o Argonne National Laboratory
9700 South Cass Avenue
Argonne, IL 60439
708-972-6333

Keith Jones
Department of Applied Science
Brookhaven National Laboratory
Buidling 815
Upton, NY 11973
516-282-4588

James A. Kaduk
Amoco Research Center
Amoco Corporation
P.O. Box 3011
Naperville, IL 60566
708-420-4547

John H. Kinney
Department of Chemistry & Material Science
Lawrence Livermore National Laboratory
L-356
P.O. Box 808
Livermore, CA 94550
415-422-6669

Thomas E. Klippert
Advanced Photon Source
Argonne National Laboratory
Building 360
9700 South Cass Avenue
Argonne, IL 60439
708-972-5874

Theodore R. Krause
Chemical Technology Division
Argonne National Laboratory
Building 205
9700 South Cass Avenue
Argonne, IL 60439
708-972-4356

Romesh Kumar
Chemical Technology Division
Argonne National Laboratory
Building 205
9700 South Cass Avenue
Argonne, IL 60439
708-972-4342

Barry P. Lai
Advanced Photon Source
Argonne National Laboratory
Building 360
9700 South Cass Avenue
Argonne, IL 60439
708-972-6405

Michael W. Lathrop
Western Montana College
Chemistry Division/ Building 200
c/o Argonne National Laboratory
9700 South Cass Avenue
Argonne, IL 60439
708-972

Leonard Leibowitz
Chemical Technology Division
Argonne National Laboratory
Building 205
9700 South Cass Avenue
Argonne, IL 60439
708-972-4333

Michele A. Lewis
Chemical Technology Division
Argonne National Laboratory
Building 205
9700 South Cass Avenue
Argonne, IL 60439
708-972-4534

Di-Jia Liu
Allied-Signal Research and Technology
P.O. Box 5016
50 East Algonquin Road
Des Plaines, IL 60017-501.
708-391-3703

Arthur R. Love
Hope College
Biological & Medical Research Div./Bldg. 202
c/o Argonne National Laboratory
9700 South Cass Avenue
Argonne, IL 60439
708-972-3884

Farrel W. Lytle
The Boeing Company
MS 2T-05
P.O. Box 3999
Seattle, WA 98124
206-544-5348

Victor A. Maroni
Chemical Technology Division
Argonne National Laboratory
Building 205
9700 South Cass Avenue
Argonne, IL 60439
708-972-4547

Keith McHenry
Amoco Corporation
P.O. Box 87703
Chicago, IL 60680-0703
312-856-5910

Carlos A. Melendres
Materials Science/Chemical Tech. Divisions
Argonne National Laboratory
Building 205
9700 South Cass Avenue
Argonne, IL 60439
708-972-4345

Susan Mini
Materials Science Division
Argonne National Laboratory
Building 223
9700 South Cass Avenue
Argonne, IL 60439
708-972-3773

Motoyasu Nukata
Nisshoiwai
Suite 2625
233 North Michigan Avenue
Chicago, IL 60601
312-938-2725

Masahiro Miyabayashi
Sumitomo Heavy Industries, Ltd.
151 Heartland Boulevard
Edgewood, NY 11717
516-254-6800

William E. O'Grady
Department of Chemistry
Naval Research Laboratory
Code 6170
Washington, DC 20375-5000
202-767-2631

David E. Moncton
Advanced Photon Source
Argonne National Laboratory
Building 360
9700 South Cass Avenue
Argonne, IL 60439
708-972-7950

Jason Y. Pahng
Materials & Components Technology Div.
Argonne National Laboratory
Building 335, Room 001
9700 South Cass Avenue
Argonne, IL 60439
708-972-3377

Chaitanya K. Narula
Chemistry Department
Ford Motor Company
MD 3083
P.O. Box 2053
Dearborn, MI 48121-2053
313-845-4928

Mark Pankuch
Illinois Benedictine College
Chemical Technology Division/Building 205
c/o Argonne National Laboratory
9700 South Cass Avenue
Argonne, IL 60439
708-972-4345

Monte Nichols
Sandia National Laboratories
8311
Livermore, CA 94550
415-294-2906

Susan Picologlou
Advanced Photon Source
Argonne National Laboratory
Building 360
9700 South Cass Avenue
Argonne, IL 60515
708-972-5105

James R. Norris
Chemistry Division
Argonne National Laboratory
Building 200, E-133
9700 South Cass Avenue
Argonne, IL 60439
708-972-3544

Tanya M. Prokop
Franciscan University
Biological & Medical Research Div./Bldg. 200
c/o Argonne National Laboratory
9700 South Cass Avenue
Argonne, IL 60439
708-972-3862

Michael J. Rixner
Iowa State University
Materials & Components Tech. Div./Bldg. 212
c/o Argonne National Laboratory
9700 South Cass Avenue
Argonne, IL 60439-4838
708-972-5115

Heinz J. Robota
Engineered Products and Processes
Allied-Signal Research and Technology
P.O. Box 5016
50 East Algonquin Road
Des Plaines, IL 60017-5016
708-391-3129

Brad M. Savall
University of Wisconsin-Stevens Point
Chemistry Division/Building 200
c/o Argonne National Laboratory
9700 South Cass Avenue
Argonne, IL 60439
708-972-6674

Alan Schriesheim
Office of the Director
Argonne National Laboratory
Building 201
9700 South Cass Avenue
Argonne, IL 60439
708-972-3872

Gopal Shenoy
Advance Photon Source
Argonne National Laboratory
Building 360
9700 South Cass Avenue
Argonne, IL 60439
708-972-5537

Eric Sirota
Exxon Research and Engineering Company
Route 22 East
Annandale, NJ 08801
908-730-3407

Per O. Spanne
Department of Applied Science
Brookhaven National Laboratory
Bulding 815
Upton, NY 11973
516-282-3322

Martin J. Steindler
Chemical Technology Division
Argonne National Laboratory
Building 205
9700 South Cass Avenue
Argonne, IL 60439
708-972-4314

W. Elane Streets
Chemical Technology Division
Argonne National Laboratory
Building 205
9700 South Cass Avenue
Argonne, IL 60439
708-972-4460

Shiu-Wing Tam
Chemical Technology Division
Building 205
Argonne National Laboratory
9700 South Cass Avenue
Argonne, IL 60439
708-972-7531

Jau Tang
Chemistry Division
Argonne National Laboratory
Building 200
9700 South Cass Avenue
Argonne, IL 60439
708-972-3539

Ben S. Tani
Chemical Technology Division
Argonne National Laboratory
Building 205
9700 South Cass Avenue
Argonne, IL 60439
708-972-4349

David C. Thomas
Department of Analytical Research
& Services
Amoco Corporation
Box 3011
Naperville, IL 60566-7011
708-420-4812

Marlon C. Thurnauer
Chemistry Division
Argonne National Laboratory
Building 200
9700 South Cass Avenue
Argonne, IL 60439
708-972-3545

Erven H. Van Deventer
Chemical Technology Division
Argonne National Laboratory
Building 205
9700 South Cass Avenue
Argonne, IL 60439
708-972-4544

Grayson H. Via
Department of Corporate Research
Exxon Research & Engineering Company
Route 22 East
Annandale, NJ 08801
908-730-2255

P. James Viccaro
Advanced Photon Source
Argonne National Laboratory
Building 360
9700 South Cass Avenue
Argonne, IL 60439
708-972-4732

Maude H. Volk
Center for Governmental Research
Northern Illinois University
148 North 3rd Street
DeKalb, IL 60510
815-753-0957

Zhiyu Wang
Chemistry Division
Argonne National Laboratory
Building 200, E-101
9700 South Cass Avenue
Argonne, IL 60439
708-972-3590

Michael J. Wassmer
Lafayette College
Mathematics & Computer Sci. Div./Bldg. 221
c/o Argonne National Laboratory
9700 South Cass Avenue
Argonne, IL 60439
708-972-6641

Randall E. Winans
Chemistry Division
Argonne National Laboratory
Building 200
9700 South Cass Avenue
Argonne, IL 60439
708-972-7479

Dale T. Woodin
Western Michigan University
Physics Division/Building 203
c/o Argonne National Laboratory
9700 South Cass Avenue
Argonne, IL 60439
708-972-4016

King Lun W. Yeung
Chemical Engineering Department
University of Notre Dame
Notre Dame, IN 46556
219-239-5802

Wenbing Yun
Advanced Photon Source
Argonne National Laboratory
Building 360
9700 South Cass Avenue
Argonne, IL 60439
708-972-5320

Gerry Zajac
Department of Analytical Research
Amoco Research Center
P.O. Box 3011
Naperville, IL 60566
708-961-7722

*U.S. GOVERNMENT PRINTING OFFICE: 1992-643-756

END

DATE
FILMED
3/16/92